Functionality of Noble-Metal Clusters: Reactivity and Optical Properties

DISSERTATION

zur Erlangung des akademischen Grades
doctor rerum naturalium
(Dr. rer. nat.)
im Fach Chemie

eingereicht an der
Mathematisch-Naturwissenschaftlichen Fakultät I
Humboldt-Universität zu Berlin

von
Diplom-Chemiker Christian Bürgel
geboren am 06.03.1979 in Berlin

Präsident der Humboldt-Universität zu Berlin:
Prof. Dr. Dr. h.c. Christoph Markschies

Dekan der Mathematisch-Naturwissenschaftlichen Fakultät I:
Prof. Dr. Lutz-Helmut Schön

Gutachter:

1. Prof. Dr. Vlasta Bonačić-Koutecký
2. Prof. Dr. Klaus Rademann
3. Prof. Dr. Piercarlo Fantucci

eingereicht am:	19.01.2009
Tag der mündlichen Prüfung:	20.02.2009

Acknowledgment

This thesis would not have come into existence without the support and inspiration of many people whose support I deeply appreciate.

Above all, I would like to express my sincere gratitude to my supervisor Prof. Vlasta Bonačić-Koutecký, who offered invaluable assistance, support and guidance. I had the privilege to join the group of Prof. Bonačić-Koutecký at an early stage as an undergraduate student in the 5th semester. She gave me the opportunity to actively participate in all aspects of the scientific research. In particular, I am truly thankful for the opportunity to interact with many excellent scientists in the field of theoretical and experimental physical chemistry and cluster science.

I am deeply grateful for the excellent and fruitful cooperations with the experimental groups of Prof. A. Welford Castleman, Prof. Thorsten M. Bernhardt, Prof. Wolfgang Eberhardt, Prof. Michael W. Linscheid, and Prof. Lai-Sheng Wang, and the invaluable and stimulating discussions with the theoretical group of Dr. Leeor Kronik.

In particular, I am deeply grateful to Prof. Castleman and his group members, namely Dr. Michele L. Kimble, Dr. Nelly M. Reilly, and Grant E. Johnson, for giving me the opportunity to visit their labs and for being excellent hosts making me feeling comfortable and welcome at the Pennsylvania State University. Furthermore, I would like to thank Dr. Leeor Kronik and Doron Naveh for stimulating scientific discussions and for personal hospitality making my stay at the Weizmann Institute unforgettable.

I would like to express my deepest gratitude to Dr. Roland Mitrić without whose knowledge and assistance this thesis would not have been successful. Moreover, I am fortunate that we shared an office for many years being always not only colleagues but also very good friends.

I wish to thank the former and current group members, in particular Ute Werner, Alexander Kulesza, and Melanie Nößler, for being close friends and wonderful colleagues. I am deeply obliged to their invaluable support and assistance. I also would like to address my gratitude to Bernd Böttcher and Katharina Pfaff for their technical and administrative support. I am indebted to Alexandra Soska for the competent proof-reading of this thesis. Financial support by the DFG-Schwerpunktprogramm 1153 „Cluster auf Oberflächen: Elektronenstruktur und Magnetismus″ is gratefully acknowledged.

Finally, I owe special gratitude to my family for always being there when I needed them most. They deserve far more credit than I can ever give them.

Contents

III Optical Properties of Small Supported Silver Clus-

List of Figures

List of Tables

Introduction

For a long time it has been assumed that the properties of small metal clusters, which are aggregates of only few atoms, can be obtained by downscaling the properties of the bulk material. However, when the particle size is reduced below a few nanometers unexpected new properties and thus functionalities arise. Since this thesis contains contributions to three scientific fields, which are cluster models in the context of the heterogeneous catalysis, the ultrafast dynamics of noble-metal clusters, and the optical properties of supported silver clusters, each of these scientific topics will be briefly outlined.

Cluster Models for the Heterogeneous Catalysis (Part I) A striking example for the influence of size reduction on the reactivity properties relevant for the heterogeneous catalysis are nano-sized gold particles which show an unusually high catalytic activity in oxidation processes even at cryogenic temperature [1–4]. In contrast, gold surfaces are known to be chemically inert - this is why gold is usually called "noble". In addition to the size effect, which is partially responsible for the observed activity, relativistic effects are very strongly pronounced in gold [see Ref. 5, and references therein]. The relativistic effects, caused by the high nuclear charge of the gold atom, are the key factors determining the chemical and physical properties of gold clusters. Consequently, the chemistry involving gold clusters is considerably different from the chemistry of alkali metals which exhibit a similar electronic configuration. The unique properties of nano-sized gold open new perspectives for using gold nano-catalysts in numerous technical applications such as pollution and emission control, chemical processing of bulk and fine chemicals and sensors to detect poisonous or flammable gases [6]. In fact, gold catalysts have already been well established within a major industrial process which is the manufacture of vinyl acetate monomer [7]. However, the origin of the high catalytic activity has not yet been fully understood and many experimental and theoretial studies aimed to unravel the nature of the active sites and the underlying mechanisms [1–4, 8–33].

Since ensembles of atoms on catalytic surfaces have been described as "cluster-like" [34], gas-phase clusters provide valuable model systems for finding and examining reactive sites [35], thereby providing complementary information that serves to unravel the mechanisms involved. Establishing the structure-reactivity relationships in gas-phase clusters can be especially valuable in catalyst development through elucidating the influence which various stoichiometries and oxidation states have on reaction mechanisms. Due to the similarity between the electronic structures of catalytically active supported gold nanoparticles [14, 25] and those of free gold clusters, it has been realized that a study of the reactions of gas-phase gold clusters can provide information which is useful in elucidating the role of the degree of aggregation, charge state, and stoichiometry on mechanisms involved in the oxidation reactions. Moreover, by examining gold clusters supported at metal oxide surfaces it has been shown that an electron transfer from the environment to the gold clusters can lead to partially negatively charged active sites, which significantly enhances the catalytic activity [14]. Furthermore, cationic gold species have been identified in gold nano-catalysts [19, 26, 30, 36] and the role of these sites remains to be unravelled. Consequently, anionic and cationic gas-phase gold clusters can serve as models for reactive centers which when embedded at surfaces might be relevant as active sites in gold nano-catalysts.

One especially active research area focuses on the removal of pollutants such as the oxidation of carbon monoxide (CO) to carbon dioxide (CO_2). Oxidation of this toxic gas is of importance for many practical applications beyond combustion exhausts, including the development of CO detection devices and improved efficiency of CO_2 lasers [3]. Despite many recent valuable experimental and theoretical contributions, the question remains whether molecular or dissociative oxygen is formed on gold clusters providing the mechanism for the reaction and removal of CO by oxidation. A general reaction mechanism has been established proposing that the O_2 molecule binds intact to the gold clusters and that dissociation of the O-O bond cannot be achieved by the gold clusters alone [9, 11, 15]. From recent studies it is known that CO and O_2 bind cooperatively to gold clusters which means that one species is assisting in binding the other [18, 21]. Furthermore, in the corresponding oxidation mechanism, intermediate species with atomic oxygen are proposed and experimentally confirmed [18, 21]. Moreover, negatively charged gold-oxide clusters with atomic oxygen have been identified as possible structural features in working gold-containing catalysts [17, 30, 37].

Therefore, a part of this thesis addresses the role of the atomic oxygen in the reactivity of gold clusters towards CO on the example of anionic gas-phase gold-oxide clusters, which can contain molecular as well as atomic oxygen (Chapter 3). It will be shown that although the atomic oxygen is highly reactive, its presence does not guarantee that an CO oxidation reaction will occur. Different reaction channels, in particular the association of CO, will be addressed to determine the importance of reaction channels competing with the oxidation (Chapters 3.2 and 3.3).

Moreover, since a part of this thesis focuses in particular on the role of the charge state, the reactivity of the anionic and cationic gold-oxide clusters will be compared. Therefore, the structure-reactivity relationships will be established for the small cationic gold-oxide clusters (Chapter 4), and the underlying mechanisms for oxidation and association of CO will be proposed. This will provide a detailed understanding of the experimental results obtained by our partner Prof. Castleman (Pennsylvania State University, USA) and his group. The theoretical and experimental findings provide new insight into the role of the charge state on the reactivity of gold clusters, and thus might contribute to better understanding the reactivity of gold-based nano-catalysts (Chapter 5).

In order to fully understand the activation of oxygen in the context of the gold-based catalysis, profound knowledge of the nature of the gold-oxygen bond is mandatory and thus Chapter 6 of this thesis focuses on the bonding in the smallest model systems, $AuO_{1,2}^-$. Moreover, the valent isoelectronic sulfide species have been examined for comparing them with the corresponding Au-O systems. However, understanding the Au-S bonding is of particular importance also in the context of self-assembled monolayers (SAMs [38]) which can be films, nanowires, and other nanostructures of disulfides or *n*-alkane thiolates. These can be bound on extented gold surfaces or nanoparticles which after preparation spontaneously self-organize into crystalline or semi-crystalline highly regular structures. This allows generating well-defined organic surfaces with useful and highly tunable chemical functionalities, which opens new perspectives for applications as biocompatible materials, chemical sensors and in lithography [38].

The Au-X (X=O, S) bondings exhibit contributions from a strong electron correlation and spin-orbit coupling due to the relativistic effects. Therefore, high-level theoretical multi-reference methods explicitly including spin-orbit coupling are employed in this thesis to gain insight into the nature of the Au-X chemical bondings. The theoretical findings are quantitatively supported by experiments from Prof. L.-S. Wang (Washington State University, USA) and his group, employing the photoelectron spectroscopy (PES) with high precision and resolution.

Ultrafast Dynamics of Noble-Metal Clusters (Part II) In the nanometer-size regime, small noble metal clusters show fascinating strongly size-dependent dynamical properties. Therefore, two topics will be presented: a) The influence of the nature of internal vibrational energy redistribution (IVR) on reactivity, and b) the time-dependent dynamics of gold clusters in the excited electronic states.

a) Differences in the reactivity of small anionic gold and silver clusters containing only a few atoms have been observed in the oxidation of CO by molecular O_2 [21, 28, 39]. In contrast to the size-selected anionic gold clusters, the corresponding silver species remain unreactive under comparable experimental conditions [39]. Moreover, it will be shown on the example of Au_n^- / Ag_n^- (n=1-6) that in the few atom-size regime the structural and binding properties of small silver and gold clusters are similar. Furthermore, the stationary energy profiles for the oxidation of CO by $Au_2O_2^-$ and $Ag_2O_2^-$ exhibit almost equal barriers. Thus deducing only from the stationary properties, similar reactivity should be expected. Therefore, Chapter 7 of this thesis aims to show that the dynamical properties are responsible for the differences in the observed reactivity. It will be demonstrated that an inherently different type of dynamical processes such as IVR can be identified in gold and silver clusters, which might be a key factor determining the efficiency of O_2 activation by noble-metal clusters.

b) Motivated by the fascinating dynamical properties of the gold clusters in the electronic ground state, the dynamics of the excited electronic states and the role of IVR in the relaxation processes will be addressed in Chapter 8 of this thesis. Combining theoretical methods for describing the nuclear dynamics in the excited electronic states with the non-adiabatic hopping to the ground electronic state made it possible for the first time to calculate time-resolved photoelectron spectroscopy (TR-PES) spectra from propagation of an ensemble of classical trajectories in the excited electronic states. Recently, powerful experimental techniques in the field of the time-resolved photoelectron spectroscopy (TR-PES) have been developed to follow cluster dynamics in the ground and excited electronic states (see e.g. [40, 41]) and thus to distinguish different dynamical processes such as IVR, geometric rearrangements and fragmentation [42]. Therefore, in this thesis the extremely size-dependent nuclear dynamics of photoexcited small gold clusters will be examined and compared to the experimental results obtained by Prof. W. Eberhardt (BESSY, Germany) and his group.

Optical Properties of Supported Silver Clusters (Part III) Another striking example for the surprising properties emerging from quantum confinement is the multi-color fluorescence of small silver particles with only a few atoms which, like all other metals, are not able to fluoresce as bulk material. In recent experiments, photoactivated intermittent fluorescence from initially non-luminescent silver-oxide thin films has been observed [43–47]. Irradiation of these films by infra-red (IR) or ultra-violet (UV) light induces a photochemical transformation in the silver-oxide films, so that after the subsequent visible light excitation irradiated areas give rise to dynamical multi-color fluorescence. It has been proposed that these luminescent properties of silver-oxide thin films are due to the formation of small silver particles. In fact this is analogeous to the process in photography which is responsible for the latent image creation [48, 49]. In that case, photo-films containing silver halogenides are photochemically reduced upon activation by photons (light) leading to the formation of small metallic silver particles.

The local photo-activation of silver-oxide films and the possibility to excite the fluorescence in the visible regime represents an attractive perspective for different applications in the context of devices for optical data storage and opto-electronics [43, 45, 47, 50–54]. However, electronic and structural properties of emissive centers, which are responsible for the observed fluorescence, as well as their creation mechanism are still unknown. Knowledge about both aspects is essential for proposing efficient new materials based on the optical properties of cluster-support systems. Interestingly, small silver clusters in bio-environments also exhibit fluorescence so that they can be used for bio-fluorophores, e.g. in cell imaging [55–57].

In this context, the optical properties of small silver clusters in the size regime in which each atom counts are of particular importance since adding a single atom strongly influences their structures, absorption patterns and possibly the nature of excited electronic states. In fact, the occurrence of fluorescence is directly connected with sufficiently long lifetimes of corresponding excited electronic states. The necessary but not sufficient requirement for this is that intense transitions involve electronic states which are bound. However, bound electronically excited states are usually not observed in gas-phase clusters larger than the trimer [58]. The situation is different when the clusters are embedded in rare-gas matrices [59–63] due to the caging effect which prevents the dissociation of excited electronic states by dissipating excess energy. This allows observing laser-induced fluorescence for silver clusters with up to nine Ag atoms, i.e. Ag_9 embedded in an argon matrix [63].

Moreover, it has been demonstrated on the example of large silver clusters embedded in different oxidic materials that interface properties can strongly influence the absorption [64]. Therefore, the examination of the influence of the interface on the optical properties of small noble-metal clusters offers the opportunity to question whether emissive properties are exclusively due to clusters by themselves while the support serves only as a stabilizing factor or whether the proper choice of the support might contribute to emissive properties as well.

In this thesis, the fluorescence of pure small silver clusters in different environments will be addressed employing density functional methods (Part III). As a first step, the optical properties of silver clusters interacting with the silver-oxide support [65] have been studied. However, due to the Ag-Ag interaction between the cluster and the oxidic silver support and the strong mixing of excitations within both subunits the inherent cluster and support contributions cannot be distinguished. Thus it is not possible to unravel the mechanism for photoemission. Consequently, an ionic MgO support offers a more suitable environment for studying optical properties of supported silver clusters since the contributions from the cluster and the support can be easier distinguished. Numerous theoretical studies of noble-metal clusters at the MgO support mainly concentrated on the ground state properties in the context of catalytic activity [66–78]. However, studies on optical properties of supported coinage-metal clusters are very scarce [79, 80] and do not address optical properties of supported silver clusters.

The structural and optical properties of gas-phase silver clusters $\mathrm{Ag_n}$ (n=1-8) have been previously investigated in the group of Prof. V. Bonačić-Koutecký using accurate quantum chemical methods accounting for electronic correlation effects based on the wavefunction approach [81, 82]. However, since these methods cannot be applied for studying complex environments such as the MgO support, the structural and optical properties of silver clusters are derived from density functional methods and will be presented in Chapter 11 of this thesis.

The part of this thesis addressing the optical properties focuses on revealing the mechanism responsible for the absorption and emission of supported silver clusters at different model sites of the MgO surface (Chapter 12). The choice of the sites has been made in order to study the influence of the stoichiometric surface and of the simplest oxygen vacancy (F_S center defect[1]) on the absorption patterns of silver clusters. Therefore, a comparison of optical and emissive properties of small silver clusters at these two different sites of the MgO support is presented in Chapters 13 and 14. Moreover, this study leads to the proposal of size-selective emissive centers. In order to describe the support, a state-of-the-art cluster embedding method has been applied to calculate accurate binding energies and transition energies for absorption and possible fluorescence of the supported clusters. The analysis of the nature of excitations within the interacting subunits allows characterizing and classifying the optical transitions as a function of the cluster size and the nature of the support site (Chapter 15). The obtained results may serve as a good starting point for further examining the absorption properties of clusters supported at other classes of defects and in different environments such as bio-matrices.

---

[1] This kind of point defect represents an oxygen vacancy which is filled by two electrons. The properties of such trapped electrons have been known for long time and they are responsible for the colors of defect-rich crystals and surfaces - hence this kind of surface defect is called F_S center which comes from the German word “Farbe” meaning “color” [83].

Part I

Reactivity of Noble-Metal Clusters in the Context of Heterogeneous Catalysis

Chapter 1

Introduction

Since the pioneering work of Haruta and co-workers [1–4] on the surprisingly high catalytic activity of small supported gold nanoparticles many studies in the gas phase as well as on the support have been performed [1–4, 8–33] aiming at understanding the fundamental factors which govern the gold nanoparticle catalysis. However, the exact mechanism of the oxidation reaction, e.g. in combustion, and the underlying processes are still subject of controvers. This introduction aims to give an overview of recent experimental and theoretical studies concerning different key aspects which are relevant in the context of heterogeneous gold-based catalysis. These aspects include fundamental questions which will be addressed in this thesis:

- How is molecular oxygen activated by gold-cluster species?
- What are the reactive centers in gold containing catalysts?
- What is the role of atomic vs. molecular oxygen? Does the presence of atomic oxygen guarantee the oxidation reaction to proceed?
- How are both reactants (CO, O_2) bound? Do they compete for adsorption sites or is there cooperative binding?
- What are the reaction channels which compete with the oxidation channel?
- How does the charge state influence reactivity?

A key step in any industry-relevant oxidation reaction is the activation of molecular oxygen. Therefore, initial studies aimed to understand why small gold particles can strongly bind oxygen, in contrast to the clean gold surface which is essentially inert. Lee and Ervin [11] performed low-pressure guided-ion beam (GIB) studies on Au_n^- (n=2-7) finding that the anionic clusters with an odd number of gold atoms (n=1, 3, 5, 7) essentially do not bind molecular O_2. In contrast, clusters with an even number of gold atoms bind exactly one oxygen molecule strongly. Cox and coworkers [9] examined the reactivity and saturation of small gold clusters, also finding that only the anions with an even number of atoms are reactive towards O_2. The authors have related their finding to the electron affinity of the gold clusters, which has been found to oscillate with the number of atoms [10]. They suggest that oxygen is bound in a dissociated form and that the electronic nature of both the cluster and the adsorbate affect the binding. In related studies, Wallace and Whetten [15] used pulsed helium flow techniques and reported that either no or at most one O_2 molecule adsorbs intactly on most even numbered clusters Au_n^- (n=1-22). Their explanation for the lack of reactivity of odd n Au_n^- is that if the di-oxygen acts as an one-electron acceptor, the anionic species will be left with an unpaired electron yielding a high electron affinity. Since their work [15] has been published it is commonly accepted that the mechanism of O_2 binding onto anionic gold clusters is due to the transfer of the unpaired electron from Au_n^- (n= even) to the $2\pi^\star$ orbital of O_2 resulting in a super-oxo species bound to the gold cluster.

After understanding has been gained on how molecular oxygen is bound to anionic gold clusters in the gas phase, the question has been raised how these gold-oxide clusters containing molecular O_2 groups are able to oxidize the CO molecule. In high-pressure gas-phase experiments on the oxidation of CO by molecular O_2 in the presence of anionic gold clusters, Wallace and Whetten [21] found cooperative adsorption of CO and O_2. Their results suggest that one adsorption partner assists the binding of the other species, e.g. Au_2^- binds CO only if O_2 is already present. Furthermore, they find that oxygen is bound molecularly in the super-oxo form O_2^- and not in atomic form. The highest rate of CO oxidation has been found for Au_6^- and a reaction cycle has been proposed in which the formation of CO_2 depends on the appearance of species that correspond to $Au_n(CO)_xO^-$ [21]. These clusters contain an odd number of oxygen atoms which indicates the existence of either atomic oxygen or a carbonate-like structure (CO_3 subunit) within the catalytic cycle. Wöste and co-workers [18] observed species of the form $Au_n(O_2)_m(CO)_x^-$ through the reaction of carbon monoxide and molecular oxygen with mass-selected gold-cluster anions. Utilizing a radio frequency ion trap mass spectrometer at low temperatures, they observed an intermediate species $Au_2CO_3^-$ with di-gold carbonate or peroxyformate-like structure [18]. Moreover, their joint experimental and theoretical work with Heiz, Häkkinen and Landman [28] provided evidence for the catalytic oxidation of CO by gas-phase Au_2^-. In contrast, this oxidation channel has not been observed in experiments performed by Castleman et al [84], and therefore the question can be raised how the observation of oxidation products depends on experimental conditions. It will be shown in this thesis that the pressure of the reactants as well as the reaction time are the crucial factors determining the observation of oxidation in one experiment as opposed to the other. Furthermore, the existence of carbonate species as intermediates in gold-based catalysis is still subject of discussion [16, 18, 28, 84–86].

Since gold-based heterogeneous catalysis involves a support, experimental and theoretical studies have been performed for clusters at model surfaces [14, 87–90] and real working catalysts [4, 13, 30, 91–93]. Heiz and co-workers [14] were able to experimentally and theoretically examine the combustion of carbon monoxide on supported, size-selected gold clusters Au_n for n up to 20. These studies showed that the oxidation is size-dependent with Au_8 being the smallest reactive cluster to catalyze the reaction. Furthermore, the theoretical studies revealed that the supported clusters strongly bind to point defects at the oxide support and that a charge transfer from the defect sites partially charges the gold cluster. They suggest that both effects, pinning the cluster at the defect and the charge transfer leading to partially negatively charged gold clusters, play an important part in the activation process of O_2 by gold nano-catalysts. Cooperative binding of CO and O_2 has been found also at the support, e.g. CO adsorbs only onto the supported Au_8 cluster if oxygen is present [14]. Furthermore, Sanchez et al. [14] suggest that dissociation of oxygen in the presence of CO is responsible for the formation of CO_2.

Different aspects such as the role of the adsorbate-support interface [13, 87, 91] and the influence of water on the reactivity [4, 30, 88, 92] have been discussed, and the attention has largely focused on how these effects, in combination with the charge transfer from defect sites of the support material, can weaken the bond in molecular oxygen in order to promote the oxidation reaction. However, more recent work [89, 90, 93] has demonstrated that charging adsorbed metals does not always involve the presence of defects on the oxide surface. Both experimental and theoretical studies have verified the presence of charged gold species on thin defect-free MgO surfaces supported on Mo and Ag [89, 90, 93]. It is proposed that by varying the thickness of the MgO layer, and thereby the work function of the underlying metal, it may be possible to tune the charging of the supported Au clusters [93].

The role of atomic oxygen in the gold nanocatalysis has not been addressed until recently. An experimental study has shown that gold oxides containing both atomic and molecular oxygen may play a role as the active site in supported gold catalysts [17, 30, 37]. In fact, it has been shown through a time-of-flight secondary ion mass spectrometry (TOF-SIMS) study that AuO^- is a structural feature found on gold-based catalysts [37]. Recent studies have also identified the presence of cationic gold centers in operational gold catalysts for the CO oxidation [19, 26, 30, 36]. Through a variety of analytical techniques, it has recently been confirmed that for gold catalysts supported on Fe_2O_3, gold is present in both the metallic and cationic forms and that the presence of the cationic gold is essential for the high CO oxidation efficiency [36]. Other experimental studies have shown that the cationic gold which is initially present in the working catalyst is reduced to metallic gold through exposure to CO, which thereby lowers the catalytic activity through poisoning [32].

Consequently, in the following a fundamental issue will be addressed focusing on the influence of the charge state and the binding of more than one CO molecule on the reactivity of gold oxides containing both atomic and molecular oxygen (Chapter 3). The findings obtained in the framework of this thesis concerning the reactivity of gold-oxide clusters are the continuation of work presented in the diploma thesis [85] in which the structure-reactivity relation of anionic gold-oxide clusters $\mathrm{Au_nO_m^-}$ (n=1-4, m=1-5) as well as the mechanism for the oxidation of CO have been established. Key results from this previous study, such as structural and binding properties of anionic gold-oxide clusters, identified reactive centers together with the structure-reactivity relationship for the oxidation reaction, and the reaction mechanism for CO oxidation will be shortly summarized in the beginning of Chapter 3.1, and will serve as a basis for further discussion. New findings on anionic gold-oxide clusters will be presented in Chapter 3.1 focusing on reaction channels competing with the oxidation reaction, such as the replacement of oxygen and the association of CO. Since the charge state is an important issue, the structural properties and the energetics of the cationic gold-oxide clusters $\mathrm{Au_nO_m^+}$ (n=1-2, m=1-4) will be presented in Chapter 4. The structure-reactivity relationship will be established and results on different reaction channels will be presented. Comparison with the reactivity of the corresponding anionic clusters will allow for discussion on how the charge state influences CO oxidation in the presence of gold-oxide clusters and which role the reaction conditions play, e.g. the effective number of CO molecules.

All results will be compared with the experimental results from the group of Prof. A. W. Castleman, Jr. (Pennsylvania State University, USA) utilizing a guided ion beam (GIB) apparatus. All findings were obtained in close cooperation with theory.

Another important issue of general interest both in gold catalysis and in the chemistry of thiolate-protected gold nanoparticles concerns the nature of the chemical bond involving gold atoms. Therefore, results on high-level ab initio calculations of AuO^- and AuO_2^- and their isoelectronic AuS^- and AuS_2^- will be addressed in Chapter 6. In combination with the extensive experimental photo-electron spectroscopy (PES) study performed by the group of Prof. L.-S. Wang (Washington State University, USA) this will allow us to obtain a comprehensive understanding of the Au-O and Au-S bond.

Chapter 2

Computational and Experimental Details

Structural properties as well as the reactivity of the anionic and cationic gold-oxide clusters $\mathrm{Au_mO_n^{\pm}}$ m=1-6; n=1-5 were studied using density functional (DFT) methods with Becke's hybrid three-parameter non-local exchange functional together with the Lee-Yang-Parr gradient-corrected correlation functional (B3LYP) [94–97]. Relativistic effects, which substantially influence the bonding properties of gold atoms, were taken into account using the 19-electron relativistic effective core potential (19e-RECP) from the Stuttgart group and the (8s7p5d1f)/[7s5p3d1f] atomic orbital AO basis set [98, 99]. For the oxygen and carbon atoms, the 6-311G(d) triple-ζ split valence basis set was employed. Previous theoretical work on the oxidation of CO in the presence of atomic gold anions [100] and the adsorption of O_2 on hydrated anionic gold clusters [22] has shown that this method provides the appropriate accuracy needed for a proper description of reactivity. This was checked by comparing of the reaction energetics with results obtained using the coupled-cluster method based on highly correlated wave functions. Moreover, the energy sequence of isomers has been confirmed by the more exact coupled-cluster calculations. All structures presented in this thesis were fully optimized using gradient minimization techniques, and frequency analysis was carried out in order to characterize the stationary points as minima or transition states. In order to check the reaction profiles and to affirm the transition states, extensive intrinsic reaction coordinate (IRC) calculations have been carried out confirming that the optimized transition states connect the specified reactants and products. Furthermore, energy profiles were calculated for reactions along several pathways allowing us to propose mechanisms with the lowest barriers. Moreover, the nature of the stationary points has been confirmed by calculating the vibrational frequencies. In order to examine the charge distribution within the clusters, charges for atoms in the clusters have been derived from the natural bonding orbital (NBO) [101] analysis.

The reaction mechanisms were also revealed by performing ab initio molecular dynamics (MD) simulations "on the fly" based on the DFT method. In order to improve the efficiency of the MD simulations, the resolution of identity (RI)-DFT procedure [102, 103] has been employed involving the Perdew-Burke-Ernzerhof (PBE) functional [104] with the 19e-RECP from the Stuttgart group for gold combined with Gaussian basis sets of triple-ζ quality for all atoms [98].

Since the presented theoretical study has been performed in close cooperation with the experimental work done in the group of Prof. A. W. Castleman, Jr., the experimental setup is briefly characterized (for details see reference [105]). Experiments were carried out using a guided ion beam (GIB) apparatus. Gold-oxide clusters were produced in a laser vaporization cluster source by pulsing oxygen seeded in helium into the plasma formed by ablating a rotating and translating gold rod with the second harmonic of a Nd:YAG laser. The clusters exit the source and are cooled by supersonic expansion into vacuum. Gold-oxide clusters are mass selected by a first quadrupole mass filter and then directed into the octapole collision cell. Reactant gas (CO) is introduced with variable pressures and reaction product ions are then extracted and mass-analyzed by a second quadrupole mass spectrometer. It is important to stress the fact that this kind of cluster formation yields gold-oxide species with both molecular and atomic oxygen. Therefore, by this unique setup, the thermodynamically most stable gold-oxide species at a given stoichiometry are formed which are not necessarily the clusters with exclusively molecular oxygen as in other experiments [9, 11, 15, 18, 21, 22, 28].

Chapter 3

Structure-Reactivity Relationship of Anionic Gold-Oxide Clusters

Molecular oxygen O_2, which accounts for a fifth of the air, is the natural oxygen source in heterogeneous catalysis, and thus several experimental and theoretical studies focused on the mechanism of binding molecular oxygen and on the nature of its activation. Although it is assumed that O_2 is molecularily bound to pure gold clusters in the gas phase and to gold clusters at model surfaces there is still an open question about the role of atomic oxygen in the oxidation reactions. Atomic oxygen might be formed when preadsorbed and thus activated molecular $O_2^\star$(ads) reacts with one CO molecule leading to an adsorbed O atom and CO_2

$$O_2^\star(\mathrm{ads}) + \mathrm{CO(g)} \rightarrow \mathrm{O(ads)} + \mathrm{CO_2}.$$

Recently, it has been suggested [16, 28, 106] that the atomic oxygen attached to the gold clusters is highly reactive and thus the oxidation of CO involving the O atom should always proceed easily without barriers. However, in this chapter the structural and electronic properties of small anionic gold-oxide clusters containing not only molecular but also atomic oxygen will be presented in order to demonstrate that although the O atom is indeed a highly reactive center at gold clusters, its existence does not guarantee that the oxidation reaction will proceed.

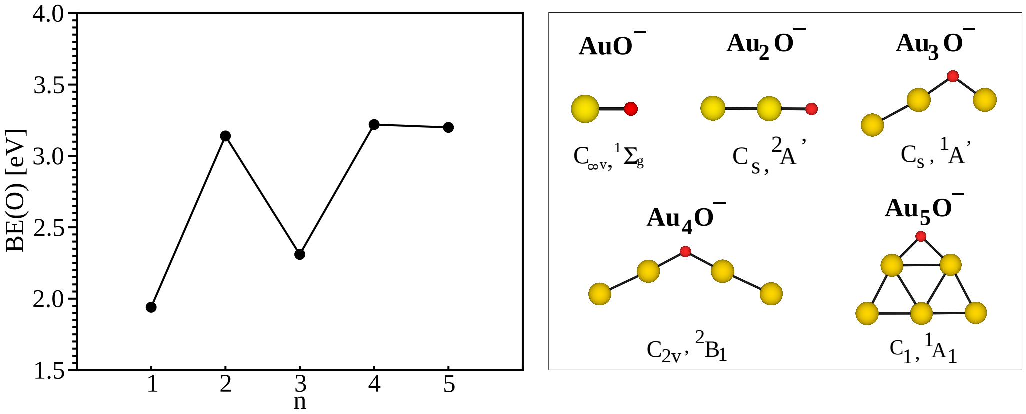

Figure 3.1: Binding energy BE(O) (left) for the most stable structures of Au_nO^- (n=1-5) (right).

3.1 Structural and Binding Properties

The anionic gold-oxide clusters exhibit fascinating structural properties which depend on the ratio between Au atoms and O atoms. Therefore, we will discuss first the binding of one O atom to anionic gold clusters (“gold rich” clusters) which bears resemblance to binding molecular oxygen. Next, structural and binding properties of two O atoms and four O atoms (“oxygen rich” clusters) in anionic gold-oxide clusters will be addressed aiming to point out that although the clusters contain an even number of O atoms, the thermodynamically most stable structures prefer binding oxygen in its dissociated form. Finally, on the basis of the structural and binding properties of the anionic gold-oxide clusters, the reactive centers in the context of oxidation of CO will be identified.

In Figure 3.1 the most stable isomers of gold-rich anionic gold-oxide clusters Au_nO^- (n=1-5) are presented together with the binding energy of the O atom. The binding energy shows an even/odd oscillation similar to the binding patterns of molecular oxygen [15]. For clusters with an even number of electrons, e.g. $Au^-_{1,3}$, electron transfer to the O atom is less favorable due to the higher ionization potential of the anionic gold species. Therefore, clusters with an odd number of electrons ($Au^-_{2,4}$) have a stronger affinity to the atomic oxygen. However, the binding energy is considerably higher in comparison to the binding of molecular oxygen due to the fact that the O atom is a much stronger electron acceptor. From the binding pattern as well as from the analysis of the charge distribution within the anionic gold-oxide

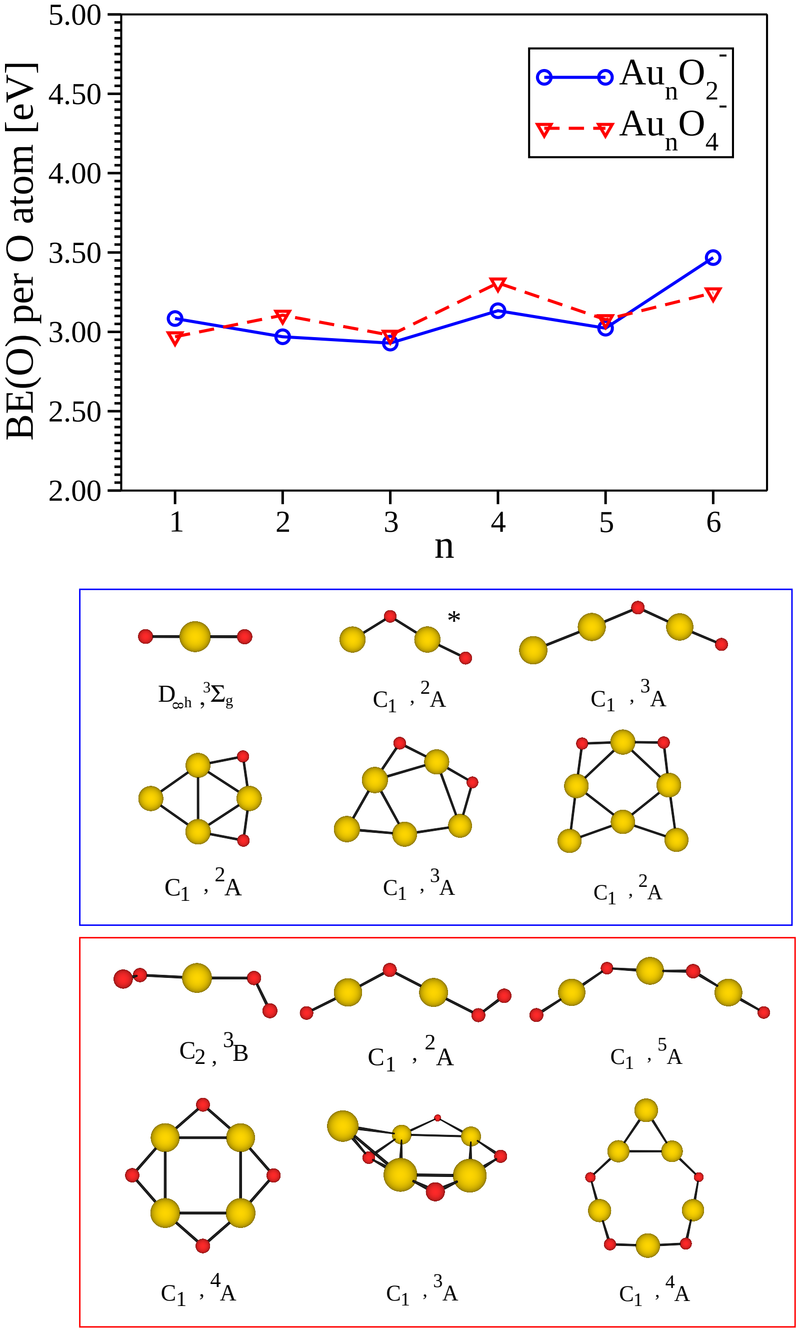

Figure 3.2: Binding energies per O atom (top) for most stable structures (bottom) of $Au_nO_2^-$ (blue) and $Au_nO_4^-$ (red) (n=1-6). Notice that the most stable structure of $Au_2O_2^-$ contains molecular oxygen, and thus the higher lying isomer (*) is given comparison.

cluster it can be concluded that the O atom acts as a $1e^-$ acceptor. Notice, that the oxygen atom is preferentially bound in a bridged position for complexes with three or more gold atoms, in contrast to the anionic gold-dimer oxide in which the O atom is bound in a “peripheral” position. Interestingly, the affinity of Au_5^- towards the O atom is quite pronounced despite the high ionization potential of the corresponding anionic gold pentamer.

The most stable isomers of gold-oxide clusters with two and four oxygen atoms $Au_nO_m^-$ (n=1-6, m=2, 4) are shown in Figure 3.2 (bottom). For clusters with two O atoms the thermodynamically most stable isomers contain dissociated oxygen. An exception is the $Au_2O_2^-$ cluster in which the O_2 is molecularily bound. However, in order to show the general binding properties of atomic oxygen in gold-oxide clusters, the higher lying isomer of $Au_2O_2^-$ with dissociated oxygen will be considered (marked with an asterisk in Figure 3.2). Notice that in clusters with more than three gold atoms, the O atoms are bound in bridged positions to a planar Au_n subunit. In the $Au_nO_4^-$ clusters with four oxygen atoms, binding oxygen is also preferred in dissociated form for n>2. Moreover, chain-like structures ($Au_3O_{3,4}^-$) and ring-like structures ($Au_{4-6}O_4^-$) are formed for clusters with more than two gold atoms. However, the anionic gold atom and dimer contain also one and two O_2 subunits, respectively. This is due to the fact that (i) gold prefers two-fold coordination of adsorbants and (ii) because the number of possible adsorption sites is drastically reduced until there are only two possible sites for adsorption of four O atoms onto Au^-. Consequently, the molecular binding of one and two O_2 molecules occurs for Au_2^- and Au^-, respectively.

Notice that the majority of the gas-phase $Au_nO_{2,4}^-$ clusters with an even number of oxygen atoms assumes structures which are only present under conditions which provide atomic oxygen in the cluster formation process, e.g. in the experiments of Castleman et al. [84, 100, 107]. This is due to the fact that the barrier for dissociation of O_2 on the clusters is very high, easily exceeding the binding energy of the O_2. This is in line with the experimental findings that if only molecular oxygen is present, anionic gold clusters Au_n^- with an odd number of Au atoms (n=1, 3, 5) do not adsorb O_2 molecules and thus do not yield $Au_nO_{2,4}^-$ clusters.

As also shown in Figure 3.2, the binding energy per O atom defined as $BE(O) = E[Au_nO_m^-] - m\,E[O] - E[Au_n^-]$ as a function of n has almost constant values around 3 eV. This is due to the fact, that in the case of an anionic gold cluster with an odd number of electrons the first O atom is strongly bound (cf. Figure 3.1) withdrawing one electron and thus leaving the metal subunit effectively neutral with an even number of electrons. Consequently, the second O atom is weaker bound. The situation is reversed for gold

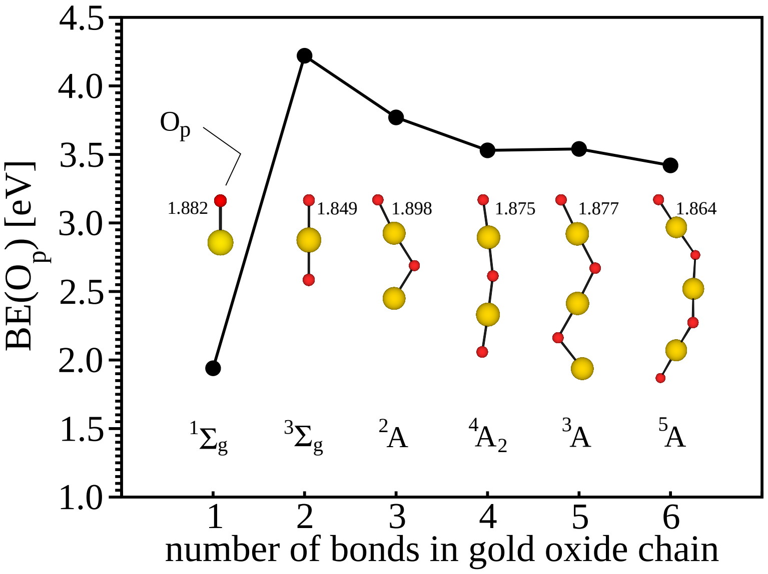

Figure 3.3: Binding energy for the peripheral O atom [BE(O_p)] as a function of the anionic gold-oxide chain length.

clusters with an even number of electrons. Although the first O atom is weaker bound it is still a strong electron acceptor and hence activates the gold clusters yielding a higher binding energy for the second O atom. The effect holds true also for the third and fourth oxygen atom. Therefore, the averaged binding energy per atom does not vary much with the cluster size.

In contrast, the binding energy of the peripheral O atom does strongly depend on the number of gold and oxygen atoms. In this context we find that anionic gold-oxide clusters show fascinating structural properties which arise from the preferred binding of dissociated oxygen. This is particularly expressed in the chain-like growth with an increasing number of gold and oxygen atoms. The chain structures with alternating Au and O atoms are favorable up to a chain length of six Au-O bonds. This is remarkably long, demonstrating the directionality of the Au-O bond and thus the activation of the d-electrons of gold. However, the attachment of a fourth gold atom to $Au_3O_4^-$ leads to the formation of a ring structure (cf. Figure 3.2). In Figure 3.3 the most stable isomers of selected anionic gold-oxide clusters [1] together with the binding energy of the peripheral O atom (O_p) as a function of the

---

[1] The most stable isomer of $Au_2O_2^-$ contains molecular oxygen. The chain-like structure is shown for discussion.

number of Au-O bonds in the gold-oxide chain are shown. As can be seen from the shown isomers, the O-Au-O subunit is linear due to the symmetry of the interacting d-orbitals of gold and the p-orbitals of oxygen and also due to the fact, that gold prefers the two-fold coordination. As will be discussed in detail in Chapter 6 on the examples of AuO^- and AuO_2^-, atomic oxygen highly activates the d-electrons of the gold anion leading to Au-O bonds with multiply bonding character. The gold-oxide chains are bent at bridging O atoms with angles of around ≈120-130°.

The gold monomer oxide AuO^- exhibits a remarkably low binding energy [$BE(O_p)=1.94$ eV] with respect to the lowest possible fragmentation channel which is the spin-forbidden formation of $^1Au^-$ and triplet oxygen atom ^3O. In contrast, the binding energy for the peripheral O_p atom in AuO_2^- is twice as large [$BE(O_p)=4.22$ eV]. Its value is only slightly decreasing with chain length yielding 3.42 eV for the $Au_3O_4^-$ cluster. Thus, the pattern in Figure 3.3 shows that (i) the binding energy of O_p is significantly influenced by the second oxygen atom and that (ii) the influence of the rest of the chain is less pronounced. Both effects should have direct consequence for the reactivity in particular of AuO^- and $OAuO^-$.

In summary, the most stable structures of the majority of the anionic gold-oxide clusters examined in this study prefer binding dissociated oxygen. The oxygen atoms act as strong electron acceptors. It has been shown that the structures of the anionic gold-oxide clusters depend on the ratio between gold and oxygen atoms leading to (a) structures with a bridged O atom in gold-rich clusters with only one O atom ($Au_{n>2}O^-$), (b) to chain-like structures for small oxygen-rich gold-oxide clusters with less than four Au atoms, and (c) ring-like structures for the larger oxygen-rich gold-oxide cluster with more than three Au atoms. Also structures with O_2 subunits have been found ($Au_{1,2}O_4^-$, $Au_2O_2^-$). Consequently, three reactive centers have been identified: a) the peripheral O atom, b) the bridging O atom and c) the molecular O_2 group. In the next chapters, the different reaction channels i) oxidation channel, ii) replacement channel and iii) association channel will be discussed and the structure-reactivity relationship for each of the three reactive centers will be established. The first two channels (i and ii) have already been addressed in the diploma thesis [85] and will be only shortly summarized. The presentation will focus on the new findings regarding the association channel (iii) for anionic gold-oxide clusters.

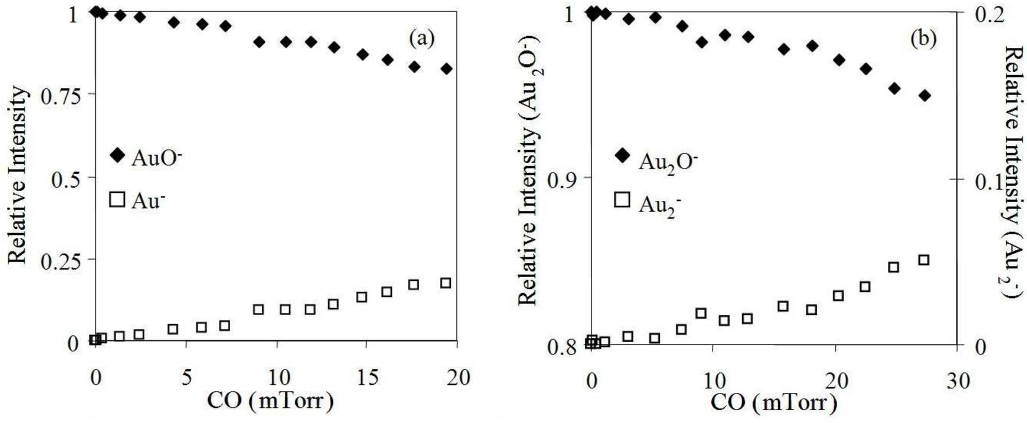

Figure 3.4: Experimental branching ratios for the reaction of AuO^- (left part) and Au_2O^- (right part) with CO.

3.2 Oxidation of CO by Anionic Gold-Oxide Clusters

Oxidation represents the perhaps most commonly used reaction in gold-based heterogeneous catalysis, and therefore discovering the underlying mechanisms is of general importance. The reactive centers of the negatively charged gold-oxide clusters, which can serve as model systems, have been presented in Chapter 3.1. In the following, findings on the oxidation channel will be presented for each of the three reactive centers, and the established structure-reactivity relationship will be discussed. Due to close cooperation with the group of Castleman also the experimental results will be shortly summarized. It will be also shown that by joint theoretical and experimental studies, the mechanisms responsible for experimental findings have been found.

3.2.1 The Peripheral Oxygen Atom

In Figure 3.5 we present experimental results [84, 100, 108] showing that the oxidation reaction with CO occurs for AuO^- and Au_2O^-. The branching ratios show the loss of signal of the parent ions $Au_{1,2}O^-$ and the corresponding increase in signal intensity for the product ions $Au^-_{1,2}$. Notice that there is no competing reaction channel such as association or replacement which would yield $Au_{1,2}O(CO)^-$ or $Au_{1,2}(CO)^-$.

The peripheral oxygen atom which is present in both species has been identified as the most reactive center for oxidation. The reaction follows an Eley-Rideal (ER) mechanism (cf. Figure 3.5) which will be described in the

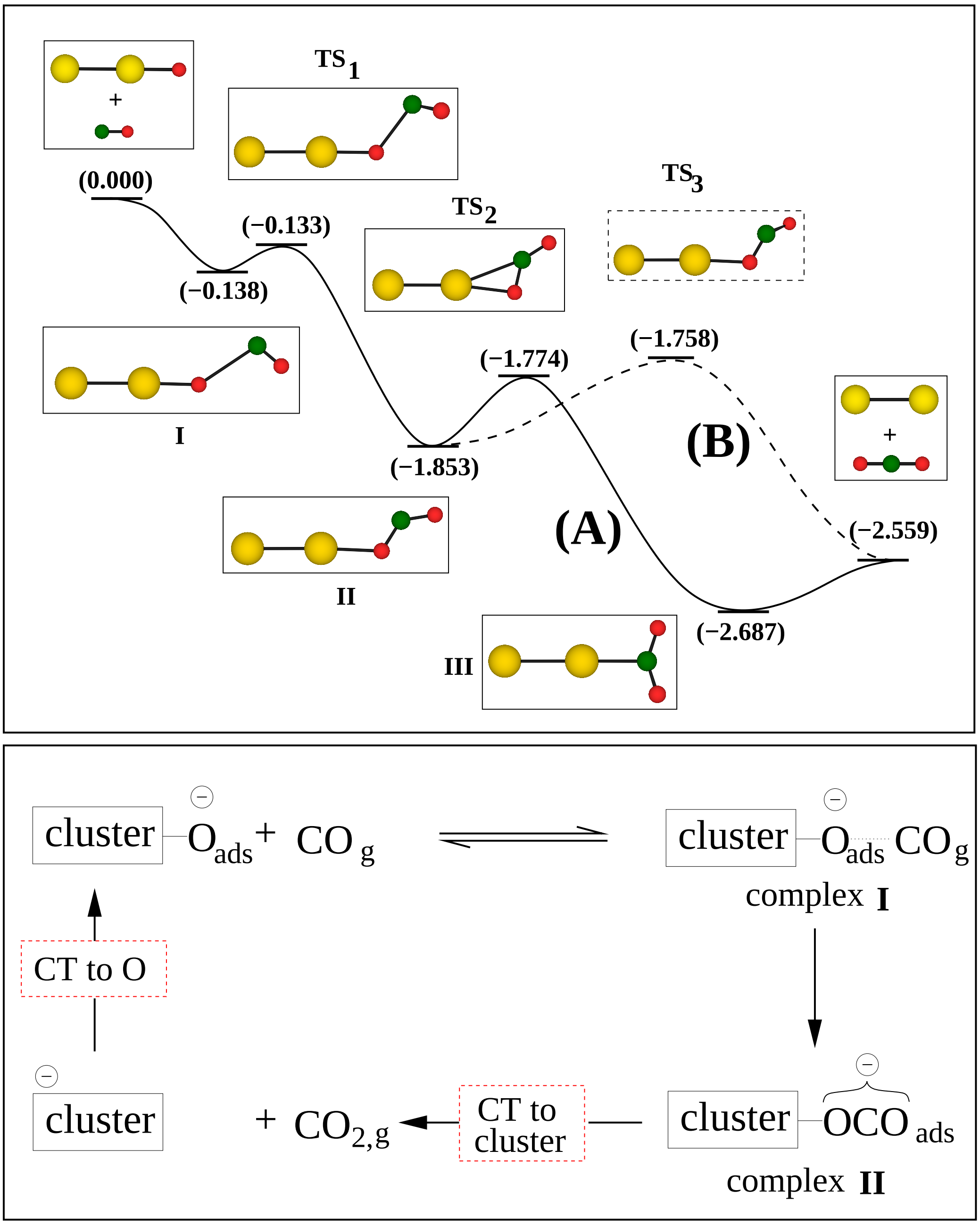

Figure 3.5: top: Energy profile for the oxidation reaction of Au_2O^- with CO along two reaction pathways A ("geometry rearrangement") and B ("rotation of CO_2 subunit"). bottom: Scheme for oxidation at the peripheral O atom in anionic gold-oxide clusters following the Eley-Rideal mechanism (CT=charge transfer).

following: The reaction at the peripheral O atom starts with the anionic gold-oxide cluster in which the adsorbed O atom carries a negative charge (O^-_{ads}). Notice that in the case of anionic gold-oxide clusters this charge transfer does not create a radical center at the O atom. In a first reaction step, the CO molecule from the gas phase is weakly attached to the O^-_{ads} atom forming a weakly bound metastable complex **I**. This complex can either fall apart (no oxidation) or alternatively react to form a strongly bound complex **II** with a newly formed O_{ads}-C_{CO} bond. The CO_2 subunit is still adsorbed on the cluster and carries a negative charge, which is reflected in a bent CO_2 subunit. Due to the exergonic nature of this process, the subsequent barriers can be easily overcome, which includes the charge transfer back to the cluster and the emanation of CO_2 as the final reaction step in the oxidation process. In order to fulfill a catalytic cycle, the peripheral O atom as the active center must be regenerated which is indicated in the scheme in Figure 3.5.

The crucial reaction step consists of forming the O-C bond, and thus it is connected with the formation of the strongly bound complex. It has been shown in detail [84, 85, 100] that the reactive species always have a corresponding transition state $\mathbf{TS_1}$ which is lower in energy than the reactants. In cases where the $\mathbf{TS_1}$ is higher in energy, this elementary reaction step serves as a kinetic bottleneck for the complex formation in the gas phase which prevents the formation and the observation of oxidation products. From the systematic theoretical and experimental studies on the anionic gold-oxide clusters with up to three gold atoms [84, 85, 100] we have found that $AuO^-_{1,3}$ and $Au_2O^-_{1,3,4}$ are active in the oxidation of CO in contrast to AuO^-_2 and $Au_3O^-_{2,3,4}$ which do not oxidize CO. This is a remarkable finding since the latter clusters also contain peripheral O atoms, which demonstrates that the presence of a peripheral O atom does not guarantee that the oxidation reaction will occur. The theoretical results are fully confirmed by the experimental findings which show oxidation of CO by $AuO^-_{1,3}$ and $Au_2O^-_{1,3,4}$ [84, 100].

We also considered the oxidation reaction according to the Langmuir-Hinshelwood (LH) mechanism which, apart from the ER mechanism, is one of the most important mechanisms by which hetrogeneous catalytic processes at surfaces proceed. In the LH mechanism, both “reactants” (CO and the O atom) are bound to the cluster and then react by intra-cluster CO_2 formation. For the oxidation reaction to proceed according to a LH mechanism, two requirements have to be fulfilled. First, the CO binding energy has to be sufficiently high to form an association complex, and second, the barriers for subsequent O-C bond formation through intra-cluster reaction have to be lower than the energy gained during the CO adsorption. Otherwise

CO simply desorbs from the cluster. In the case of the anionic AuO^- and Au_2O^-, the calculated binding energies of CO to the gold sites are 2.3 and 0.4 eV, respectively (see also Chapter 3.3). However, the barrier for the subsequent rearrangement in which the carbon atom migrates from the gold site and internally attacks the oxygen atom is higher than 2 eV, making the LH mechanism for the oxidation reaction difficult for AuO^- and unfeasible for Au_2O^-. Therefore, the ER mechanism is favored over the LH mechanism for anionic gold-oxide clusters.

3.2.2 The Bridging O Atom and Molecular O_2 Group

The most stable isomers of anionic gold-oxide clusters i) often contain O atoms in bridging position bound to two gold atoms, in particular if more than one O atom is present (see e.g. Figures 3.2 and 3.3) and ii) can contain molecular O_2 subunits (e.g. $Au_2O_2^-$).

For the oxidation at the bridging O atom, in principle, the same processes are involved as in the case of the peripheral O atom. These are a) the formation of the weakly bound associative complex with CO, b) the formation of the strongly bound complex and c) the emanation of the final products. However, CO cannot be oxidized through a transfer of the bridging O atoms in cases that electron acceptor groups are present in the cluster (O atom, O_2 group). There are two reasons for this which are both expressed by the larger negative charge at the bridging O atoms. First, the nature of the bridging O atoms is closer to the oxygen di-anion (O^{2-}) which is known to be less reactive in chemical oxidation. Second, the strength of the Au-O_{bridged} bonds is increased because of larger ionic contributions to the Au-O bond resulting in higher binding energy, which is unfavorable for the transfer of a neutral O atom to CO. Consequently, none of the gold-dimer or -trimer oxide clusters can oxidize CO by transferring the bridging O atom, with the exception of Au_3O^- for which it has been shown that oxidation is theoretically feasible since there is no further electron acceptor group [84, 86].

The oxidation at the molecular O_2 site has been exemplarily studied on the prototype example of $Au_2O_2^-$ [84, 86]. The binding of molecular oxygen is much weaker ($BE(O_2) \approx 1$ eV) than the binding of atomic oxygen and is accompanied by a charge transfer from Au_2^- to the $2\pi^*$ orbital of O_2. Under reaction conditions in which the gold-oxide cluster reacts statistically with only one CO molecule, the involved barriers for breaking the strong O-O bond are too high, thus preventing the oxidation channel. Furthermore, the formation of a very stable carbonate species [$Au_2CO_3^-$] suggested in literature [18, 28] is connected with a high barrier, which makes the presence of this species in experiments questionable. However, a second CO molecule opens new reaction pathways through cooperative effects with drastically lower barriers for the O-O breaking. This leads to intermediate species with an OOCO peroxyformate structure and subsequently a simultaneous formation of two CO_2 molecules [84, 86]. In conclusion, our theoretical findings allowed the prediction that the oxidation reaction with CO at the molecular O_2 site can take place only under the influence of cooperative effects. In this case, more than one CO molecule is involved and the second CO assists in breaking the O-O bond. This also explains why the oxidation reaction has been observed under different experimental conditions [28] and why the oxidation reaction of species with molecular oxygen groups was not observed in experiments from Castleman et al [84]. In the former experimental setup, the high CO pressure and the long reaction times ensured the presence of cooperative effects enabling the oxidation channel.

3.3 Association channel

Another reaction channel which can compete with oxidation, is the association of the CO molecule according to the equation:

$$\mathrm{Au_mO_n^-} + \mathrm{CO} \rightarrow \mathrm{Au_mO_nCO^-}$$

Therefore, the association channel involves the binding of the CO molecule to an Au atom or an Au-Au subunit of the gold-oxide anions[2]. Figure 3.6 shows the structures of the anionic gold-oxide carbonyl complexes and the corresponding binding energies of CO on the lowest energy structures of $Au_2O_n^-$ (n=1-2) and $Au_3O_n^-$ (n=1-3). In addition, for $Au_2O_2^-$ also the energetically higher lying isomer with dissociated oxygen has been considered for comparison. A qualitative relationship between the binding energy of CO and the energy of the LUMO of the gold-oxide cluster (Figure 3.7) has been established and provides general rules for this reaction channel. For clusters which have an energetically low lying LUMO, e.g. $Au_2O_2^-$ (diss.), Au_3O^-, $Au_3O_3^-$ (II), a large binding energy of CO is found, thus the association channel is preferred. Interestingly, the anionic gold clusters with low lying LUMO exhibit an atomic Au site (red-colored Au atoms in Figure 3.7), and therefore

---

[2] If CO binds to an oxygen atom of the cluster, the association leads to a weakly bound complex (cf. scheme in Figure 3.5). This complex has two options: Either fragmentation leading to the reactants could occur due to the low binding energy of CO to the cluster or formation of the O_p-C_{CO} bond takes place whereupon the formed complex will easily fall apart to emanate CO_2. Thus, due to this characteristic of the weakly bound complex, the association to the oxygen atom should not play an important role.

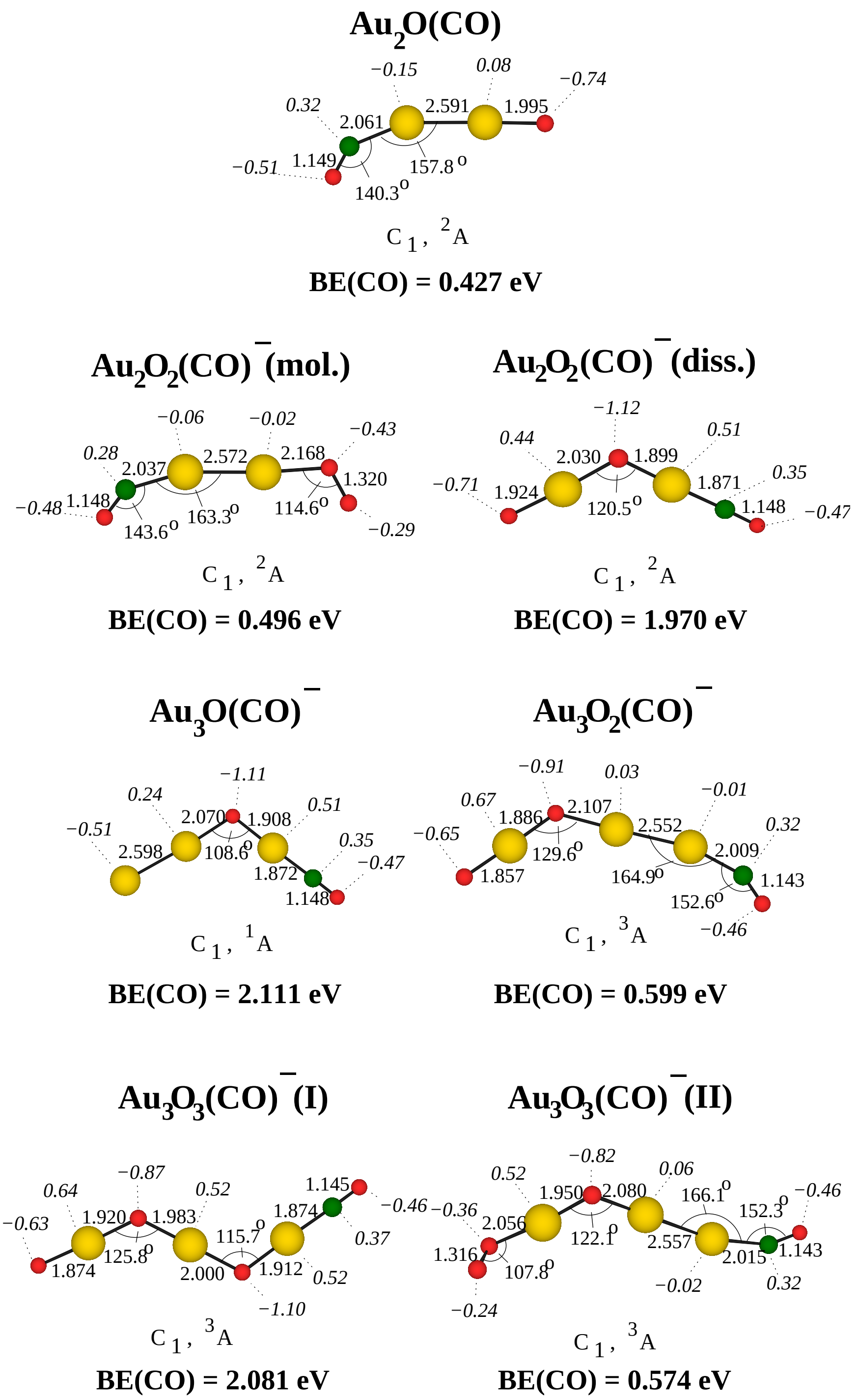
Au$_2$O(CO)

C$_1$, ^{2}A

BE(CO) = 0.427 eV

Au$_2$O$_2$(CO)$^-$ (mol.)

C$_1$, ^{2}A

BE(CO) = 0.496 eV

Au$_2$O$_2$(CO)$^-$ (diss.)

C$_1$, ^{2}A

BE(CO) = 1.970 eV

Au$_3$O(CO)$^-$

C$_1$, ^{1}A

BE(CO) = 2.111 eV

Au$_3$O$_2$(CO)$^-$

C$_1$, ^{3}A

BE(CO) = 0.599 eV

Au$_3$O$_3$(CO)$^-$ (I)

C$_1$, ^{3}A

BE(CO) = 2.081 eV

Au$_3$O$_3$(CO)$^-$ (II)

C$_1$, ^{3}A

BE(CO) = 0.574 eV

Figure 3.6: Most stable isomers of the carbonyl complexes Au$_2$O$_{1,2}$(CO)$^-$ and Au$_3$O$_{1-3}$(CO)$^-$. Binding energies for the CO molecule are given in bold below the structures. Bond lengths in Å, angles in ° and NBO charges in italic are also given.

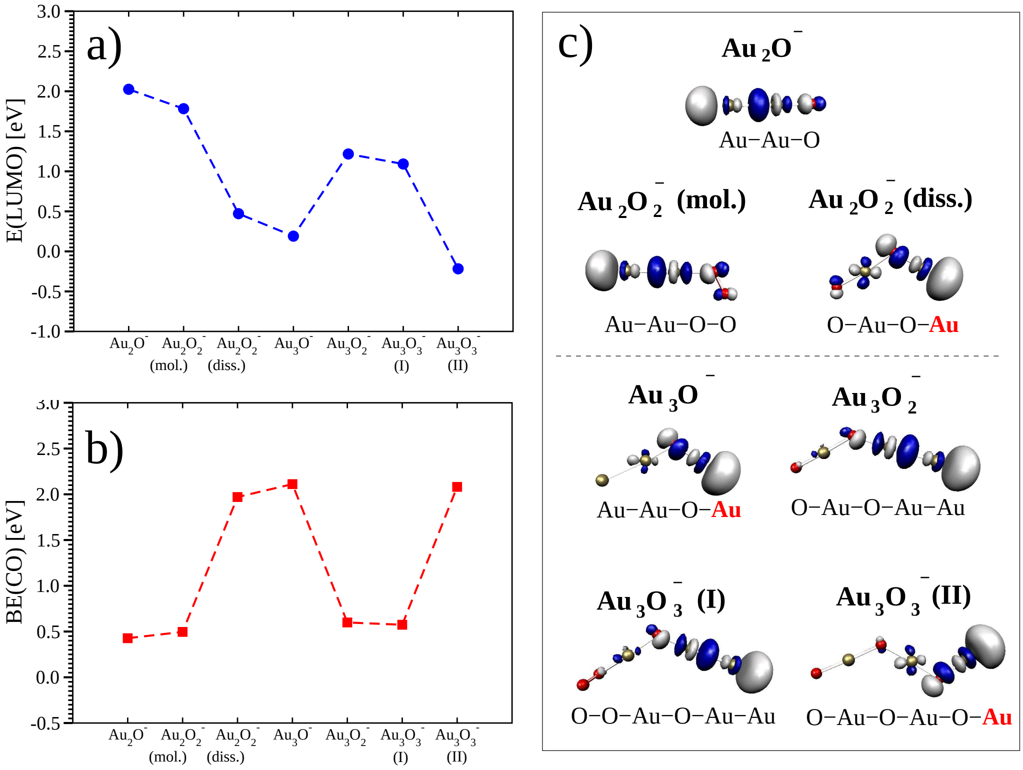

Figure 3.7: a) Energy of the LUMO of the anionic gold-oxide clusters $Au_2O^-_{1,2}$ and $Au_3O^-_{1-3}$. b) Binding energy of CO for the corresponding carbonyl complexes (cf. Figure 3.6). c) LUMO of the gold-oxide clusters before adsorption of CO. The atomic Au site is highlighted in red.

it can be concluded that association is energetically favorable only for the Au site of anionic gold-oxide clusters. For clusters which contain a Au-Au subunit, the peripheral gold atom has a considerable negative charge. Therefore, due to the repulsion between this negative charge and the donor electrons from CO, the binding energy of this site should be low.

In the following, the theoretical rules will be used to explain the experimental findings on the association channel for anionic gold-oxide clusters with an increasing number of gold atoms.

3.3.1 Anionic Gold-Monomer and -Dimer Oxide Clusters

In general, the association channel was not observed for atomic Au^- or for the dimer-oxide species. In the case of the gold monomer oxides, only AuO^- contains a free adsorption site, and the most favorable reaction channel for this species is oxidation (cf. Chapter 3.2). The most stable isomers of anionic gold dimer oxides inherit no atomic Au adsorption site and therefore the CO association is not likely to occur for Au_2O^- and $Au_2O_2^-$. From a theoretical point of view, according to the binding energies and the absence of barriers association can also take place for these species (cf. Figure 3.6). However, in order for the association to occur, the energy released by the complex formation has to be dissipated fast enough so that the complex does not fragment. This is particularly important for weak interactions. An efficient internal vibrational energy redistribution (IVR) is one possible explanation for why the complex formation is more favorable for larger oxide clusters with more than one or two gold atoms.

However, because of the above considerations and due to the fact, that gold dimer oxides with more than two O atoms do not exhibit a free gold site for the CO binding, no association has been observed experimentally for anionic gold dimer oxide clusters [84].

3.3.2 Anionic Gold-Trimer Oxide Clusters

In agreement with the theoretical predictions, the association channel was found experimentally to be favorable for Au_3O^- [84]. In the case of Au_3O^-, there are two possible adsorption sites for the binding of CO. In the first case, CO binds to the atomic Au in a barrierless reaction, leading to a complex which is more stable by 2.111 eV than the reactants. Another reaction channel leads to a complex in which CO binds to the peripheral gold atom of the Au_2 subunit. This reaction, which is also barrierless, is connected with a lower binding energy of only 0.522 eV. Indeed, according to our qualitative rule presented in the first part of this Chapter 3.3, the LUMO of Au_3O^- has a relatively low energy and exhibits strong localization at the atomic Au, indicating that CO might preferentially bind to this site (cf. Figure 3.7). This is in agreement with the higher binding energy of $\sim$2 eV (atomic Au site) versus $\sim$0.5 eV (Au-Au subunit).

In the case of the association of CO onto $Au_3O_2^-$, it was found that CO can bind only to the Au_2 subunit with a binding energy of 0.599 eV. This moderate binding energy correlates with the high energy of the LUMO (cf. Figure 3.7), which is not convenient for adsorption of CO. Indeed, in mass-selected experiments no association of CO to $Au_3O_2^-$ has been observed [84].

Considering the association reaction channel for $Au_3O_3^-$, we find that the most stable isomer $Au_3O_3^-$(**I**) (cf. Figure 3.7) containing a molecular O_2 group can bind CO only moderately strong (BE=0.574 eV). This is due to the fact that CO is bound to the peripheral gold atom of the Au_2 subunit yielding the carbonyl complex $Au_3O_3CO^-$(**II**) (Figure 3.6). In contrast, the binding of CO to the second isomer $Au_3O_3^-$(**II**) (cf. Figure 3.7) which has a chain-like structure with an atomic Au site leads to the carbonyl complex $Au_3O_3CO^-$(**I**) (Figure 3.6). This is considerably more stable by 2.081 eV with respect to the reactants ($Au_3O_3^-$ (**II**) and CO). Again, this is in agreement with the low energy of the LUMO (cf. Figure 3.7). Due to the fact that both isomers **I** and **II** of $Au_3O_3^-$ are energetically degenerated and thus both are present in the experiment, the association complex $Au_3O_3CO^-$ has been observed [84].

3.3.3 Anionic Gold-Oxide Clusters with More Than Three Gold Atoms

As already mentioned, the binding of CO to the atomic Au site is accompanied by a large reaction energy (∼2 eV). In fact, this large energy can induce significant geometrical rearrangements, as will be shown on the examples of the $Au_4O_2^-$ and $Au_4O_3^-$ clusters [107]. Both species assume structures in which two O atoms or one O atom and one O_2 group, respectively, are bound to a rhombic Au_4 subunit. Therefore, it is not obvious from the structures that adsorption of the first CO molecule is favorable for both species. However, the binding energies for CO are high (1.9 eV and 1.3 eV, respectively), and both resulting carbonyl complexes contain the stable O-Au-CO subunit. This is achieved by breaking up the Au_4 subunit, for which a little more energy is required in case of $Au_4O_3^-$ explaining the slightly lower CO binding energy [107].

Another striking example is the reaction of Au_5O^- with multiple CO molecules (Figure 3.8). In the upper part of Figure 3.8, the snapshots of the MD simulation for the reaction of CO with Au_5O^- are shown. The CO binds first to the gold atom at which the O atom is bound ($t<120$ fs). Subsequently, due to excess energy the metal subunit is rearranged yielding the preferred O-Au-CO subunit and an Au_4 subunit ($t>1000$ fs). Therefore, even in cases where at first glance no preferred atomic Au site exists from the beginning in the gold-oxide clusters, the strong interaction with CO can induce a cluster rearrangement which “generates” an atomic Au site. This leads to a very stable carbonyl complex with a rigid O-Au-CO subunit. In

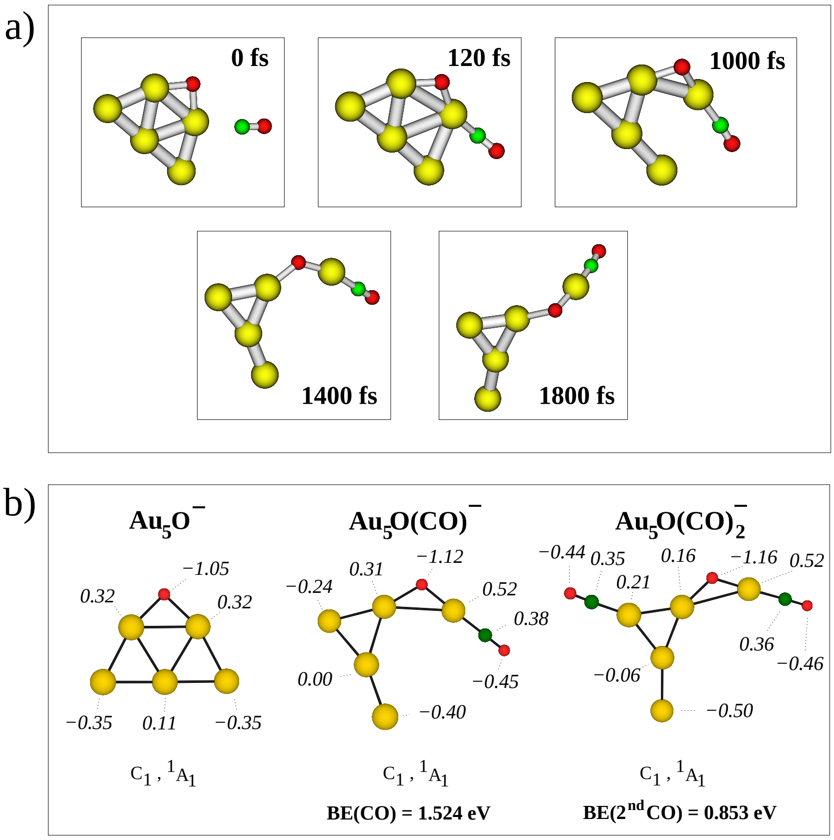

Figure 3.8: a) Snapshots for the MD simulation of the reaction of Au_5O^- with CO. b) Most stable structures of $Au_5O(CO)^-_{0-2}$. NBO charges (italic) and binding energies for the CO molecule (bold) are also given. Colors for Au, O and C are yellow, red and green, respectively.

order to accomplish this rearrangement, the metal subunit must consist of at least four gold atoms, so that, after the break up of the metal subunit and formation of the O-Au-CO unit, a gold subunit of at least three Au atoms remains intact.

The results from the qualitative MD simulation are supported by calculations on the binding of CO in the carbonyl complexes of Au_5O^-. The most stable structures of the carbonyl complexes $Au_5O(CO)^-_{0-2}$ and the corresponding binding energies of CO are shown in Figure 3.8b. The peripheral gold atoms of the Au_5O^- cluster are partially negatively charged and consequently a small energy for CO at these sites is expected. In contrast, the binding of CO to the Au atom closest to the adsorbed O atom leads to very stable carbonyl complex (BE(CO)=1.524 eV). Thus, the energy which is required to break the Au-Au bonds in order to form a Au_4 subunit and an

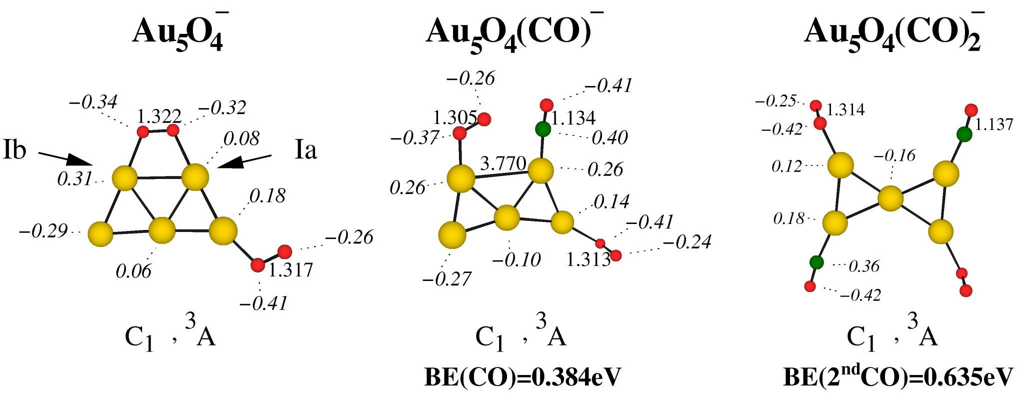

Figure 3.9: Most stable structures of $Au_5(O_2)_2(CO)^-_{0-2}$. NBO charges (italic) and binding energies for the CO molecule (bold) are also given.

"atomic site" can be easily compensated. The tips of this newly formed Au_4 subunit are negatively charged, and therefore the binding of a second CO is not as strong as for the first one. However, a binding energy of 0.835 eV denotes a considerably stable complex for that cluster size, confirming the experimental findings regarding the uptake of multiple CO molecules [107].

So far, the presence of atomic oxygen has been mandatory in order to obtain highly stable carbonyl complexes with a stable O-Au-CO subunit. We also investigated the adsorption of CO onto clusters having only molecular oxygen bound, e.g. the prototype example $Au_5O_4^-$. Notice that the thermodynamically most stable isomer of $Au_5O_4^-$ assumes a ring structure with dissociated oxygen (cf. Figure 3.2) which can be formed only in experiments providing atomic oxygen during the cluster formation process. In contrast, experiments with only molecular oxygen will produce the $Au_5(O_2)_2^-$ cluster shown in Figure 3.9, and therefore the results presented here are relevant in particular for experiments with molecular O_2. Figure 3.9 shows the most stable structures for the $Au_5O_4^-$ cluster containing only molecular oxygen and its carbonyl complexes with one and two CO molecules, respectively. The most favorable sites for the attack of CO are marked **Ia** and **Ib** which are in direct vicinity to the oxygen molecule adsorbed in the "side-on" configuration. The CO molecule binds to the cluster with only 0.384 eV which is not enough to break Au-Au bonds, thus leaving the Au_5 subunit intact. As a result, the O_2 and CO are bound in direct vicinity to each other ready to form the peroxyformate complex with an OOCO group which represents an important intermediate in the oxidation at the molecular O_2 group [28, 84, 86]. Since there is still a free adsorption site at one peripheral Au atom of the $Au_5O_4(CO)^-$ cluster, a second CO molecule can weakly bind (BE(CO) =

0.635 eV), now providing sufficient energy to change the geometry of the Au_5 subunit.

3.3.4 Summary

In summary, the structure-reactivity relationship for the association channel of CO onto anionic gold-oxide clusters has been established providing a rule for estimating the adsorption energy. The binding of CO to an atomic Au site is accompanied by a large adsorption energy of ∼2 eV yielding clusters with a very stable O-Au-CO subunit. It has been shown on the example of larger gold-oxide clusters ($Au_4O_{2,3}^-$, Au_5O^-) that a part of the adsorption energy can be used to break Au-Au bonds in order to enable the “in situ” formation of an atomic Au site. However, a gold subunit of at least four gold atoms and the presence of atomic oxygen is required in order to enable this CO-induced geometry rearrangement.

On the other hand, the binding of CO to anionic gold-oxide clusters bearing only molecular O_2 subunits, e.g. $Au_5(O_2)_2^-$, is weak and barely influences the geometry of the gold subunit. However, in the case of $Au_5(O_2)_2^-$, the gold cluster binds both reaction partners (CO, O_2) in close vicinity which is favorable for forming an important intermediate in the oxidation reactions.

Moreover, the theoretical findings explain why carbonyl complexes of gold-dimer oxide ($Au_2O_2^-$) are not observed in experiments performed by Castleman et al. [84, 100], but can be present under different experimental conditions [18]. In the latter experimental setup, cryogenic temperature and long reaction times are favorable for stabilizing the weak adsorbate complex.

Chapter 4

Structure-Reactivity Relationship of Cationic Gold-Oxide Clusters $Au_{1,2}O^+_{1-4}$

4.1 Structural properties

Many studies have indicated that the charge state of the clusters can significantly affect their catalytic activity. Thus in order to address the influence of the charge state on the reactivity of gold, the structure-reactivity relationship will be established for the cationic gold-oxide clusters. For this purpose, the most stable isomers of small cationic gold-oxide clusters have been determined. The geometries as well as the symmetry of the electronic ground states are shown in Figure 4.1. In contrast to the anionic gold-oxide clusters, the cationic species exhibit the tendency to bind oxygen preferentially in molecular form (e.g. $AuO_2^\pm$, $Au_2O_4^\pm$, $Au_4O_2^\pm$). The binding energy for the peripheral O atom (BE(O)<1.5 eV) is lower than for the anions. Moreover, the charge at the peripheral oxygen atom is close to zero according to the NBO analysis. In the following we will focus on the smallest prototype species AuO^+ and Au_2O^+ in order to analyze exemplarily the chemical bonding and the reactivity of the cationic gold-oxide clusters.

Taking out one electron from each of the non-bonding π^* (Au($d_{xz/yz}$) / O($p_{x/y}$)) and the bonding σ (Au(d_{z^2}) / O(p_z)) orbital from AuO^- leads to the cationic AuO^+ species. As a consequence, the bond order is reduced due to the cationic charge state. Accordingly, the binding energy of the oxygen atom is lower (1.44 eV vs. 1.94 eV) and the equilibrium distance is longer (1.929 Å vs. 1.882 Å). The nature of the Au-O bond will be discussed in detail later and thus the reader is referred to Chapter 6.

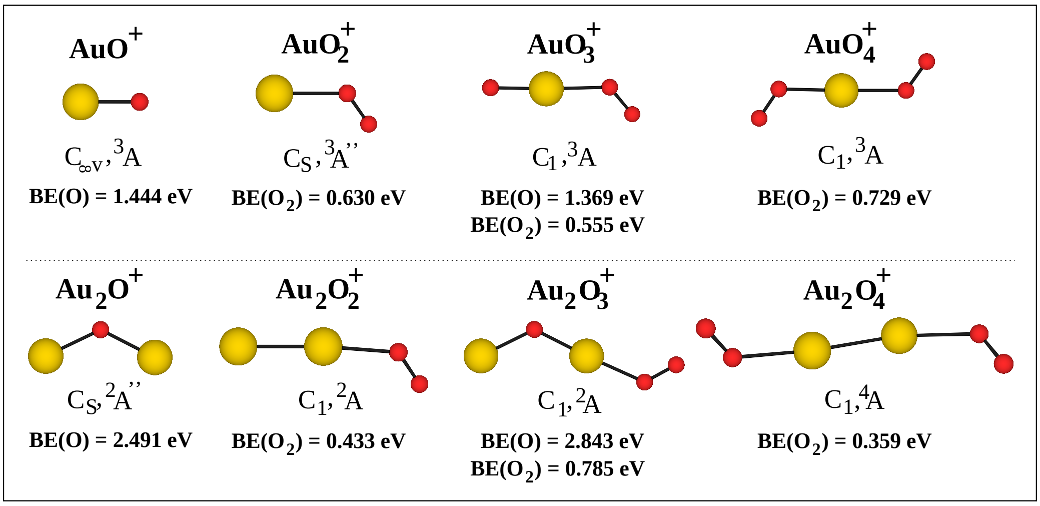

Figure 4.1: Most stable structures of $Au_{1,2}O^+_{1-4}$. Binding energies for different subunits are given in bold.

In contrast to the peripheral O atom, the bridging O atom in Au_2O^+ is strongly bound ($BE(O) = 2.49$ eV) which, however, is less than in the anionic case (3.14 eV for Au_2O^-). Similar to the anionic oxides, the bridging oxygen atom serves as an electron acceptor. Consequently, this O atom is partially negatively charged ($q = -0.62e$) and the Au-atoms are strongly positively charged. The situation for the bridging O atom in $Au_2O_3^+$ is similar.

The binding energy of molecular O_2 is in general lower than for the corresponding anionic clusters. In AuO_2^+, the low binding energy of O_2 (0.63 eV) is mainly due to electrostatic interactions, e.g. ion-induced dipole interaction, which is weaker than the electron transfer binding mechanism in case of the anions. Therefore, the O_2 subunit appears neutral and is only slightly polarized. The same situation has been found in all studied cationic gold monomer and dimer oxide clusters containing molecular oxygen.

In summary, the same three reactive centers as in the anionic gold-oxide clusters have been identified. However, due to the cationic charge state the binding properties are considerably different from the corresponding anionic clusters and thus different reactivity is expected. For example, the binding of a peripheral oxygen is considerably weaker and also the binding energy for a molecular O_2 is very weak. Moreover, the gold atoms in the cationic oxide clusters exhibit positive partial charges. Therefore, in addition to the oxidation channel for the cationic gold-oxide clusters, the results on different competing reaction channels, such as the adsorption of a CO molecule or the replacement of the O atom or the O_2 group, will be presented in the next

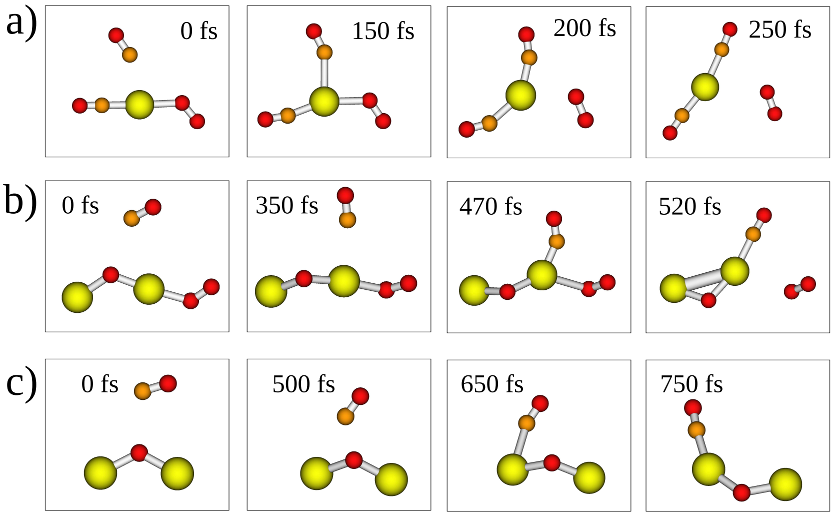

Figure 4.2: Snapshots from MD simulations for the reaction of CO with a) $AuO_2(CO)^+$, b) $Au_2O_3^+$ and c) Au_2O^+. Colors for Au, O and C are yellow, red and orange, respectively.

Chapter.

4.2 Reaction channels

The fact that the peripheral O atom as well as the O_2 group are only weakly bound leads to interesting and distinctly different reactivities compared to the corresponding anions. In order to gain insight into the reactivity, several MD simulations have been performed for the reaction of CO with a) $AuO_2(CO)^+$, b) $Au_2O_3^+$, and c) Au_2O^+. The corresponding snapshots are presented in Figure 4.2 showing the replacement of the O_2 group in a) and b) and the association of CO in c). This can be explained by the large binding energy of CO onto cationic gold clusters. The corresponding carbonyl complexes for selected gold monomer species and selected dimers are shown in Figure 4.3. The bond between the cationic gold site and the CO molecule, which acts as $2e^-$ donor, is very strong (BE>2 eV). As a consequence, the CO molecule can easily substitute a peripheral O atom or the molecular oxygen (O_2) and ozone (O_3) groups, respectively, in the cationic gold-oxide species. In contrast, species with bridging oxygen atoms seem to be resistant to the replacement of this O atom and rather adsorb CO either a) without fragmentation or b) under loss of a weakly attached adsorbant according to the following reaction equations

$$\begin{aligned} \text{a)}\quad & Au_2O^+ + CO \quad \rightarrow \quad Au_2O(CO)^+ \\ \text{b)}\quad & Au_2O_3^+ + CO \quad \rightarrow \quad Au_2O(CO)^+ + O_2 \end{aligned}$$

This strong binding of CO has direct consequences in the context of the oxidation reaction which will be discussed in the following.

4.3 Reactivity of Cationic Prototype Clusters Au_nO^+ (n=1,2) towards CO

In order to determine the influence of the charge state on the oxidation of CO, the reactions of carbon monoxide with AuO^+ and Au_2O^+ have been studied in detail. As already discussed in the previous section, the oxidation channel is preferred for the corresponding anionic species and the oxidation reaction occurs at the peripheral oxygen atom via an Eley-Rideal mechanism.

In contrast, by changing the charge state, different reactivity is observed. The branching ratios in Figure 4.4 for AuO^+ and Au_2O^+ show that the dominant reaction channel is apparently the loss of a single O atom and the association of a CO molecule (cf. Figure 3.4). However, this process is calculated to be only moderately exothermic by 0.63 eV for AuO^+ and endothermic by 0.81 eV for Au_2O^+. Therefore, the simple direct loss of atomic O and the association of CO cannot explain the experimental branching ratios shown in Figure 4.4 for Au_2O^+ and it is also unlikely to occur for AuO^+.

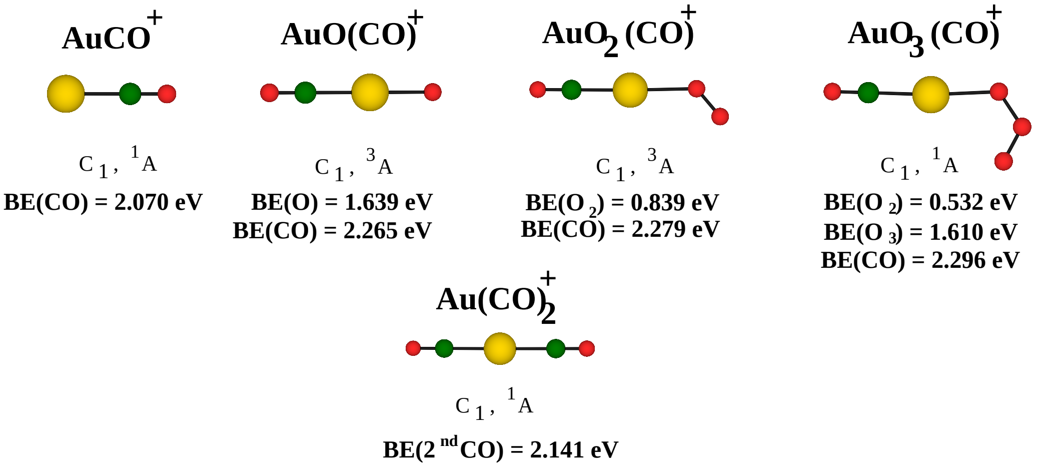

Figure 4.3: Most stable structures of $AuO_{0-3}(CO)^+_{1-2}$ together with spacial and electronic symmetries. Binding energies for different subunits are given in bold.

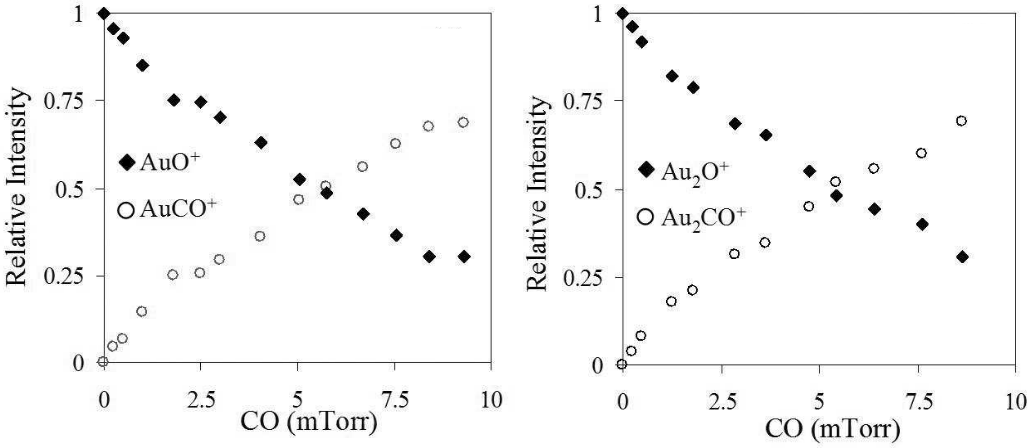

Figure 4.4: Branching ratios for the reaction of CO with AuO^+ (left) and Au_2O^+ (right).

Moreover, carbide formation by CO cleavage and subsequent loss of an O atom according to the reaction equation

$$AuO^+ + CO \rightarrow O - Au - C^+ + O$$

can be excluded since it is energetically highly unfavorable (endothermic by >8 eV; barrier for breaking the C-O bond >6.8 eV).

In the following we will provide evidence that the observed "O-atom replacement" channel is in fact the result of a combined oxidation and association reaction. An oxidation reaction involving two CO molecules according to the formula

$$Au_{1,2}O^+ + 2CO \rightarrow Au_{1,2}CO^+ + CO_2$$

is possible and leads to the same products as those observed in the experiments. Moreover, these reaction channels are calculated to be thermodynamically favorable for both AuO^+ (-3.25 eV) and Au_2O^+ (-4.90 eV). In order to shed light on the underlying reaction mechanisms, we present the energy profiles for the oxidation reactions involving two CO molecules in Figure 4.5. In the case of AuO^+, the adsorption of the first CO molecule leads to the formation of a O-Au-CO^+ complex which is 2.26 eV more stable than the reactants (Figure 4.5a). From this point, the reaction with the second CO molecule can occur either by an LH- or ER-type mechanism. According to the LH mechanism, the CO molecule which is attached to the Au atom internally attacks the peripheral O atom. This process, which requires the bending of the linear species, involves a barrier of about 1.73 eV which directly reflects the rigid character of the O-Au-CO subunit. Subsequently, the

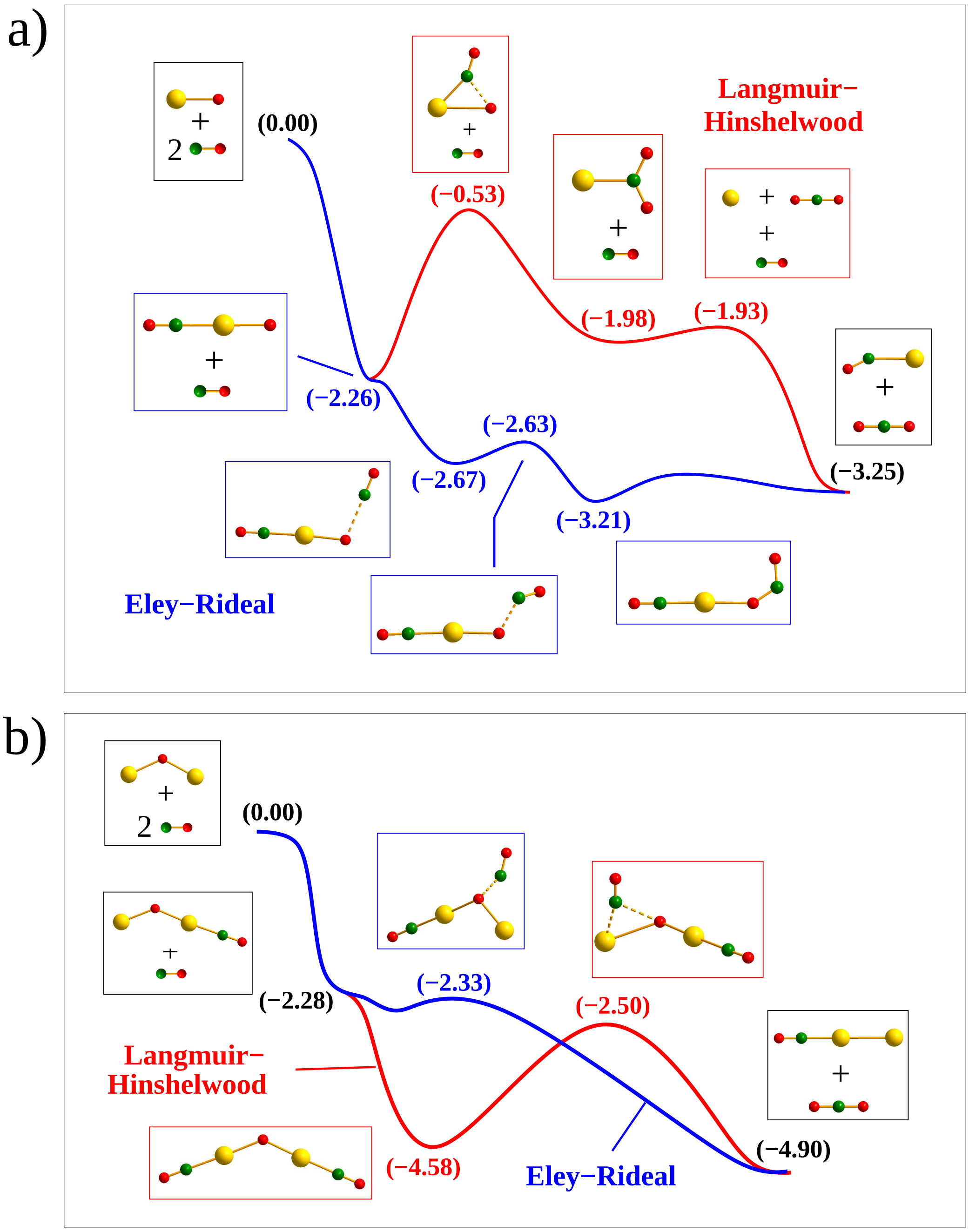

Figure 4.5: Energy profiles for the reaction of two CO molecules with a) ^{3}AuO$^+$ and b) ^{2}Au$_2$O$^+$. All energies are given in eV relative to the energy of the reactants (Au$_{1,2}$O$^+$+ 2CO) at 0 K. The reaction paths according to ER (blue) and LH (red) mechanisms are shown.

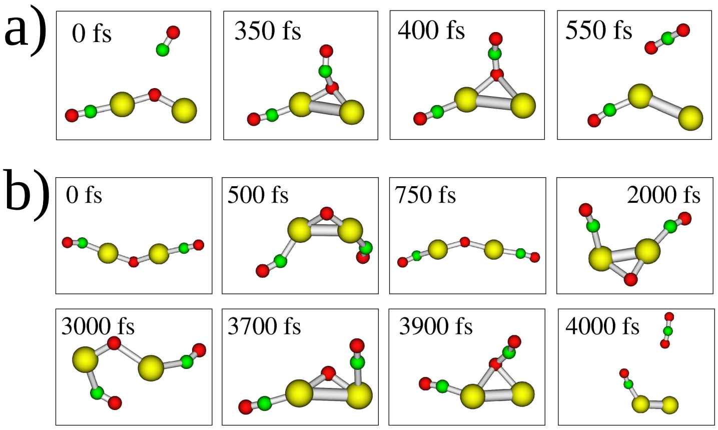

Figure 4.6: MD snapshots for the reaction Au_2O^++ 2CO → Au_2CO^+ + CO_2 according to a) the ER-like mechanism and b) the LH-like mechanism.

CO_2 is released, and the second CO adsorbs to the Au^+ ion, giving rise to the observed final product. According to the ER mechanism, the second CO molecule from the gas phase reacts directly with the peripheral O atom of the O-Au-CO^+ complex leading to the formation of the experimentally observed products. However, since this process occurs without significant barriers, the oxidation according to an ER mechanism is more favorable than the LH mechanism for AuO^+. A third pathway involving binding of the second CO to the gold atom in O-Au-CO^+ would cause fragmentation of the O atom leading to $Au(CO)_2^+$. However, this is not observed experimentally.

In the case of Au_2O^+ (cf. Figure 4.5b), the adsorption of the first CO molecule yields a complex which is more stable by 2.28 eV than the reactants. Similar to AuO^+, the oxidation of a second CO molecule can easily occur according to the ER-like mechanism since the involved small barriers (0.2 eV[1]) can be easily overcome as depicted in Figure 4.5b. However, the Au-O-Au-CO^+ complex can directly bind a second CO molecule due to a free Au adsorption site. Notice that this is not the case for O-Au-CO^+ because the binding of a second CO leads to the already mentioned loss of the weakly bound O atom. In contrast, the binding of the second CO onto $Au_2O(CO)^+$ provides an additional energy of 2.30 eV. Therefore, the overall energy gain

---

[1] The weakly bound complex between O-Au-CO^+ and the second CO molecule are not shown in Figure 4.5b. The relative energy with respect to the reactants is about -2.5 eV.

of 4.58 eV is sufficient to easily overcome the barrier (2.08 eV) for the internal attack of one bound CO molecule on the bridging O atom according to the LH mechanism. Therefore, both the ER and the LH mechanisms are viable for CO oxidation on Au_2O^+. The findings on the reaction mechanism are further supported by the MD simulations presented in Figure 4.6, which show that the reaction can proceed according to both types of mechanisms. However, in agreement with the simple modeling of the relative rate constants according to the Rice-Ramsperger-Kassel (RRK) theory [109, 110], the LH process would occur considerably more slowly.

It is important to point out that at least two CO molecules have to be involved in this complex "replacement" reaction in contrast to the corresponding anionic species, where one CO molecule was sufficient for the observation of the oxidation channel.

Chapter 5

Discussion

The findings presented in the first part of the thesis, which are supported by several experimental studies, provide new insight in the gold-based catalysis. Due to the fact that catalytically active gold clusters can be negatively charged at defect sites of a support, anionic gas-phase clusters serve as ideal model systems. Moreover, selected reaction steps, such as the activation of O_2, binding of the reaction partner CO, and formation of CO_2, can be examined in a controlled environment as a function of the cluster size, the stoichiometry and the experimental conditions (e.g. temperature, pressure).

For example, until recently experimental and theoretical work on gold-based catalysis focused on the question how the O-O bond in molecular O_2 can be activated in order to oxidize e.g. CO. It has been found that a charge transfer occurs to the $2\pi^*$ anti-bonding orbital of O_2 which is molecularily bound in anionic gold clusters. We have shown that clusters alone cannot break the O-O bond but that a further activation such as cooperative effects combined with resonant IVR (see Chapter 7) is required.

The role of atomic oxygen in the gold nano-catalysis has not been addressed before. Clusters with atomic oxygen whose existence has been postulated as a possible intermediate species in oxidation reactions with molecular oxygen were considered to be always highly reactive leading to oxidation products. Our studies on anionic gold-oxide clusters containing both molecular and atomic oxygen, however, demonstrate, that this is not generally the case. For example, AuO^- has been found to be highly reactive in oxidation of CO, and indeed AuO^- has been identified as part of the active site in real catalysts [37]. In contrast, the oxidation channel has been predicted to be unfavorable in case of e.g. anionic gold trimer oxides, showing that the presence of the O atom is not sufficient for the oxidation reaction to proceed. Our theoretical predictions have been also experimentally confirmed [84, 100, 111].

We considered also another reaction channel, which is the association of CO. In the case of the anionic gold-oxide clusters, a qualitative rule for the binding of CO has been established. According to this rule, the binding of CO in anionic clusters is favorable only at an atomic Au site ("peripheral Au atom") due to the fact that this gold atom is positively charged. Furthermore, we have demonstrated that such a favorable adsorption site can be created "in situ" by dynamical rearrangement in the case of larger gold-oxide clusters $\mathrm{Au_nO_m^-}$ (n>3) if atomic oxygen is present.

Cationic gold sites have been postulated in gold nano-catalysts [36] and consequently the examination of cationic gold-oxide clusters in the gas phase allows us to study the influence of the charge state on the reactivity. It has been pointed out in Chapter 4 that by changing the charge state from anionic to cationic, the structural and binding properties of gold-oxide clusters strongly change. Therefore, in the cationic charge state, oxygen binds preferentially in molecular form and moreover, the binding energies of the molecular O_2 group and the peripheral O atom are considerably lower. This directly alters the importance of different reaction channels. In fact, the binding properties of CO play a crucial role due to its $2e^-$ donor nature yielding very strong adsorption energies onto the cationic gold-oxide clusters. Therefore, the association channel is much more favorable in case of cationic gold-oxide clusters, in contrast to anions for which a structure-dependent qualitative rule for the binding of CO has been established.

The strong binding of CO also influences the oxidation mechanism. In fact, it has been shown that in the case of $\mathrm{Au_{1,2}O^+}$ at least two CO molecules are involved in the oxidation pathway. This enables the oxidation reaction to occur according both to the ER and the LH mechanism. However, the ER mechanism will dominate for kinetic reasons.

The first CO molecule acts as a kind of "energy supplier" due to the large adsorption energy, so that the internal kinetic energy can be used to overcome subsequent energy barriers. In this context, an experimental study on larger gold-oxide clusters shows that the binding of multiple CO molecules indeed introduces a large amount of energy which can even cause cluster fragmentation [112, 113]. On the basis of our findings we conclude that this "heating" might be an important role of cationic gold sites which are present in nano-catalysts [36]. We propose that the adsorption energy is transferred to the cluster and the role of nearby neutral or partially negative charged gold species is to serve as binding sites for CO and O_2 enabling the catalytic reaction. Notice that if too much energy is gained from CO adsorption, this can lead to fragmentation, potentially destroying the catalytically active cluster site. However, under well-controlled reaction conditions, the oxidation reaction is self-promoting in the presence of cationic gold species at high pressures of CO, i.e. the oxidation of one CO molecule is promoted by the binding of a second.

Chapter 6

The Nature of the Au-O and Au-S Bond

6.1 Introduction

Our conclusions presented in previous chapters contributed to understand the role of the charge state on the reactivity of gold-oxide clusters containing molecular and atomic oxygen. This was particularly important in the context of unique catalytic properties of nano-sized gold particles, in particular for CO oxidation at low temperatures [1–4, 8, 12–14, 24, 27, 31, 32, 75, 114–122]. Despite extensive research efforts, the exact mechanisms of the nano-catalytic effects of gold are still controversial, and several aspects have been addressed in previous chapters. In order to gain further understanding of the reactivity properties, it is desirable to have detailed knowledge of the nature of the chemical Au-O bond. In order to achieve this goal, mono-gold oxide species may be considered as the simplest model system since they are relevant to CO oxidation in gold nano-catalysis. Indeed, AuO^- has been identified as an important structural feature in working catalysts [37].

Mono-gold oxide clusters have been the subject of numerous experimental gas-phase [123–128] and matrix studies [129–134]. A gold di-oxygen complex $Au(O_2)$ was reported in matrix experiments and a side-on structure (C_{2v}) was proposed, in which the two O atoms are equivalently coordinated to Au [129, 131–133]. However, a recent matrix study concluded that $Au(O_2)$ possesses two nonequivalent oxygen atoms and should take a bent structure (C_S) [134]. A linear gold di-oxide species OAuO ($D_{\infty h}$) was also identified [133, 134]. In the gas phase, the electronic structure of AuO^- and AuO_2^- and their neutrals has not been studied experimentally until very recently [23, 25, 123–128, 135]. Ganteför and co-workers conducted the first photoelectron spectroscopy (PES) study on AuO^- using UV excitation at 193 nm [135]. A short time later, Lineberger and co-workers [124] reported a highly resolved PES spectrum for AuO^-, as well as for AuS^-, at 364 nm for the ground-state transition, clearly resolving the two spin-orbit components for the ground state of AuO and AuS ($^2\Pi_{3/2}$ and $^2\Pi_{1/2}$). At the same time, O'Brien et al. [125, 127] reported a near-infrared electronic spectrum of the $^4\Sigma^-$ excited state of AuO. More recently, Okabayashi et al. [126] reported a pure rotational spectrum of the $^2\Pi_{3/2}$ ground state of AuO. Little spectroscopic information is available for other excited states of AuO. Ganteför and co-workers also obtained the PES spectra of AuO_2^- [25, 135].

Theoretical studies on the mono-gold oxides have also been relatively scarce [127, 133–137]. The valent isoelectronic mono-gold sulfide species, AuS_n and AuS_n^- (n = 1, 2), have received even less attention. Very few spectroscopic data are available except for the recent study of AuS^- by Lineberger and co-workers along with that of AuO^- [124]. However, the Au-S bonding is important not only for the purpose of comparison to the corresponding Au-O system, but also because the Au-S bond plays an important role in the formation of self-assembled monolayers and thiolate-protected gold clusters [38, 138].

In this chapter we present results providing fundamental insight into the Au-O and Au-S bond on the basis of high-level ab initio calculations in combination with a comprehensive PES study of AuO^- and AuO_2^- and their isoelectronic AuS^- and AuS_2^- species at 355, 266, and 193 nm photon energies. The concerted computational and experimental data allow for a complete understanding of the equilibrium geometries, electronic structure and chemical bonding in these systems. Both a linear $SAuS^-$ and a bent $Au(S_2)^-$ isomer have been calculated to be stable and thus were observed for AuS_2^-. In contrast, only a linear $OAuO^-$ species was observed for AuO_2^-. This observation is in agreement with the theoretical prediction that O_2 is not bound in $Au(O_2)^-$, whereas S_2 is bound to Au^- by 1.388 eV in $Au(S_2)^-$. An extensive analysis of the electronic structure based on the molecular orbital analysis and spin orbit coupling calculations were carried out to obtain insight into the nature of the chemical bonding in the AuX^- and the AuX_2^- systems. Strong electron correlation effects and covalent bonding with multiple bond characters were found for both systems. The non-bonding nature of the $Au(O_2)^-$ complex is compared with the size-dependent reactivity of Au_n^- clusters with O_2. Findings on AuO^- will be compared to the corresponding cationic species AuO^+ to elucidate the influence of the charge state.

6.2 Computational Methods

Ground-state properties of the anionic species AuX_n^- (X = O, S; n = 1,2) were determined using the coupled-cluster level of theory with explicit inclusion of single and double excitations and pertubative treatment of triple excitations (CCSD(T)). For closed-shell species, a restricted Hartree-Fock (HF) wave function was used as reference, and for open shell systems high-spin restricted open shell HF wave functions were employed. Relativistic effects were taken into account by using a two-component relativistic pseudopotential (i.e., scalar-relativistic and spin-orbit (SO) potentials) for gold replacing the inner 60 electrons (ECP60MDF [139]). This is combined with the an energy-optimized aug-cc-pVTZ-PP atomic orbital (AO) basis set with the contraction scheme (11s10p9d3f2g) / [6s6p5d3f2g] [140]. The standard aug-cc-pVTZ-PP AO basis set was used for oxygen ((11s,6p,3d,2f) / [5s,4p,3d,2f]) and sulfur ((16s10p3d2f) / [6s5p3d2f]). The energetically lowest orbitals, consisting mainly of Au-(5s, 5p) orbitals and O-(1s) / S-(1s, 2s, 2p) orbitals, were frozen. The ground-state geometries of all species were optimized and properties such as binding energies and vertical detachment energies (VDEs) were determined.

The spin-orbit interactions were treated by using the contracted SO configuration interaction method after the electron-correlation step, diagonalizing the SO matrix in the space of all SO-free electronic states of interest. For this purpose, the SO-free states for the neutral species in the geometry of the optimized anions were obtained according to the following procedure:

First, a state-averaged complete active space self-consistent field calculation (CASSCF) was performed leading to the following active spaces in which all electrons were correlated: AuO / AuS: 10 orbitals for 17 electrons [CASSCF(17,10)], OAuO / SAuS / Au(S_2): 14 orbitals for 23 electrons [CASSCF(23,14)]. Since only excited states with one-electron excitation character dominate the experimental photoelectron spectra, only neutral electronic states with doublet multiplicity are experimentally observable for species in which the anionic electronic ground state is singlet (AuO^-/AuS^-/$Au(S_2)^-$). Within the one-electron approximation, the doublet final states $^2\Pi$, $^2\Sigma$, $^2\Delta$, $2^2\Sigma$ and $2^2\Pi$ dominated by one-electron excitations are obtained for ^{2}AuX (X = O, S) by detaching one electron from an orbital of the closed-shell anion. These and a few more doublet states with multielectron excitation characters, as well as the lowest $^4\Pi$ and $^4\Sigma$ states, were included in the state-averaged CASSCF. For $^2Au(S_2)$ (C_S $^2A''$), four ^{2}A' and two ^{2}A" states, which are dominated by one-electron excitations, were included in the correlation. Additionally, some doublet as well as quartet states representing multielectron excitations were added.

For AuO_2^- ($D_{\infty h}$ $^3\Sigma_g^-$) and AuS_2^- ($D_{\infty h}$ $^3\Sigma_g^-$) with a triplet electronic ground state, both doublet as well as quadruplet states of the corresponding neutral species are accessible via one-electron detachment processes. Therefore, in calculations for AuO_2 ($D_{\infty h}$ $^2\Pi_g$), the following states were included: $^2\Pi_g$, $^{2,4}\Pi_u$, $^{2,4}\Sigma_g^-$, $^{2,4}\Sigma_u^-$, $^4\Delta$, $2^2\Pi_g$ and some states with multielectron excitation characters. Analogous states were considered also for AuS_2 ($D_{\infty h}$ $^2\Pi_g$).

Employing the natural orbitals from the state-averaged CASSCF calculation, highly correlated wave functions were calculated using the internally contracted multi-reference configuration interaction (MR-CI) method [141, 142]. From these, the SO-matrix has been constructed and diagonalized yielding the spin-orbit eigenstates.

The first peak in a photoelectron spectrum represents the first experimental vertical detachment energy (VDE) and thus corresponds to the VDE obtained at the CCSD(T) level of theory. Other higher binding energy peaks in a photoelectron spectrum represent excited states of the neutral species, and their VDEs were computed by adding the excitation energies of the corresponding neutral at the anion geometry to the first VDE. All calculations were performed using the MOLPRO program suite [143].

6.3 Theoretical Results and Interpretation of the Photoelectron Spectra

6.3.1 Ground-State Properties

Table 6.1 summarizes the ground-state properties of $AuX_{1,2}^-$ (X=O, S). The two diatomic species AuX^- are similar, both with a singlet ground state ($^1\Sigma^+$) and similar bond strengths. The Au-S$^-$ bond (D_e: 2.677 eV) seems slightly stronger than the Au-O$^-$ bond (D_e: 2.082 eV). The calculated bond lengths and strengths for AuX^- are consistent with a previous study using a similar level of theory [124]. The calculated first VDEs for AuX^- (2.312 eV for AuO^- and 2.452 eV for AuS^-) are in excellent agreement with the experimental measurements (2.378±0.015 eV for AuO^- and 2.475±0.015 eV for AuS^-). The most stable structures of the two AuX_2^- species also behave similarly, both possessing a linear $XAuX^-$ structure with a triplet spin state ($^3\Sigma_g^-$). The Au-X bond is significantly strengthened in AuX_2^- relative to the AuX^- diatomics, as can be seen from the shortened Au-X bonds and increased dissociation energies in AuX_2^- (Table 6.1). The calculated first

Table 6.1: Summary of the ground-state properties obtained at the CCSD(T) level of theory for $AuX_{1,2}^-$ (X = O, S). Spatial and electronic symmetry of the ground-state species and relative energies (ΔE) of isomers, calculated equilibrium bond lengths (r_{Au-X} and r_{X-X}) in Å, calculated dissociation energies (D_e) for X atom and X_2 group in eV and the first VDE for each species are given.

		State	ΔE	r_{Au-X}	r_{X-X}	$D_e(X)^a$	$D_e(X_2)^b$	VDE
AuO^-	$C_{\infty v}$	$^1\Sigma^+$	-	1.882		2.082		2.312
$OAuO^-$	$D_{\infty h}$	$^3\Sigma_g^-$	0.000	1.847		4.046		3.473
$AuOO^-$	C_S	$^3A''$	1.421	2.169	1.314	2.626	-0.272	2.058
AuS^-	$C_{\infty v}$	$^1\Sigma^+$	-	2.216		2.677		2.452
$SAuS^-$	$D_{\infty h}$	$^3\Sigma_g^-$	0.000	2.202		3.388		3.468
$AuSS^-$	C_S	$^1A'$	0.568	2.301	2.030	2.820	1.388	2.282

[a] Dissociation energy for the most stable fragments regardless of spin, defined as $E(AuX_n^-)$ - $[E(AuX_{n-1}^-) + E(X)]$ with n = 1, 2 and X = O, S.

[b] Dissociation energy of molecularily bound X_2 (X = O, S) to Au^- is defined as $E(AuX_2^-)$ - $[E(Au^-) + E(X_2)]$.

VDEs for AuX_2^- (3.473 eV for AuO_2^- and 3.468 for AuS_2^-) are also in excellent agreement with the experimental measurements (3.40±0.03 eV for AuO_2^- and 3.47±0.03 eV for AuS_2^-).

Interestingly, AuS_2^- is calculated to possess a low-lying isomer containing a molecular S_2 unit with C_S symmetry and a singlet electronic state ($^1A'$). The Au^- and S_2 bonding is quite strong with a dissociation energy of 1.388 eV. However, a similar isomer for AuO_2^- is much higher in energy with a triplet electronic ground state (C_S, $^3A''$). More importantly, it is found theoretically that Au^- and O_2 are unbound (Table 6.1). These theoretical predictions are consistent with the experimental observations, that is, no $Au(O_2)^-$ isomer was observed for AuO_2^-, but a $Au(S_2)^-$ isomer was indeed observed for AuS_2^- (Figure 6.6). The calculated first VDE (2.282 eV) for the $Au(S_2)^-$ isomer is in excellent agreement with the experimental measurement (2.24±0.03 eV). Although the $Au(S_2)^-$ isomer is higher in energy than the linear AuS_2^- global minimum by 0.568 eV, the dissociation from the singlet $Au(S_2)^-$ to Au^- (^1S) and S_2 ($^3\Sigma_g^-$) is spin forbidden. Thus the observation of the $Au(S_2)^-$ isomer in the experiment should be mainly due to kinetic reasons.

6.3.2 AuO^- and AuS^-

The qualitative molecular orbital diagram for the anionic $^1AuX^-$ species is given in Figure 6.1. The $O(2p_{x/y})$ and $S(3p_{x/y})$ orbitals, respectively, form

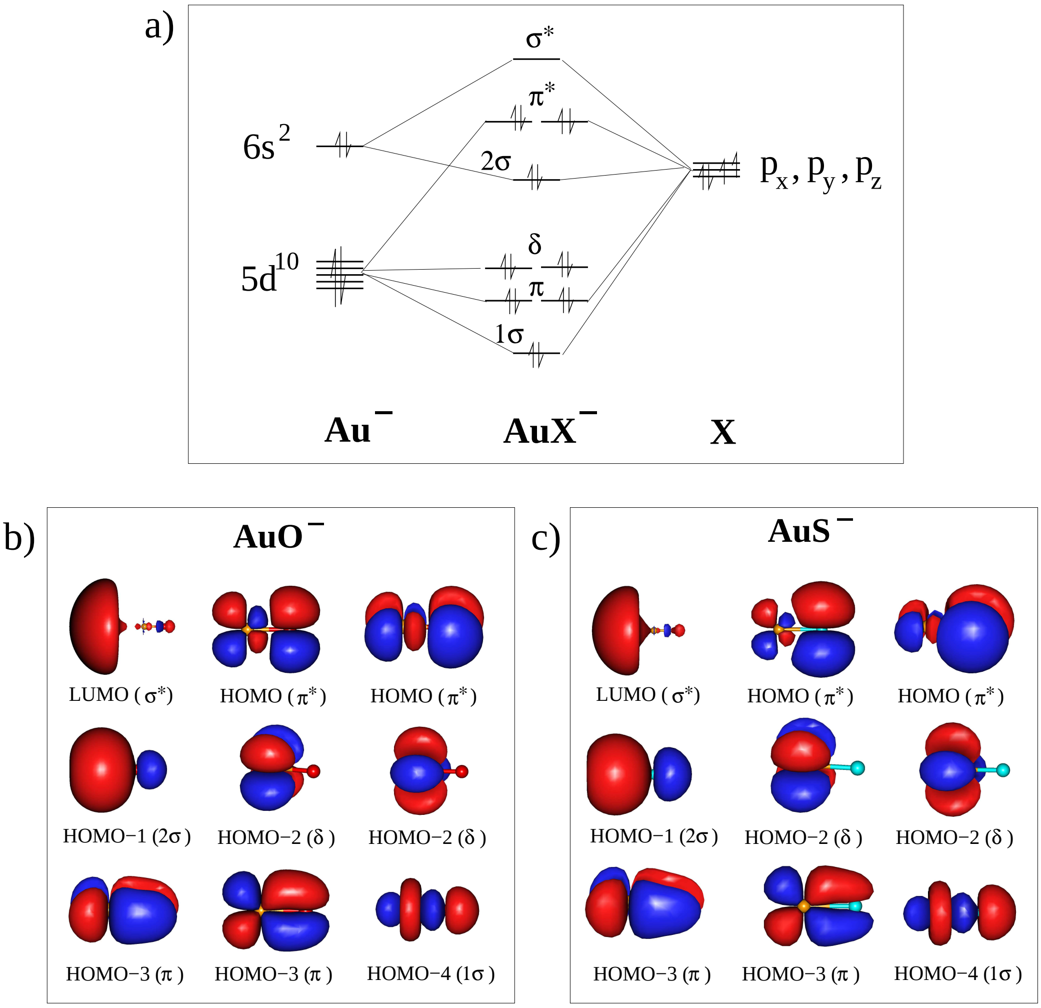

Figure 6.1: a) MO diagram for ^{1}AuX$^-$ (X = O, S). Molecular orbital pictures for b) AuO$^-$ and c) AuS$^-$ are also given.

Table 6.2: Calculated vertical detachment energies (VDE) for AuO$^-$ compared to the experimental values.[a]

		VDE (eV)		
final state	Ω	theory	experiment	contribution of basis states to SO eigenstates
X ($^2\Pi_{3/2}$)	3/2	2.312	2.378 ± 0.015	97% [$1^2\Pi_{3/2}$]
($^2\Pi_{1/2}$)	1/2	2.464	2.556 ± 0.015	97% [$1^2\Pi_{1/2}$]
a ($^4\Sigma_{1/2}$)	1/2	3.797	3.745 ± 0.020	36% [$1^2\Sigma_{1/2}$] + 43% ($1^4\Sigma_{1/2}$) + 18%($^4\Pi_{1/2}$)
A ($^2\Sigma_{1/2}$)	1/2	3.925	3.945 ± 0.020	56% [$1^2\Sigma_{1/2}$] + 38% ($1^4\Sigma_{1/2}$)
B ($^2\Delta_{5/2}$)	5/2	5.443	5.24 ± 0.03	96% [$^2\Delta_{5/2}$]
C ($^2\Pi_{1/2}$)	1/2	5.818	5.72 ± 0.04	12% [$2^2\Sigma_{1/2}$] + 39% ($^2\Pi_{1/2}$) + 27% ($^2\Sigma_{1/2}$)
D ($^2\Pi_{3/2}$)	3/2	6.111	5.97 ± 0.04	57% [$2^2\Pi_{3/2}$] + 17% [$^2\Delta_{3/2}$] + 13% ($^2\Pi_{3/2}$)
E ($^2\Sigma_{1/2}$)	1/2	6.248	6.11 ± 0.04	61% [$2^2\Sigma_{1/2}$] + 21% [$2^2\Pi_{1/2}$]

[a] Ω is the quantum number for the projection of the total angular momentum on the molecular axis. Symmetries of excited states with dominant single excitation corresponding to experimentally allowed states are given in square brackets; labels for forbidden states with contributions from multiple excitations are given in round brackets.

Table 6.3: Calculated vertical detachment energies (VDE) for AuS$^-$ compared to the experimental values.[a]

		VDE (eV)		
final state	Ω	theory	experiment	contribution of basis states to SO eigenstates
X ($^2\Pi_{3/2}$)	3/2	2.452	2.475 ± 0.015	98% [$1^2\Pi_{3/2}$]
($^2\Pi_{1/2}$)	1/2	2.562	2.637 ± 0.015	98% [$1^2\Pi_{1/2}$]
a ($^4\Sigma_{1/2}$)	1/2	4.146		9% [$1^2\Sigma_{1/2}$] + 78% ($1^4\Sigma_{1/2}$)
A ($^2\Sigma_{1/2}$)	1/2	4.242	4.402 ± 0.015	87% [$1^2\Sigma_{1/2}$] + 10% ($1^4\Sigma_{1/2}$)
B ($^2\Delta_{5/2}$)	5/2	5.525	5.54 ± 0.03	85% [$^2\Delta_{5/2}$]
C ($^2\Sigma_{1/2}$)	1/2	6.315	~6.1	32% [$2^2\Sigma_{1/2}$] + 21% ($^2\Pi_{1/2}$) + 21% ($^4\Delta_{1/2}$)
D ($^2\Pi_{3/2}$)	3/2	6.319	~6.1	82% [$2^2\Pi_{3/2}$]
E	3/2	7.134		23% [$^2\Delta_{3/2}$] + 10% [$2^2\Pi_{3/2}$] + 37% ($^4\Phi_{3/2}$)

[a] Ω is the quantum number for the projection of the total angular momentum on the molecular axis. Symmetries of excited states with dominant single excitation corresponding to experimentally allowed states are given in square brackets; labels for forbidden states with contributions from multiple excitations are given in round brackets.

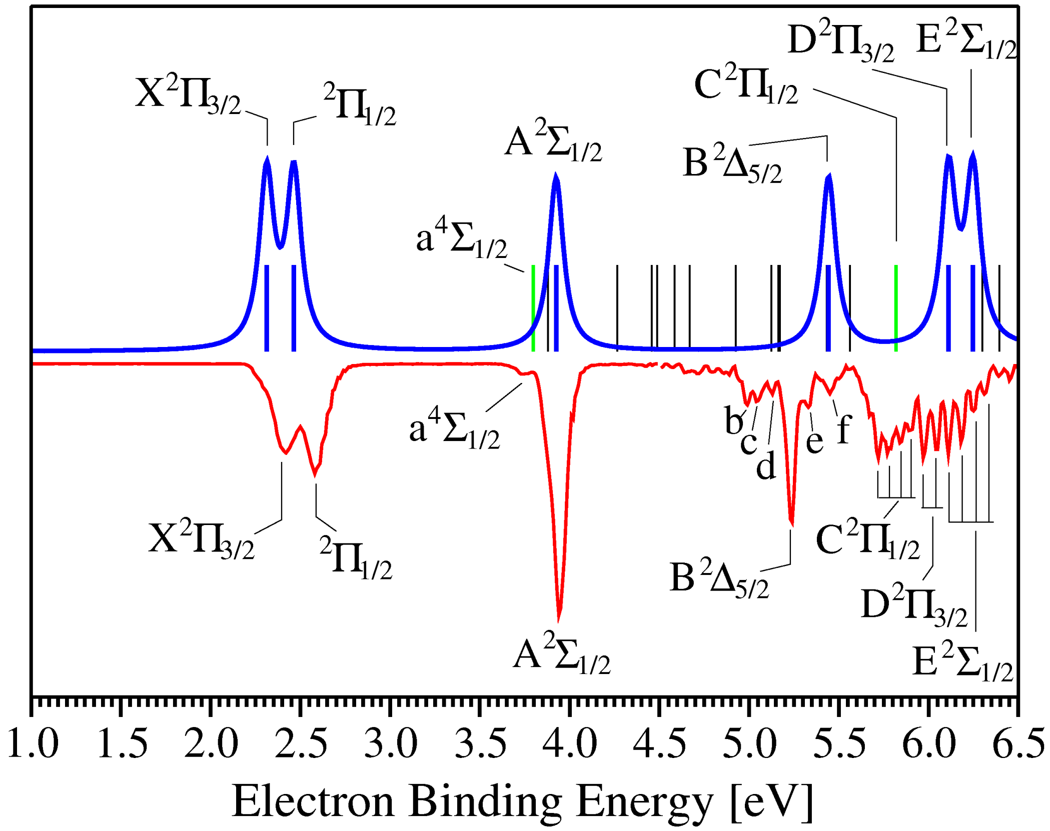

Figure 6.2: top (blue): Calculated photoelectron peaks T_e [eV] of ^{1}AuO$^-$. Energies of the calculated SO-eigenstates with dominant one-electron excitation character are given as thick blue lines; states with multielectron excitation character are given as thin black lines. The SO-eigenstates are labelled according to the assignments in Table 6.2. The green line indicates a SO-eigenstate with contribution from the allowed $^2\Sigma_{1/2}$ state (see text). Lorentzian broadening is used for eye guidance accounting the degeneracy of states. bottom (red): Experimental PES spectrum of AuO$^-$ at 193 nm (6.424 eV). The experimental PES spectrum for BE $>$ 4.5 eV is enlarged by a factor 3. Resolved vibrational structures are labelled with vertical lines.

the bonding π and antibonding π^* orbitals which are both occupied in the anionic ground state. The linear combination of the O(2p$_z$) [S(3p$_z$)] with the Au(6s) and Au(5d$_{z^2}$) orbitals yields three σ-MOs two of which are occupied by two electrons each (cf. 1σ and 2σ orbitals in Figure 6.1) leading to the strong bond between gold and oxygen/sulfur.

The spectral assignments and comparisons between computed and experimental VDEs for AuO$^-$ and AuS$^-$ are given in Tables 6.2 and 6.3, respec-

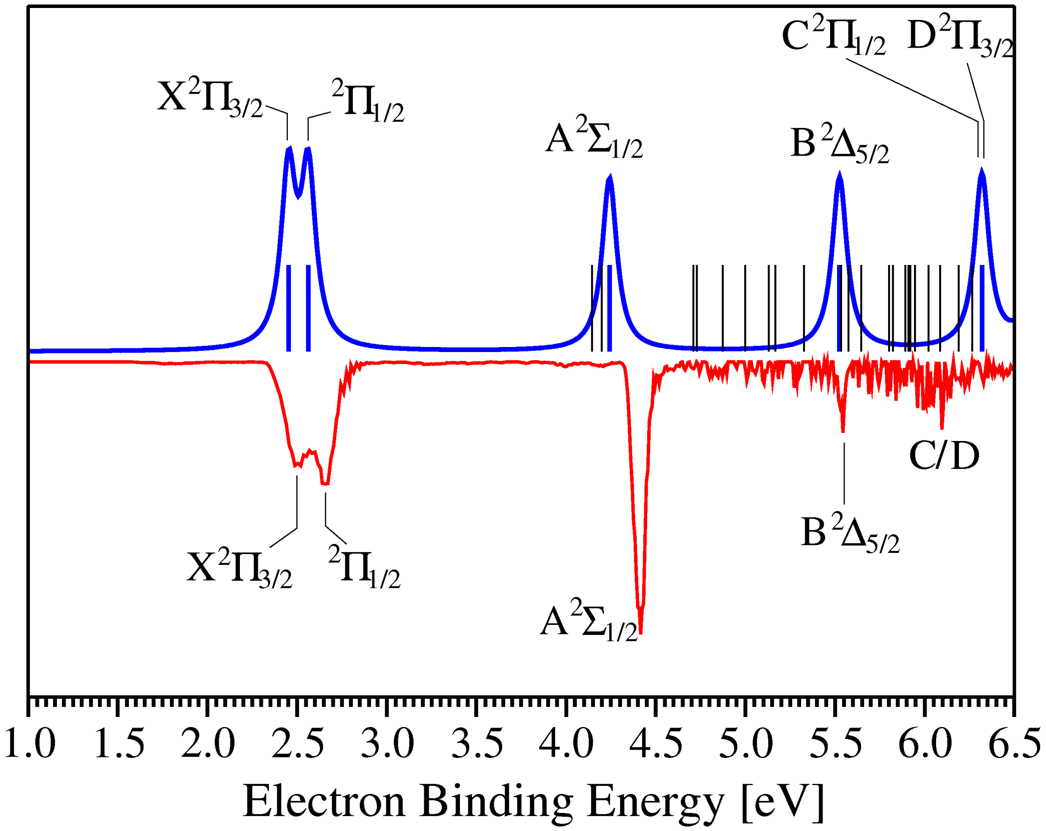

Figure 6.3: top (blue): Calculated photoelectron peaks T_e [eV] of ^{1}AuS$^-$. Energies of the calculated SO-eigenstates with dominant one-electron excitation character are given as thick blue lines; states with multielectron excitation character are given as thin black lines. The SO-eigenstates are labelled according to the assignments in Table 6.3. Lorentzian broadening is used for eye guidance accounting the degeneracy of states. bottom (red): The experimental PES spectrum of AuS$^-$ at 193 nm (6.424 eV).

tively. The ground state of AuX$^-$ was predicted to be $^1\Sigma^+$ with a closed-shell electron configuration: $1\sigma^2\pi^4\delta^4 2\sigma^2\pi^{\star 4}$ (Figure 6.1). Pictures of the MOs for AuO$^-$ and AuS$^-$ are shown in Figure 6.1. The 1σ, π, and δ MOs are primarily of Au 5d character with contributions from the O/S p orbitals, whereas the 2σ and $\pi^\star$ MOs are mainly from the O/S p orbitals with contributions from the Au 5d and 6s orbitals. Photodetachment from the $\pi^\star$ HOMO of AuX$^-$ produces the $^2\Pi$ ground state of AuX, corresponding to band X in the PES spectra of AuO$^-$ (Figure 6.2) and AuS$^-$ (Figure 6.3). The calculated VDEs and SO splittings for this detachment channel agree well with the experimental data (Tables 6.2 and 6.3).

The next major detachment channel is from the 2σ MO, resulting in the $^2\Sigma_{1/2}$ excited state for AuX. This corresponds to the intense A band in the spectra of AuX$^-$ (Figure 6.2). The calculated VDE for this detachment channel (3.925 eV) for AuO$^-$ is in excellent agreement with the experimental result (3.945±0.020 eV), whereas the calculated VDE (4.242 eV) for AuS$^-$ is slightly underestimated in comparison to the experimental result (4.402±0.015 eV). As shown in Tables 6.2 and 6.3, there is a considerable configuration mixing in the A $^2\Sigma_{1/2}$ state, in particular in AuO, where there is a mixing of 38% from a $^4\Sigma_{1/2}$ state (10% in the case of AuS). According to the calculation, the weak PES band (a) observed at 3.797 eV (Figure 6.2b) corresponds to a final state with considerable configuration mixing, with the dominating component coming from the $^4\Sigma_{1/2}$ state. The $^4\Sigma_{1/2}$ state derives from a MO configuration of $\pi^{\star 2}\sigma^{\star 1}$, i.e., a two-electron detachment transition (detachment of an electron from the $\pi^\star$ orbital with another $\pi^\star$ electron excited to the $\sigma^\star$ MO). Such two-electron transitions are forbidden in one-electron detachment processes. But this transition in AuO$^-$ gains intensity from the significant mixing with the $^2\Sigma_{1/2}$ state (36%, see Table 6.2). Interestingly, this two-electron transition in AuS$^-$ is negligible, in excellent agreement with the theoretical prediction that there is a very small mixing with the $^2\Sigma_{1/2}$ state (only 9%, see Table 6.3).

The next detachment channel occurs from the δ MO, resulting in the $^2\Delta$ final state and corresponding to the B band in the PES spectra of AuX$^-$. The calculated VDE (5.443 eV) for AuO$^-$ is slightly overestimated relative to the experimental result (5.24±0.03 eV), whereas the calculated VDE (5.525 eV) for AuS$^-$ is in quantitative agreement with the experimental result (5.54±0.03 eV).

The next major detachment channels are from the π and 1σ MOs. The calculations show considerable configuration mixing for these detachment channels in both systems (Tables 6.2 and 6.3). In the case of AuS$^-$, there was an insufficient signal-to-noise ratio in the 193 nm spectrum (Figure 6.3) to allow definitive resolution of individual states for these high binding energy detachments. Therefore, the discussion focuses mainly on the AuO$^-$ case, for which well-resolved and rich spectral features were observed in the 193 nm spectrum in the high binding energy range (Figure 6.2).The detachment channel from the π MO results in the $^2\Pi$ state, which can have strong SO splitting. The calculations show that both SO states have major configuration mixings. The bands C and D at 5.72 and 5.97 eV each with a broad vibrational progression are assigned to the $^2\Pi_{1/2}$ and $^2\Pi_{3/2}$ states, respectively, with calculated VDEs of 5.818 and 6.111 eV, in good agreement with the experimental values (Table 6.2). The detachment from the 1σ MO leads to the $^2\Sigma_{1/2}$ final state, which is assigned to the E band with a broad vibrational progression. The calculated VDE of 6.248 eV is in good agreement with the experimental value of 6.11±0.04 eV. There are a number of weak features (b-f) between ∼5–5.5 eV, which are not assigned. They are likely due to multi-electron transitions. Numerous multi-electron transitions with severe configuration mixing have indeed been predicted in these energy ranges (see black sticks in Figure 6.2).

The broad vibrational progressions which resulted from detachments from the 1σ and π MOs of AuO^- suggest that they are strongly bonding orbitals, whereas the experimental PES spectra suggest that the 2σ and $\pi^\star$ MOs are primarily non-bonding. This is a significant observation because it reveals directly the strong covalent nature and strong participation of the Au 5d orbitals in the Au-O bonding, as will be discussed further in Sections 6.4.1 and 6.4.2.

6.3.3 Linear AuO_2^- and AuS_2^-

The ground states of AuO_2^- and AuS_2^- have a linear $XAuX^-$ structure with a triplet spin state ($D_{\infty h}$ $^3\Sigma_g^-$) and an open-shell configuration ($1\sigma_g^2 1\pi_g^4 \delta^4$-$1\sigma_u^2 2\sigma_g^2 1\pi_u^4 2\pi_g^2$), as shown in Figure 6.4. The pictures of the MOs for both $OAuO^-$ and $SAuS^-$ are also shown in Figure 6.4. The $1\sigma_g$, $1\pi_g$, δ and $2\pi_g$ MOs are primarily of mixed Au 5d / O/S p character, and the other occupied valence orbitals are mainly of O/S p character. The $2\pi_g$ HOMO is an antibonding MO, whereas the $1\pi_u$ MO is weakly bonding. The configurations of $OAuO^-$ and $SAuS^-$ are similar, except the ordering of the $1\sigma_u$ and $2\sigma_g$ MOs is different in the two molecules (Figure 6.4). The open-shell anions allow both doublet and quartet final states to be reached via one-electron detachment, yielding more complicated PES spectra. The spectral assignments and detailed comparisons between the calculated VDEs and experimental data are given in Table 6.4 for AuO_2^- and Table 6.5 for AuS_2^-.

Detachment from the $2\pi_g$ HOMO leads to the neutral $^2\Pi_g$ ground state of AuX_2 with a SO splitting ($^2\Pi_{g,1/2}$ and $^2\Pi_{g,3/2}$). The calculated VDE for the transition to the $^2\Pi_{g,1/2}$ ground state (3.473 eV for AuO_2^- and 3.468 eV for AuS_2^-) are in excellent agreement with the experimental measurements (3.40±0.03 eV for AuO_2^- and 3.47±0.03 eV for AuS_2^-). Moreover, the calculated VDEs for the $^2\Pi_{g,3/2}$ state (3.627 eV for AuO_2^- and 3.585 eV for AuS_2^-) agree well with the experimental values (3.60±0.04 eV for AuO_2^- and 3.54±0.04 eV for AuS_2^-) giving a SO splitting of 0.154 eV (exp: 0.20 eV) and 0.117 eV (exp: 0.12 eV) for AuO_2^- and AuS_2^-, respectively. The substantial vibrational excitations accompanying the detachment from the $2\pi_g$ HOMO in both AuO_2^- and AuS_2^- are consistent with the antibonding nature of this MO. This is also evident from the enhanced Au-O symmetric stretching frequency

Table 6.4: Calculated vertical detachment energies (VDE) for OAuO^- ($D_{\infty h}$ ${}^3\Sigma_g^-$) compared to the experimental values.[a]

		VDE (eV)		contribution of basis states to SO eigenstates
final state	Ω	theory	experiment	
X (${}^2\Pi_{g,1/2}$)	1/2	3.473	3.40 ± 0.03	93% [$1^2\Pi_{g,1/2}$]
(${}^2\Pi_{g,3/2}$)	3/2	3.627	3.60 ± 0.04	96% [$1^2\Pi_{g,3/2}$]
A (${}^4\Pi_{u,i}$)	5/2	4.283	4.23 ± 0.03	99% [${}^4\Pi_{u,5/2}$]
	3/2	4.285		94% [${}^4\Pi_{u,3/2}$]
	1/2	4.288		96% [${}^4\Pi_{u,1/2}$]
	-1/2	4.297		95% [${}^4\Pi_{u,-1/2}$]
B (${}^2\Pi_{u,1/2}$)	1/2	4.713	4.70 ± 0.04	98% [${}^2\Pi_{u,1/2}$]
(${}^2\Pi_{u,3/2}$)	3/2	4.785	4.78 ± 0.04	95% [${}^2\Pi_{u,3/2}$]
C (${}^4\Sigma_g^-$)	3/2	4.939	4.99 ± 0.03	96% [${}^4\Sigma^-_{g,3/2}$]
	1/2	4.964		94% [${}^4\Sigma^-_{g,1/2}$]
D (${}^2\Sigma^-_{g,1/2}$)	1/2	5.076	5.08 ± 0.03	96% [${}^2\Sigma^-_{g,1/2}$]
E (${}^4\Sigma_u^-$)	3/2	5.341	5.21 ± 0.03	98% [${}^4\Sigma^-_{u,3/2}$]
	1/2	5.343		100% [${}^4\Sigma^-_{u,1/2}$]
F (${}^2\Sigma_u^-$)	1/2	6.106	5.79 ± 0.04	97% [${}^2\Sigma^-_{u,1/2}$]
		6.216		11% [${}^4\Delta$] + 88% (${}^4\Pi_g$)
		6.382		31% [$2^2\Pi_g$] + 59% (${}^4\Pi_g$)
		6.612		98% [${}^4\Delta$]

[a] Ω is the quantum number for the projection of the total angular momentum on the molecular axis. Symmetries of excited states with dominant single excitation corresponding to experimentally allowed states are given in square brackets; labels for forbidden states with contributions from multiple excitations are given in round brackets.

Table 6.5: Calculated vertical detachment energies (VDE) for SAuS$^-$ ($D_{\infty h}$ $^3\Sigma_g^-$) compared to the experimental values.[a]

		VDE (eV)		contribution of basis states
final state	Ω	theory	experiment	to SO eigenstates
X ($^2\Pi_{g,1/2}$)	1/2	3.468	3.47 ± 0.03	92% [$1^2\Pi_{g,1/2}$]
($^2\Pi_{g,3/2}$)	3/2	3.585	3.54 ± 0.04	97% [$1^2\Pi_{g,3/2}$]
A ($^4\Pi_{u,i}$)	5/2	3.991	3.96 ± 0.03	99% [$^4\Pi_{u,5/2}$]
	3/2	3.994		94% [$^4\Pi_{u,3/2}$]
	1/2	3.995		96% [$^4\Pi_{u,1/2}$]
	-1/2	4.003		95% [$^4\Pi_{u,-1/2}$]
B ($^2\Pi_{u,1/2}$)	1/2	4.344	4.35 ± 0.05	98% [$^2\Pi_{u,1/2}$]
($^2\Pi_{u,3/2}$)	3/2	4.405	4.40 ± 0.05	95% [$^2\Pi_{u,3/2}$]
C ($^4\Sigma_u^-$)	3/2	4.935	4.86 ± 0.03	99% [$^4\Sigma^-_{u,3/}$]
	1/2	4.937		99% [$^4\Sigma^-_{u,1/2}$]
D ($^4\Sigma_g^-$)	1/2	5.170	5.07 ± 0.05	85% [$^4\Sigma^-_{g,1/2}$] + 8% ($^4\Pi_u$)
	3/2	5.198		84% [$^4\Sigma^-_{g,3/2}$] + 10% ($^4\Pi_u$)
E ($^2\Sigma_g^-$)	1/2	5.251	5.24 ± 0.06	78% [$^2\Sigma^-_{g,1/2}$] + 12% ($^4\Pi_u$)
F ($^2\Sigma_u^-$)	1/2	5.476	5.34 ± 0.06	99% [$^2\Sigma^-_{u,1/2}$]
G ($2^2\Pi_{g,3/2}$)	3/2	6.006		74% [$2^2\Pi_{g,3/2}$]
	1/2	6.160		82% [$2^2\Pi_{g,1/2}$]
H ($^4\Delta_{7/2}$)	7/2	6.480		100% [$^4\Delta_{7/2}$]

[a] Ω is the quantum number for the projection of the total angular momentum on the molecular axis. Symmetries of excited states with dominant single excitation corresponding to experimentally allowed states are given in square brackets; labels for forbidden states with contributions from multiple excitations are given in round brackets.

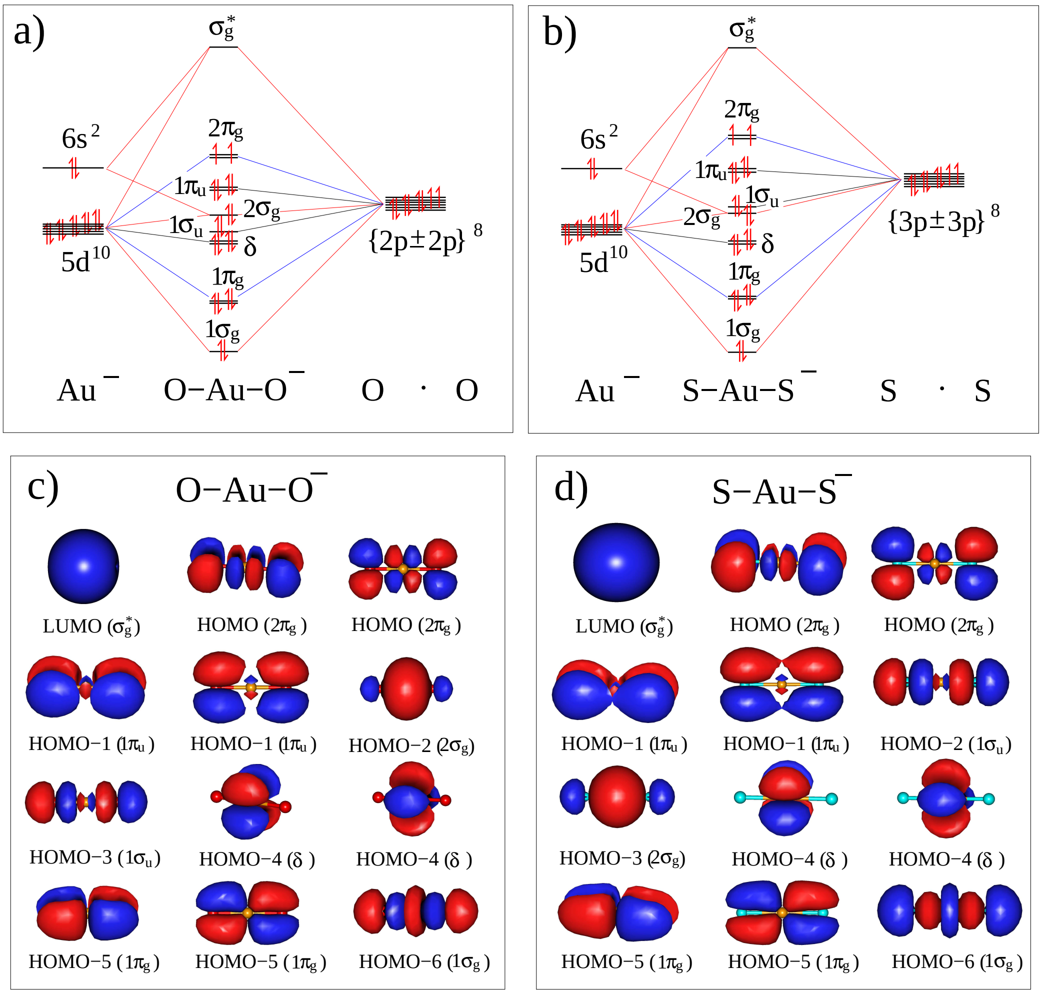

Figure 6.4: MO diagrams for a) ^{3}OAuO^{-} and b) ^{3}SAuS^{-} with corresponding molecular orbital pictures c) and d).

(740±60 cm^{-1}) observed for the ground state of AuO$_2$ relative to the AuO$_2^-$ anion ground state ($\sim$600 cm^{-1}) estimated from the hot-band transition in the experimental PES.

The next detachment channel comes from the fully occupied $1\pi_u$ MO, which can lead to both quartet ($^4\Pi_u$) and doublet ($^2\Pi_u$) final states of AuX$_2$. Both of these final states can have multiple SO components. The calculated SO splitting for the $^4\Pi_u$ state ($^4\Pi_{u,5/2,3/2,1/2,-1/2}$) is very small in both molecules, with the SO eigenstate energies ranging from 4.283 to 4.297 eV for AuO$_2$ (Table 6.4) and 3.991 to 4.003 eV for AuS$_2$ (Table 6.5). These small SO splittings are smaller than the experimental resolution and thus could not be resolved in the experiment. The intense A band is assigned to the $^4\Pi_u$

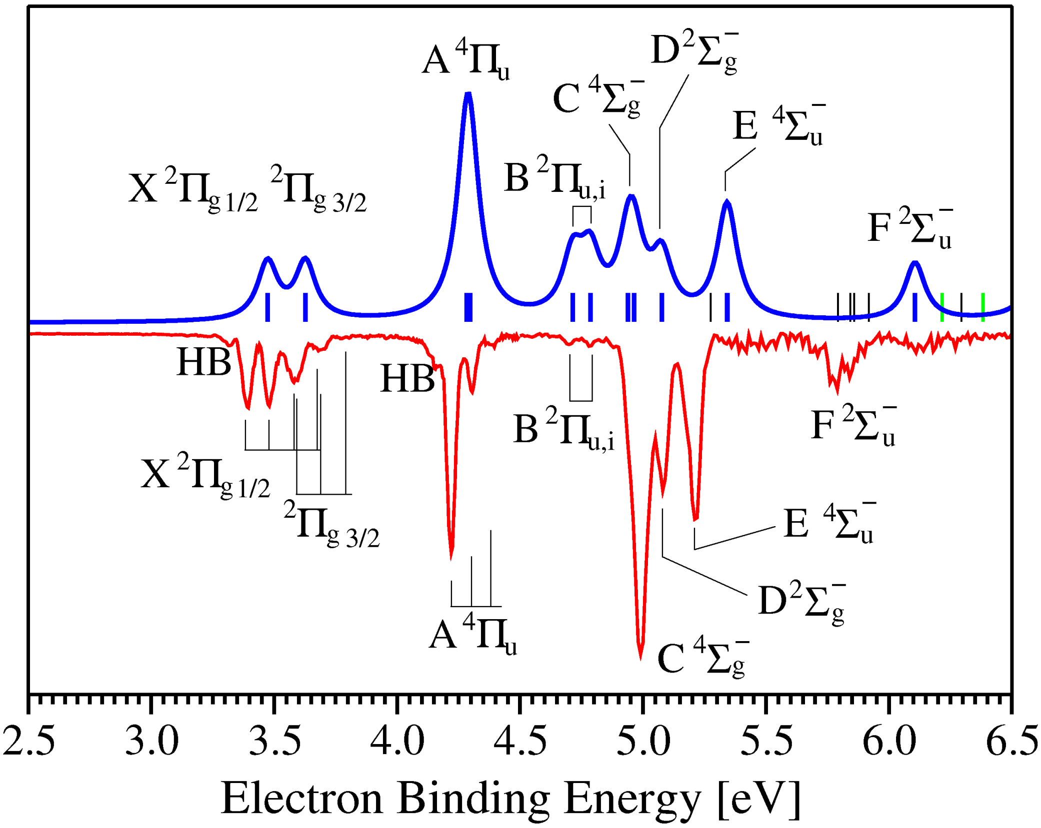

Figure 6.5: top (blue): Calculated photoelectron peaks T_e [eV] of linear $OAuO^-$ ($D_{\infty h}\ {}^3\Sigma_g^-$). Energies of calculated SO-eigenstates with dominant one-electron excitation character are given as thick blue lines; states with multielectron excitation character are given as thin black lines. The SO-eigenstates are labelled according to the assignments in Table 6.4. The green lines indicate SO-eigenstates with contribution from allowed states (see text). Lorentzian broadening is used for eye guidance accounting the degeneracy of states. bottom (blue): Experimental PES spectrum of AuO_2^- at 266 nm (4.661 eV) for BE $<$ 4.5 eV and at 193 nm (6.424 eV) for BE $>$ 4.5 eV.

state (Figures 6.5 and 6.6): the calculated VDE is indeed in excellent agreement with the observed VDE (4.23±0.03 eV for AuO_2^- and 3.96±0.03 eV for AuS_2^-). The short vibrational progression resolved for the A $^4\Pi_u$ state in AuX_2 suggests that the $1\pi_u$ MO has slightly Au-X antibonding character. The $^2\Pi_u$ state was predicted to have a significant SO splitting. In the case of AuO_2^-, the predicted SO eigenstate energies of 4.713 eV ($^2\Pi_{u,1/2}$) and 4.785 eV ($^2\Pi_{u,3/2}$) (Table 6.4) are in excellent agreement with the two weak PES bands at 4.70 and 4.78 eV (Figure 6.5). In the case of AuS_2^-, the pre-

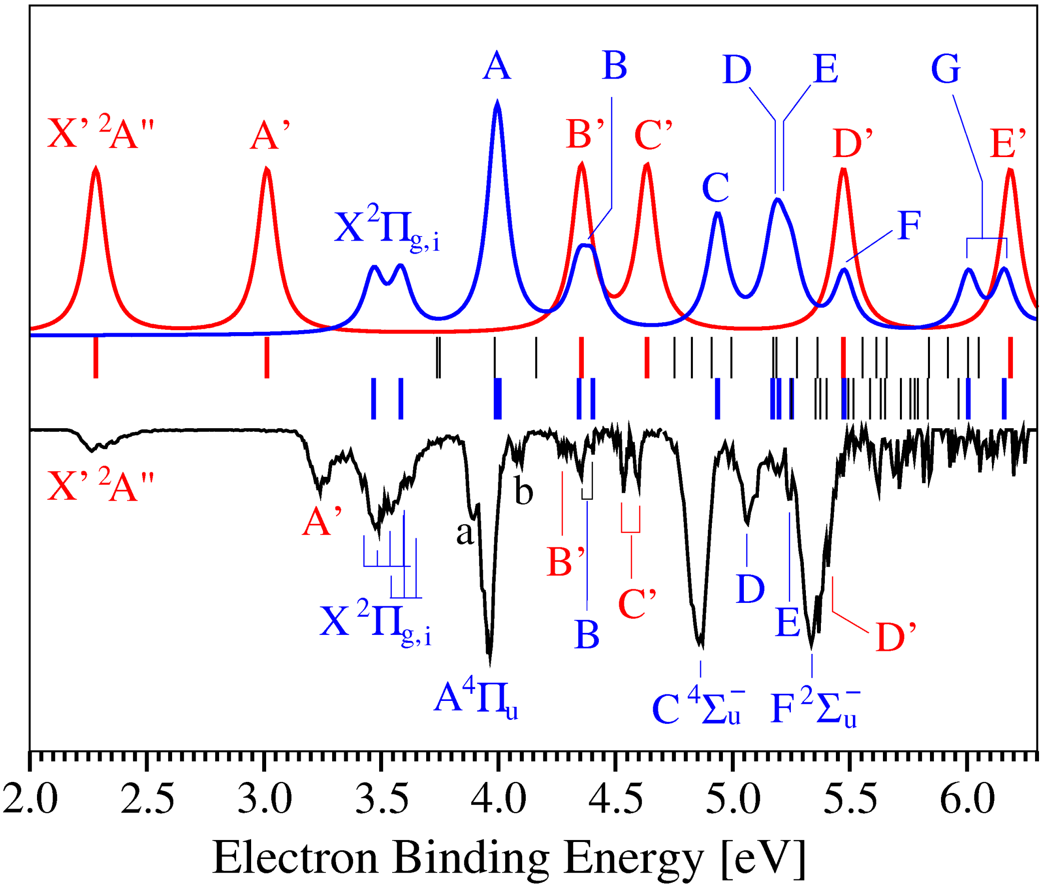

Figure 6.6: top: Calculated photoelectron peaks T$_e$ [eV] of linear SAuS$^-$ ($D_{\infty h}$ $^3\Sigma_g^-$) (blue) and bent Au(S$_2$)$^-$ (C_S $^1A'$) (red). Energies of calculated SO-eigenstates with dominant one-electron excitation character are given as thick blue and red lines, respectively. SO states with multielectron excitation character are given as thin black lines. The SO-eigenstates are labelled according to the assignments in Tables 6.5 and 6.6. Lorentzian broadening is used for eye guidance accounting the degeneracy of states. bottom: Experimental PES spectrum of AuS$_2^-$ at 266 nm (4.661 eV) for BE $<$ 4.7 eV and at 193 nm (6.424 eV) for BE $>$ 4.7 eV. Resolved vibrational structures for the X $^2\Pi_{g,i}$ state are labelled with vertical lines.

dicted VDEs for the $^2\Pi_{u,1/2}$ and $^2\Pi_{u,3/2}$ SO states are 4.344 and 4.405 eV, respectively. However, in the PES spectra, numerous weak peaks were observed in the vicinity of these transitions due to spectral features from the Au(S$_2$)$^-$ isomer (see Section 6.3.4). The two peaks at 4.35 and 4.40 eV were assigned to the $^2\Pi_{u,1/2}$ and $^2\Pi_{u,3/2}$ states (band B) based on the theoretical predictions.

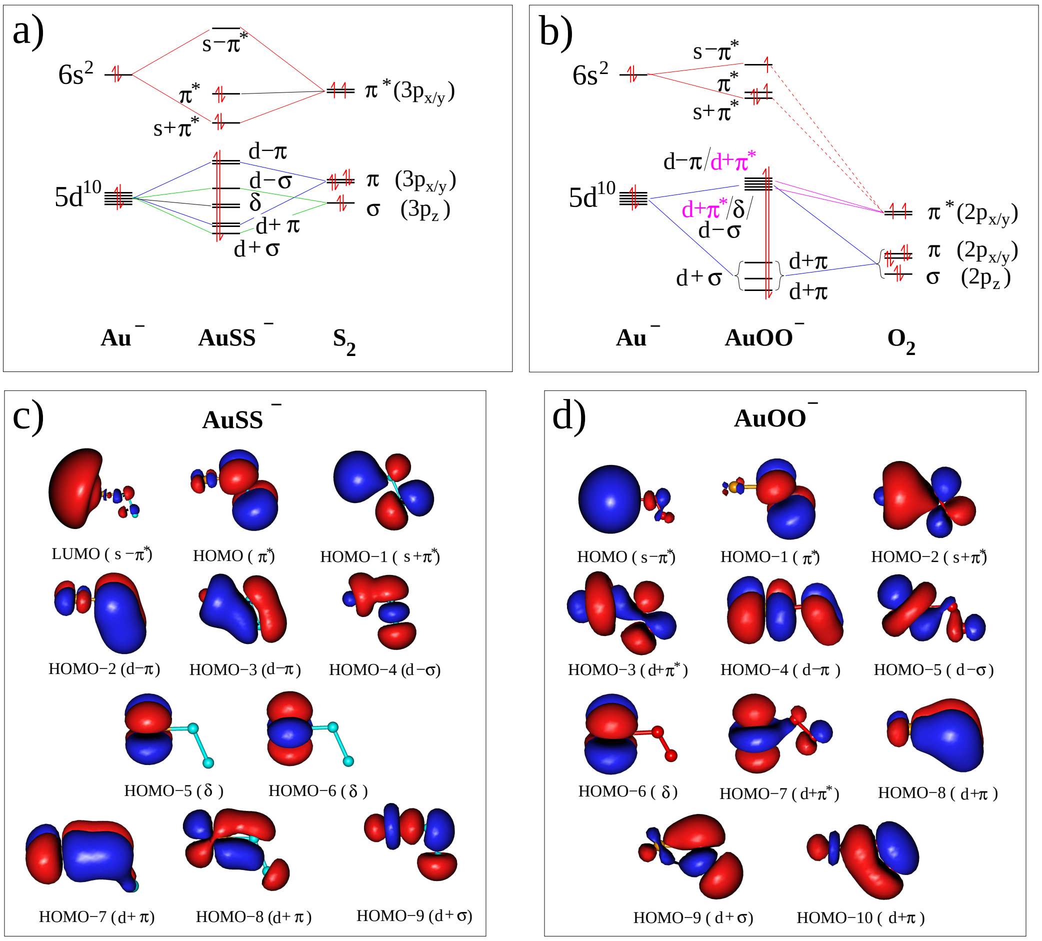

Figure 6.7: MO diagrams for a) ^{1}AuSS$^-$ and b) ^{3}AuSS$^-$ with corresponding molecular orbital pictures c) and d).

The higher energy detachment channels become more congested and the state ordering also becomes different for AuO_2^- and AuS_2^- according to the theoretical predictions. However, the observed spectral features can all be well assigned based on the theoretical predictions, as shown in Figure 6.5 and Table 6.4 for AuO_2^- and in Figure 6.6 and Table 6.5 for AuS_2^-, respectively. It should be pointed out that detachments from Au 5d based MOs ($1\sigma_g$, $1\pi_g$, δ) were predicted to occur at VDEs above 6 eV for both AuO_2^- and AuS_2^- and they were not observed due to the poor signal-to-noise ratios in the higher binding energy range at 193 nm.

Table 6.6: Calculated vertical detachment energies (VDE) for $Au(S_2)^-$ (C_S $^1A'$) compared to the experimental values.[a]

	VDE (eV)		contribution of basis states
final state	theory	experiment	to SO eigenstates
X′ ($^2A''$)	2.282	2.24 ± 0.03	99% [$1^2A''$]
A′ ($^2A'$)	3.013	3.22 ± 0.03	98% [$1^2A'$]
B′ ($^2A''$)	4.355	4.27 ± 0.06	64% [$2^2A''$] + 29% [$2^2A'$]
C′ ($^2A'$)	4.634	4.54 ± 0.05	29% [$2^2A''$] + 56% [$2^2A'$]
D′ ($^2A'$)	5.473	5.40 ± 0.05	33% [$3^2A'$]
E′ ($^2A'$)	6.186		23% [$3^2A'$] + 44% [$4^2A'$]

[a] Symmetries of excited states with dominant single excitation corresponding to experimentally allowed states are given in square brackets.

6.3.4 $Au(S_2)^-$

Figure 6.7 shows the MO correlation diagram and MO pictures of the bent $Au(S_2)^-$ isomer (C_S $^1A'$). The corresponding figure for the unbound $Au(O_2)^-$ species (C_S $^3A''$) is also shown for comparison. It is seen clearly that the $\pi^\star$ HOMO of S_2 can interact favorably with the Au 6s orbital to form a strongly bound $s + \pi^\star$ MO, a somewhat non-bonding MO ($\pi^\star$) mainly localized on the S_2 fragment, and a strongly antibonding $s - \pi^\star$ MO. The strong Au 6s and S_2 $\pi^\star$ interactions result in a large separation between the bonding and antibonding MOs, leading to a closed-shell configuration for $Au(S_2)^-$. On the other hand, the unfavorable interaction between the Au 6s and the O_2 $\pi^\star$ MO leads to an unbound $Au(O_2)^-$ with an open shell configuration. The calculated detachment channels and spectral interpretations for $Au(S_2)^-$ are given in Table 6.6. Detachment from the $\pi^\star$ HOMO of $Au(S_2)^-$ leads to the $^2A''$ ground state of neutral $Au(S_2)$. The observed vibration (~610 cm^{-1}) accompanying the ground-state detachment transition should be due to the S-S stretching, supporting the theoretical prediction that the HOMO is mainly localized on the S_2 unit (Figure 6.7).

The next detachment channel takes place from the $s + \pi^\star$ bonding MO, resulting in the first excited state ($^2A'$) of $Au(S_2)$. The calculated VDE (3.013 eV) is in good agreement with the VDE of the A' band (3.22±0.03 eV). The VDEs for the next two detachment channels were calculated to be at 4.355 and 4.634 eV, both with strong configuration mixings. The final states are designated with the major contributions as $^2A''$ and $^2A'$ and are assigned to the weak peaks at 4.27 eV (B') and 4.54 eV (C'), respectively (Figure 6.6 and Table 6.6). The next detachment channel (D' $^2A'$) was predicted to have a VDE of 5.473 eV, which would overlap with the F $^2\Sigma_u^-$ band of the linear

AuS_2^- (Figure 6.6).

Overall the theoretical results allow a quantitative description of the electronic structure of the anionic gold monomer oxides and sulfides which have been fully confirmed by experimental observations. Strong electron correlation effects were revealed in particular for the detachments from the AuX^- diatomics and the $Au(S_2)^-$ isomers, as can be seen from the contributions of basis states to the final SO eigenstates in Tables 6.2, 6.3, and 6.6. The electron correlation effects are somewhat less pronounced for the detachments from the two linear AuX_2^- molecules at least for the low-lying transitions, which are dominated by single electron excitations.

6.4 Chemical Bonding in AuX^- and $XAuX^-$: O vs. S

6.4.1 AuO^- vs. AuS^-

The MO pictures for AuO^- and AuS^- are displayed in Figure 6.1. The O(S) $p_{x/y}$ orbitals and Au $5d_{xz/yz}$ orbitals form the bonding π (HOMO-3) and antibonding $\pi^\star$ HOMO, which are both fully occupied in the anionic ground state. The O(S) p_z orbital interacts with the Au $6s$ and $5d_{z^2}$ orbitals to form the bonding 1σ (HOMO-4), non-bonding 2σ (HOMO-1) and the unoccupied antibonding $\sigma^\star$ LUMO, whereas the δ MO (HOMO-2) is purely non-bonding. The non-bonding nature of the 2σ and δ MOs in AuX^- is confirmed by the PES spectra, which show very little Franck-Condon activity upon electron removals from these MOs (Figures 1 and 3 in [144]). On the basis of the MO configuration, the AuX^- molecules possess a single σ bond derived from the 1σ bonding MO because the bonding 1π and the antibonding $\pi^\star$ MOs cancel each other. However, while the strong bonding nature of the 1σ and 1π MOs are confirmed by the PES spectra (strong Franck-Condon activities and the reduced vibrational frequencies in the C, D, and E PES bands of AuO^-, as shown in Figure 6.2b), the $\pi^\star$ MO is somewhat non-bonding as evidenced by the very weak Franck-Condon activities in the X bands (Figures 1 and 3 in [144]). Thus, the AuX^- species contain some π bonding character. If the $\pi^\star$ MO were completely non-bonding, the bond in AuX^- could be characterized as a triple bond. Indeed, the calculated bond lengths of AuX^- (Table 6.1) are only slightly smaller than the sums of the Au and X triple bond covalent radii proposed by Pyykkö et al. [145] (1.76 Å for AuO and 2.18 Å for AuS). Since the $\pi^\star$ MO does have some antibonding character, as evidenced by the stronger bonds in neutral AuX, the chemical bonds in AuX^- or neutral

AuX are less than a triple bond. Removing all the four $\pi^\star$ electrons would lead to a real triply bonded AuX diatomic species, which corresponds to the electron configuration of AuC$^+$ or AuSi$^+$. Interestingly, these species have indeed been identified previously as containing a triple bond [145].

The Au-S bond is stronger than the Au-O bond in AuX$^-$, as indicated by the dissociation energies (Table 6.1): 2.677 eV for AuS$^-$ vs. 2.082 eV for AuO$^-$. The stronger bond in AuS$^-$ is also reflected in its shorter bond length. The calculated bond length of 2.216 Å for AuS$^-$ is much closer to the putative AuS triple bond length of 2.18 Å than the 1.882 Å bond length of AuO$^-$ to the putative AuO triple bond length of 1.76 Å. The stronger AuS$^-$ bond can be understood as being due to the less antibonding nature of its $\pi^\star$ HOMO. As shown in Figure 6.1, the Au 5d contributions to the $\pi^\star$ HOMO is smaller in AuS$^-$ than in AuO$^-$, leading to the stronger AuS$^-$ bond. The smaller 5d contribution to the $\pi^\star$ HOMO is also reflected in the smaller SO splitting in the $^2\Pi$ ground state in AuS (0.111 eV) than in AuO (0.152 eV).

6.4.2 OAuO$^-$ vs. SAuS$^-$

The bonding in OAuO$^-$ and SAuS$^-$ is also very similar, as can be seen from their MOs in Figure 6.4. As shown in Figure 6.4a) and b), the O(S) $p_{x/y}$ orbitals interact with the Au($5d_{yz/xz}$) orbitals to form the strong bonding $1\pi_g$ HOMO-5, the non-bonding $1\pi_u$ HOMO-1, and the antibonding $2\pi_g$ HOMO. The $2\pi_g$ HOMO is half occupied, resulting in the triplet ground state for AuX$_2^-$ ($^3\Sigma_g^-$). The interactions of O(S) p_z with Au $6s$ and $5d_{z^2}$ yield the strong bonding $1\sigma_g$, the bonding $2\sigma_g$, the weakly bonding $1\sigma_u$, and the antibonding $\sigma_g^\star$ LUMO. The antibonding character of the $2\pi_g$ HOMO is clearly revealed by the substantial Franck-Condon activities in the ground-state detachment transition [144] (see also Figure 6.6 for the SAuS$^-$) and the increased Au-X stretching vibrational frequency in the neutrals compared to the anions. The $1\pi_u$, $2\sigma_g$, and $1\sigma_u$ MOs are basically non-bonding according to the PES spectra since there is very little Franck-Condon activity upon electron removals from these orbitals. Thus, the Au-X bonding in AuX$_2^-$ should also have substantial multibonding characters.

Interestingly, the Au-X bond is significantly strengthened in AuX$_2^-$ compared to that in the AuX$^-$ diatomics, as seen in Table 6.1. In particular, the dissociation energy of 4.046 eV for AuO$_2^-$ → AuO$^-$ + O is almost twice as large as the AuO$^-$ dissociation energy (2.082 eV for AuO$^-$→Au$^-$+O). This enhanced Au-X bonding in AuX$_2^-$ is also reflected in their shortened Au-X distances. The enhanced Au-X bonding in AuX$_2^-$ is most likely due to the only partially occupied $2\pi_g$ antibonding orbitals and the strong covalent bonding interactions between the Au $5d$ and O(S) p atomic orbitals embodied in the $1\sigma_g$ and $1\pi_g$ MOs (Figure 6.4) yielding formally a double bond whose strength is partially enhanced by the weakly bonding $2\sigma_g$ orbital.

It is also interesting to note that, even though the AuO^- bond is slightly weaker than the AuS^- bond, the Au-O bond in AuO_2^- is actually stronger than the Au-S bond in AuS_2^-. This is partially due to the stronger Au 5d contributions to the $2\pi_g$ HOMO, as reflected in its stronger SO splitting, and partially due to the stronger interactions between the Au 5d and O 2p orbitals. Overall, the Au-O and Au-S bonds in the diatomic AuX^- and linear $XAuX^-$ molecules are strongly covalent due to the bonding capacities of the Au 5d orbitals as a result of the relativistic effects.

6.5 Chemical Bonding in $Au(X_2)^-$: Au^- Does Not Bind to O_2

6.5.1 Chemical Bonding in $Au(S_2)^-$

The MOs of $Au(S_2)^-$ are compared with those of $Au(O_2)^-$ in Figure 6.7. As shown in Figure 6.7a, the antibonding $\pi^\star$ MO of S_2 is well separated from its bonding π and σ MOs. This separation of bonding and antibonding MOs in S_2 makes them well matched energetically to interact with the Au 6*s* and 5*d*, respectively. However, the interactions of Au 5*d* and S_2 (σ and π) result in equal numbers of σ- and π-bonding and antibonding orbitals. Therefore, these interactions contribute little to the net chemical bonding in $Au(S_2)^-$. The bonding in $Au(S_2)^-$ originates primarily from the strong Au 6*s* and S_2 $\pi^\star$ interactions, which lead to a σ-bonding orbital ($s + \pi^\star$), a non-bonding $\pi^\star$ orbital, and an antibonding σ orbital ($s - \pi^\star$). Because of the strong σ interactions, the antibonding $s - \pi^\star$ orbital is much higher in energy, leading to the closed-shell electronic structure for $Au(S_2)^-$ (C_S $^1A'$). The fully occupied $\pi^\star$ HOMO is mainly localized on the S_2 fragment which is supported by the S-S stretching vibrational progression observed in the ground-state PES transition (X′ in Figure 6.6). The A′ band derives from detachment from the $s + \pi^\star$ bonding orbital. The unresolved vibrational features in the A′ band should consist of both Au-S stretching and Au-S-S bending vibrations according to the nature of the $s + \pi^\star$ MO. The separation of ∼1 eV between the A′ and X′ bands in the PES spectra of $Au(S_2)^-$ (Figure 6.6 and Table 6.6) indicates qualitatively the strength of the Au 6*s* and the S_2 $\pi^\star$ σ-interactions. The fact that this quantity is close to the calculated binding energy (1.388 eV) of $Au(S_2)^-$ suggests that indeed the Au 6*s* and S_2 $\pi^\star$ σ-interaction is mainly responsible for the covalent bonding in $Au(S_2)^-$.

6.5.2 Chemical Bonding in $Au(O_2)^-$

As shown in Figure 6.7, the main difference in bonding between $Au(O_2)^-$ and $Au(S_2)^-$ is the orbital energy mismatch between Au^- and O_2, resulting in little bonding interaction. This can also be seen quite clearly in the MO pictures of $Au(O_2)^-$ (Figure 6.7d). In particular, the weak interactions between the Au 6s and the O_2 $\pi^\star$ MO result in three closely-lying frontier orbitals: $s+\pi^\star$, $\pi^\star$, and $s-\pi^\star$, which are responsible for the open-shell $^3A''$ configuration of $Au(O_2)^-$. The fact that the oxygen orbitals are lower in energy is also evident by the mixing of the O_2 $\pi^\star$ orbitals with the Au 5d orbitals in contrast to $Au(S_2)^-$, where only the S_2 π and σ orbitals interact with the Au 5d orbitals (see Figure 6.7a). The calculations predict that at the chemical bonding distance $Au(O_2)^-$ is in fact repulsive with a negative dissociation energy (-0.272 eV), consistent with the MO analysis about the unfavorable interactions between Au^- and O_2. Therefore, the Au^- anion cannot chemisorb an O_2 molecule. This conclusion is consistent with the fact that no contributions from $Au(O_2)^-$ complexes exist in the AuO_2^- spectra (Figure 6.5). It should be pointed out that in a similar experiment on CuO_2^- previously both a linear $OCuO^-$ species and a $Cu(O_2)^-$ complex were observed [146, 147]. Thus, the failure to observe $Au(O_2)^-$ is not due to experimental conditions, but rather an indication of the non-bonding nature between Au^- and O_2.

The current observation is significant and relevant to the question of O_2 activation by gold clusters. It is generally believed that the activation of O_2 is the primary rate-limiting step in nano-gold catalysis. Interestingly, even-sized Au_n^- anion clusters were previously shown to react with O_2 primarily via charge transfer to superoxide-like $Au_n(O_2)^-$ complexes, in which the dioxygen is activated but still molecularily chemisorbed on the Au clusters [9, 11, 15, 18, 21, 23, 25, 28, 135]. However, odd-sized Au_n^- clusters were shown not to react with O_2. This was well understood from the closed-shell electronic nature of the odd-sized Au_n^- clusters, which makes it unfavorable for charge transfer to occur. The Au^- anion has a closed-shell electronic ground state and is the smallest odd-sized Au_n^- species, thus its inactivity to O_2 is not surprising.

One interesting question is how the linear $OAuO^-$ species are formed. In light of the non-bonding nature of the $Au(O_2)^-$ complex, it is not likely that it can be formed via dissociative chemisorption of O_2 on Au^-, as suggested previously [135]. Furthermore, a barrier of more than 3 eV has been calculated for dissociation of O_2 on either a Au^- anion or a neutral Au atom [135]. There was evidence of the formation of the neutral OAuO molecules in a low temperature matrix via the reaction of AuO and O [133]. Thus, the formation of the $OAuO^-$ molecule is most likely through reactions of gold atoms with an O atom in the cluster source to form AuO^-, which then reacts with another O atom to form AuO_2^-.

6.6 Conclusions

In conclusion, our high-level ab initio study combined with the photoelectron spectroscopy of mono-gold oxide and sulfide clusters AuO_n^- and AuS_n^- (n=1, 2) provided a wealth of information on the low-lying electronic states of the corresponding neutral species allowing a complete understanding of the equilibrium geometries, electronic structure, and chemical bonding in the AuX^- diatomics and the AuX_2^- triatomic systems. The bonding in AuO^- and AuS^- and therefore the spectra were found to be similar, but more spectroscopic information was obtained from the AuO^- spectra due to the high quality data. Specifically, a double excitation predicted by theory was observed in the spectra of AuO^- due to a shake-up process.

Both strong spin-orbit coupling and electron correlation effects were found to be important to achieve good agreement between the calculated electron detachment energies and the experimental data. Comprehensive molecular analyses were carried out to understand the chemical bonding in the AuX^- and AuX_2^- systems and to understand the differences and similarities in the oxides vs. sulfides. Strong covalent bonding was found in both the AuX^- diatomics and the linear $XAuX^-$ species. Based on the theoretical results, in combination with the experimental characterization of the nature of the orbitals, AuX^- exhibits a single bond. However, there is a strong contribution from π bonds formed by Au $5d_{xz/yz}$ and X $p_{x/y}$ orbitals due to the fact that the corresponding fully occupied $\pi^\star$ orbitals are of non-bonding nature. Consequently, the Au-X bond distance is considerably shorter. In contrast, strongly bonding orbitals $1\sigma_g$ and $1\pi_g$ formed by Au $5d_{z^2}$ / X p_z and Au $5d_{xz/yz}$ / X $p_{x/y}$ orbitals, respectively, have been found in $XAuX^-$. Due to the non-bonding nature of the δ, $1\sigma_u$ and $1\pi_u$ and the only partial occupation of the anti-bonding $2\pi_g^\star$ orbitals in $XAuX^-$, the Au-X bond is stronger than in AuX^- (cf. also Figure 3.3), and its strength is partially enhanced by the weakly bonding character of the $2\sigma_g$ orbital.

Interestingly, Au^- was shown not to bind molecular O_2, whereas S_2 was found to bind Au^- by ~1.4 eV, in agreement with the experimental observations [144]. Therefore, whereas only a linear $OAuO^-$ species was observed for AuO_2^-, both a linear $SAuS^-$ and a bent $Au(S_2)^-$ isomer were observed for AuS_2^-. In conclusion, the much stronger Au-S bond in AuS_2^- is originated in the energetically favorable orbital interaction between Au^- and S_2, in contrast to O_2.

Comparison with cationic species cannot be achieved by a PES study since the required photon energies are too high. However, calculations do not have this limitation and therefore a few remarks on cationic AuO^+ will be made, which is also important in the context of the reactivity presented above. Removing two electrons from the closed-shell AuO^- leads to AuO^+ with a triplet electronic ground state. One electron is taken from the π^* orbital while the second electron is removed from the binding 2σ orbital (cf. Figure 6.1a). This is a direct consequence of the low energy of the unoccupied 6s orbital and the occupied 5d orbitals of Au^+ and results in an energy mismatch to the orbitals of the O atom. Therefore, the splitting of the 2σ and the $\sigma^\star$ orbitals is smaller, leading to the triplet electronic structure in $^3AuO^+$. Accordingly, the bond order is reduced to one half.

Finally, the findings presented here demonstrate that photoelectron spectroscopy in combination with theoretical calculations based on highly correlated wave functions is a powerful tool for obtaining precious information on the electronic structure of clusters and molecules. Relativistic effects are very strongly pronounced in gold, and thus effects such as spin-orbit coupling have to be taken into account in order to achieve quantitative accuracy allowing us to distinguish contributions of several isomers in experiments.

Part II

Size-Dependent Dynamical Properties of Noble-Metal Clusters in the Ground and Excited Electronic States

Chapter 7

Dynamical Aspects in Metal-Cluster Catalysis - IVR as a Reactivity Criterion

7.1 Introduction

It has been demonstrated in the first chapters of this thesis, that surprisingly new chemical and physical properties arise in the nanometer regime which cannot be derived by simply downscaling the properties of the corresponding bulk materials. This has been shown on the example of the small gold clusters which exhibit strong size- and structure-sensitive chemical reactivity. So far, establishing the relationships between structure, charge and the size-dependent reactivity of small gold and silver clusters in the gas phase or at the support based on stationary energetics has been the focus of numerous studies [11, 14, 15, 21, 28, 33, 75, 100, 148, 149]. It has been demonstrated that the energetics are a very important aspect [84, 100] identifying reaction mechanisms and experimental conditions under which reactivity can be observed. However, until now only few studies [150] have considered the possibility that dynamical aspects might significantly influence the reactivity of supported gold clusters. In the study of groups of Landman and Heiz, the concept of "fluxionality" has been introduced [150]. They find that small clusters exhibit several isomers close in energy, which leads to a structural variability. This enabels the active center to rearrange the structure allowing the reaction to evolve on the energetically most favorable path. They suggest that this "fluxionality" might be responsible for the high catalytic activity of gold. However, the concept of "fluxionality" accounts only for the stationary aspect but disregards that catalysis is only enhanced in conjunction

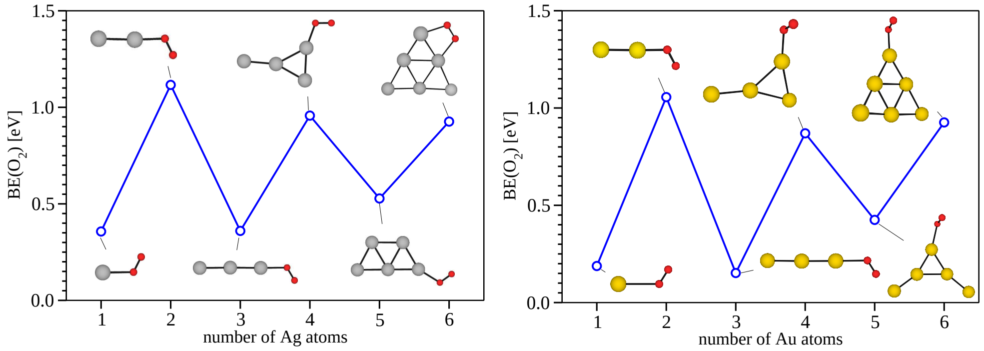

Figure 7.1: Binding energies of molecular oxygen O_2 onto (a) Au_n^- and (b) Ag_n^- (n=1-6).

with an efficient internal vibrational energy redistribution (IVR) enabeling dynamical interconversion between different local structures. Therefore, the dynamical process of IVR between interacting subunits involving the cluster and a selected molecule during the reaction will be addressed in this chapter.

It will first be shown that the structural properties and reactivity on the basis of energetics are very similar for the investigated gold and silver clusters and therefore the same catalytic activity should be expected provided that the energetics is the only criterion. In the second part, the new aspect involving dynamical properties will be addressed predicting a different reactivity of silver and gold clusters in the low-pressure regime. The important influence of the dynamical aspects and the role that IVR plays for the potential deactivation of adsorbates will be illustrated on the examples of anionic gold and silver clusters reacting with molecular oxygen.

7.2 Reactivity of Silver and Gold: Comparison of Energetics

The binding of molecular oxygen onto anionic coinage metal clusters has been intensively studied [11, 15, 28, 33, 75, 148, 151], and the mechanism of the O_2 activation has been explained by the frontier orbital model. According to this, clusters with an odd number of electrons bind O_2 strongly by transferring one electron into the $2\pi^\star$ orbital of O_2 leaving the metal cluster effectively neutral. In case of clusters with an even number of electrons, electron transfer is unfavorable resulting in a strong even/odd alternation of

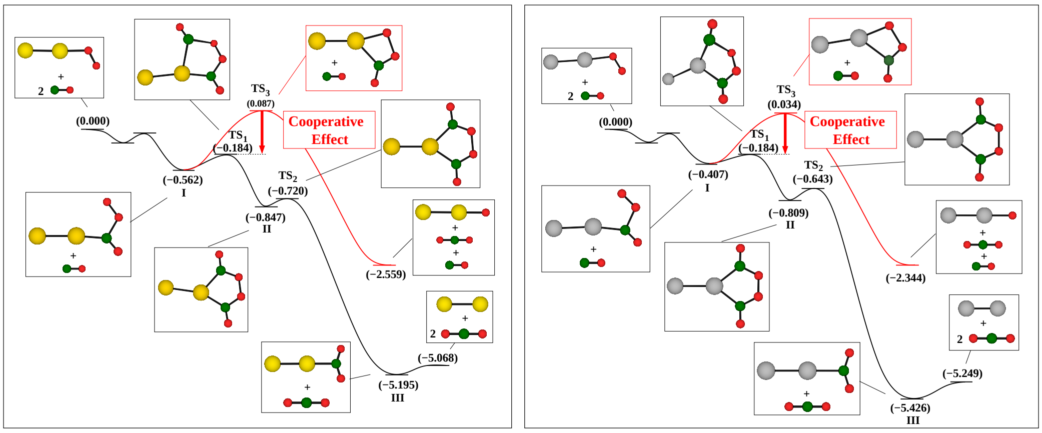

Figure 7.2: Comparison of energetics for the oxidation of CO by $Au_2O_2^-$ (left) and $Ag_2O_2^-$ (right).

binding energies of O_2. This is very pronounced for both the anionic gold and silver clusters, as can be seen from Figure 7.1 for the adsorption energy of O_2 onto Au_n^- and Ag_n^- (n=1-6), respectively. Notice that the clusters with odd number of electrons (Au_n^- / Ag_n^-; n=2, 4, 6) bind O_2 very strongly (BE≈1 eV). Moreover, the adsorption energy for molecular oxygen is very similar for both the gold and the silver species.

The findings on O_2 activation initiated further examinations of the oxidation of CO by anionic gold and silver clusters [14, 21, 28, 75, 100]. It has been recognized that the cluster alone cannot break the strong O-O bond but that the reaction can proceed only due to cooperative effects [28, 152]. This involves at least two CO molecules which cooperate in order to achieve bond breaking. However, an astonishing difference between reactivity of gold and silver clusters has been observed under comparable experimental conditions: $Au_2O_2^-$ [28] and $Au_6O_2^-$ [21] oxidize CO but the corresponding silver species $Ag_2O_2^-$ and $Ag_6O_2^-$ remain unreactive [39]. In both cases structural and energetic properties of these gold and silver oxides are very similar. Furthermore, the energetics for oxidation of CO by the anionic dimer oxide cluster $Ag_2O_2^-$ (cf. Figure 7.2) is not only qualitatively but also quantitatively almost identical to the corresponding gold species.

Therefore, the question can be raised whether differences in their catalytic activity are a consequence of inherently different reaction dynamics. In this context, it is important to realize that the connection between relativistic effects and reaction dynamics may play the key role. In fact, due to a substantially smaller s-d energy gap in the Au than in the Ag atom, caused by the stronger relativistic effects in the former case, the contribution of d-electrons invokes directional bonding [153, 154]. As a consequence, small anionic gold clusters remain planar until n≈12 [154, 155]. In contrast, silver clusters behave closer to s-like metallic systems such as sodium and assume 3D structures already at n≈7 for anionic clusters [156, 157].

The question why gold clusters of a given size promote the reactivity of O_2 and corresponding silver species do not has been adressed by investigating reaction dynamics and internal vibrational energy redistribution (IVR) during the collisions of Au_6^- and Ag_6^- with O_2. The different nature of IVR in $Au_6O_2^-$ and $Ag_6O_2^-$ leads to the proposal that the nature of IVR should be considered as a new criterion for promoting reactivity by activating molecular oxygen. It will be shown that the resonant IVR between reaction partners favors oxygen activation in contrast to the dissipative IVR. The latter increases the sticking probability of O_2 but prevents the subsequent reactivity of such a complex due to vibrationally unactivated O_2.

7.3 Computational Details

To study the reaction dynamics of Au_6^- and Ag_6^- with O_2, molecular dynamics simulations have been performed in the framework of the density functional theory (DFT) using the Perdew-Burke-Ernzerhof (PBE) functional [104] with a 19-electron relativistic effective core pseudopotential (19e-RECP) for gold and silver combined with Gaussian basis sets of triple zeta quality for all atoms [98]. This level of theory allows including scalar relativistic effects. Full treatment of relativistic effects is beyond the scope of dynamical simulations. Furthermore, the resolution-of-identity (RI) approximation [102, 103] has been emloyed which speeds up the DFT calculations by an order of magnitude. The classical equation-of-motion has been integrated employing the Verlet algorithm [158] at constant energy. Dynamics "on the fly" allow including all degrees of freedom which is mandatory to account for energy redistribution. The temperature dependency of the Lindemann index indicates the range in which a "melting-like" behaviour of the noble metal cluster takes place. The Lindemann index δ which shows a steep rise at the corresponding microscopic "melting temperature" is defined as the uncertainty $\Delta \langle r \rangle$ of the interatomic distances r averaged over time relative to the mean distance $\langle r \rangle$

$$\delta = \tfrac{\Delta\langle r\rangle}{\langle r\rangle} = \frac{1}{N\cdot(N-1)}\sum_{i\neq j}\frac{\sqrt{\left\langle r_{ij}^2\right\rangle - \langle r_{ij}\rangle^2}}{\langle r_{ij}\rangle} \tag{7.1}$$

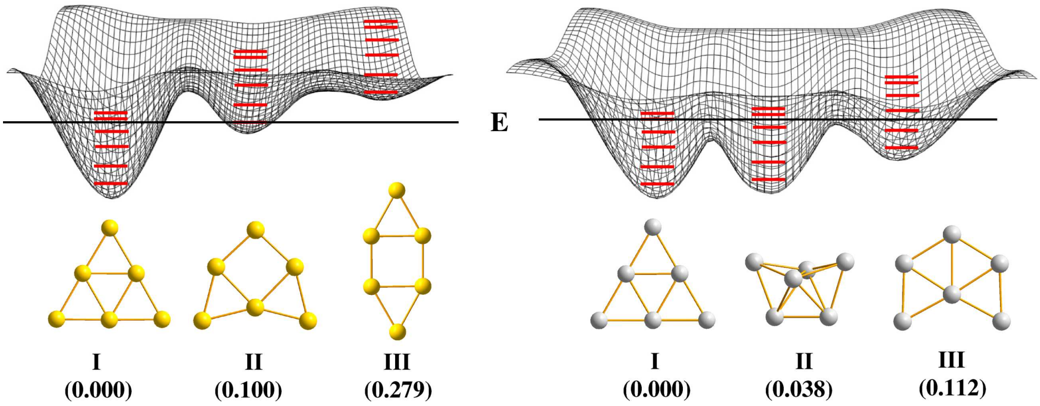

Figure 7.3: Lowest energy structures for Au_6^- (left) and Ag_6^- (right). Schematically, the PES with vibrational levels (red) are shown to demonstrate higher vibrational density of states for Ag_6^- for some given energy E (black).

with N being the number of atoms in the system and r_{ij} the distance between atoms i and j.

7.4 IVR in Anionic Noble Metal Hexamers Au_6^- and Ag_6^-

The lowest energy structures of Ag_6^- and Au_6^- are shown in Figure 7.3 with the most stable isomer assuming a planar triangular shape for both the silver and the gold cluster (D_{3h} symmetry). The second and third isomer of Au_6^- are higher in energy by 0.100 eV and 0.279 eV, respectively, and all three most stable isomers of Au_6^- are planar. In contrast, the isomers of Ag_6^- are closer in energy. The second one is separated by only 0.038 eV from the most stable structure and is already three-dimensional assuming a bicapped tetrahedral structure (right part of Figure 7.3).

Collisions with molecular oxygen O_2 have been performed starting with the most stable isomers of Ag_6^- and Au_6^-. The collisional impact orientations defined by the angles α, β and γ as well as the distance of O_2 to the cluster (cf. Figure 7.4) have been sampled over a sphere around the cluster resulting in a set of 400 initial conditions for each cluster. However, due to the high D_{3h} symmetry of the planar structures ≈40 trajectories have been propagated for Ag_6^- and Au_6^-, respectively. An impact kinetic energy of 0.25 eV has been chosen corresponding to T≈300 K.

In Figure 7.5 snapshots of MD simulations are presented in which all propagated trajectories have been superimposed. The snapshots at t=0 fs show the initial ensemble for Au_6^- (top) and Ag_6^- (bottom). Common aspects of reaction dynamics are: First, the O_2 molecules collide with the clusters at t≈100 fs and then either stick or bounce off. The snapshots further show that, independently from the initial orientation, the O_2 molecules bind to the tips of the cluster which is the energetically most favorable binding site. Moreover, Figure 7.5 shows that reactive collisions occur when O_2 collides with an edge or a tip of the cluster.

However, in spite of these common aspects the MD simulations reveal important differences which shall be addressed in the following.

Deviation from planarity The magnitude of the structural changes can be visualized by the deviation from planarity of the metal hexamer subunit. Hereby, the "cluster plane" is defined by the three inner atoms of the noble metal subunit, and deviation from planarity expresses the distance of the outer atoms with respect to the plane. For example, Figure 7.6 shows deviation from planarity for successful collisions for Ag_6^- (top) and Au_6^- (bottom) with O_2 under same initial conditions. It is obvious that the out-of-plane motions are present to a large extent in Ag_6^- with large deviations from the equillibrium structure due to the vibrationally excited silver subunit. In contrast, almost only in-plane motions are present in the Au_6 subunit upon collision with O_2, reflecting the larger rigidity of the cluster. Consequently, only the "collisional Au atom"(dashed red line in Figure 7.6) is significantly moving out of plane and the deviation from planarity of the metal subunit is less pronounced.

Sticking probability In collisions, O_2 sticks to the Ag_6^- cluster more efficiently although the binding energy of O_2 is similar to the one calculated

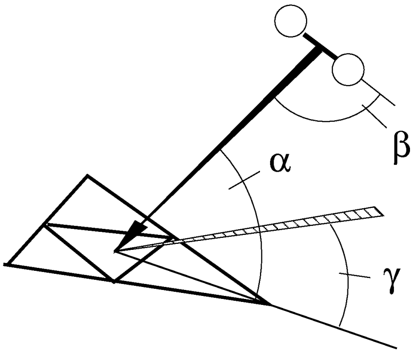

Figure 7.4: Definition of collisional impact angles α (out-of-plane), γ (in-plane) and β (side-on/end-on).

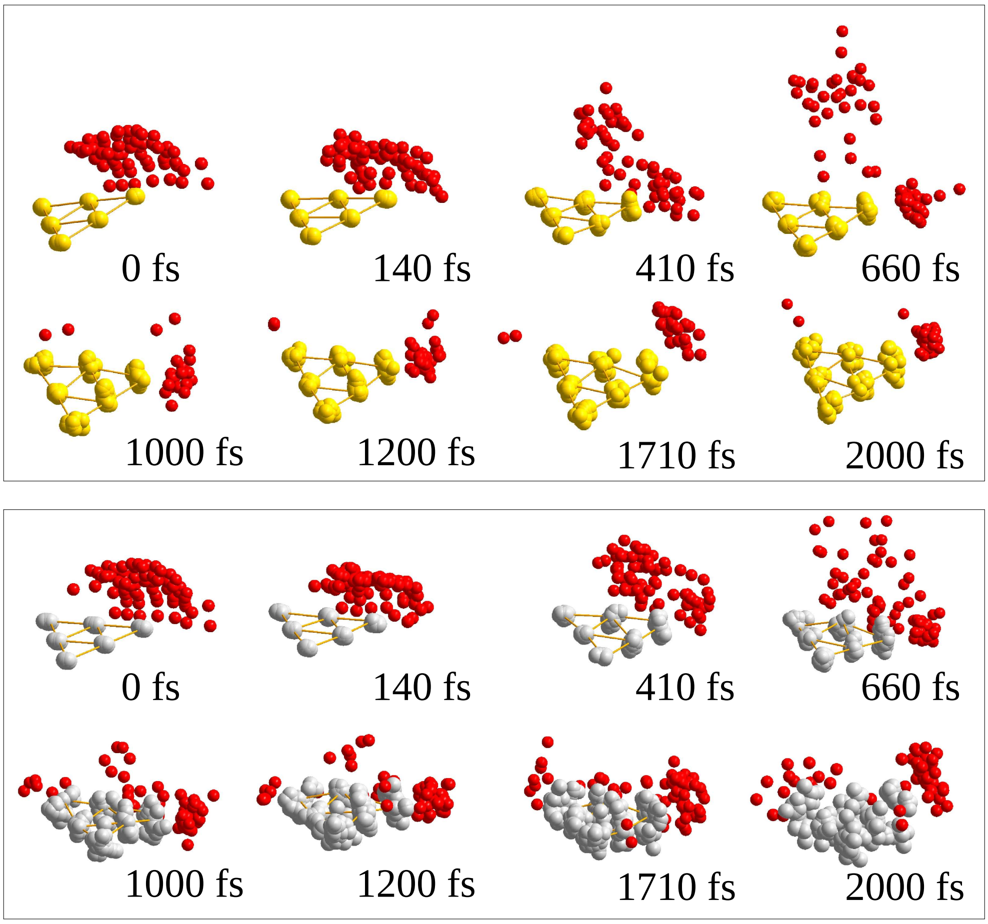

Figure 7.5: Snapshots of MD simulations for the collision of Au_6^- (top, yellow) and Ag_6^- (bottom, grey) with molecular O_2 (red). Initial conditions (t=0 fs) sample the whole space due to the D_{3h} symmetry of the noble-metal hexamer.

for Au_6^-. Therefore, the calculated sticking probabilities for O_2 onto Ag_6^- and Au_6^- are 78.4 % and 48.7 %, respectively. This finding is visualized in Figure 7.7 in which the orientational dependence of the sticking probability is projected onto a sphere. Red regions represent impact orientations for successful collisions of O_2 with the cluster, while blue marks unreactive impact parameters. Notice that the oxygen molecule only binds to Au_6^- when O_2 collides with the tip of the triangular cluster. In contrast, for Ag_6^- also collisions with the edges lead to sticking of O_2, and impact angles of about 40^o with respect to the cluster plane still lead to successful reactive collisions in contrast to Au_6^-.

It is important to emphasize that the found differences are not due to

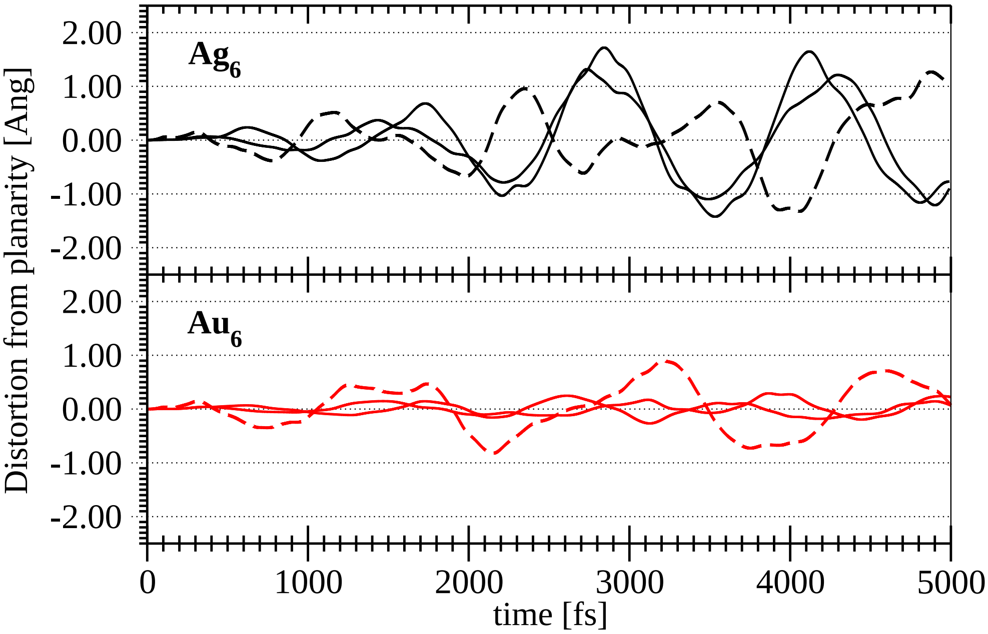

Figure 7.6: Deviation from planarity for successful collisions of silver (top, black) and gold (bottom, red) hexamer with O_2. The displacement of the atom at which O_2 is bound is shown by dashed lines.

the different mass of gold and silver but are caused by inherently different dynamical processes connected with the higher rigidity of Au_6^- in contrast to the floppy-like behaviour of Ag_6^- due to delocalized s-electrons in Ag. This has been proven by a series of MD simulations with varying masses of the metal atoms (cf. Figure 7.8a) under equal initial conditions. For collisions of O_2 and Au_6^-, it is found that the transferred kinetic energy increases with decreasing mass. However, in these simulations O_2 does not stick to Au_6^- independently from the mass. In contrast, the O_2 sticks to the Ag_6^- cluster under the same initial conditions even when the mass is increased to that of gold. The higher rigidity of Au_6^- is also demonstrated by the temperature-dependent Lindemann indices (cf. Figure 7.8b), which are used as a signature for phase transition in infinite systems. They show that the melting-like behavior for Au_6^- occurs at a significantly higher temperature (≈450 K) than for Ag_6^- (≈200 K). Figure 7.9 shows the superposition of the structures obtained by the MD simulation at a constant temperature of T=300 K. Clearly, the Ag_6^- cluster exposes substantial geometrical fluctuations evidencing the “melting-like” behaviour. In contrast, the Au_6^- cluster remains rigid and shows only small geometrical fluctuations around the equillibrium structure.

Further, the efficiency and nature of IVR are examined in order to show

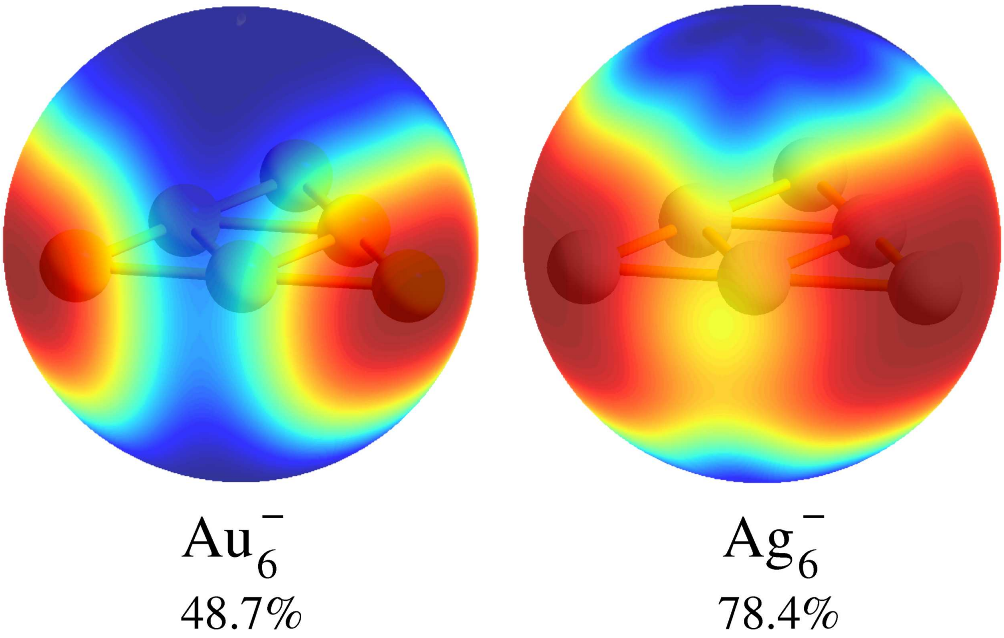

Figure 7.7: Sticking probability for O_2 projected onto a sphere around the metal cluster. Red color reflects impact orientations for successful collision with O_2.

that the differences in sticking probabilities are due to specific dynamical properties. Since usually the efficiency of IVR is proportional to the vibronic density of states (DOS) [159, 160], IVR is expected to be more efficient for Ag_6^- due to the fact that the isomers are closer in energy. Therefore, their contribution to the total vibronic DOS is significantly higher than in the case of Au_6^-, in which the DOS is reduced because the isomers are higher in energy and remain planar (cf. Figure 7.3). Indeed, for Ag_6^- the reaction energy gained due to complex formation with O_2 is efficiently dissipated into the cluster subunit (Figure 7.10) within the first 750 fs. This leads to the heating of the Ag_6 subunit and a large deviation from planarity (cf. Figure 7.8b). Consequently, the oxygen molecule sticks to Ag_6^- under these impact conditions. In contrast, due to the inefficient energy transfer by IVR, O_2 bounces off the Au_6^- under the same conditions (right side in Figure 7.10) Therefore, the Au_6 subunit remains planar and only little kinetic energy is transferred to the Au_6 subunit.

In addition to the differences in efficiency also a different nature of IVR has been identified in Ag_6^--O_2 and Au_6^--O_2 which has been analyzed along representative reactive trajectories. Due to the chemical attraction, the projectile molecule O_2 is accelerated and hits the anionic metal cluster at t≈120 fs with an impact velocity of $v_o(O_2)≈2.3\ \frac{km}{s}$ exciting all vibrational modes as a consequence of the delta character of the impact. More importantly, the impact initiates a microshock wave [161] expanding from the "collisional tip atom" through the planar hexamer with velocities of $u_S(Ag_6)≈3.9\ \frac{km}{s}$ and $u_S(Au_6)≈3.2\ \frac{km}{s}$. It is interesting to note that the microshock wave propagation velocities are in the same range as the sound velocities of the silver

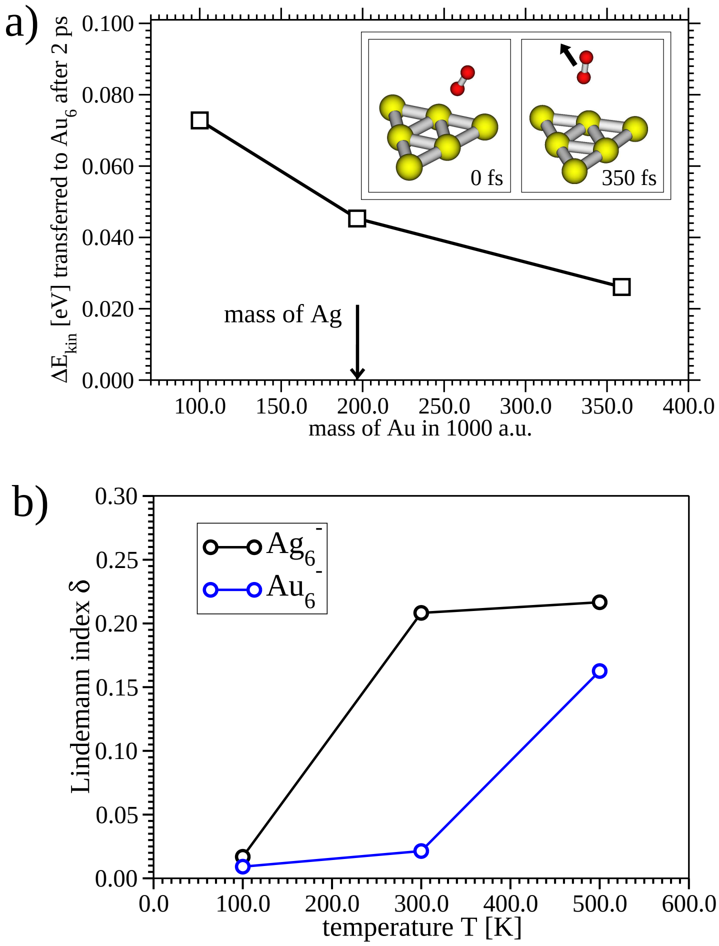

Figure 7.8: a) Kinetic energy transferred from O_2 to the Au_6^- upon collision is shown for different masses of gold. Notice that ΔE_{kin} is showing a mass dependence but that in contrast to silver, O_2 does not bind in any of the MD simulations for gold with the given initial conditions. b) Lindemann indices for Ag_6^- and Au_6^- according to expression 7.1. The curve for gold is shifted to higher temperatures indicating a higher rigidity of the cluster.

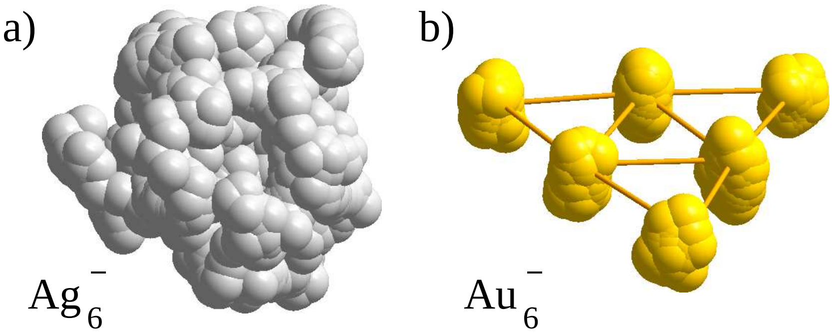

Figure 7.9: Superposition of the structures obtained from MD simulations of Ag_6^- (left) and Au_6^- (right) at a constant temperature T=300 K.

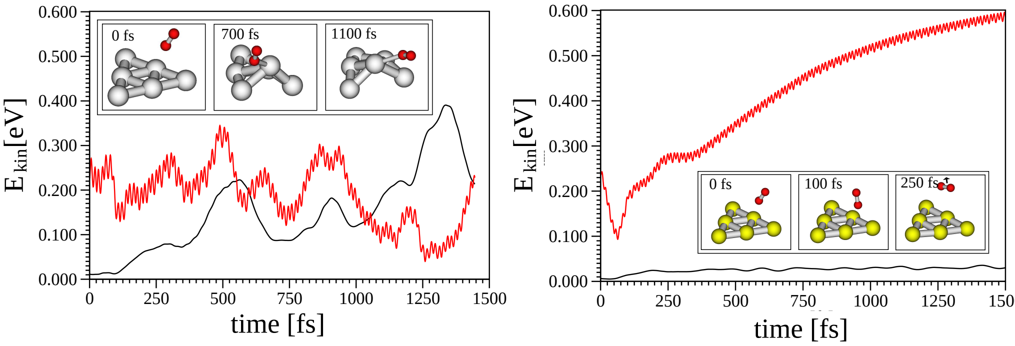

Figure 7.10: Kinetic energy partition between Ag_6 (left) and Au_6 (right), indicated by black curves, and O_2 (red curves) subunits showing a reactive collision for Ag_6^- and an unreactive one for Au_6^- under equal initial conditions. The insert shows the snapshots of the dynamics.

(3.65 $\frac{\mathrm{km}}{\mathrm{s}}$ [162]) and gold (3.24 $\frac{\mathrm{km}}{\mathrm{s}}$ [162]) bulk. In the case of Ag_6^-, efficient *dissipative IVR* leads to accumulation of this kinetic energy in the cluster subunit after ≈1.4 ps (cf. Figure 7.11a, left part). Consequently, the O-O bond remains only weakly vibrationally excited. In contrast, *resonant IVR* has been identified for Au_6^- with oscillatory exchange of kinetic energy between the metallic and the oxygen subunits (cf. Figure 7.11a, right). This behaviour is also evident from the time-dependent Fourier transform of the velocity autocorrelation function along the chosen trajectories (Figure 7.11b). In $\mathrm{Ag}_6\mathrm{O}_2^-$, the vibrations of the metal subunit below 500 cm^{-1} are strongly excited while the O-O bond ($\nu_{\mathrm{O-O}} \approx 1250\ \mathrm{cm}^{-1}$) is weakly vibrationally excited. In contrast, in the case of Au_6^- the resonance of the IVR is evident from the strong excitation of many vibrational modes below

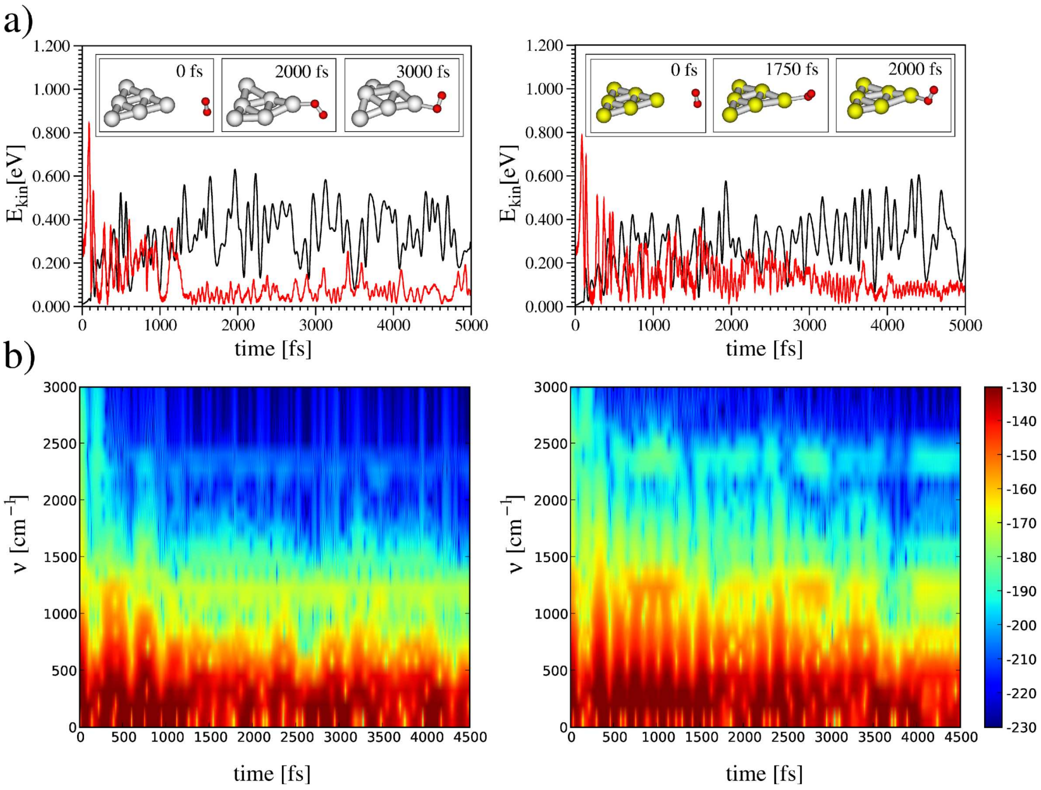

Figure 7.11: (a) Kinetic energy partition between Ag_6 (left), Au_6 (right) and O_2 for two reactive collisions demonstrating a dissipative IVR for Ag_6^- and resonant IVR for Au_6^-. For illustration, a representative single trajectory has been chosen. (b) Fourier transform of the velocity autocorrelation function along the chosen trajectories for Ag_6^- (left) and Au_6^- (right). Excited vibrational modes are indicated in red.

$1000\ \mathrm{cm}^{-1}$. Moreover, the pronounced occurrence of the overtone of the O-O vibration ($2\nu_{\mathrm{O-O}}\approx 2400\ \mathrm{cm}^{-1}$) evidences the much stronger vibrational excitation of the O_2 group. Consequently, the kinetic energy remains localized at the O_2 adsorption site leading to a vibrationally excited O-O bond which is convenient for promoting reactivity towards other molecules, e.g. CO.

7.5 Conclusions

In summary, the efficiency of the internal vibrational energy redistribution upon collision of Ag_6^- and Au_6^- with O_2 has been investigated. Due to the lower vibrational density of states in gold the efficiency of IVR is significantly reduced resulting in a lower sticking probability. Collision-induced microshock waves have been found in Ag_6 and Au_6 which propagate with velocities very similar to the bulk values. It has been demonstrated that the nature of IVR can serve as a new criterion for promoting the reactivity. In addition to the chemical activation of the strong O-O bond by charge transfer, the *resonant IVR* between the cluster and adsorbate provides an additional activation mechanism. The kinetic energy oscillates between the metal subunit and the O_2 group which facilitates overcoming the reaction barriers and therefore enhances the oxidation reactivity. This vibrational excitation induced by Au_6^- is responsible for the higher oxidation activity, confirming experimental observations [21]. In contrast, *dissipative IVR* as in the case of Ag_6^- leads to a higher sticking probability of the adsorbate. However, the adsorption energy is efficiently dissipated into the metal subunit and thus cannot be used to enhance the reactivity. Therefore, the nature of IVR as a result of the strongly pronounced relativistic effects in gold leads to i) the preservation of the local strucure at the binding site and ii) the temporal localization of kinetic reaction energy at the adsorbates. We suggest that both of these effects play an important role for the high reactivity of nanosized gold.

Chapter 8

Size-Dependent Dynamics in Excited Electronic States of Anionic Gold Clusters Au_n^- (n=5-8)

8.1 Introduction

The importance of the intrinsic dynamical properties such as IVR of gold clusters in the electronic ground state [163] has been demonstrated in Chapter 7 on the example of the reaction between Au_6^-/Ag_6^- with O_2. In principle, due to the impulsive character of excitation during collision with O_2, all vibrational modes should be unselectively activated. However, in case of Au_6^- due to the higher rigidity of the gold cluster and the inherently weaker coupling of in-plane and out-of-plane vibrational modes, the vibrational energy goes mainly into the in-plane vibrational modes. It has been demonstrated that these can strongly couple to the O-O vibration in the O_2 subunit, and therefore the resonant IVR is responsible for a higher reactivity of gold as opposed to silver.

These inherent dynamical properties of gold clusters should be expressed also in the relaxation dynamics in excited electronic states. In this case, by the absorption of a photon an excited state is populated which relaxes selectively along the vibrational modes which are different in ground and excited electronic states. Coupling to other vibrational modes with associated IVR then leads to a radiationless decay of the electronic excitation causing an energy flow into the nuclear system. Since by adding or removing a single atom the properties can dramatically change, extreme size dependence of the excited-state dynamics can be expected, and thus a series of small gold anionic clusters Au_n^- (n=5-8) has been studied [164]. However, this presentation will focus on theoretical results obtained for Au_5^- and Au_7^-, and experimental results (collaboration with in group of Prof. W. Eberhardt) will be given for all species.

Femtosecond time-resolved photoelectron spectroscopy (TR-PES) using the pump-probe technique is a powerful tool for the real-time investigation of electronic and nuclear dynamics (see e.g. [40, 41]). It is based on the preparation of a non-equilibrium configuration by optical excitation of a stable species in the pump step and exploration of its time evolution by the probe step. The binding energy of the emitted electron corresponds to the energy difference between the intermediate excited anionic state and the final neutral state. Thus, TR-PES offers the unique opportunity to follow structural changes with high precision in real time, e.g. wavepacket motion [165], isomerization [166], desorption [167] and photoinduced melting.

So far, photoinduced geometry changes have been difficult to observe in metal clusters owing to a relatively high electronic density of states in the valence region [168–170]. For instance, in open d-shell metal clusters like Pt_3^- [168], electronic relaxation processes dominate as internal conversion is very likely to occur between a manifold of different electronically excited states. As a consequence, various excited states may be reached upon photodetachment, and the measured binding energy is not directly related to electronic transition into one specific excited state. In small mercury clusters, relaxation of the electronically excited state resulting in transfer of relaxation energy into the vibrational system has been observed [169, 170].

Gold clusters behave differently with respect to the above examples and are therefore well-suited to follow nuclear dynamics using TR-PES. For example, excited-state lifetimes in the nanosecond range have been recently reported in Au_6^- [171]. Gold has nominally a closed d-shell. However, due to relativistic effects, the d-contribution to the valence orbital space is increased [153, 154]. The d-contribution, however, is not as prominent as in transition metals and, therefore, a relatively large HOMO-LUMO band gap and discrete level density exists in small Au clusters [172]. In particular, for small anionic gold clusters, the transition-dipole allowed excited state near 1.5 eV is a well isolated electronic state [173]. Therefore, small gold clusters are excellent candidates to study nuclear dynamics using TR-PES.

In the following, the photoinduced nuclear dynamics of Au_{5-8}^- in real time will be presented. Oscillatory motion has been found in a bound excited electronic state of Au_5^-, but an extraordinary long lived excited state in Au_6^- and photoinduced melting are observed in Au_7^- and Au_8^-. This means that dynamics in excited electronic states of small anionic gold clusters are strongly size-dependent. This will be demonstrated by the theoretical study of Au_5^- and Au_7^- in combination with corresponding experiments. For example, for the first time a photoinduced melting-like behavior of a finite system has been found to take place on a time scale of $\sim$1 ps. This occurs due to large excess of energy after return from the excited state to the ground state after internal conversion.

8.2 Theoretical and Computational Details for Simulating TR-PES Spectra

TR-PES spectra were simulated in the framework of the Wigner distribution approach [42, 174] based on the propagation of an ensemble of classical trajectories "on the fly". This approach enables an accurate simulation of ultrafast processes and femtosecond signals in complex systems, involving both adiabatic and nonadiabatic dynamics [42].

The TR-PES spectra can be simulated by a modification of the equation for the zero electron kinetic energy pump-probe signals which takes into account that a part of the probe-pulse energy E_{pr} changes into the kinetic energy of the electrons E

$$\begin{aligned} S(t_d, E) \sim \int\int d\mathbf{q}_0 d\mathbf{p}_0 \int_0^\infty d\tau_1 \exp\left\{-\frac{(\tau_1 - t_d)^2}{\sigma_{pu}^2 + \sigma_{pr}^2}\right\} \times \\ \exp\left\{-\frac{\sigma_{pr}^2}{\hbar^2}[E_{pr} - V_{21}(\mathbf{q}_1(\tau_1; \mathbf{q}_0, \mathbf{p}_0)) - E]^2\right\} \times \\ \exp\left\{-\frac{\sigma_{pu}^2}{\hbar^2}[E_{pu} - V_{10}(\mathbf{q}_0)]^2\right\} P_{00}(\mathbf{q}_0, \mathbf{p}_0). \end{aligned} \tag{8.1}$$

In this expression σ_{pu} (σ_{pr}) and $E_{pu} = \hbar\omega_{pu}$ ($E_{pr} = \hbar\omega_{pr}$) are the pulse durations and excitation energies for the pump and probe step with the time delay t_d. The initial coordinates and momenta $\mathbf{q}_0$ and $\mathbf{p}_0$ are sampled from the anionic thermal Wigner distribution $P_{00}(\mathbf{q}_0, \mathbf{p}_0)$. $V_{10}(\mathbf{q}_0)$ represents the initial excitation energies of the initial ensemble. The signal is calculated by averaging over the whole initial distribution $P_{00}(\mathbf{q}_0, \mathbf{p}_0)$ represented by an ensemble of trajectories. $V_{21}(\mathbf{q}_1(\tau_1; \mathbf{q}_0, \mathbf{p}_0))$ indicates the time-dependent energy gap between the anionic excited electronic state and the neutral electronic ground state obtained from the ab initio MD "on the fly" [42].

The simulation of the TR-PES spectra involves three steps: (i) The ensemble of the initial conditions has been generated by sampling the Wigner distribution function corresponding to a canonical ensemble at T=300 K. (ii) In the second step, the trajectories are propagated on the excited electronic state allowing nonadiabatic transition to the ground state when the conical intersection is reached. Parallel to the propagation of the ensemble, the time-dependent energy gaps to the neutral state are calculated for each trajectory. (iii) The TR-PES spectrum is calculated by averaging over the ensemble of trajectories employing the analytical expression (8.1) derived in the framework of the Wigner distribution approach [42]. The simulations of excited-state dynamics and TR-PES spectra were carried out for two prototype examples: Au_5^- and Au_7^-.

Since the dynamics in excited electronic states of anionic gold clusters is required, at this point the time-dependent density functional theory (TDDFT) in its linear response formulation is employed for calculation of the needed forces. The gradient corrected Perdew-Burke-Ernzerhof (PBE) functional [104] has been used together with the Stuttgart group 19-electron relativistic effective core potential (19e-RECP) with the corresponding Gaussian atomic orbital (AO) basis set which has been optimized for better description of optical properties of gold clusters [173].

The obtained theoretical results will be compared to the experiments performed by the group of Prof. W. Eberhardt and Dr. M. Neeb, and therefore also the experimental procedure is shortly discussed. The details of the experimental setup can be found in Ref. [175]. In short, gold cluster anions are produced in a pulsed laser vaporization source, mass selected and decelerated. The kinetic energy of the detached electrons is analyzed by a magnetic bottle time-of-flight photoelectron spectrometer. The fundamental (1.56 eV) of the Ti:sapphire laser is used as the pump and the 2^{nd} harmonic (3.12 eV) as the probe pulse. Absorption of a pump photon leads to the population of an excited electronic state. The ensuing dynamics of the excited intermediate state is mapped by photodetachment with the probe pulse. The photon energy of the pump pulse is distinctly lower than the photodetachment and/or dissociation energy of the clusters [176] which assures the observation of bound state dynamics. Another important point for the real-time observation of the photoinduced nuclear dynamics in clusters is the initial cluster temperature before irradiation with the pump laser. In this experiment, the gas aggregation source delivers clusters at $T_{\text{vib}} \approx 200$ K [177], which is far below the melting temperature of small gold clusters (cf. Ref. [178] and results on Au_7^- presented below).

8.3 Results and Discussion

The investigation of the excited-state dynamics and TR-PES spectra will be presented for the anionic gold clusters Au_{5-8}^- with an increasing size. The findings can be classified according to two types of behaviour: presence of a long-lived bound excited state (e.g. Au_5^- and Au_6^-) and fast internal conversion (IC) leading to photoinduced melting (e.g. Au_7^- and Au_8^-).

The experimental time-dependent spectra of Au_5^- are shown in Figure 8.1a. Up to ∼3 ps the photodetachment peak oscillates between 1.5 and 1.8 eV. An oscillation period of 315 fs is deduced from a sine fit to the electron binding energy maximum [164].

The theoretically obtained oscillation period amounts to 420 fs and is in qualitative agreement with the experiment as shown in Figure 8.1b. This oscillatory behaviour is due to the vibrational wavepacket motion after the population of the first excited state ($T_{e,eq}$=1.43 eV). Snapshots of the nuclear positions of the 30 calculated trajectories are shown in Figure 8.1c. Periodic motions corresponding to breathing-like modes of Au_5^- can be recognized from the snapshots. With increasing time delay the wavepacket or ensemble of trajectories broadens due to the population of different vibrational modes, which might be an explanation for the fading photoelectron intensity observed at 10 ps and later. The experimentally observed energy shift and decrease in intensity at $t >4$ ps indicates that internal conversion (IC) might occur at a later time.

For Au_6^-, only experimental data are available, and the character of the excited electronic state has been addressed by Walter et al. [179]. In the TR-PES spectrum a peak appears at 0.55 eV and persists for at least 90 ns. From the overall constant peak shape, intensity and energy an excited-state lifetime of 730 ns is deduced. The experimental data indicate an excitation close to the minimum of the potential energy surface without any essential geometry change, which has been indeed found theoretically [179]. The long lifetime can be explained by the fact that the excited state is z-polarized and can only relax radiationlessly if the cluster undergoes significant out-of-plane nuclear vibrations in order to couple with other electronic states. However, we demonstrated that this is unlikely to occur in Au_6^- (see Chapter 7).

TR-PES spectra of Au_7^- are shown in Figure 8.2a for the delay times 0.1 ps$\leq t \leq$750 ps [1]. At t=0.1 ps, a peak is seen at a binding energy of 2 eV which

---

[1] For t<0.1 ps, photoelectrons from electronically excited states that are populated due to the probe pulse (probe-pump process) additionally contribute. Therefore, the data for t<0.1 ps are not shown. This is also the reason why the oscillatory wavepacket motion in the calculated spectra in Figure 8.2c is not visible in Figure 8.2a.

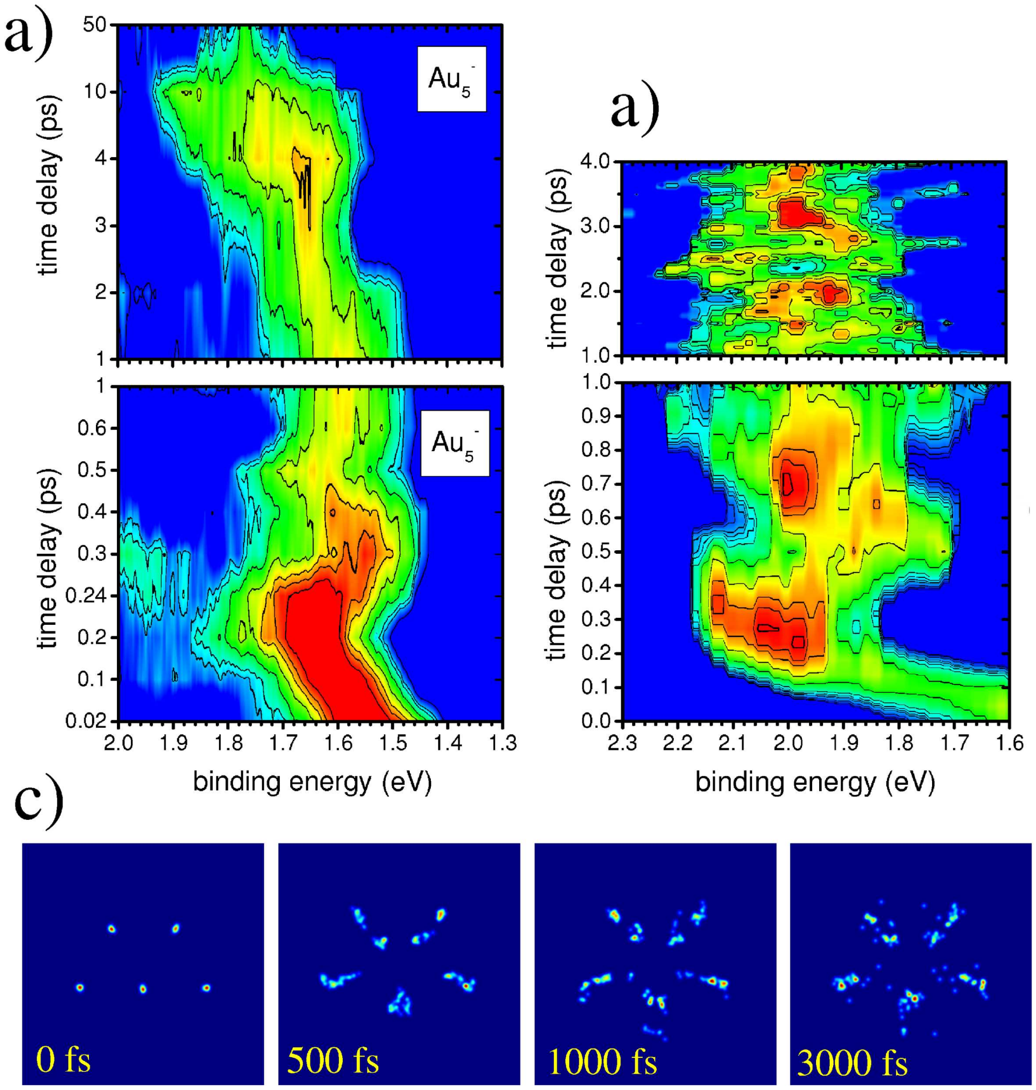

Figure 8.1: Au$_5^-$. (a) Experimental TR-PES spectra shown as contour plots. The scale representing the photoelectron intensity is shown in Figure 8.2. Lower panel: time delay range from 0 ps to 1 ps. Upper panel: time delay range from 1 ps to 50 ps. (b) Simulated TR-PES spectra. Lower panel: time delay range from 0 ps to 1 ps. Upper panel: time delay range from 1 ps to 4 ps. (c) Geometry snapshots calculated for 30 trajectories. At t = 3000 fs the atoms are still localized reflecting the trapezoidal geometry of the initial ground state.

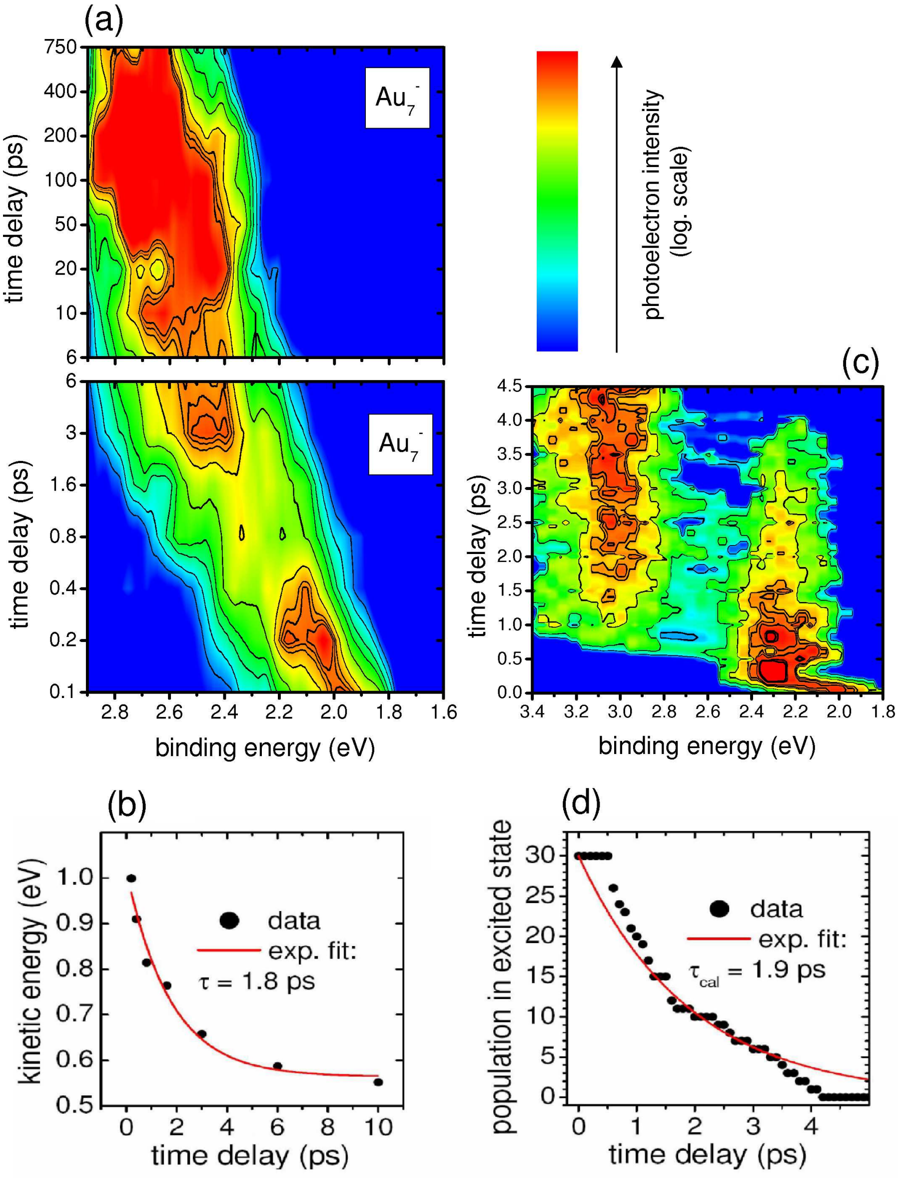

Figure 8.2: Au$_7^-$. (a) Experimental TR-PES spectra shown as contour plots. Lower panel: time delay range from 0.1 ps to 6 ps. Upper panel: time delay range from 6 ps to 750 ps. (b) Kinetic energy of the experimental peak maximum plotted as a function of time. The data are fitted to an exponential function with a decay time of τ=1.8 ps. (c) Simulated TR-PES spectrum shown as contour plot. (d) Calculated population dynamics of the excited state A$^-$ as a function of time obtained from 30 trajectories. Exponential fit corresponds to a lifetime of τ_{calc}=1.9 ps.

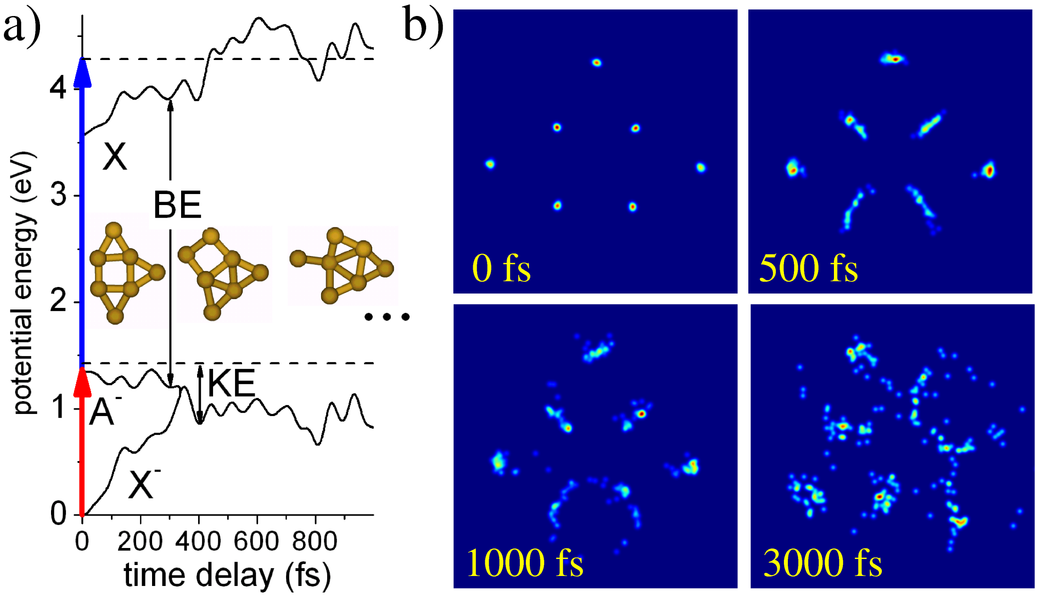

Figure 8.3: Au_7^-. (a) Temporal evolution of the potential energy of X^-, A^- and X. (b) Calculated geometry snapshots for the 30 trajectories. Each point corresponds to the position of a single atom (30×7 atoms in total). At t=0 fs the initial conditions involve the ground-state structure at room temperature. At t=3000 fs the atomic positions are blurred due to melting-like behaviour.

corresponds to the transition from the first electronically excited state A^-, to the neutral ground state X. The peak shifts to higher binding energy until it stabilizes at BE=2.6 eV after $\sim$ 10 ps. The simulated TR-PES spectra of Au_7^- are presented in Figure 8.2c. Both experimental and theoretical TR-PES spectra show one disappearing photoelectron peak at the binding energy of 2.0-2.2 eV and one peak at higher binding energies which emerges after $\sim$1 ps. The experimentally observed binding energy shift as well as the time scales are in agreement with the simulated spectrum (cf. Figure 8.2). The TD-DFT calculations reveal that the energy shift can be explained by internal conversion (IC) from the initially populated A^- state to the anionic ground state X^- which takes place on the same time scale as the experimentally observed energy shift. In Figure 8.2b the experimentally obtained kinetic energy of the peak maximum (E_{el}=$h\nu_{probe}$ − BE) is plotted as a function of time and fitted to an exponential function with τ=1.8 ps. This time constant is in agreement with the IC time obtained from the calculated population dynamics (τ_{calc}=1.9 ps, Figure 8.2d). The interpretation of the energy shift as evidence for internal conversion is supported by the theoretical analysis presented in Figure 8.3a where the time evolution of the potential energy of

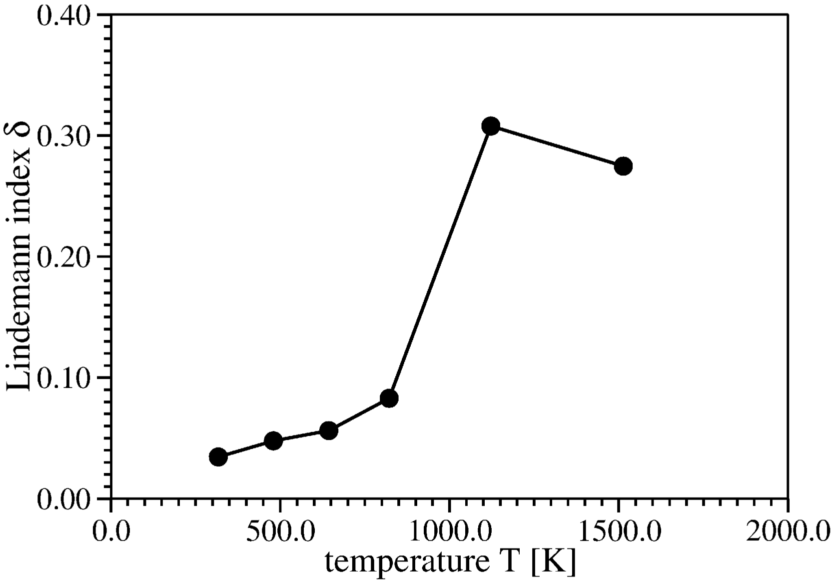

Figure 8.4: Lindemann indices for Au_7^- indicating a melting-like transition at ~800-900 K.

A$^-$, X$^-$ and X is shown for a selected trajectory. The binding energy of the detached electron corresponds to the calculated energy difference between X and A$^-$. At t=0 fs the dynamics is initiated on A$^-$. After 340 fs A$^-$ crosses with X$^-$ and the kinetic energy of the nuclear system (KE) rises rapidly. This is associated with an increase in the binding energy of the detached electron. Note that the calculations reveal an energy flow into the nuclear system of 0.69 eV on average, which corresponds to a vibrational temperature of ~1070 K. This leads to strong structural fluctuations of Au_7^-. This loss of well defined structures corresponds to a melting-like transition in finite systems. According to the Lindemann criterion [180] the melting transition for Au_7^- occurs at a vibrational temperature between 800 K and 900 K as shown in Figure 8.4. The interpretation that the energy flow into the vibrational system is sufficient for a melting-like transition of Au_7^- is additionally supported by the geometry snapshots presented in Figure 8.3b.

The observed dynamics in Au_8^- is qualitatively similar to that of Au_7^-. The time-dependent peak exhibits a shift to a higher binding energy which is accompanied by a significant peak broadening. The time scale of IC can be derived from the evolution of the photoelectron intensity. A lifetime of τ_{exp}=650 fs for the excited state A^- has been determined. The IC is accompanied by an energy transfer into the nuclear system which initiates a melting-like transition in Au_8^- similar to Au_7^-. In contrast to Au_7^-, where a thermal equilibrium is reached after hundreds of picoseconds, in the case of Au_8^- the intensity drops exponentially after 3 ps with a time constant of 15 ps. This means that the potential energy difference between the photoexcited anionic state and the neutral final state becomes larger than the probe photon energy, in analogy to the calculations shown in Figure 8.3a.

8.4 Conclusions

In summary, the theoretical study presented here in combination with the experiments shows an extremely size-dependent nuclear dynamics of photoexcited small Au_{5-8}^- clusters. An oscillating wavepacket movement has been found in Au_5^- due to the population of a well-separated bound excited electronic state. A long-lived bound state character of the lowest excited state has been found experimentally for Au_6^- (τ_{exp}>90 ns in Au_6^-). In contrast, in Au_7^- and Au_8^-, fast IC into the electronic ground state leads to an energy flow into the nuclear system which initiates a melting-like transition after $\tau_{exp}\sim$1.8 ps in Au_7^- (τ_{calc}=1.9 ps) and ∼680 fs in Au_8^-. This documents that the excited-state dynamics in small metallic nano-clusters is highly non-scalable, which may give rise to a number of new phenomena such as cluster fluorescence or specific cluster photo-chemistry.

Part III

Optical Properties of Small Supported Silver Clusters

Chapter 9

Introduction

Small silver clusters in different environments exhibit intense optical transitions in the ultra-violet (UV) or in the visible regime and they fluoresce. It has been shown that silver clusters with few atoms embedded in rare-gas matrices can emit light [61–63, 181–185]. Ertl and co-workers [184, 185] observed emission upon aggregation of silver clusters in a matrix of noble metal atoms. They attribute the chemiluminescence to the presence of small electronically excited silver clusters ($Ag^{\star}_{2-4}$) which were created from fragmentation of large silver clusters. But the exact size could not be determined. However, in mass-selected experiments on small silver clusters embedded in rare-gas matrices [61–63, 181–183] strong fluorescence under ultra-violet (UV) or visible light excitations has been observed, e.g. for Ag_4 [61] (T'_e∼3 eV), Ag_8 [62] (T'_e∼4 eV) and Ag_9 [63] (T'_e∼4 eV). Due to the almost negligible influence of rare-gas matrices or a helium-droplet environment [186] on the optical properties of silver clusters, the theoretical work on the absorption and emission properties of gas-phase silver clusters in the non-scalable size regime [63, 81, 82] provided the mechanism for the excitations responsible for the experimental findings. The role of the matrix is to prevent cluster fragmentation and to slightly shift the fluorescence band to the visible. It has been shown that the optical properties are strongly structure- and size-dependent due to the discrete molecular-like nature of the electronic states in such small metallic particles. Notice that larger metallic particles with a few tenth or hundreds of atoms exhibit strong absorption, but no fluorescence can occur due to a favorable and fast non-radiative relaxation of the excited electronic state.

After the discovery that small silver clusters fluoresce also at surfaces it was recognized that the photo-activated fluorescence upon illumination of silver-oxide films caused by formation of silver clusters might be useful for different applications such as optical storage with high data capacities [43].

For this purpose, the written data have to be stable for a sufficiently long time, and moreover, both fast data writing and readout are required. Both requirements are essential for the successful application as an efficient storage medium. Bernhardt et al. have shown that the efficiency of the write and readout process can be increased by using femtosecond laser excitation and furthermore, that the created probes were stable for a very long time [47, 54]. Dickson et al. have demonstrated that small silver clusters can be harnessed to create single molecule light emitting diodes (LEDs) and opto-electronic logical gates [45, 53] which are basic elements for opto-electronic devices. Interestingly, small silver clusters in bio-environments exhibit also fluorescence so that they can be used as bio-fluorophores, e.g. in cell imaging [55–57].

Since the mechanism responsible for the emissive properties of clusters formed by photoreduction of silver-oxide films is unknown, first the optical properties of silver clusters interacting with silver-oxide support [65] have been theoretically studied. For this purpose a simple finite cluster model has been used for representing of the Ag(I)-oxide surface. The point defect (F_S center) has been created by removing the central top layer O atom, and the silver cluster Ag_4 has been put at this defect. Relaxation of the supported silver cluster leads to the formation of an Ag_7 unit which is not directly bound to surface oxygen atoms and which furthermore exhibits strong absorption at $T_e \sim 3$ eV. However, due to the strong Ag-Ag interaction between the cluster and the silver-oxide support and thus the strong mixing of excitations within both subunits [65] it was not possible to distinguish the inherent cluster and support contributions and to unravel the mechanism for photoemission. In contrast, an ionic MgO non-reducable support offers a more suitable environment for studying the optical properties of supported silver clusters since the contributions from the cluster and the support can be better distinguished.

In fact, due to easy preparation of the MgO support it has been widely used in studies of properties of supported clusters. However, there has been much discussion on the possible location of the different types of defects over the past decades, and it is thus still a subject of intense experimental and theoretical studies [187–200]. It has been shown that the anion vacancies of the MgO (100) surface which are filled with one or two electrons (F_S centers) are present at MgO thin films and crystalline surfaces. Moreover, it has been proposed that these provide good adsorption sites for clusters.

Theoretical studies of noble metal clusters at the MgO support mainly focused on the ground state properties in the context of the catalytic activity [66–78]. The investigation of optical properties of small gold clusters at the MgO support aimed also to identify the active centers for the oxidation reaction [80]. Recently, the lowest-energy structures of small silver clusters with up to four atoms supported at the MgO surface and F_S center defect have been published [72, 74, 77, 78, 201, 202]. Absorption properties of the coinage metals at the MgO support have also been recently investigated for small copper clusters $Cu_{1,2,4}$ [79] and gold clusters $Au_{1,2,4,8}$ [80].

To the best of our knowledge, there have been no reports in literature on systematic studies of optical properties of supported small silver clusters. The study on supported silver clusters at the defect-free MgO (100) surface as well as the F_S center presented in this thesis aims to unravel the influence of the support on absorption and emission properties of silver clusters. For this purpose, state-of-the-art cluster embedding techniques in combination with hybrid density functional theory have been employed to accurately predict absorption and emission properties (Chapter 10). The ultimate goal is to determine the cluster size for efficient emission in the visible regime.

The structural and optical properties of gas-phase Ag_n silver clusters (n=2, 4, 6, 8) have already been intensively studied in the group of Prof. Bonačić-Koutecký using highly correlated quantum chemical methods [81, 82]. However, they will be addressed together with a newly proposed characterization and classification of optical transitions in Chapter 11 using appropriate DFT methods. This will serve as basis for identifying characteristic features of cluster absorption when the support will be introduced. In Chapter 12, the structural and optical properties of the stoichiometric MgO (100) surface (O_{5c} terrace site) and of F_S center defect (F_{5c} terrace site) will be presented allowing for a full characterization of the different support sites. The structural and optical properties of the supported clusters will be presented in Chapters 13 and 14. First, the absorption of Ag_n (n=1-8) clusters at the O_{5c} site of a perfect MgO (100) surface will be considered ($Ag_n@O_{5c}$), and then the F_S center defect will be explored ($Ag_n@F_{5c}$). Since the occurrence of fluorescence is directly connected with sufficiently long lifetimes, the necessary requirement is the presence of bound electronic states. Therefore, results on geometry optimization in excited electronic states will be presented for clusters at both types of support sites. This will enable us to suggest potential candidates for fluorescence in the visible regime.

It will be shown that interaction with the F_S center defect is considerably stronger than in the case of the defect-free MgO (100) support due to linear combination of empty cluster orbitals and occupied F_S center orbitals giving rise to a considerable charge transfer from the support towards the cluster. Therefore, in addition to optical transitions localized “purely” within the cluster as in the gas phase and on the MgO (100) support, new hybrid transitions arise which are neither “pure” transitions within the cluster nor characteristic for the F_S center alone. Although the electronic structure is complex, full understanding can be achieved through a systematic analysis of electronic transitions in terms of contributing excitations. It will be shown that new spectral features arise for individual $\mathrm{Ag_n@F_{5c}}$ cluster-support species and that the smallest silver cluster such as Ag_2 and Ag_4 supported at F_S center defect site represent the best candidates for emissive centers at MgO support.

Chapter 10

Theoretical and Computational Aspects

In order to describe the ionic MgO support, the embedded cluster approach has been used in which a quantum mechanically (QM) described MgO cluster is embedded into a polarizable environment of point charges [203].

QM Part: For studying supported clusters, a magnesium oxide cluster $Mg_{13}O_{13}$ is chosen to represent the model surface. However, in order to avoid strong polarization by neighboring positive point charges, Mg^{2+} cations are introduced at the boundary of the QM model finally resulting in a $Mg_{13}O_{13}(Mg^{2+})_{16}$ QM cluster. For the creation of the F_S center defect, the central O atom is removed leaving an oxygen vacancy (F_{5c} site). For the Mg, O and Ag atoms, triple-ζ plus polarization (TZVP) atomic basis sets have been used [98]. In order to take into account scalar relativistic effects, the core electrons of the Ag atoms are replaced by a 19-electron relativistic effective core potential (19e-RECP) from the Stuttgart group [98]. The boundary Mg^{2+} cations have been described by effective core potentials from Hay and Wadt [204], replacing the 1s, 2s and 2p electrons, combined with a single s basis function contracted from two s-type primitive functions.

Classical Environment: The QM cluster is embedded in a large array of point charges which simulate the ions of the surrounding lattice ensuring the correct distant part of the electrostatic field of the quasi-infinite crystal (Madelung potential). In order to take into account lattice polarization, these charges are described by the shell model introduced by Dick and Overhauser [205]. In the shell model, an ion is represented by two charges, a point charge core and shell, which are connected by a spring to simulate the dipole polarizability of the surrounding. They interact between themselves and with the

QM cluster ions via specified inter-atomic potentials (Coulomb and Buckingham potentials). Corresponding shell model parameters suitable for the MgO surface have been taken from Ref. [206]. A small cube of polarizable shell ions ("region I") has been chosen to describe the nearest surrounding of the QM cluster in which all ions are allowed to relax. The ions outside region I ("region II") consist of fixed non-polarizable ions which provide the correct potential in the QM cluster and in region I. For simulating the MgO surface, a rectangular box of 20×20×10 point charges with formal ionic charges (Mg: +2.0; O: -2.0) is used, which contains a rectangular box of 10×10×8 polarizable shell ions ("region I").[1]

The density functional theory (DFT) method with Becke's three-parameter non-local exchange functional together with the Lee-Yang-Parr gradient-corrected correlation functional (B3LYP [94–97]) has been used to determine ground-state structural and binding properties of $\mathrm{Ag_n}$ clusters at support. For optical and emissive properties the time-dependent DFT (TD-DFT) in its linear response formulation has been used employing the same density functional and combination of basis sets and shell-model parameters.

Since the discussion of fluorescence properties will be based on the Einstein coefficients, it is important to recall basic relations in the context of light absorption and emission. The rate for the radiative decay of an excited electronic state by spontaneous fluorescence is proportional to the Einstein coefficient A

$$A_{fi} = \left(\frac{8\pi^2\nu_{fi}^3}{3\epsilon_0\hbar c^3}\right)|\mu_{fi}|^2 \tag{10.1}$$

where ν_{fi} is the absorption energy for the transition between the excited electronic state f (final) to the electronic ground state i (initial), ϵ_0 is the vacuum permittivity, $\hbar$ is Planck's constant $h/2\pi$, c is the vacuum speed of light and μ_{fi} is the electric transition dipole moment. The radiative lifetime τ_{rad} for the excited electronic state is defined as

$$\tau_{rad} = 1/A_{fi} \tag{10.2}$$

Notice that A_{fi} is proportional to the square of the transition dipole moment μ_{fi} which determines also the intensity of absorption bands expressed

---

[1] The procedure for obtaining an appropriate model for the MgO surface is described in Ref. [203]. Shortly, a nanocluster of 20×20×10 classical shell ions is completely relaxed using exclusively classical interactions. Then the ions in region II are kept fixed and QM atoms are placed at the center of the surface in region I. Notice that the nanocluster is slightly deformed from a perfect rectangular box with little rounded corners in region II [203].

by the oscillator strength $\mathrm{f_e}$

$$\mathrm{f_e} = \left(\frac{4\pi m_e \nu_{fi}}{3e^2\hbar^2}\right) |\mu_{fi}|^2 \tag{10.3}$$

where m_e and e are the electron mass and charge, respectively. Consequently, the radiative lifetime of bound excited electronic states with a corresponding, very intense absorption (large μ_{fi}) is short and thus radiative processes will dominate. In contrast, for transitions with low intensity the lifetimes of spontaneous emission will be longer according to Equations 10.1 and 10.2, which means that competitive secondary photochemical reactions can occur in the excited electronic state.

All calculations have been performed using the program package TURBOMOLE [207] which provides energies and analytic gradients acting on QM atoms and point charges for ground as well as excited electronic states [208, 209]. An interface program has been written in order to perform the corrections due to the classical environment as well as to provide the interface to the L-BFGS [210] optimization routine. For geometry optimizations in the ground and excited electronic states all QM atoms and classical ions within region I are allowed to relax. Structures have been considered fully relaxed if the energy was converged to 10^{-6} Hartree and the norm of the gradient was smaller than 10^{-4} Hartree/Bohr. Vertical, unrelaxed ionization potentials $\mathrm{IP_0}$ are calculated as the energy difference between the fully relaxed geometry of the neutral ground state and the energy of the cation with the same coordinates for QM atoms and classical point charges. For taking into account the response of the lattice due to ionization, the point charge shells in region I are relaxed in the cationic state while the QM atoms and point charge cores in region I are kept fixed. This yields the vertical, relaxed ionization potential $\mathrm{IP_I}$. In contrast to the calculation of the ionization potential, where the lattice response has to be taken into account, test calculations have shown that for the absorption properties it is not necessary to relax the shells in region I in the excited electronic states due to the localized nature of the optical transitions ($\Delta\mathrm{T_e}\approx 0.05$ eV).

Chapter 11

Structural and Optical Properties of Gas-Phase Silver Clusters $\mathrm{Ag}_{\mathrm{n}=2,4,6,8}$

The structural and optical properties of gas-phase clusters Ag_n (n=1-8) have been previously calculated based on highly correlated wave functions at the configuration-interaction (CI) and coupled-cluster (CCSD) level of theory [81, 82]. However, these methods are restricted to small systems due to the computational demand. Therefore, density functional methods are used for studying the influence of the support, and the calculations have been done also for pure clusters given the need of analysis and comparison.

The lowest-energy isomers of gas-phase Ag_n (n=2, 4, 6, 8) clusters obtained at the DFT level of theory are shown in Figure 11.1. Before structural and optical properties will be discussed for each individual cluster size, general considerations about the electronic structure in small Ag_n clusters as well as a classification of optical transitions are presented.

In the Ag_n (n=2, 4, 6, 8) gas-phase clusters, linear combinations of the silver orbitals give rise to one S-, three $\mathrm{P}_{x/y/z}$- and five D-type cluster orbitals which are filled by n electrons. The orbitals can be characterized according to the number of nodal planes. Furthermore, they can be labelled according to similar shaped 5D atomic orbitals with an index corresponding to their orientation (e.g. P_z, D_{xy}, D_{z^2}). This notation allows for a classification of electronic transitions in terms of leading excitations between initial and final orbitals of different character, e.g. $\mathrm{S}\rightarrow\mathrm{P}_x$ or $\mathrm{P}_y\rightarrow\mathrm{D}_{yz}$. This is useful not only for characterizing transitions but also for explaining intensity due to fact that the orbital angular momentum quantum numbers of the initial and final orbital must differ by one (e.g. P→P transitions are forbidden). Notice

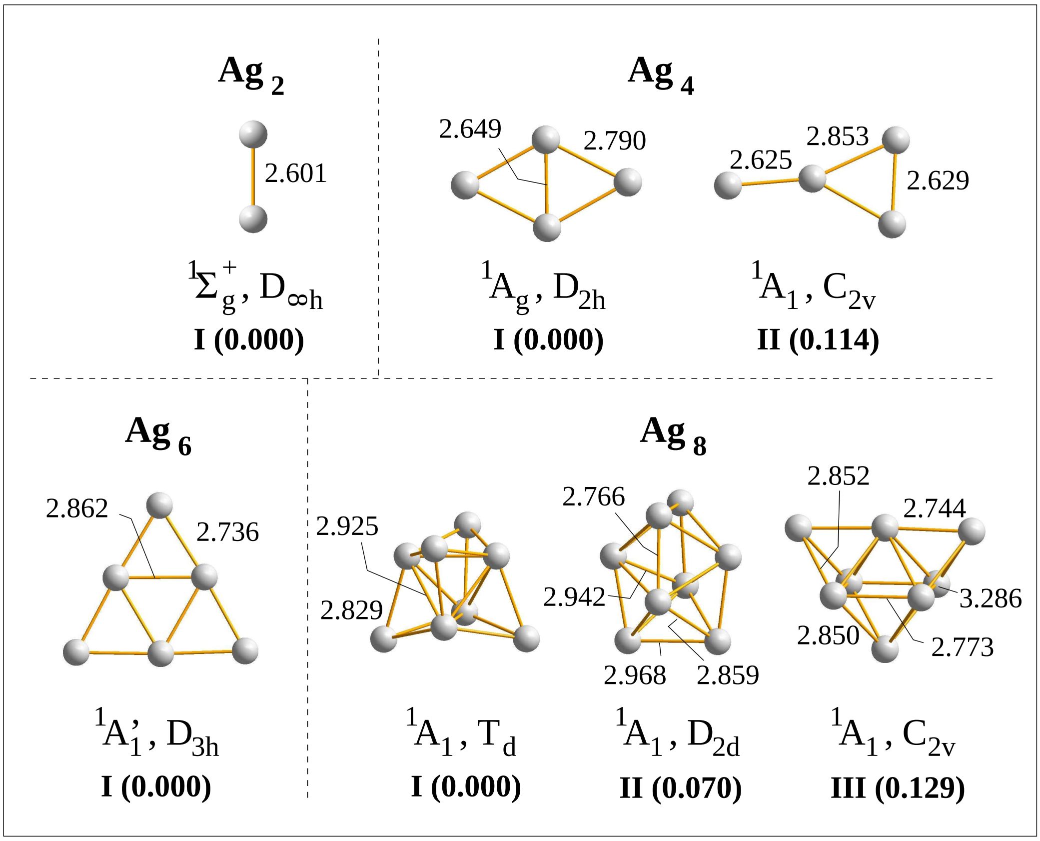

Figure 11.1: Lowest-energy isomers of neutral gas-phase Ag_n clusters (n=2, 4, 6, 8). Isomers are labelled with **I-III**. Relative energies in eV, bond lengths in Å as well as spatial symmetry and symmetry of the electronic ground state are given.

that due to the large s-d gap usually only the valence s-electrons from silver are "optically active" and that only in few cases (e.g. Ag_4) d-electrons are directly involved.

It should be noted that throughout the discussion the orientation of the gas-phase clusters is chosen such that the *xy*-plane is in parallel to the MgO surface in the corresponding cluster-support species for easier comparison. The polarization of the electronic transitions will also be presented since this might give useful information for an experimental identification of electronic transitions in the framework of the polarization-resolved optical spectroscopy.

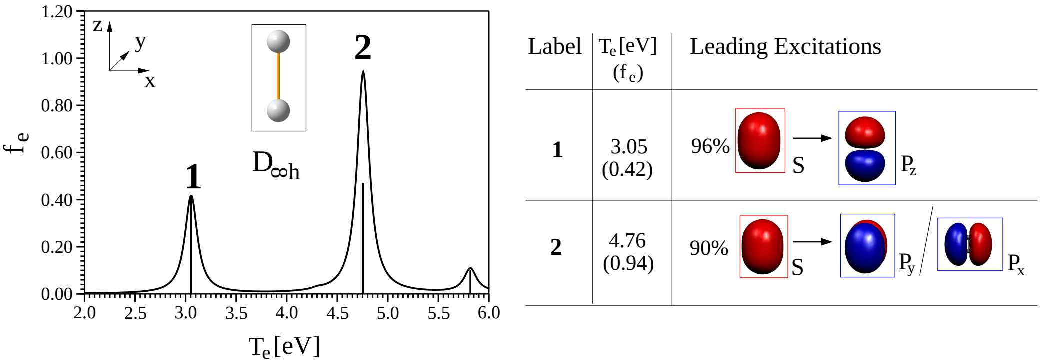

Label	T_e [eV] (f_e)	Leading Excitations
1	3.05 (0.42)	96% S → P_z
2	4.76 (0.94)	90% S → P_y / P_x

Figure 11.2: Optical spectrum and optimized structure of neutral gas-phase Ag_2 ($D_{\infty h}$). The table shows the transition energies T_e in eV, oscillator strengths f_e and the leading excitations in the labelled transitions (**1**, **2**) together with their weights. The frames around the orbitals are colored in order to illustrate the character of the orbitals (red: S-type, blue: P-type).

11.1 Ag_2

The equilibrium distance of the gas-phase silver dimer ($D_{\infty h}$, $^1\Sigma_g^+$) has been calculated to be r_e=2.601 Å which compares well to the experimental value of 2.530 Å [211]. The optical spectrum of Ag_2 is dominated by two intense transitions located at ∼3 eV and ∼4.8 eV (Figure 11.2). Both are mainly due to excitation from the S-type valence orbital (HOMO) to P-orbitals. The transition **1** at a lower energy is polarized along the Ag-Ag axis while the other is polarized perpendicularly to the Ag-Ag bond (see Figure 11.2). The absorption properties are in satisfactory agreement with results from the previous study by Bonačić-Koutecký et al. [81]. It is important to note that the excited electronic state corresponding to intense transition **1** is bound [212] in accordance with the observed fluorescence [184, 185].

11.2 Ag_4

The silver tetramer has two energetically low lying isomers (Figure 11.1). The most stable gas-phase isomer **I** assumes D_{2h} symmetry (rhombic structure, ^1A_g, D_{2h}) and the second isomer **II** is C_{2v} symmetric (T-shaped, $^1A_1$, C_{2v}, ΔE=0.114 eV). Although the energy difference is quite large, optical properties of both isomers will be discussed since both structures are present at support, as will be shown later. Notice that the orientation of the clusters

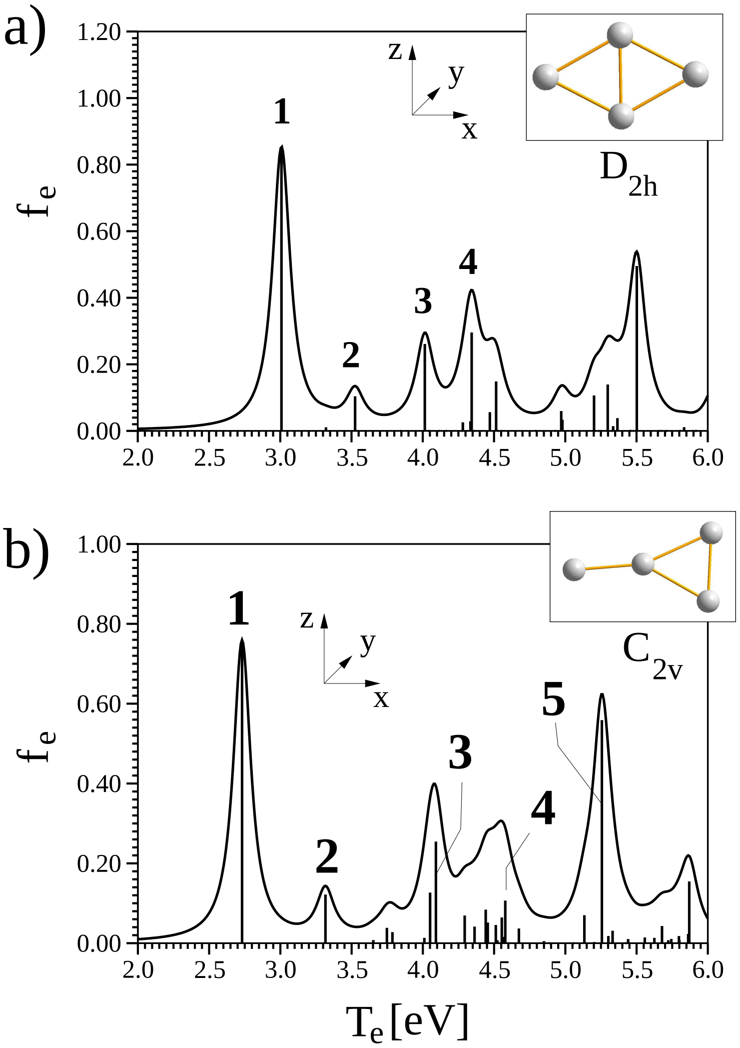

Figure 11.3: Optical spectra for neutral gas-phase a) Ag_4 (**I**, D_{2h}) and b) Ag_4 (**II**, C_{2v}). The transition energies T_e in eV and oscillator strengths f_e as well as leading excitations in the labelled transitions (**1-5**) together with their weights are given in Table 11.1.

Table 11.1: Weights of leading excitations for transitions in gas-phase a) rhombic Ag_4 (**I**, D_{2h}) and b) T-shaped Ag_4 (**II**, C_{2v}). Transition energies T_e are in eV, oscillator strengths f_e are given in parenthesis. Transitions are labelled with **1-5** according to their notation in the spectra (Figure 11.3). In cases where the same leading excitations with different weights are involved in two transitions, the contributing excitations are shown only once, and weights in corresponding transitions are separated by horizontal dashed lines.

a)

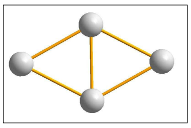

D_{2h}

Label	T_e[eV] (f_e)	Leading Excitations
1	3.01 (0.85)	93% 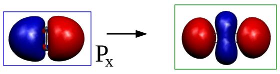 $P_x \rightarrow D_{x^2}$
2	3.53 (0.10)	99% 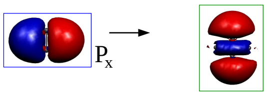 $P_x \rightarrow D_{z^2}$
3	4.01 (0.26)	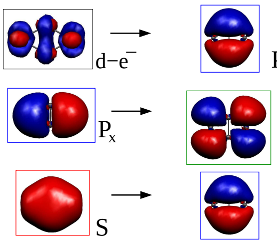 43% ┄ 41% $d\text{−}e^- \rightarrow P_z$ 40% ┄ 19% $P_x \rightarrow D_{xz}$ 14% ┄ 10% $S \rightarrow P_z$
4	4.34 (0.30)	

b)

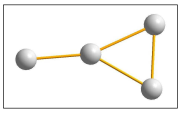

C_{2v}

Label	T_e[eV] (f_e)	Leading Excitations
1	2.73 (0.75)	95% 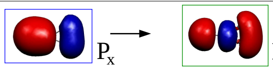 $P_x \rightarrow D_{x^2}$
2	3.32 (0.12)	84% 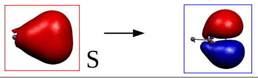 $S \rightarrow P_z$
3	4.09 (0.25)	47% 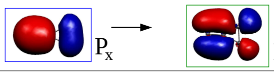 $P_x \rightarrow D_{xz}$
4	4.58 (0.11)	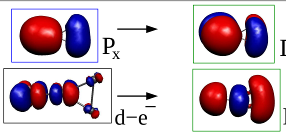 50% $P_x \rightarrow D_{xy}$ 29% $d\text{−}e^- \rightarrow D_{x^2}$
5	5.26 (0.56)	78% 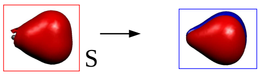 $S \rightarrow P_y$

has been chosen such that coordinate systems of the gas-phase isomers as well as of clusters at support are the same, e.g. the D_{2h} isomer is put into the xz-plane and the long diagonal is oriented along the x-axis.

The absorption spectra for both isomers of Ag_4 look very similar (Figure 11.3). The most prominent spectral feature is transition **1** which can be found at T_e=3.01 eV (f_e =0.85) for rhombic Ag_4 (**I**) and at T_e=2.73 eV (f_e =0.75) for the T-shaped Ag_4 isomer **II**. In both cases, transition **1** is polarized in x-direction with leading excitation P_x(HOMO)→ D_{x^2}(LUMO+1). The corresponding excited state in **I** and **II** has a close lying minimum and thus fluorescence can occur from this excited state [65].

The electronic transitions with intensity dominating the higher energy part of the spectrum mainly consist of excitations from the occupied S and P_x orbitals to the unoccupied $P_{y/z}$ and D orbitals, and their corresponding weights can be found in Table 11.1. It is interesting to note that in case of rhombic Ag_4(**I**), excitation from d-electrons to the P_z orbital contributes to the $P_x \rightarrow D_{xz}$ excitation in transitions **3** and **4** ($T_e \approx$4.0-4.5 eV). In contrast, in the case of the T-shaped Ag_4(**II**) isomer, there is no d-electron contribution to the $P_x \rightarrow D_{xz}$ transition **3** at $T_e \sim$4 eV. However, a small contribution from d-electron excitations can be found in several low intense transitions at higher energy $T_e \sim$4.5 eV (e.g. in transition **4**).

11.3 Ag_6

The gas-phase Ag_6 cluster assumes a highly symmetric triangular structure (D_{3h}, $^1A_1'$) (Figure 11.1) which is energetically well separated from higher lying isomers (ΔE=0.312 eV). The optical spectrum (Figure 11.4) essentially consists of a very intense doubly degenerated transition **1** at T_e=3.35 eV (2.01) with excitations from two-fold degenerated HOMO ($P_{x/z}$, e') to two-fold degenerated LUMO+1 (in-plane D orbitals, e'). This transition also has a contribution from the $P_{x/z} \rightarrow$2S excitation. The transition is polarized along the z-axis which lies in the symmetry plane of the cluster in the chosen orientation. The corresponding minimum in the excited state is very close to the ground state equilibrium geometry [212]; thus a possible fluorescence band is very close in energy to the absorption band.

11.4 Ag_8

For gas-phase Ag_8, the lowest three isomers have been considered for studying the optical properties (Figure 11.1). The most stable isomer **I** assumes

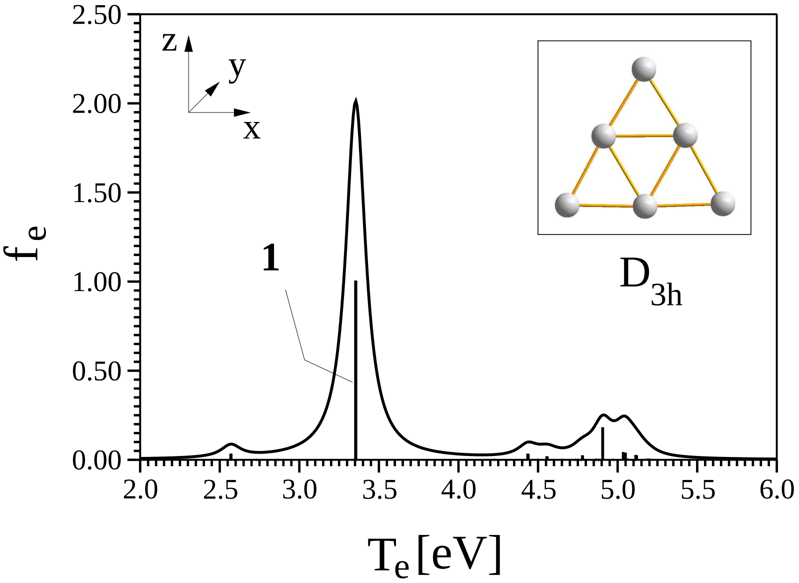

Label	Te [eV] (fe)	Leading Excitations
1	3.35 (2.01)	62% 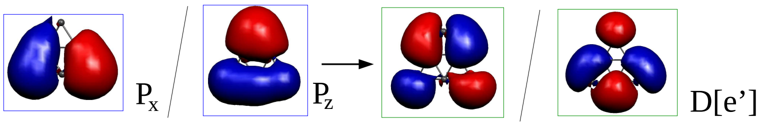
		24% 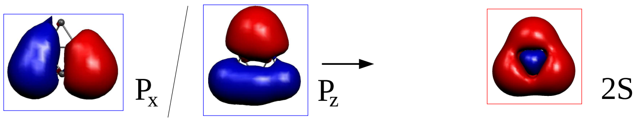

Figure 11.4: Optical spectrum for neutral gas-phase Ag_6 (D_{3h}). The table shows the transition energy T_e in eV, the oscillator strength f_e and the leading excitations in the labelled transition (**1**) together with their weights.

tetrahedral symmetry (T_d, $^1A_1$), and the second isomer **II** (D_{2d}, $^1A_1$) is only 0.070 eV higher in energy. The third isomer **III** (C_{2v}, $^1A_1$) is 0.129 eV higher in energy than the most stable isomer **I** and can be rationalized as octahedron with two face-capping Ag atoms.

All three isomers are "compact" 3D structures with delocalized s-electrons occupying the S and the three P cluster orbitals. Moreover, in these isomers the S-type orbital is energetically very low and lies within the manifold of

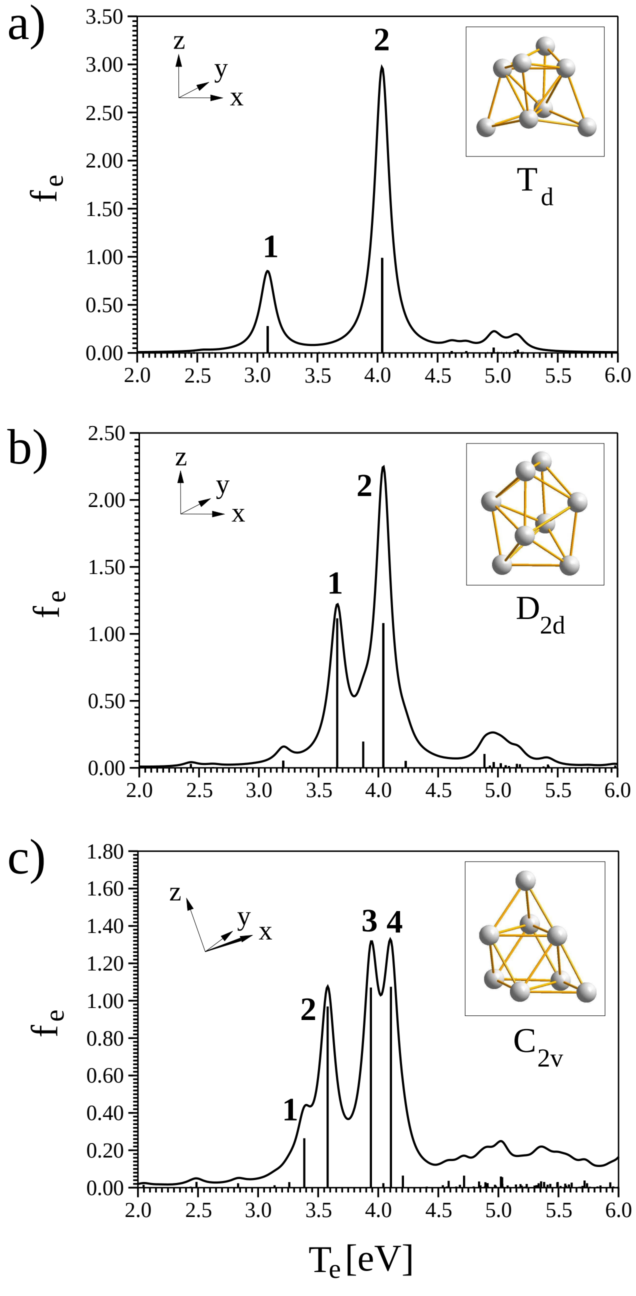

Figure 11.5: Optical spectra for neutral gas-phase a) Ag_8 (**I**, T_d), b) Ag_8 (**II**, D_{2d}) and c) Ag_8 (**III**, C_{2v}). The transition energies, oscillator strengths as well as leading excitations in the labelled transitions (**1**-**4**) are given in Table 11.2 for **I** and **II**, and in Table A.2 in Appendix A for the third isomer **III** (C_{2v}).

Table 11.2: Weights of leading excitations for transitions in gas-phase a) Ag_8 (**I**, T_d) and b) Ag_8 (**II**, D_{2d}). Transition energies T_e are in eV, oscillator strengths f_e are given in parenthesis. Transitions are labelled with **1-2** according to their notation in the spectra (Figure 11.5). In cases where the same leading excitations with different weights are involved in two transitions, the contributing excitations are shown only once, and weights in corresponding transitions are separated by horizontal dashed lines.

a)

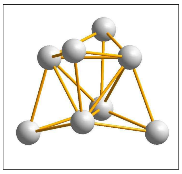

T_d

Label	T_e[eV] (f_e)	Leading Excitations		
1	3.09 (0.83)	46% 15%	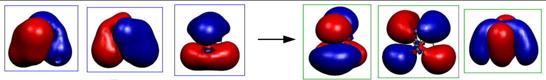	$P_{x/y/z}$ → D [t_2]
		27% 6%	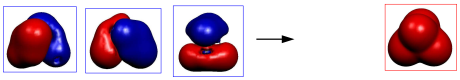	$P_{x/y/z}$ → 2S
2	4.04 (2.96)	26% 67%	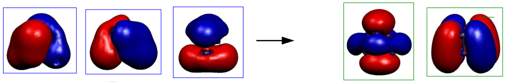	$P_{x/y/z}$ → D [e]

b)

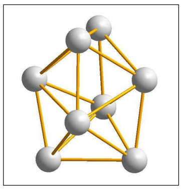

D_{2d}

Label	T_e[eV] (f_e)	Leading Excitations		
1	3.66 (1.12)	59%	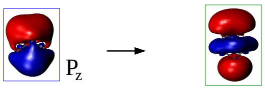	P_z → D_{z^2}
		28%	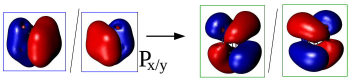	$P_{x/y}$ → $D_{xz/yz}$
2	4.04 (2.16)	36%	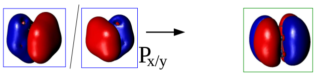	$P_{x/y}$ → D_{xy}
		20%	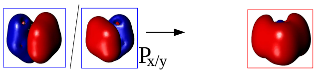	$P_{x/y}$ → 2S
		16%	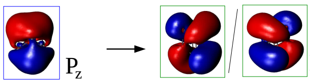	P_z → $D_{xz/yz}$
		11%	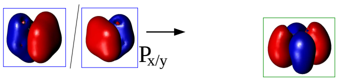	$P_{x/y}$ → D

orbitals formed by the d-electrons of the silver octamer. Therefore, the spectral features below ≈5 eV are dominated only by excitations from the P-type orbitals. Contributions by excitations from the S-type orbital or from d-electrons do not play a significant role for the silver octamers, as will be shown for isomers **I** - **III** in the following.

Due to the high symmetry, the optical spectrum of the T_d isomer **I** is dominated by one intense transition at ∼4 eV (Figure 11.5a). Another much weaker transition is located at $T_e \sim 3$ eV. Due to 3D structure the dominant transition is located at a considerably higher energy (∼4 eV) than for smaller planar structures of smaller clusters ($T_e \sim 3$ eV). The same leading excitations with different weights contribute to both transitions (see Table 11.2), which are excitations from the degenerated P-type orbitals to the three-fold degenerated D-type orbitals (t_2 symmetry), to the two-fold degenerated D-type orbitals (e symmetry) and to the second S-type orbital (2S).

The absorption spectrum of the second isomer **II** with D_{2d} symmetry is dominated by two intense transitions **1** and **2** at an energy of $T_e \sim 4$ eV. The character of both transitions is very similar to the most intense transition **2** in the T_d isomer. The splitting in case of the D_{2d} isomer is caused by the lower symmetry which is the reason why the degeneracy of the set of P orbitals is removed. Therefore, the differently polarized components of the most intense transition in the T_d isomer are separated into the z-polarized transition **1** at lower energy and the transition **2** at higher energy. The latter is doubly degenerated exhibiting an x- and y-polarized component (see Table 11.2b).

In the isomer **III**, the symmetry (C_{2v}) is considerably lower than T_d or D_{2d} and thus the degeneracy of P- and D-type orbitals is completely lifted. Consequently, the optical spectrum is dominated by four intense transitions between 3.0 and 4.5 eV (Figure 11.5c). The leading excitations in the transitions **1** and **2** at $T_e \sim 3.5$ eV are both of $P_z \rightarrow D$ and $P_z \rightarrow D_{z^2}$ character with different weights (see Table A.2 in Appendix A). The other two transitions **3** and **4** at $T_e \sim 4$ eV are dominated by many leading excitations which are of similar character as in the other two isomers of Ag_8, namely transitions from P-type orbitals to different D-type orbitals and to the 2S orbital, respectively.

11.5 Summary

The structures and optical properties of neutral gas-phase silver clusters have been obtained employing DFT methods. In agreement with previously published results [81, 82, 156], the smaller neutral clusters with up to six Ag atoms remain planar while the larger cluster Ag_8 assumes a 3D structure. The low-energy part of the absorption spectra for the Ag_n clusters with n=2, 4, 6 is dominated by an intense transition at $T_e \sim 3$ eV with S→P (Ag_2), P→S (Ag_4) and P→D/S character (Ag_6), respectively. The corresponding excited electronic states have a bound character, and fluorescence can occur from these states.

In the 3D structures in the Ag_8 isomers, the most intense transitions are shifted by 1 eV to a higher energy ($T_e \sim 4$ eV) compared to smaller planar silver clusters. It has been shown for the T_d and D_{2d} isomers that the corresponding excited states are also bound and therefore fluorescence at $T'_e \sim 4$ eV occurs [62, 65].

Chapter 12

MgO (100) Surface and F_S Center Defect

12.1 Structural Properties

The model for the MgO support which is suitable for examining the properties of adsorbed silver clusters has been described in Chapter 10. The relaxation of the Mg and O atoms in the surface model compared to the ideal lattice positions was small. With the given parameter set, deviation from the experimental lattice constant is smaller than 1% ($a_{0,\mathrm{calc}}$=2.092 Å vs. $a_{0,\mathrm{exp}}$=2.106 Å). The calculated ionization potential for the ideal MgO (100) surface (IP_I=6.72 eV) is in excellent agreement with the experimental value of 6.7±0.4 eV obtained from metastable impact electron spectroscopy (MIES) studies [213]. Notice that it is important to take into account the polarization of the lattice upon ionization, since otherwise the calculated ionization potential is exceeded by ∼0.7 eV (IP_0=7.41 eV). This is due to the limited size of the QM model which cannot account for the changes in the electron density of the extended MgO surface upon ionization. However, it has been shown [203] that the explicit treatment of the lattice polarization leads to quick convergence of the ionization potential as a function of the size of the QM model cluster.

Removing the central O atom from the MgO (100) surface requires 9.40 eV. Since the coordination number of the removed O atom was five, this kind of defect is called F_{5c} defect site. Creation of this anion vacancy causes only a slight relaxation of the nearest QM atoms with all atom displacements being smaller than 0.045 Å. The relaxed vertical ionization potential of the F_S center is considerably smaller (IP_I=3.46 eV) than for the ideal MgO (100) surface. Interestingly, the difference to the unrelaxed vertical ionization potential (IP_0=4.12 eV, ΔIP=0.7 eV) is the same as in case of the defect-free MgO (100) surface.

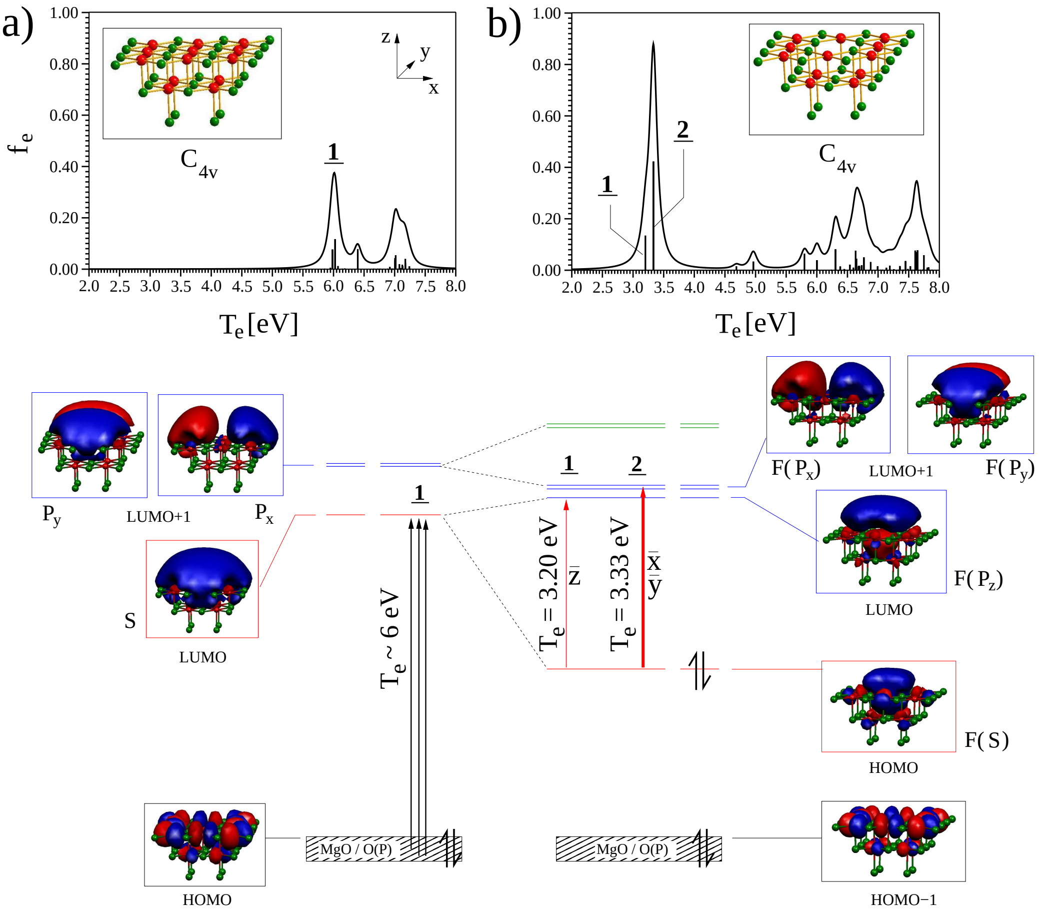

Figure 12.1: Absorption spectra and molecular orbital diagram for a) the defect-free MgO (100) surface (O_{5c}) and b) the F_S center defect (F_{5c}). Leading configurations in transitions are represented by arrows with the corresponding transition energies T_e in eV and polarizations (e.g. $\overrightarrow{z}$). The frames around the orbitals and the corresponding energy levels are colored in order to illustrate the character of the orbitals (red: S-type, blue: P-type, green: D-type). The positive and negative lobes of the molecular orbitals are shown as dark blue and red iso-surfaces.

12.2 Optical Properties

The top of the MgO valence band is formed by the p-electrons from the surface O atoms from which excitation takes place (see Figure 12.1a). The bottom of the MgO conduction band is formed by empty Mg S-orbitals and the corresponding orbitals can be characterized according to the number of nodal planes. The LUMO of the MgO surface has no nodal plane and is thus of S-type (see red-framed orbital at the bottom left in Figure 12.1). The next two unoccupied orbitals have one nodal plane which is characteristic for P-type orbitals ($P_{x/y}$). The optical band gap of the MgO surface is calculated to be 6.0 eV. The corresponding intense transitions (**1** in Figure 12.1a) are characterized by excitations from orbitals of the valence band to the S-type LUMO of the MgO conduction band. Notice that the corresponding excited states are delocalized over the whole surface, which is difficult to describe with DFT methods. However, the calculated value for the optical band gap is very close to the experimental value of 6.2 eV obtained from electron-energy loss spectroscopy (EELS) on an MgO single-crystal surface [214, 215].

Before the optical properties of the F_S center defect will be addressed, the electronic structure of the F_{5c} defect site will be discussed. Removing the central O atom essentially creates an electron pair which is trapped in a vacancy. The pair of electrons features an occupied S-type orbital and unoccupied P-type orbitals, which are all confined to the boundaries of the cage. The properties of such trapped electrons have been known for long time since they are responsible for the blue color of alkali metals soluted in liquid ammonia [216] and colors of the defect centers in crystals [83], for example. However, the orbitals of the trapped electron pair are able to interact with the orbitals of the MgO surface which leads to the molecular orbitals which are typical for the F_{5c} defect site. The MO diagram in Figure 12.1 illustrates this situation: The linear combination of the S-type orbital from the electron pair (not shown) and the unoccupied S-type surface orbital (MgO LUMO, bottom left) leads to the bonding S-type orbital F(S) and the anti-bonding P-type orbital $F(P_z)$ (bottom right). Furthermore, the P-orbitals of the MgO surface (LUMO+1 of MgO surface) are slightly stabilized due to a linear combination with the corresponding orbitals of the trapped electron pair, which is also illustrated in Figure 12.1.

The overall effect of the F_S center defect formation is the creation of one occupied S-type orbital, one empty P_z-type orbital perpendicular to the surface and two empty $P_{x/y}$-type orbitals in parallel to the surface plane (Figure 12.1b). Notice that the set of P-orbitals is located energetically slightly below the MgO conduction band. The F(S) orbital lies energetically roughly in the middle between the MgO valence and conduction band. Consequently, intense optical transitions arise at $T_e \sim 3.3$ eV which are lying energetically within the optical band gap of MgO. They are dominated by an excitation of electrons from the F(S) orbital to the F(P_z) orbital [**1**, T_e=3.20 eV (f_e =0.14)] and F($P_{x/y}$) orbitals [**2**, T_e=3.33 eV (f_e =0.85)], respectively. The excited state corresponding to the first intense transition **1** is bound, and fluorescence occurs from that state in the visible part of optical spectrum. This is not surprising since emission in the visible regime is characteristic for F_S centers.

Chapter 13

Silver Clusters at the MgO (100) Support [$Ag_{n=2,4,6,8}@O_{5c}$]

13.1 Structural Properties

Before the optical properties of Ag_n clusters supported at the defect-free MgO (100) surface will be addressed, the most stable isomers have been determined, and Figure 13.1 shows the most stable structures of the $Ag_n@O_{5c}$ clusters. The corresponding binding energies are given in Figure 13.2. The small silver clusters are weakly bound to the defect-free surface (BE≈1.2 eV) resulting in a high mobility at room temperature. The binding energy is only slightly increasing as a function of the number of silver atoms (Figure 13.2), and consequently the binding energy per Ag atom decreases with increasing cluster size. As a consequence of the weak electrostatic interaction, the geometry as well as the electronic structure is almost unperturbed compared to the gas phase. This can also be seen from the ionization potentials for $Ag_n@O_{5c}$ species compared to the gas-phase silver clusters (Figure 13.3; values can be found in Table A.1 in Appendix A). Both exhibit analogous behaviour as a function of the cluster size. The gas-phase ionization potential is simply reduced at MgO support by ∼2 eV which is connected with the modified surface work function (work function Φ_{MgO} for "pure" MgO: 2.7 eV [217]). In the following, the structural properties of the supported clusters will be presented according to individual cluster sizes:

$Ag_2@O_{5c}$ The most stable structure **I** of the $Ag_2@O_{5c}$ dimer assumes upright geometry with direct binding to the O_{5c} site. The equilibrium bond distance is unchanged compared to the gas phase (r_e=2.601 Å). The distance from the O_{5c} site is large (2.281 Å) reflecting the small binding energy

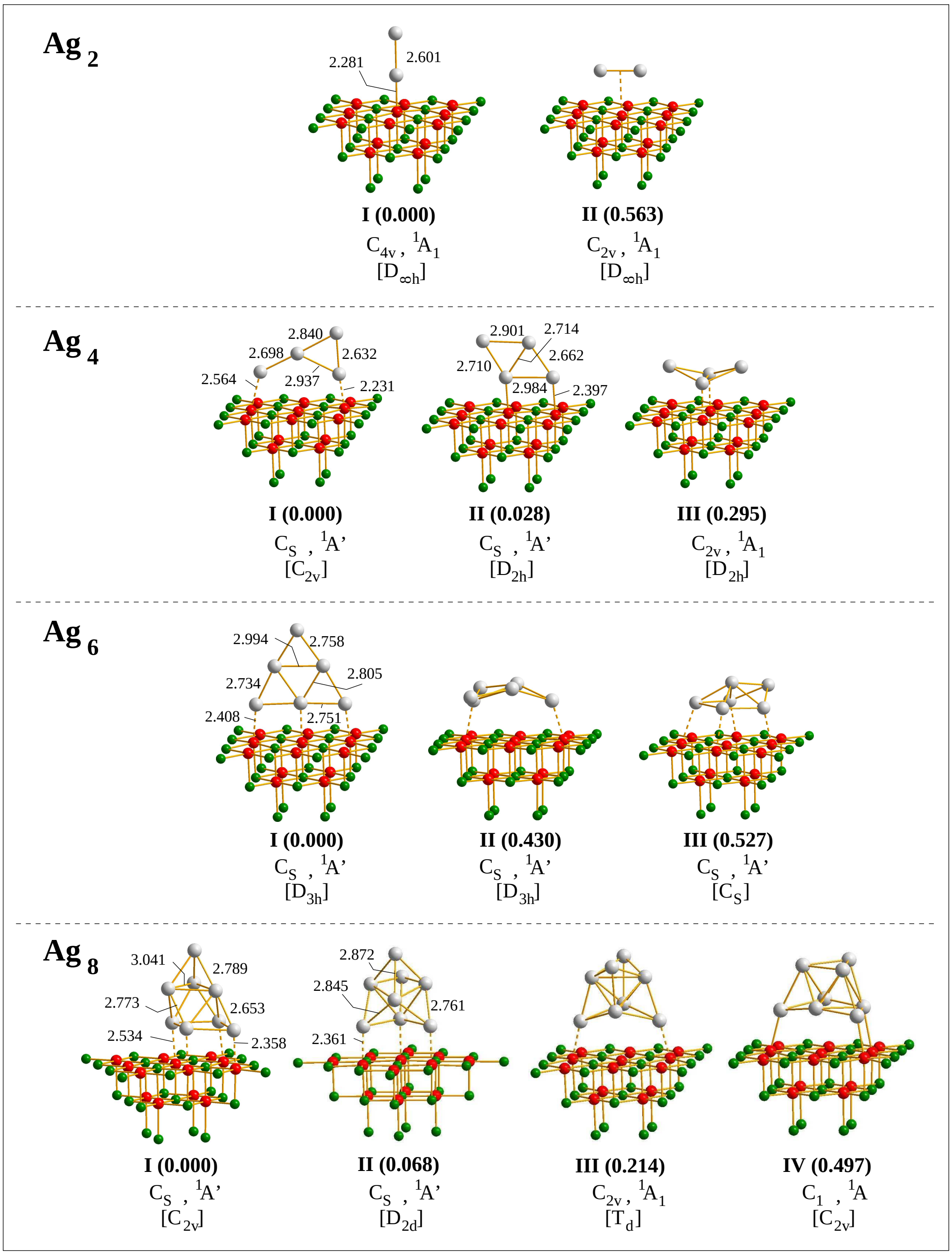

Figure 13.1: Lowest-energy isomers of Ag_n clusters supported at the MgO defect-free surface (n=2, 4, 6, 8). Isomers are labelled with **I-IV**. Relative energies in eV, bond lengths in Å for the lowest-energy structures within 0.1 eV as well as spatial symmetry and symmetry of electronic ground state are given. In square brackets, the local symmetry of the supported silver cluster is shown.

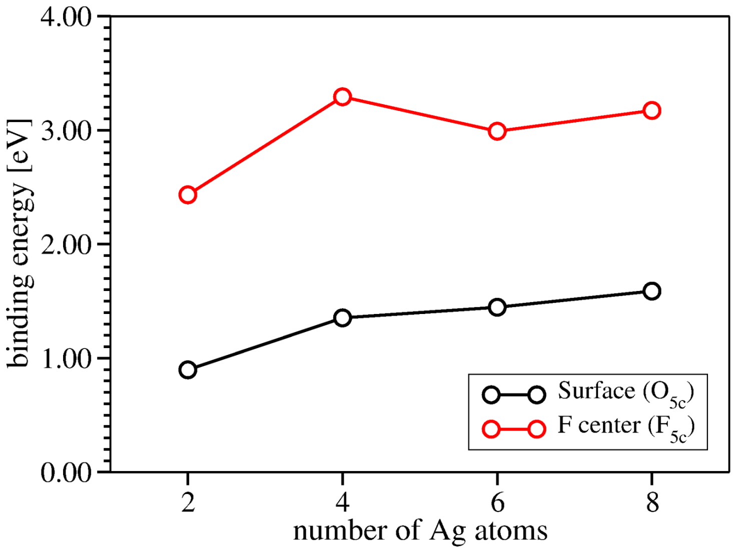

Figure 13.2: Binding energies in eV of silver clusters to the MgO surface (black) and the F_S center defect (red).

of 0.90 eV (Figure 13.2).

Ag_4@O_{5c} In the case of Ag_4@O_{5c} two isomers are close in energy. The local symmetry of the Ag_4 moiety in the most stable isomer **I** is close to the T-shaped Ag_4 gas-phase cluster (C_{2v} symmetry), and the second isomer **II** ($\Delta E = 0.028$ eV) resembles the rhombic Ag_4 isomer (D_{2h} symmetry). Notice that although interaction with the defect-free support is weak, it is strong enough to change the ordering of isomers compared to the gas phase. However, in both isomers the Ag_4 unit interacts with two surface O atoms, and the symmetry of the cluster-support species is reduced to C_S symmetry.

Ag_6@O_{5c} In the most stable isomer **I** of Ag_6@O_{5c} (C_{2v}, $^1A_1$), the silver cluster hexamer assumes an upright triangular geometry closely related to the most stable gas-phase structure ($\Delta r_{e,max}$=0.13 Å). Therefore, due to the MgO (100) support, the high D_{3h} symmetry of gas-phase Ag_6 is reduced to C_{2v} symmetry at the surface.

Ag_8@O_{5c} In the case of Ag_8@O_{5c}, the ordering of gas-phase isomers ($T_d < D_{2d} < C_{2v}$) is changed at the MgO (100) support ($C_{2v} < D_{2d} < T_d$). The most stable isomer of Ag_8@O_{5c} (**I**, C_S, $^1A'$) resembles the C_{2v} isomer of gas-phase Ag_8 [Ag_8(**III**)] which is coordinated with one facet to four O atoms of the MgO (100) support. The second isomer of Ag_8@O_{5c} (**II**, C_S, $^1A'$) which is energetically almost degenerated with the most stable isomer (ΔE=0.068 eV) corresponds to the gas-phase D_{2d} structure [Ag_8(**II**)]. The cluster is slightly tilted and interacts with a total of three surface O atoms. The local symmetry

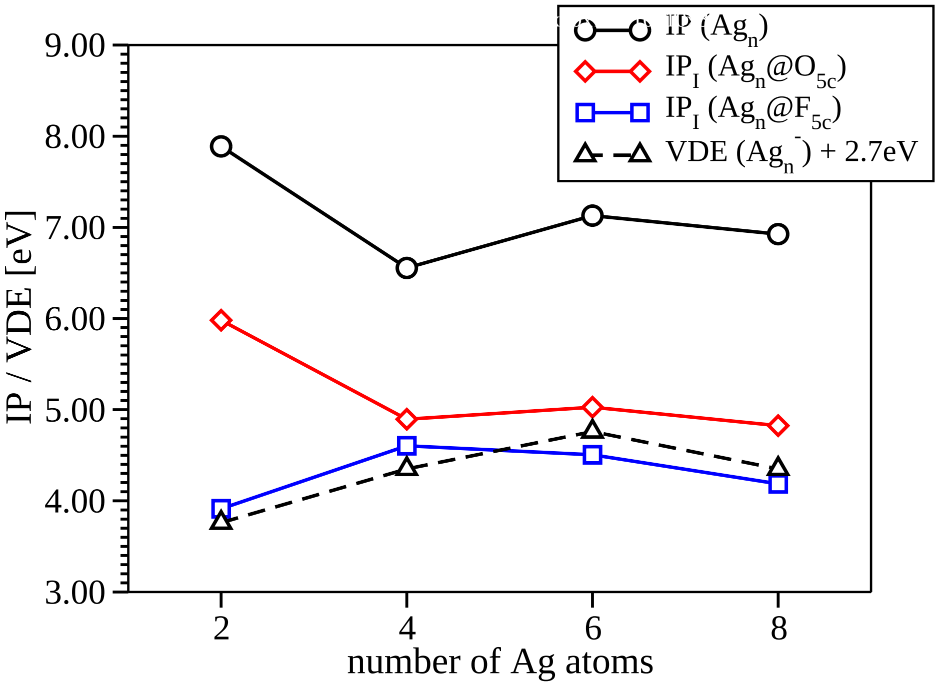

Figure 13.3: Vertical ionization potential in eV for the most stable isomers of gas-phase Ag_n clusters [IP(Ag_n), black circles] and relaxed vertical ionization potentials in eV for lowest-energy isomers of silver clusters at MgO (100) surface [$Ag_n@O_{5c}$, red diamonds] and at F_S center defect [$Ag_n@F_{5c}$, blue squares] (n = 2, 4, 6, 8). VDE for anionic gas-phase Ag_n^- clusters shifted by 2.7 eV is also shown (black triangle).

of the silver unit in the third isomer of $Ag_8@O_{5c}$ (**III**, C_{2v}, $^1A_1$, ΔE=0.214 eV) is very close to the T_d structure, which corresponds to the most stable gas-phase isomer Ag_8(**I**).

In summary, the weak interaction with the MgO support can change the ordering of isomers with respect to the corresponding gas-phase isomers (e.g. in Ag_4 and Ag_8). Furthermore, the ionization potentials of the clusters at support are reduced by ≈2 eV with respect to the gas phase which is in the order of the MgO work function. However, the electronic structure of the gas-phase silver clusters remains preserved. Therefore, the optical properties of the supported $Ag_n@O_{5c}$ clusters are expected to be similar to the gas-phase Ag_n clusters. It is expected that the lowering of the symmetry due to the support and the influence of the surface electrostatic potential on the clusters will slightly affect absorption energies and intensities of optical transitions which will be shown in the next section.

13.2 Absorption Properties

13.2.1 $Ag_2@O_{5c}$

The optical spectrum of the supported $Ag_2@O_{5c}$ shown in Figure 13.4 is very similar to the gas-phase spectrum (cf. Figure 11.2). The two intense transitions present in gas-phase Ag_2 are shifted at the support. Transition **1** at lower energy which is dominated by the S→P_z excitation orbital is slightly blue-shifted by 0.17 eV and now located at T_e=3.22 eV (Figure 13.4). In contrast, transition **2** at higher energy which involves excitation to the $P_{x/y}$ orbitals is red-shifted by ~0.7 eV (T_e=4.08 eV) compared to the corresponding transition **2** in the gas phase. Both effects can be qualitatively explained by analyzing the MO diagram for the interaction of Ag_2 with the MgO surface (Figure 13.5). It can be seen that at support all orbitals are shifted to higher energy due to the surface potential. However, the effect depends on the type and the orientation of the orbitals, and thus the effect is most pronounced for the P_z orbital, quite pronounced for the S orbital and only weakly pronounced for the $P_{x/y}$ orbitals. As a result, the energy for the S→P_z excitation is increased while the S→$P_{x/y}$ excitation energy is decreased, which qualitatively explains the blue and red shift of the corresponding electronic transitions. However, for quantitative argumentation electron correlation effects have to be taken into account.

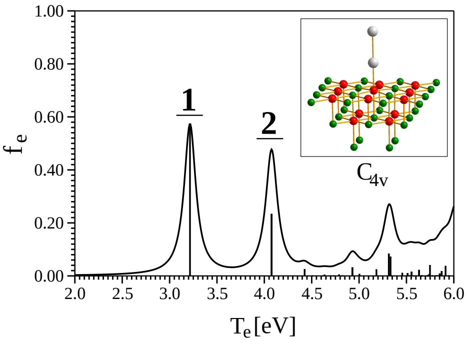

Label	T_e[eV] (f_e)	Leading Excitations			
1	3.22 (0.57)	94%	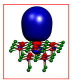 S	→	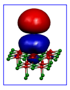 P_z
2	4.08 (0.46)	95%	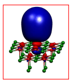 S	→	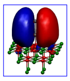 P_x / 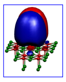 P_y

Figure 13.4: Optical spectrum and optimized structure of $Ag_2@O_{5c}$(**I**) [$D_{\infty h}$]. The table shows the transition energies T_e in eV, the oscillator strengths f_e and the leading excitations in the labelled transitions (**1**, **2**) together with their weights.

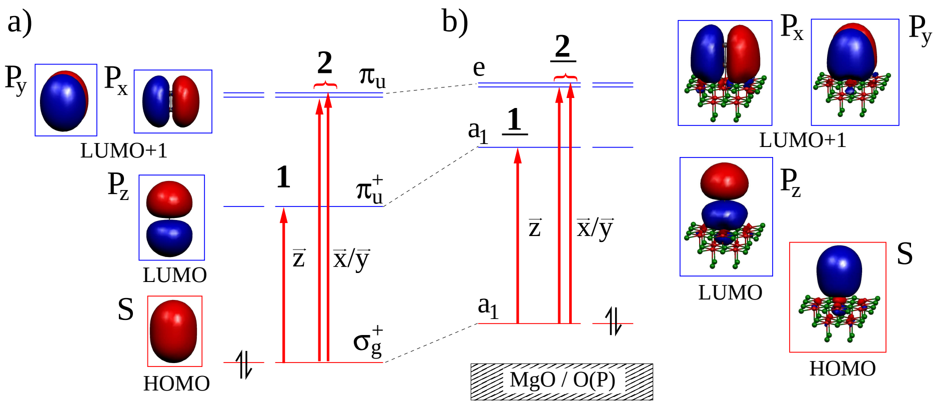

Figure 13.5: MO diagram for a) gas-phase Ag_2 and b) $Ag_2@O_{5c}$(**I**). Corresponding orbitals are connected by dashed lines. The frames around the orbitals and the corresponding energy levels are colored in order to illustrate the character of the orbitals (red: S-type, blue: P-type). Leading excitations are indicated by vertical lines from initial to final orbitals (for weights see tables in Figures 11.2 and 13.4) and $\overrightarrow{x}/\overrightarrow{y}/\overrightarrow{z}$ indicate the polarization of the corresponding transitions [**1**, **2** for a) and $\underline{\mathbf{1}}$, $\underline{\mathbf{2}}$ for b)].

13.2.2 $Ag_4@O_{5c}$

Figure 13.6 shows the optical spectra and tables with excitation energies for the lowest-energy isomers of $Ag_4@O_{5c}$ assuming local C_{2v} and D_{2h} symmetry, respectively. In both isomers, the ordering and the shape of the orbitals of the free cluster remain overall preserved at support. However, the orbitals are shifted to higher energies similar to what has been found for $Ag_2@O_{5c}$. This leads to a coupling of leading excitations which have not been resonant in the gas phase. This will be addressed in detail on the example of the first isomer $Ag_4@O_{5c}$ (**I**) [C_{2v}]. The findings are valid also for the second isomer of $Ag_4@O_{5c}$ and the corresponding MO diagram can be found in Figure A.1 in Appendix A).

The electronic transitions in the spectrum of the supported $Ag_4@O_{5c}$(**I**) [C_{2v}] species are very similar to the transitions in gas-phase Ag_4 (C_{2v}) (cf. Figure 11.3). The dominant spectral feature in the low energy region is the x-polarized transition $\underline{\mathbf{1}}$ which has the same character as in the gas phase ($P_x \rightarrow D_{x^2}$). However, it is slightly red-shifted by 0.13 eV and is now located at T_e=2.6 eV.

Several moderately intense transitions dominate the higher energy part of the absorption spectrum. They do not play a significant role for emission in the visible. However, an analysis of this part of the spectrum allows for the identification of the influence of the support on the electronic transitions. We

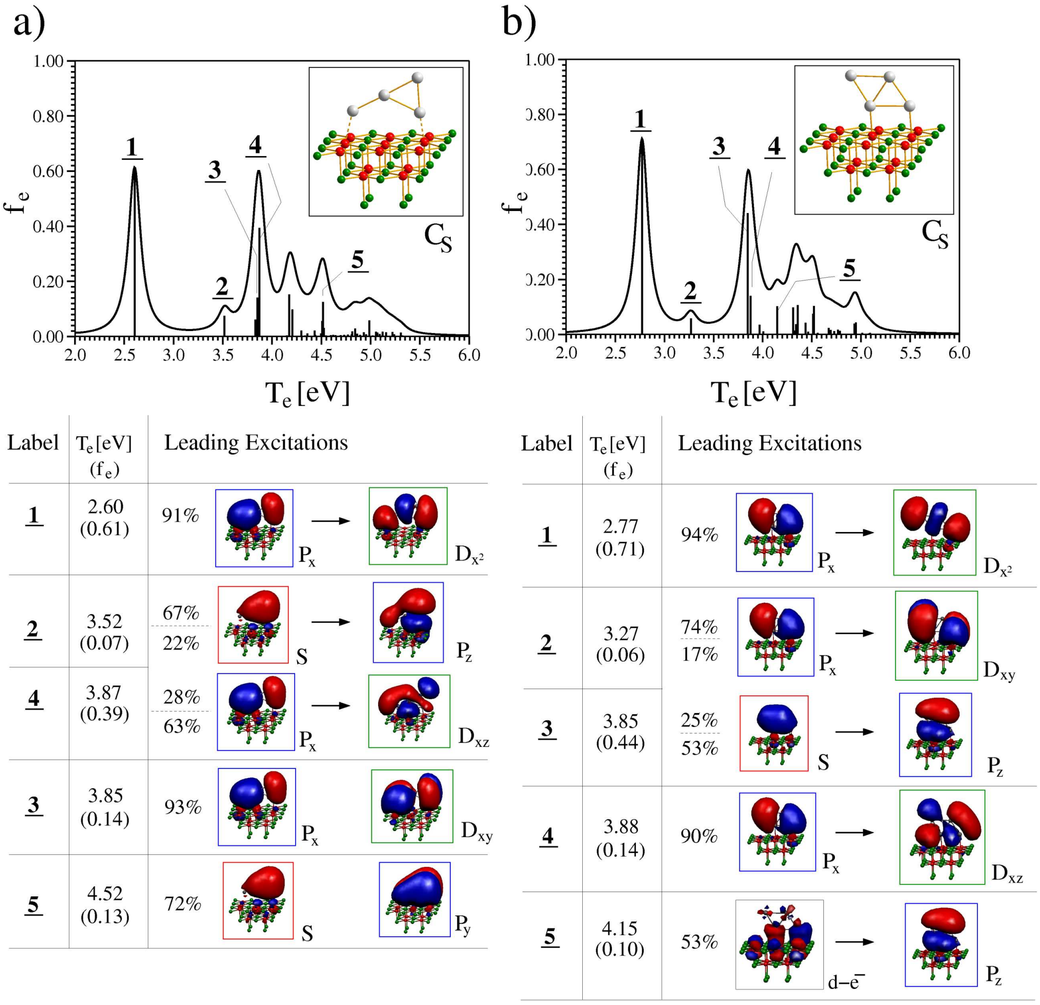

a)

Label	T_e [eV] (f_e)	Leading Excitations			
1	2.60 (0.61)	91%	P_x	→	D_{x^2}
2	3.52 (0.07)	67% 22%	S	→	P_z
4	3.87 (0.39)	28% 63%	P_x	→	D_{xz}
3	3.85 (0.14)	93%	P_x	→	D_{xy}
5	4.52 (0.13)	72%	S	→	P_y

b)

Label	T_e [eV] (f_e)	Leading Excitations			
1	2.77 (0.71)	94%	P_x	→	D_{x^2}
2	3.27 (0.06)	74% 17%	P_x	→	D_{xy}
3	3.85 (0.44)	25% 53%	S	→	P_z
4	3.88 (0.14)	90%	P_x	→	D_{xz}
5	4.15 (0.10)	53%	d–e^-	→	P_z

Figure 13.6: Optical spectra and optimized structures of a) $Ag_4@O_{5c}$(**I**) [C_{2v}] and b) $Ag_4@O_{5c}$(**II**) [D_{2h}]. The tables show the transition energies T_e in eV, the oscillator strengths f_e and the leading excitations in the labelled transitions (1-5) together with their weights. In cases where the same leading excitations with different weights are involved in two transitions (e.g. **2** and **4** in a), the contributing excitations are shown only once, and weights in corresponding transitions are separated by horizontal dashed lines.

will focus on three aspects which have relevance also for larger silver clusters and thus are of general importance:

(i) Excitations can become "resonant" at support which means that excitations within the cluster contribute to an electronic transitions at the support in contrast to the bare clusters in which they are leading excitations in different transitions. For example, in the gas-phase cluster Ag_4 (C_{2v}),

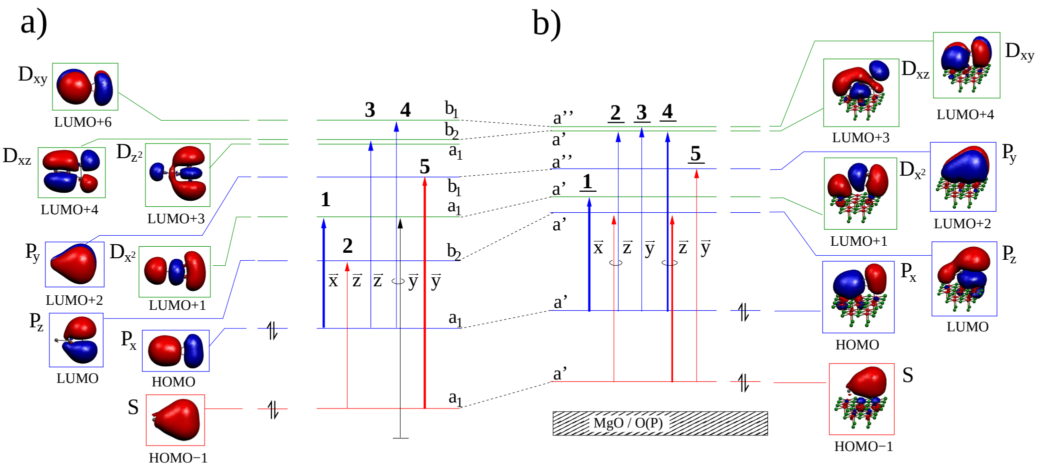

Figure 13.7: MO diagram for a) gas-phase Ag_4 (C_{2v}) and b) $Ag_4@O_{5c}$(**I**) [C_{2v}]. Corresponding orbitals are connected by dashed lines. The frames around the orbitals and the corresponding energy levels are colored in order to illustrate the character of the orbitals (red: S-type, blue: P-type, green: D-type). Leading excitations are indicated by vertical lines from initial to final orbitals (for weights see tables in Figures 11.3 and 13.6) and $\overrightarrow{x}/\overrightarrow{y}/\overrightarrow{z}$ indicate the polarization of the corresponding transitions [**1**-**5** for a) and **1**-**5** for b)].

the S→P_z excitation was leading excitation in transition **2** and P_x→D_{xz} was leading excitation in transition **3**. In contrast, at support, both excitations are resonant and therefore both contribute with different weights to the two transitions **2** and **4** at T_e∼3.5 eV and ∼3.9 eV, respectively (Figure 13.6). This is also illustrated in the MO diagram in Figure 13.7, where each of the gas-phase Ag_4 (C_{2v}) transitions **2** and **3** has only one leading excitation (left), in contrast to $Ag_4@O_{5c}$(**I**) (right) where the two excitations contribute to both transitions **2** and **4**.

(ii) Excitations can be "decoupled" at support, where excitations which were resonant in the gas phase no longer contribute to the same transition. This is found for transition **3** in $Ag_4@O_{5c}$(**I**) which has only one leading excitation (P_x→D_{xy}), in contrast to the gas phase, where also d-electron excitation contributes to the corresponding electronic transition **4** (cf. Figures 11.3 and 13.7).

(iii) Transitions at higher energy which are polarized in parallel to the surface ($\overrightarrow{y}$) experience a considerable red shift of up to ≈0.7 eV (e.g. transitions **3** and **5**).

13.2.3 $Ag_6@O_{5c}$

The spectrum of $Ag_6@O_{5c}$(**I**) (Figure 13.8) exhibits a group of three transitions with low intensities (**1**-**3**) at $T_e\sim3$ eV and one intense transition **4** which is located at $T_e\sim3.4$ eV. Notice that the electronic transitions at lower energies are polarized in parallel to the surface ($\overrightarrow{x}$), in contrast to the most intense transition **4**, which is polarized perpendicularly to the surface ($\overrightarrow{z}$). Interestingly, the latter exhibits the same character, polarization and transition energy as the most intense transition **1** in the corresponding gas-phase Ag_6.

The splitting of the spectrum as compared to the gas-phase spectrum is due to the described reduction of the high D_{3h} symmetry of gas-phase Ag_6 to the C_S symmetry at MgO support which leads to the removal of the degeneracy of the occupied $P_{x/z}$-orbitals (HOMO) and D-orbitals (LUMO+1). Consequently, the excitations which were contributing to very intense transition in gas-phase Ag_6 (cf. Figure 11.4) are no longer resonant at support. The MO diagram can be found in Appendix A (Figure A.2). The information

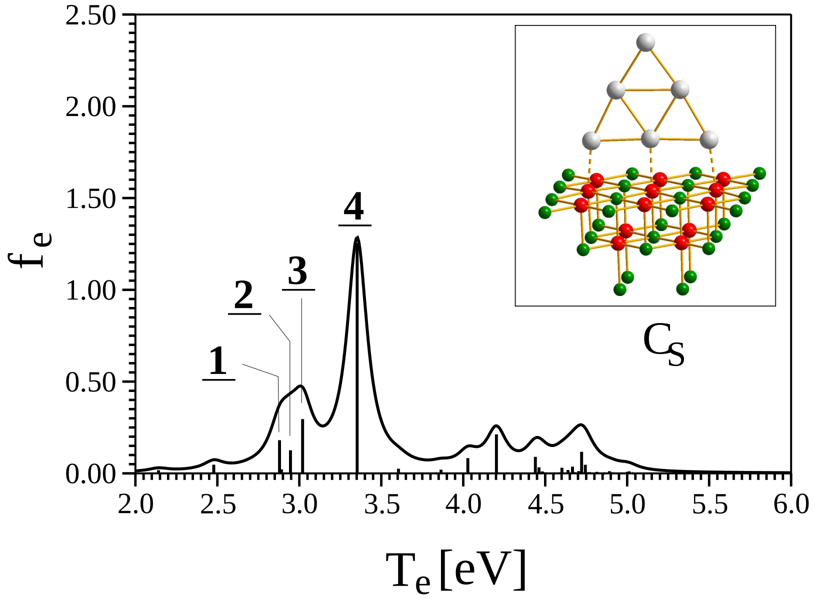

Figure 13.8: Optical spectrum and optimized structure of $Ag_6@O_{5c}$(**I**) [$D_{\infty h}$]. The transition energies, oscillator strengths as well as leading excitations in the labelled transitions (**1**-**4**) together with their weights are given in Table A.3 in Appendix A.

about the leading excitations and their weights in the electronic transitions can be found in Table A.3 in Appendix A.

13.2.4 $\mathrm{Ag_8@O_{5c}}$

The optical spectra for the two lowest-energy structures of $\mathrm{Ag_8@O_{5c}}$ with local C_{2v} and D_{2d} symmetry, respectively, are very similar to the corresponding gas-phase spectra. The optical spectrum of the most stable isomer $\mathrm{Ag_8@O_{5c}}$(**I**) [C_{2v}] (Figure 13.9) is dominated by four intense transitions in the range between 3.2−3.7 eV. Due to the influence of the support the interval of intense transition energies is red-shifted (≈0.3 eV) and narrower ($\Delta T_{e,\underline{\mathbf{1}}-\underline{\mathbf{4}}}$=0.44 eV vs. $\Delta T_{e,\mathbf{1},\mathbf{4}}$=0.73 eV) than in the gas phase (see also Figure 11.5). Analysis reveals that i) the contributing excitations within the cluster are mixed differently at the support than in gas-phase Ag_8, and ii) the excitations contributing to one gas-phase transition contribute to different transitions at the support. However, the electronic transitions at the support are still mixtures of P→D and P→S excitations between cluster orbitals. Thus it can be concluded that the overall character of transitions at support remains preserved with respect to the gas phase.

The absorption spectrum of the second isomer $\mathrm{Ag_8@O_{5c}}$(**II**) [D_{2d}] shows also a small number of intense transitions ($\underline{\mathbf{1}}$-$\underline{\mathbf{3}}$) which are located at T_e∼3.5-3.8 eV (Figure 13.9). Transitions $\underline{\mathbf{1}}$ and $\underline{\mathbf{2}}$ correspond directly to the x- and y-polarized components of the very intense transition **2** from gas-phase Ag_8

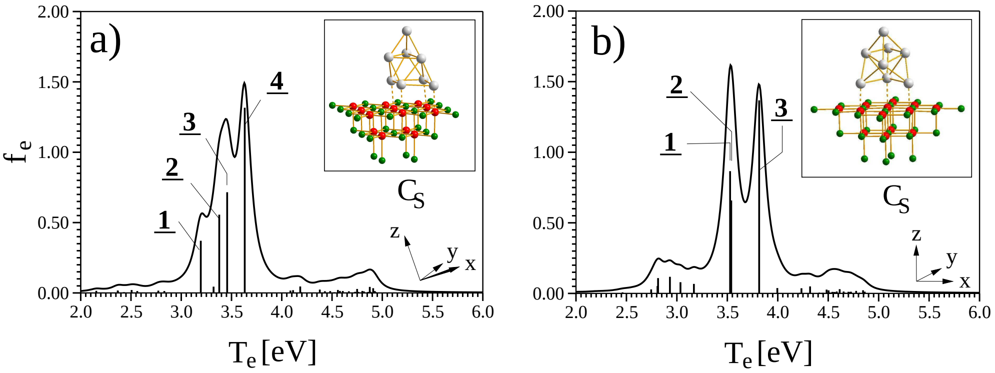

Figure 13.9: Optical spectra and optimized structures of a) $\mathrm{Ag_8@O_{5c}}$(**I**) [C_{2v}] and b) $\mathrm{Ag_8@O_{5c}}$(**II**) [D_{2d}]. The transition energies, oscillator strengths as well as leading excitations in the labelled transitions ($\underline{\mathbf{1}}$-$\underline{\mathbf{4}}$) together with their weights are given in Tables A.4 and A.5.

(D_{2d}). However, these two transitions which are polarized in parallel to the surface are red-shifted by ≈0.5 eV due to the support similar to what has been found for the smaller clusters. On the other hand, the z-polarized transition **3**, which corresponds to the lowest intense transition **1** in the gas phase, is slightly blue-shifted (ΔT_e=0.16 eV). This is due to the contribution of excitation to the D_{z^2} orbital, which is shifted to higher energy more than the other orbitals. This can be derived also from the qualitative MO diagram in Figure A.4. As a result, two absorption bands dominate the optical spectrum of the second isomer at almost the same transition energy as the gas phase, only that the polarization is reversed.

13.3 Emissive Properties

It has been shown that the structural properties as well as the absorption spectra of the silver clusters at the MgO (100) surface are very similar to the gas phase. However, transitions which are polarized in parallel to the surface, can experience considerable red shifts of absorption energies, in particular if they are located at higher transition energies. In contrast, a blue shift has been found for selected z-polarized transitions. Leading excitations in the intense transitions in the gas-phase clusters can be differently mixed at the MgO support ("coupling / decoupling" of excitations). However, the overall character of the electronic transitions remains preserved and is dominated by excitations within the cluster (e.g. P→D) similar to the corresponding gas-phase clusters.

Therefore, also the emissive properties should remain preserved. Indeed, the excited electronic states corresponding to most intense electronic transitions are also bound at surface for individual Ag_n/MgO support species, which has been explicitly demonstrated using a cluster-embedding model with a non-polarizable classical environment employing the non-hybrid PBE functional [212]. Notice that this simpler model gives qualitatively very similar characters of the excited electronic states. However, a sophisticated cluster-embedding scheme including a polarizable environment is necessary for calculating accurate absorption energies.

The excited electronic states of the Ag_n@O_{5c} clusters corresponding to the most intense transitions exhibit close-lying local minima and thus the fluorescence energy is only slightly red-shifted by <0.2 eV with respect to the absorption energy [212]. By applying this finding to the accurate absorption energies of the lowest intense transitions for silver clusters at the surface the possible fluorescence energies given in Table 13.1 can be estimated.

Table 13.1: Absorption lines ($T_{e,abs}$ in eV) and possible fluorescence lines ($T'_{e,emiss}$ in eV) in the Ag_n clusters (n=2, 4, 6, 8) supported at the defect-free MgO (100) surface.

Species	Excited State	$T_{e,abs}$ [eV]	$T'_{e,emiss}$ [eV]
$Ag_2@O_{5c}$(**I**)	$\underline{\mathbf{1}}$	3.22	≈3.0
$Ag_4@O_{5c}$(**I**)	$\underline{\mathbf{1}}$	2.60	≈2.4
$Ag_4@O_{5c}$(**II**)	$\underline{\mathbf{1}}$	2.77	≈2.6
$Ag_6@O_{5c}$(**I**)	$\underline{\mathbf{4}}$	3.35	≈3.2
$Ag_8@O_{5c}$(**I**)	$\underline{\mathbf{1}}$-$\underline{\mathbf{4}}$	3.2 - 3.6	≈3.0 - 3.4
$Ag_8@O_{5c}$(**II**)	$\underline{\mathbf{1}}$-$\underline{\mathbf{3}}$	3.5 - 3.8	≈3.3 - 3.6

It can be concluded that the silver clusters at the defect-free MgO (100) surface most likely fluoresce between T_e∼2.4 eV (Ag_4) and T_e∼3.6 eV (Ag_8). Consequently, from the small silver clusters supported at the MgO surface only Ag_4 should exhibit a possible fluorescence line in the visible regime.

Chapter 14

Silver Clusters at the $\mathbf{F_S}$ Center Defect $[\mathbf{Ag_{n=2,4,6,8}@F_{5c}}]$

14.1 Structural Properties

The most stable structures of the silver clusters supported at the F_S center defect ($Ag_n@F_{5c}$, n=2, 4, 6, 8) are shown in Figure 14.1. Before the most stable isomers of the specific cluster / F_S center species will be presented, first the general findings on the binding to the F_{5c} site will be discussed which is common for all silver clusters in this study.

The binding energies of the silver clusters to the F_S center are given in Figure 13.2. Ag_2 is bound by 2.4 eV and larger clusters are bound even stronger. Thus the Ag_n clusters bind considerably stronger to the F_{5c} site than to the defect-free MgO surface. Since the binding energy increases only slightly with the cluster size, the binding energy per Ag atom is decreasing. Moreover, binding to the F_S center is accompanied by a charge transfer of almost one electron from the F_S center defect to the Ag_n clusters ($\Delta q \approx 0.7$-$0.9\ e^-$). The charge transfer is also expressed in very low ionization potentials for $Ag_n@F_{5c}$ clusters compared to the neutral gas-phase Ag_n clusters (Figure 13.3). As can be seen, the IPs do not correlate well with the IPs of the neutral gas-phase clusters, which is most pronounced for the silver dimer. However, as a function of the number of silver atoms the IPs show similar behavior as the VDEs of the corresponding anionic gas-phase Ag_n^- clusters. These are only shifted to higher energies at the F_S center support by ~2.7 eV. This is due to the fact that the detachment of an electron from the $Ag_n@F_{5c}$ clusters requires additional energy which corresponds approximately to the MgO work function (Φ_{MgO}=2.7 eV [217]).

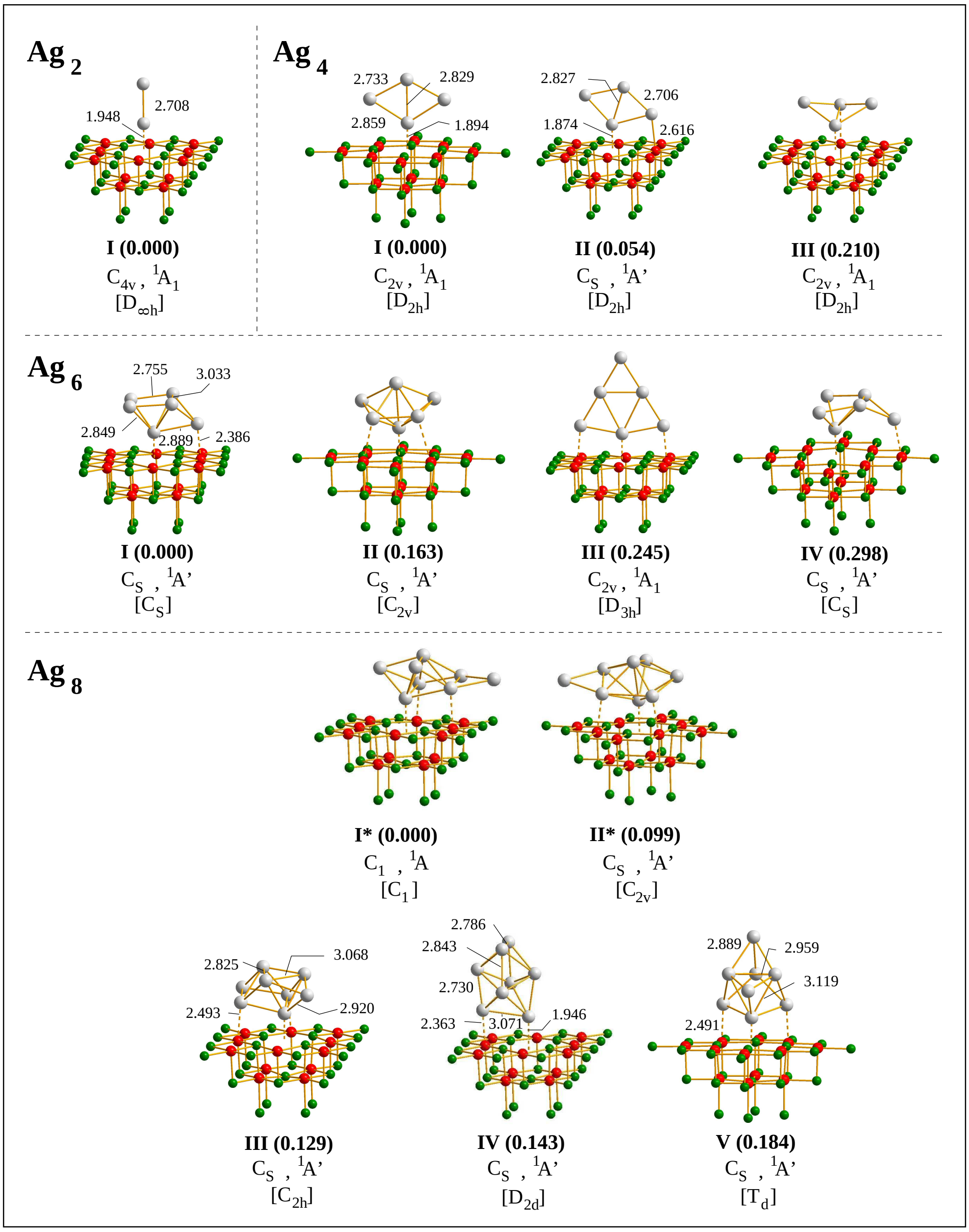

Figure 14.1: Lowest-energy isomers of Ag_n clusters (n=2, 4, 6, 8) supported at the F_S center defect (F_{5c}). Isomers are labelled with **I-V**. Relative energies in eV and spatial symmetry and symmetry of the electronic ground state are given. In square brackets, the local symmetry of the supported silver cluster is also shown. Bond lengths in Å are given for the most stable structures of $Ag_{2,4,6}@F_{5c}$ and for the energetically degenerated isomers **III-V** of $Ag_8@F_{5c}$. For details concerning isomers **I** and **II** of $Ag_8@F_{5c}$ marked with an asterisk see text.

Ag_2@F_{5c} In the most stable isomer **I** of Ag_2@F_{5c}, the Ag_2 assumes an upright geometry and is bound directly at the F_{5c} defect site. The Ag-Ag bond is significantly elongated (2.708 Å vs. 2.601 Å) due to the charge transfer towards the dimer. Moreover, the silver dimer is bound closer to the top surface layer than to the perfect MgO surface thus penetrating the defect site ($\mathbf{r}_{\mathrm{Ag_2-surf}}\approx 1.95$ Å).

Ag_4@F_{5c} In the case of the Ag_4@F_{5c} system, two isomers are almost energetically degenerated (ΔE=0.054 eV). In both isomers, the silver subunits assume the rhombic D_{2h} symmetric geometry. In the most stable isomer **I** (C_{2v}, $^1A_1$) the Ag_4 subunit is symmetrically bound to the F_{5c} site. In contrast, in the second isomer **II** (C_S, $^1A'$) it is tilted so that one silver atom of the Ag_4 subunit interacts with an O atom near the defect site. In both isomers a considerable charge transfer occurs ($\Delta q \sim 0.8$ e^-) which leads to slightly elongated bonds with respect to the gas-phase geometry.

Ag_6@F_{5c} The most stable structure of Ag_6@F_{5c} (**I**, C_S, $^1A'$) contains a three-dimensional Ag_6 subunit with a face-capped square pyramidal geometry. The tip of the pyramid is pointing towards the defect site and the face-capping atom is coordinated to a neighboring O atom. As in the case of the silver dimer and tetramer, the Ag_6 moiety is negatively charged (q=0.77 e^-) due to the charge transfer from the F_S center. In this context, it is interesting to note that the transition from a two-dimensional (2D) to a three-dimensional (3D) structure occurs at a cluster size of six Ag atoms at the F center support. This is indeed similar to the gas-phase Ag_6 in neutral and anionic charge state. In the case of the neutral Ag_6 gas-phase cluster, the most stable 2D isomer is well separated from 3D structures (pentagonal pyramid: ΔE=0.316 eV; distorted octahedron: ΔE=1.258 eV). In contrast, in the anionic charge state, 2D and 3D structures are almost energetically degenerated (see also Chapter 7). Therefore, it is not surprising that the charge transfer at the F_S center leads to a 3D structure for the Ag_6 subunit, and that the most stable 2D structure is found at a higher energy (ΔE=0.245 eV, isomer **III**).

Ag_8@F_{5c} Figure 14.1 shows the lowest-energy isomers of Ag_8@F_{5c}. The two most stable isomers **I*** (C_1, ^1A) and **II*** (C_S, $^1A'$, ΔE=0.060 eV) have a similar local geometry which is close to a capped pentagonal pyramidal structure. However, in both isomers one Ag atom is located outside the QM part of the surface model which means that it does not interact with quantum-mechanically described surface atoms. Consequently, the model used in this study is most likely not adequate for these two isomers and a larger QM area might be necessary for proper description. Therefore, at this point, the two isomers will be only briefly discussed, and focus will be put on the next isomers.

The next three isomers of Ag_8@F_{5c} (**III**-**V**) are very close in energy, all lying within 0.055 eV. Isomer **III** contains an Ag_8 subunit with C_{2h} symmetry and symmetry of the cluster-support species is C_S. The silver subunits in the next two isomers correspond to the D_{2d} (isomer **IV**) and T_d (isomer **V**) symmetric structures known from the gas phase. However, due to the support the symmetry is reduced to C_S. In both isomers, one silver atom binds directly to the F_{5c} defect site and one and two Ag atoms, respectively, bind to nearby O atoms of the surface. This leads to an upright geometry in the D_{2d} isomer **IV** and a tilted geometry in case of the T_d isomer **V**.

A considerable charge transfer has been found for all species (e.g. for Ag_8@F_{5c}(**I**): $\Delta q \sim 0.8$ e^-) which is connected with a high binding energy (BE(**I**)=3.173 eV).

14.2 Electronic Structure

For the small silver clusters supported at the F_S center defect, large binding energies in conjunction with a considerable charge transfer from the defect site to the clusters have been found. This is a consequence of the orbital mixing between cluster and F_S center orbitals of appropriate symmetry and energy. In contrast to the defect-free MgO surface, at the F_S center this mixing significantly modifies the electronic structure of the clusters. In order to fully understand the influence of the F_S center support, a characterization of the orbitals which are involved in the leading excitations of electronic transitions is mandatory.

In the small silver clusters, the S-type orbital of the F_S center and the silver-cluster P_z orbital have the appropriate symmetry and energy for a favorable linear combination. This leads to the formation of a binding orbital P_z+F_S(S) $\equiv$ P'_z with P-type character and an anti-bonding combination P_z-F_S(S) $\equiv$ D' of D-type character. Both are oriented along the z-axis which is perpendicular to the surface. This favorable orbital interaction is illustrated in Figure 14.2 (red lines) on the example of Ag_4 (D_{2h}) interacting with the F_S center defect. In contrast, the energy mismatch between the $P_{x/y}$ orbitals of the cluster and the F($P_{x/y}$) orbitals of the F_S center does not lead to a strong stabilization of the cluster $P_{x/y}$ orbitals (blue lines in Figure 14.2). The orbitals which are not involved in the pronounced orbital mixing are affected in a similar way as at the defect-free MgO surface: Their shapesand

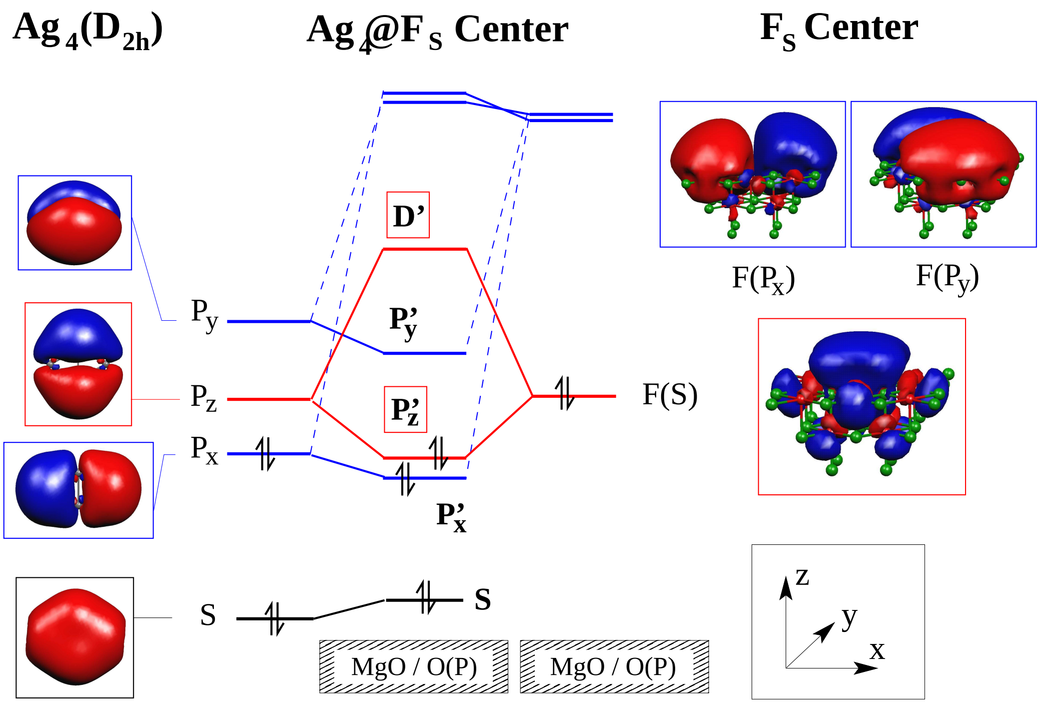

Figure 14.2: Qualitative MO diagram showing the interaction of silver-cluster orbitals (here exemplary for Ag_4 on the left) with F_S center orbitals (right). Linear combination of cluster P_z and F_S center F(S) orbitals (red lines) lead to the new orbitals P'_z and D' which are unique to the cluster / F_S center support system. Cluster $P_{x/y}$ orbitals in parallel to the surface (blue) are only slightly stabilized due to the energy mismatch.

relative energetic orders basically remain preserved as compared to the gas phase, and the total energy of the orbitals is shifted to higher energies merely due to the support (see Chapter 13.2). The valence orbitals are filled with n electrons from the Ag_n cluster and two electrons from the F_S center.

In summary, as a consequence of the linear combination of cluster and F_S center orbitals of proper symmetry and energy, new orbitals are formed which are neither characteristic for the cluster nor the F_S center alone. These unique orbitals are involved in the leading excitations of the intense electronic transitions and therefore alter the spectral features compared to the gas phase. This will be discussed in the next chapter for the different cluster sizes.

14.3 Optical Properties

14.3.1 Ag_2@F_{5c}

Figure 14.3 shows the optical spectrum of Ag_2@F_{5c}(**I**). The spectrum is dominated by two intense transitions at T_e~3.0 eV and T_e~4.5 eV. Although the transition at lower energy appears at almost the same transition energy as in the gas-phase silver dimer, the character has completely changed due to contribution of the F_S center electrons. The MO diagram (Figure 14.4) clearly shows that the transition is now of P→D character with the leading excitation $P'_z \rightarrow D'$. Notice that the intensity is large due to the excitation from the P'_z orbital. This orbital has a contribution from the F_S center electrons and thus this transition is unique to the supported cluster. The second intense transition <u>**2**</u> [T_e=4.44 eV (f_e=1.00)] is very similar to the corresponding transition **2** in the gas-phase Ag_2 (see Figure 11.2) and is only red-shifted by ≈0.3 eV. Notice that this transition gained intensity due to the contribution of an excitation from the P'_z orbital.

It should be noted that the overall sum of oscillator strengths below 5 eV is increased by more than 0.5 compared to the gas-phase Ag_2 which is due to the contribution of the F_S center electrons in the electronic transitions.

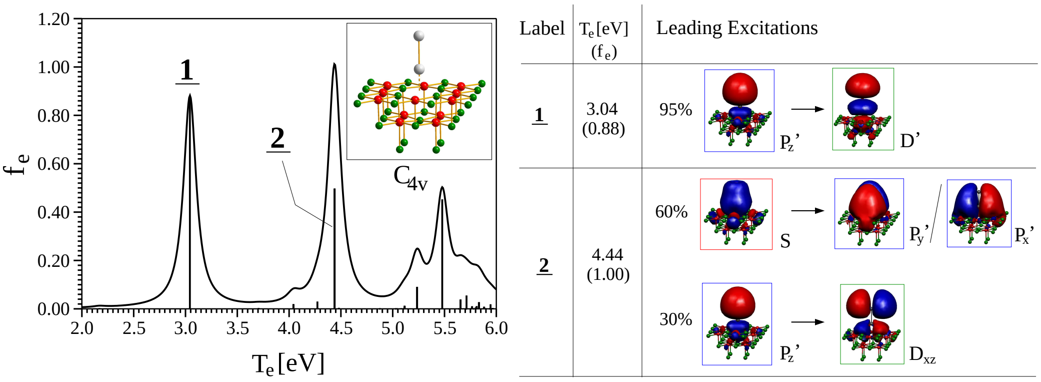

Figure 14.3: Optical spectrum and optimized structure of Ag_2@F_{5c}(**I**) [$D_{\infty h}$]. The table shows the transition energies T_e in eV, the oscillator strengths f_e and the leading excitations in the labelled transitions (<u>**1**</u>, <u>**2**</u>) together with their weights.

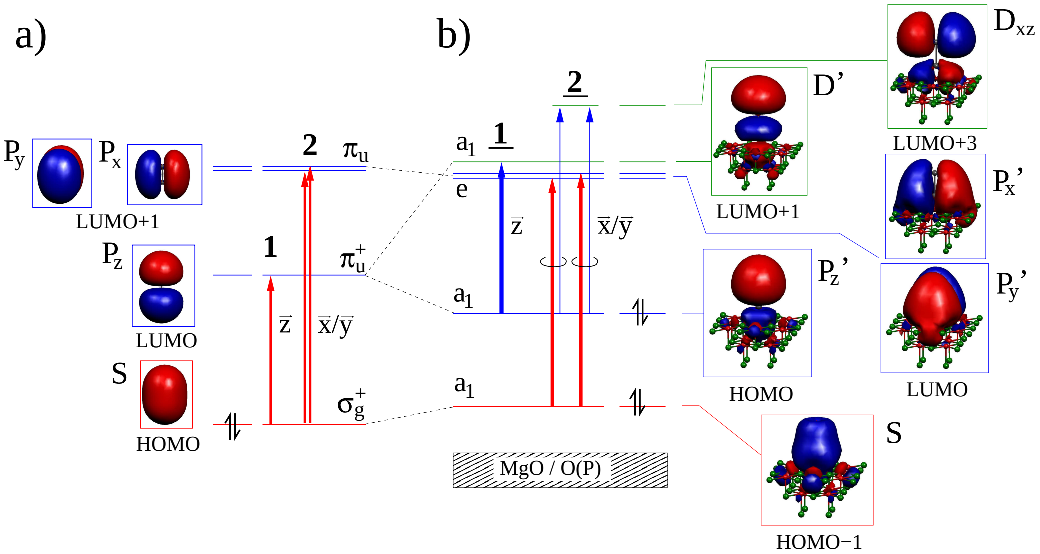

Figure 14.4: MO diagram for a) gas-phase Ag_2 ($D_{\infty h}$) and b) $Ag_2@F_{5c}(\mathbf{I})$ [$D_{\infty h}$]. Corresponding orbitals are connected by dashed lines. The frames around the orbitals and the corresponding energy levels are colored in order to illustrate the character of the orbitals (red: S-type, blue: P-type, green: D-type). Leading excitations are indicated by vertical lines from initial to final orbitals (for weights see tables in Figures 11.2 and 14.3) and $\overrightarrow{x}/\overrightarrow{y}/\overrightarrow{z}$ indicate the polarization of the corresponding transitions [**1**, **2** for a) and $\underline{\mathbf{1}}$, $\underline{\mathbf{2}}$ for b)].

14.3.2 $Ag_4@F_{5c}$

The first two isomers of $Ag_4@F_{5c}$ both have similar optical spectra due to the same symmetry of the Ag_4 subunit (D_{2h}). Therefore, only the most stable isomer will be discussed in detail.

The spectrum of $Ag_4@F_{5c}(\mathbf{I})$ [D_{2h}] is shown in Figure 14.5. It consists of three moderately intense transitions between 2.4 and 3.0 eV ($\underline{\mathbf{1}}$-$\underline{\mathbf{3}}$) and two very intense transitions at ∼3.5 eV ($\underline{\mathbf{4}}$, $\underline{\mathbf{5}}$). Thus it is significantly different from the gas-phase spectrum (cf. Figure 11.3). From the analysis of the contributing excitations in the electronic transitions, the presence of excitations within the cluster can be identified, e.g. $P'_x \rightarrow D_{x^2}$ in $\underline{\mathbf{1}}$ or $P'_x \rightarrow D_{xz}$ in $\underline{\mathbf{5}}$ (Table in Figure 14.5).

However, due to the mixing of cluster and F_S center orbitals and the formation of the unique P'_z and D' molecular orbitals, new excitations arise. For example, excitations from the cluster P orbitals to the newly formed D' orbital can be found in the transitions $\underline{\mathbf{1}}$ and $\underline{\mathbf{2}}$, which were not present in the gas phase.

Moreover, excitation from the unique P'_z orbital into D orbitals con-

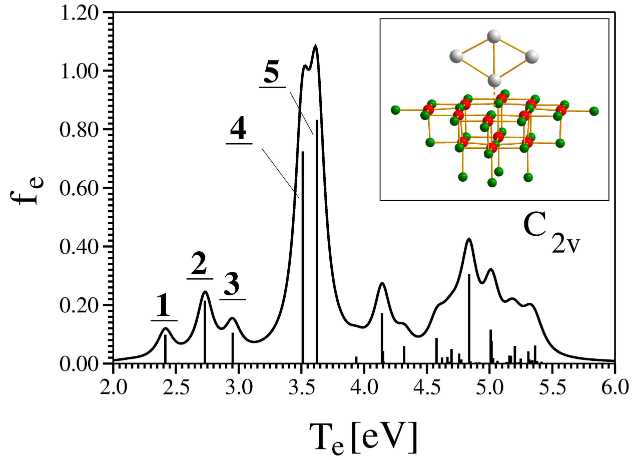

Label	T_e [eV] (f_e)	Leading Excitations
1	2.41 (0.10)	67% 19% 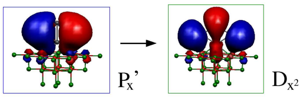 P_x' → D_{x^2} 28% 68% 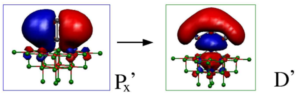 P_x' → D'
2	2.73 (0.21)	<1% 13% 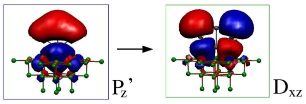 P_z' → D_{xz}
3	2.95 (0.11)	66% 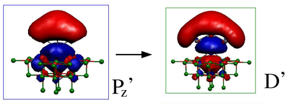 P_z' → D' 32% 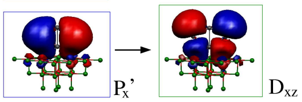 P_x' → D_{xz}
4	3.51 (0.72)	95% 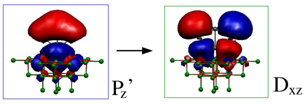 P_z' → D_{xz}
5	3.62 (0.83)	60% 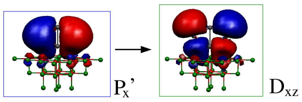 P_x' → D_{xz} 25% 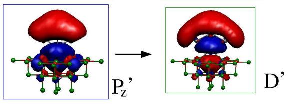 P_z' → D'

Figure 14.5: Optical spectrum and optimized structure of $Ag_4@F_{5c}(\mathbf{I})$ $[D_{2h}]$. The table shows the transition energies T_e in eV, the oscillator strengths f_e and the leading excitations in the transitions labelled with **1**-**5** together with their weights. In the case where the same leading excitations with different weights are involved in two transitions, e.g. **1** and **2**, the contributing excitations are shown only once, and weights in corresponding transitions are separated by horizontal dashed lines.

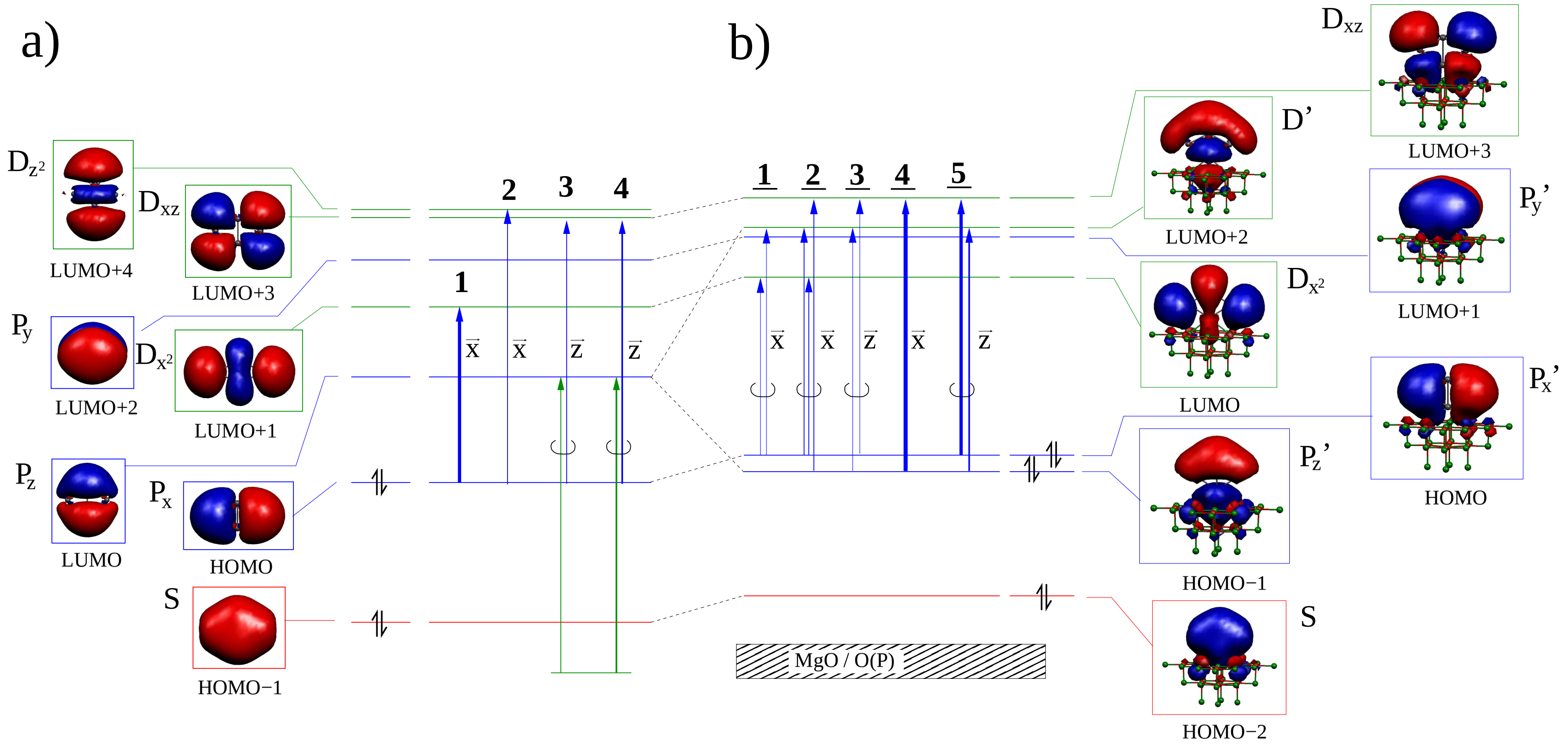

Figure 14.6: MO diagram for a) gas-phase Ag_4 (D_{2h}) and b) Ag_4@F_{5c}(**I**) [D_{2h}]. Corresponding orbitals are connected by dashed lines. The frames around the orbitals and the corresponding energy levels are colored in order to illustrate the character of the orbitals (red: S-type, blue: P-type, green: D-type). Leading excitations are indicated by vertical lines from initial to final orbitals (for weights see tables in Figures 11.3 and 14.5) and $\overrightarrow{x}/\overrightarrow{y}/\overrightarrow{z}$ indicate the polarization of the corresponding transitions [**1-5** for a) and $\underline{\mathbf{1}}$-$\underline{\mathbf{6}}$ for b)].

tributes to all transitions **1**-**5** (see Figure 14.5). Interestingly, this lowers the intensity of transitions at lower energy, in contrast to transitions at higher energy ($T_e \sim$ 3.5 eV) which gain intensity. For example, the most intense transition **1** in the gas-phase Ag_4 (D_{2h}) was mainly of $P_x \rightarrow D_{x^2}$ character with high intensity (f_e=0.85). However, at the F_S center the intensity drops to only f_e=0.10 because it mixes with the excitation from the P'_z orbital. On the other hand, the electronic transition **5** has increased intensity (f_e=0.83) as compared to the corresponding gas-phase transitions **3** and **4** ($f_e \approx 0.3$). Indeed, this is because the leading excitation $P_x \rightarrow D_{xz}$ within the cluster mixes with the excitation from the P'_z orbital ($P'_z \rightarrow D'$).

This orbital interaction is also illustrated in the MO diagram of $Ag_4@F_{5c}$(**I**) [D_{2h}] in Figure 14.6. Clearly, the linear combination of the cluster P_z orbital and the S-type orbital from the F_S center can be seen, while all other orbitals are shifted merely by the influence of the surface.

In summary, the optical spectrum for $Ag_4@F_{5c}$(**I**) is strongly influenced by the support. This is due to the mixing of leading excitations within the cluster with excitations from the unique P'_z orbital. This leads to transitions with low intensity at lower energy ($T_e \sim$2.4-2.9 eV) and intense transitions at higher energy ($T_e \sim$3.5 eV).

14.3.3 $Ag_6@F_{5c}$

Since in the most stable isomer of the $Ag_6@F_{5c}$ the cluster subunit assumes a 3D geometry in contrast to the high symmetric planar gas-phase Ag_6 cluster, the absorption spectrum for the corresponding non-optimized bare Ag_6 subunit has been calculated without the support. This will serve to analyze the influence of the electronic interaction with the F_S center on the absorption properties.

The absorption spectra for both the $Ag_6@F_{5c}$(**I**) and the corresponding structure of the bare cluster Ag_6 [C_S] are shown in Figure 14.7a) and b), respectively. The spectrum of the supported cluster consists of two parts. Part one (labelled with **A**) has several transitions with low intensity between $T_e \sim$2.5-3.2 eV. Exemplary, the leading excitations in the electronic transitions **1**-**4** are shown in Table A.6 in Appendix A. The higher energy part of the spectrum (labelled with **B**) is dominated by a number of moderately intense transitions (**5**-**9**) resulting in a narrow and very intense absorption band at $T_e \sim$3.5-3.9 eV. The leading excitations for these transitions can also be found in Table A.6 in Appendix A.

The optical spectrum of the corresponding 3D bare cluster is presented in Figure 14.7b), and an analysis of transitions in terms of leading excitations

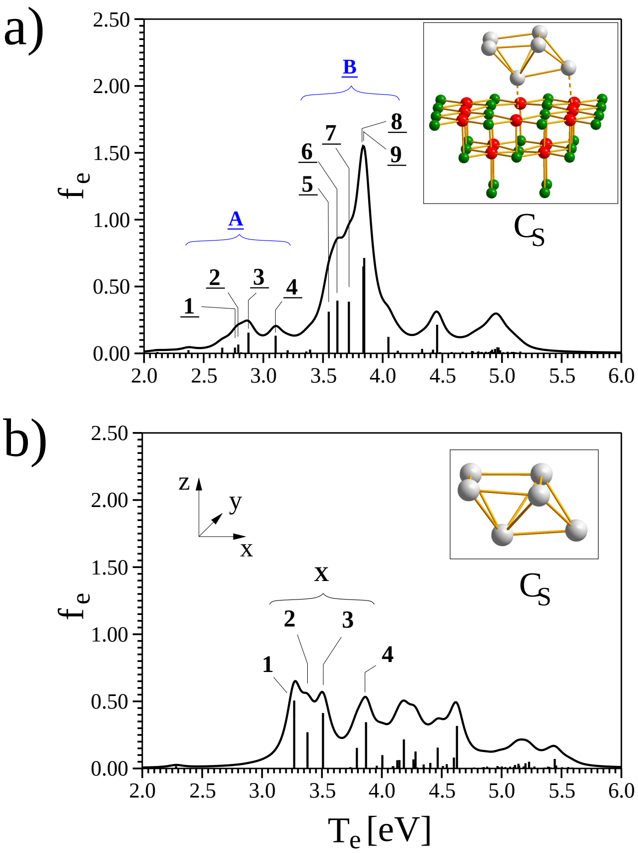

c)

Label	T_e [eV] (f_e)	Leading Excitations		
1	3.27 (0.51)	46%	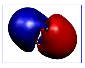 P_x	→ 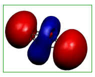 D_{x^2}
		27%	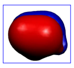 P_y	→ 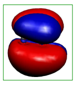 D_{yz}
2	3.38 (0.27)	44%	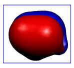 P_y	→ 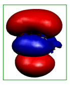 D
		33%	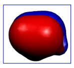 P_y	→ 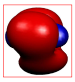 2S
3	3.51 (0.41)	52%	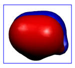 P_y	→ 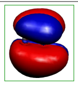 D_{yz}
		18%	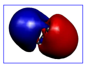 P_x	→ 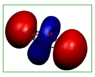 D_{x^2}
4	3.87 (0.34)	33%	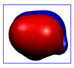 P_y	→ 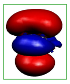 D
		26%	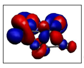 d−e$^-$	→ 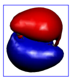 P_z

Figure 14.7: Optical spectra and optimized structures of a) Ag$_6$@F$_{5c}$(**I**) [C$_S$] and b) corresponding bare cluster in the same geometry as at the support [Ag$_6$ (C$_S$)]. c) Table corresponding to spectrum (b) is also given with transition energies T$_e$ in eV, oscillator strengths f$_e$ and leading excitations in the labelled transitions (**1**-**4**) together with their weights. The excitations which contribute to electronic transitions **1**-**9** in (a) can be found in Appendix A (Table A.6). For details concerning labels A, B and X see text.

is shown in part c) of the same figure. The Ag_6 (C_S) structure shows a very broad absorption band between T_e~3.2-4.0 eV, which is dominated by only a few moderately intense transitions **1-4**. In contrast, the higher energy part (T_e~4.0-4.7 eV) consists of many transitions with low intensity. An analysis of the transitions at lower energy shows that the transitions **1-4** are mainly of P→D character with a partial contribution of P→S (transition **2**) or d-electron excitations (transition **4**) (see Figure 14.7c). Notice that the character of the contributing orbitals is different as compared to the most stable gas-phase isomer [$Ag_6(D_{3h})$] due to the 3D structure. Therefore, the influence of the geometry on the optical spectrum of Ag_6 is very pronounced.

Now, the influence of the F_S center support can be examined by comparing leading excitations in both the bare Ag_6 subunit and the Ag_6@F_{5c} cluster-support species. First, notice that the orbital mixing between the P_z cluster orbital and the F_S center S-type orbital, which has been discussed above, leads to the new occupied orbital P'_z and the new unoccupied orbital D'. As a result, in addition to excitations "purely" within the cluster, also excitations to the D' orbital and excitations from the P'_z orbital arise, which are unique to the supported Ag_6 cluster. This orbital mixing which is typical for the F_S center support is illustrated in the corresponding MO diagram given in Appendix A (Figure A.5). It can be clearly seen that the cluster P_z orbital mixes with the F_S center orbital and that all other cluster orbitals are only slightly influenced by the support.

Consequently, apart from the geometrical rearrangement induced by the charge transfer from the F_S center towards the cluster, two effects on the optical properties can be identified :

1) "Decoupling": Leading excitations which were contributing to one transition in the bare cluster contribute to different transitions at the support (they are "decoupled"). For example, in the gas phase two leading excitations can be identified in transition **1**: $P_x \rightarrow D_{x^2}$ and $P_y \rightarrow D_{yz}$ (Figure 14.7c). At the F_S center support, both contribute to different transitions: The $P'_x \rightarrow D_{x^2}$ excitation now contributes to transitions $\underline{\mathbf{1}}$ and $\underline{\mathbf{3}}$, in contrast to the $P'_y \rightarrow D_{yz}$ excitation which contributes to transitions $\underline{\mathbf{2}}$, $\underline{\mathbf{4}}$, $\underline{\mathbf{8}}$ and $\underline{\mathbf{9}}$.

2) "Interference": The excitations from the unique P'_z orbital to D orbitals contribute to all presented transitions $\underline{\mathbf{1}}$-$\underline{\mathbf{9}}$. These unique excitations mix with the leading excitations within the cluster, leading to an absorption interval with low intensity (T_e~2.8 eV, $\underline{\mathbf{A}}$, "destructive interference") and one with increased intensity at higher energy (T_e~3.7 eV, $\underline{\mathbf{B}}$, "constructive interference"). Therefore, these two absorption intervals $\underline{\mathbf{A}}$ and $\underline{\mathbf{B}}$ are the result of the orbital interaction with the F_S center and can be rationalized as a splitting of the absorption band **X** in the bare Ag_6 (C_S) structure (compare

Figures 14.7a and b).

In summary, the absorption properties of Ag_6 at the F_S center support are influenced by two effects: First, as a consequence of the charge transfer from the F_S center towards the silver cluster, the most stable isomer assumes a compact 3D structure. This leads to a split spectrum which has moderately intense transitions at the same energy (T_e~3.4 eV) as the corresponding intense transition in the most stable gas-phase structure of Ag_6. The second effect arises from mixing cluster and F_S center orbitals, which leads to the emergence of excitations which are unique to the cluster-support species. These excitations (mainly from the P'_z orbital) mix with the leading excitations for transitions within the cluster, which leads to a group of low intense transitions at lower energy (T_e~2.8 eV) due to "destructive interference" and a group of intense transitions at higher energy (T_e~3.7 eV) which is similar to the effect of "constructive interference".

14.3.4 $Ag_8@F_{5c}$

It has been mentioned earlier that the surface model used in this study is most likely inadequate for large silver clusters which extend beyond the QM part of the system (Chapter 14.1). Therefore, the optical properties of the two most stable isomers **I** and **II** of $Ag_8@F_{5c}$ will be only shortly discussed. The absorption spectra as well as the molecular orbitals are shown in Figure 14.8. Both spectra are similar and have a broad absorption between 2.5 and 5 eV with many transitions with low and moderate intensity. Notice that the orbitals of both isomers have very similar shapes and energies. However, it is not possible to classify the character of the orbitals into S-type, P-type and so on just by counting the number of nodal planes. Furthermore, comparison with the gas-phase spectrum is not possible since without the support the Ag_8 subunits exhibit structures close to the degeneracy point which cannot be described by TD-DFT.

The silver subunit of the third isomer $Ag_8@F_{5c}$(**III**) assumes a structure with the C_{2h} symmetry. The absorption spectrum shown in Figure 14.9 exhibits a single moderately intense transition at T_e~2.66 eV ($\underline{\mathbf{1}}$) and a broad absorption band of nearly constant intensity between 3 and 5 eV. This band originates from several moderately intense transitions which are labelled with $\underline{\mathbf{2}}$-$\underline{\mathbf{8}}$. The detailed composition of the electronic transitions into contributing leading excitations can be found in Appendix A (Table A.7). The MO pictures can also be found in Appendix A (Figure A.6). The corresponding gas-phase isomer in C_{2h} symmetry does not exist and therefore, the effect of the geometrical distortion and the influence of the orbital mixing at the

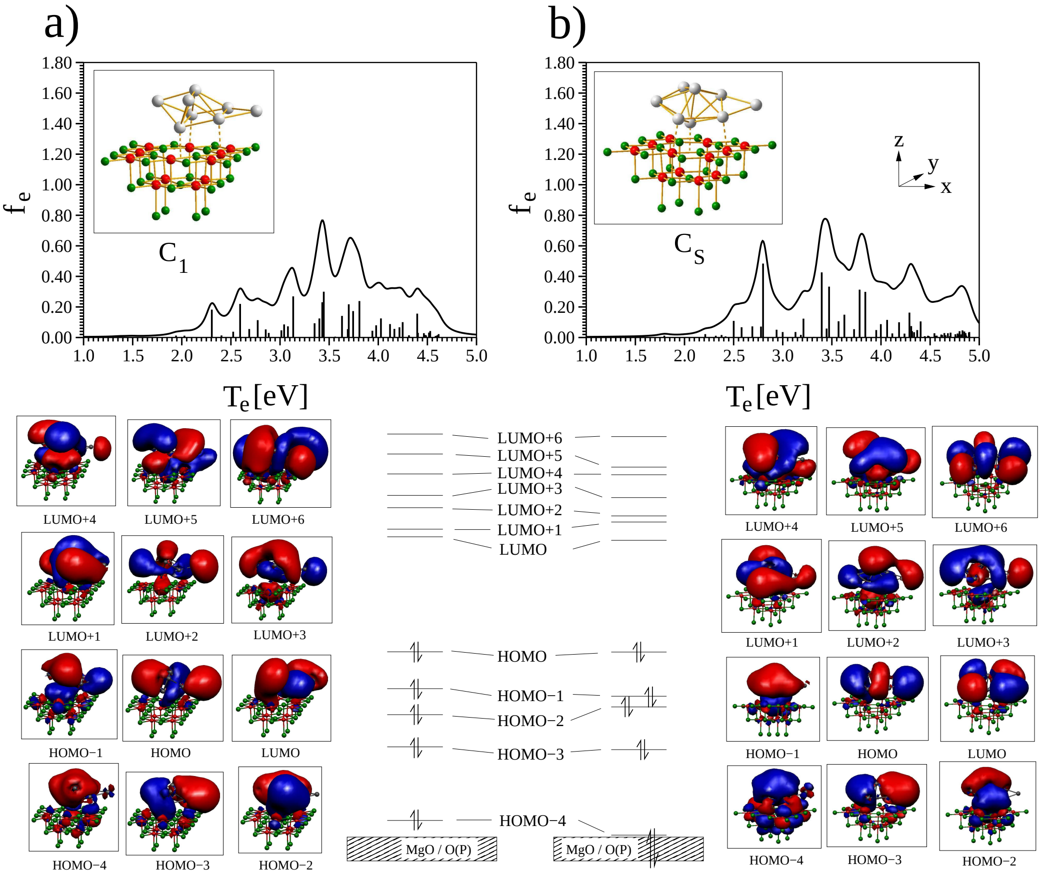

Figure 14.8: top: Optical spectra and optimized structures of a) Ag_8@F_{5c}(**I**) [C_1] and b) Ag_8@F_{5c}(**II**) [C_S]. bottom: The molecular orbitals are shown for both isomers. For details see text.

F_S center support cannot be distinguished. However, on the basis of the detailed analysis in combination with findings from smaller clusters the following conclusion on the influence of the F_S center support can be drawn:

1) Geometrical distortion from the highly symmetric gas-phase Ag_8 leads to the removal of the orbital degeneracy which, in general, is responsible for the split spectrum, which has been demonstrated before on the example of the smaller silver clusters. Furthermore, due to the geometrical rearrangement the P_z orbital is unoccupied and the D_{x^2} orbital becomes the HOMO.

2) The orbital mixing of cluster and F_S center orbitals leads to the formation of the unique occupied P'_z and unoccupied D' orbitals as has been discussed in detail before. Consequently, in the cluster-support species the S-type orbital, the three P-type orbitals ($P'_{x/y}$, P'_z) and the D_{x^2} orbital (HOMO) are doubly occupied by the ten valence electrons. The fact that the HOMO

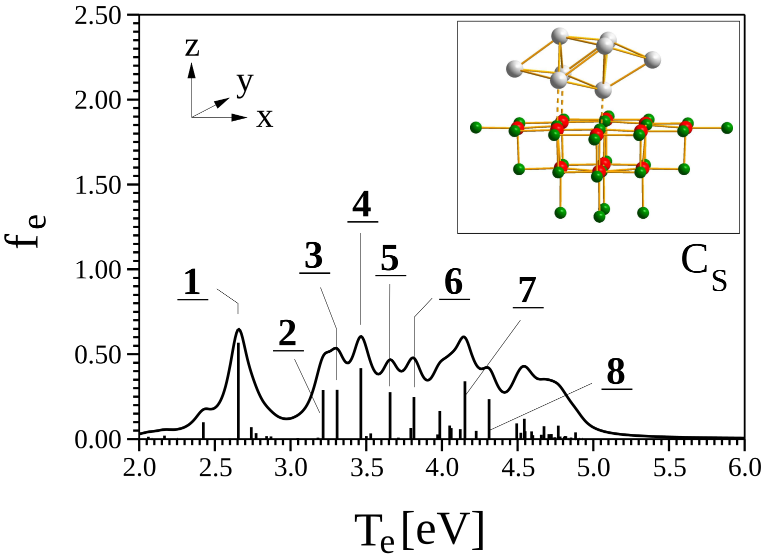

Figure 14.9: Optical spectrum and optimized structure of Ag$_8$@F$_{5c}$(**III**) [C$_{2h}$]. The table with transition energies, oscillator strengths f_e and leading excitations in the labelled transitions (**1**-**8**) together with their weights is given in Table A.7 in Appendix A.

has D-type character has direct consequences for the character of the electronic transitions and consequently optically allowed D→F excitations contribute to all labelled transitions **1**-**8**.

(3) Transitions within the cluster are mixed with contributions of excitations from the P'_z orbital (**1**, **3**-**5**, **7**-**8**) as has been shown for smaller silver clusters already.

Similar to the spectrum of Ag$_8$@F$_{5c}$(**III**) [C$_{2h}$], the absorption spectra of both Ag$_8$@F$_{5c}$(**IV**) [D$_{2d}$] and Ag$_8$@F$_{5c}$(**V**) [T$_d$] exhibit broad absorption bands between T_e~2.5-5.0 eV which mainly consist of many low intense transitions (Figure 14.10). However, in contrast to Ag$_8$@F$_{5c}$(**III**) [C$_{2h}$], there is a small number of intense transitions (**2**-**4** and **4**-**5** for isomers **IV** and **V**, respectively). By comparing with the corresponding gas-phase spectra the influence of the F center on the optical properties can be demonstrated, which will be done for both isomers separately.

Ag$_8$@F$_{5c}$(IV) [D$_{2d}$]: Due to the fact that the symmetry of the Ag$_8$ subunit at the F_S center is close to the gas-phase Ag$_8$ (D$_{2d}$) structure, the influence of the geometry distortion will be small and thus orbital interaction

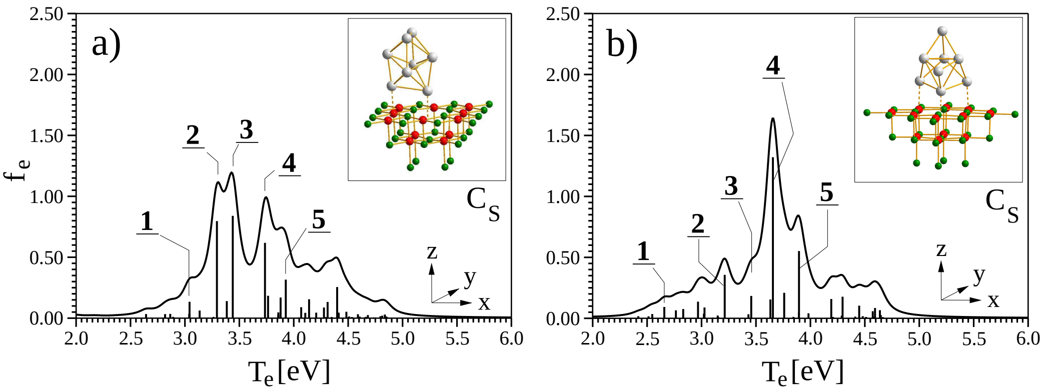

Figure 14.10: Optical spectra and optimized structures of a) $Ag_8@F_{5c}$(**IV**) [D_{2d}] and b) $Ag_8@F_{5c}$(**V**) [T_d]. The tables with transition energies T_e, oscillator strengths f_e and leading excitations in the labelled transitions (**1**-**5**) together with their weights are given in Tables A.8 and A.9 in Appendix A.

with the F_S center will be the main factor responsible for the different optical spectrum compared to the gas phase. Notice that in the case of $Ag_8@F_{5c}$(**IV**) [D_{2d}], the typical mixing of the cluster P_z orbital with the S-type orbital of the F_S center does not contribute to the net-chemical bonding due to the fact that both orbitals are doubly occupied (cf. Figure A.7 in Appendix A). However, in the corresponding bare cluster Ag_8 (D_{2d}) also the D_{z^2} orbital has proper symmetry *and* energy and thus it is also involved in the orbital interaction. Therefore, due to interaction of the cluster P_z and D_{z^2} orbitals with the F_S center S-type orbital, three molecular orbitals are formed: a bonding P'_z orbital (occupied), a non-bonding D' orbital (occupied) and an anti-bonding F' orbital (unoccupied) which is oriented perpendicularly to the surface (cf. Figure A.7 in Appendix A). As a consequence, excitations which can occur from the P'_z orbital are similar to excitations from the P_z orbital in the gas-phase cluster. But notice that at support electrons from the F_S center are involved. However, the excitations from the HOMO (D') are completely new and unique to the cluster supported at the F_S center.

Having established understanding of the electronic structure of the cluster-support species, the transitions can be analyzed in terms of leading excitations (Table A.8). It can be concluded that at the support, the leading excitations from the intense gas-phase transitions are split and mixed with the new and unique excitations from the D' orbital. This results in an overall increase of oscillator strength in the energy interval up to 4.5 eV ($\sum f_e$=3.74 in the gas phase versus 4.46 at the F_S center). Furthermore, the spectrum of Ag_8@F_{5c}(**IV**) [D_{2d}] exhibits most intense transitions (**2**-**4**) at T_e∼3.5 eV. Notice that this is roughly in the middle of the intense absorption in both separated parts, the gas-phase Ag_8 (D_{2d}) and the F_S center.

Ag_8@F_{5c}(V) [T_d]: The situation for the isomer **V** with the T_d symmetric silver subunit is very similar to the isomer **IV** [D_{2d}]. As can be seen from the MO diagram in Figure 14.11, the geometry of the supported cluster is quite distorted from the perfect local T_d symmetry which is expressed in the relatively large splitting of the $P_{x/y/z}$- and D-orbitals which were degenerated in the gas-phase Ag_8 (T_d). Consequently, the intense optical transition from the gas-phase Ag_8 is split at the F_S center support. Furthermore, due to the orbital mixing similar to Ag_8@F_{5c}(**IV**) [D_{2d}] the HOMO (D') has D character and thus D→F excitations are contributing to all presented transitions. Notice that these are the new excitations with contribution from the F_S center electrons. The intensity of transitions is highest at T_e∼3.7 eV (transition **4**) which, interestingly, is also the middle between the most intense transition in gas-phase Ag_8 (T_d) and the most intense absorption of the F_S center alone.

In summary, the Ag_8 cluster supported at the F_{5c} defect site shows broad absorption features between T_e∼2.5-5.0 eV. It has been found that many leading excitations contribute to theses electronic transitions. Two effects are important at the F_S center defect: First, the charge-transfer-induced change of cluster geometry and the reduction of the symmetry due to the support leads to the splitting of electronic transitions with respect to the gas phase. Furthermore, excitations within the cluster couple with excitations from orbitals which have a contribution from the F_S center. It has been shown that the excitations from these unique P'_z and D' orbitals contribute to all analyzed transitions. Furthermore, it has been demonstrated, that this mixing is indeed responsible for the very intense narrow absorption at T_e∼3.7 eV which is most pronounced for the structures with high symmetric silver cluster (e.g. Ag_8@F_{5c}(**V**) [T_d]). However, this broad absorption with a pronounced maximum at one transition energy can also be interpreted as a beginning nanoparticle-like behavior. Interestingly, the corresponding transition energy is exactly in the middle between the very intense transitions from gas-phase Ag_8 and from the F_S center alone.

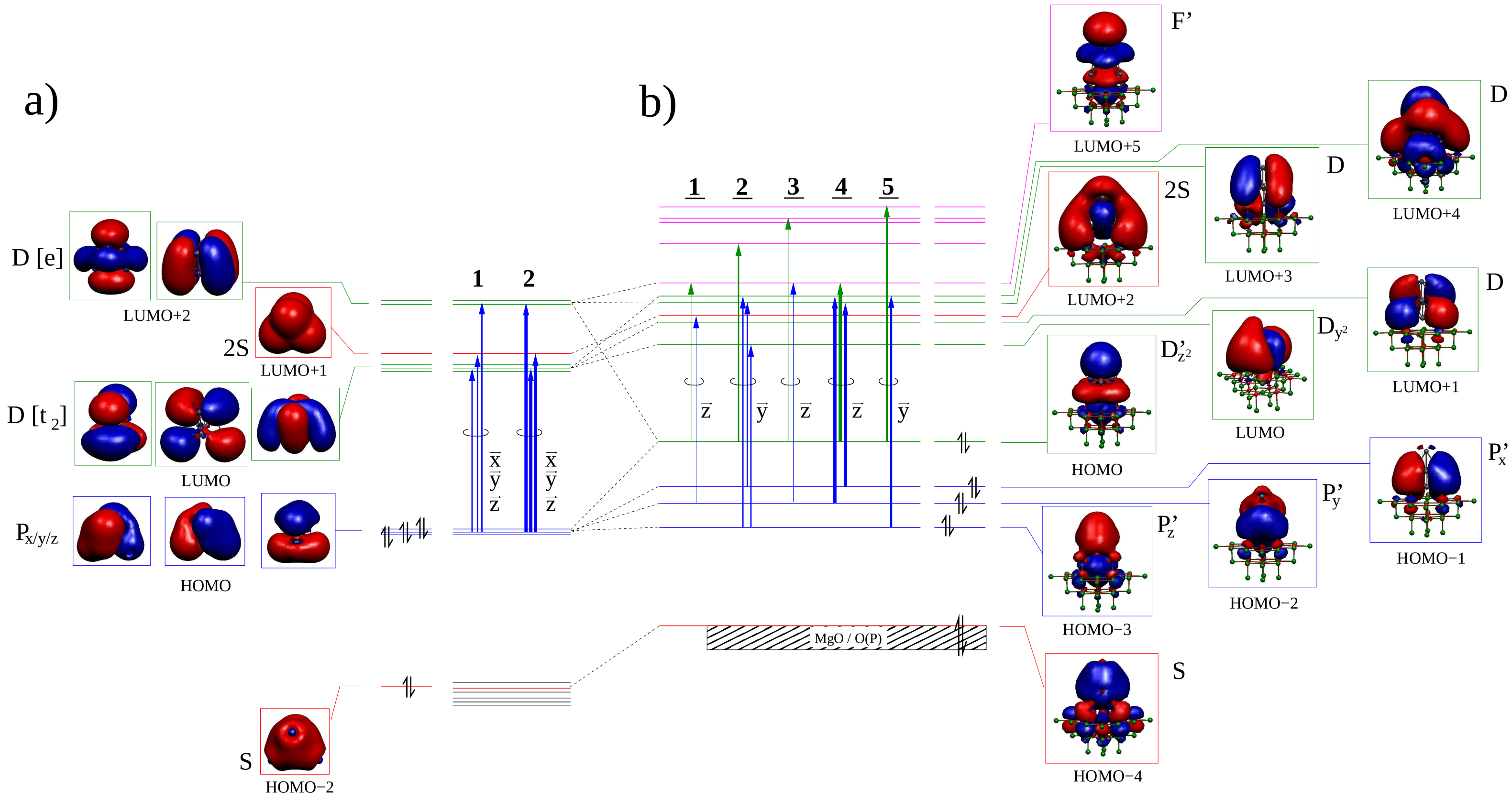

Figure 14.11: MO diagram for a) gas-phase $\mathrm{Ag_8}$ (T_{2d}) and b) $\mathrm{Ag_8@F_{5c}}$(**V**) [T_d]. Corresponding orbitals are connected by dashed lines. The frames around the orbitals and the corresponding energy levels are colored in order to illustrate the character of the orbitals (red: S-type, blue: P-type, green: D-type, purple: higher MO angular momentum quantum number). Pictures for highest F-type orbitals of supported species are not shown. Leading excitations are indicated by vertical lines from initial to final orbitals (for weights see Table 11.2 and Table A.9 in Appendix A). The $\overrightarrow{x}/\overrightarrow{y}/\overrightarrow{z}$ indicate the polarization of the corresponding transitions [**1-2** for a) and **1**-**5** for b)].

14.4 Emissive Properties

In a previous preliminary study [212], bound excited electronic states have been found for the $\mathrm{Ag_n}$ (n=2, 4, 6, 8) clusters supported at the F_S center defect. The relaxation in the excited electronic states is small and thus the possible fluorescence bands are close to the absorption lines ($\Delta\mathrm{T_e}<0.2$ eV). However, combining of state-of-the-art embedding techniques and appropriate DFT methods is mandatory for obtaining accurate absorption and emission energies. Therefore, the excited electronic states corresponding to intense transitions in $\mathrm{Ag_2@F_{5c}}$(**I**) and $\mathrm{Ag_4@F_{5c}}$(**I**) have been fully relaxed with the methods described in Chapter 10. It will be demonstrated, that the $\mathrm{Ag_n@F_{5c}}$ clusters indeed exhibit a similar relaxation in the excited states to the close-lying minima. Moreover, almost the same shift of the fluorescence band with respect to the absorption line is found.

In $\mathrm{Ag_2@F_{5c}}$(**I**), the first intense transition $\underline{\mathbf{1}}$ is located at $\mathrm{T_e}$=3.04 eV with dominant $\mathrm{P}'_z\rightarrow\mathrm{D}'$ character (95%). A close-lying minimum has been found ($\Delta\mathrm{E_{rel,exc.state}}$=0.088 eV) in which the Ag-Ag bond is significantly elongated (Δr=0.217 Å). The transition energy is shifted by 0.2 eV to T'_e=2.84 eV. Since this electronic state is well separated from other excited states by more than 0.65 eV, and due to the fact that the intensity is high (f'_e=0.92), fluorescence should occur at an energy of T'_e=2.84 eV which is in the blue part of the visible spectrum.

In principle also the excited electronic state corresponding to transition $\underline{\mathbf{2}}$ is a candidate for emission. However, since the ultimate goal is to generate fluorescence properties in the visible, we focus on the first intense transition at lower energy.

For $\mathrm{Ag_4@F_{5c}}$(**I**), four excited states corresponding to intense transitions $\underline{\mathbf{1}}$, $\underline{\mathbf{2}}$, $\underline{\mathbf{4}}$ and $\underline{\mathbf{5}}$ have been optimized. Excited state $\underline{\mathbf{1}}$ shows electronic relaxation of $\Delta\mathrm{E_{rel,exc.state}}$=0.170 eV and final emission at T'_e=2.17 eV which is in the yellow part of the optical spectrum. The character of the state remains unchanged upon relaxation as is evidenced by the almost same weight of the contributing leading excitations. The excited state $\underline{\mathbf{2}}$ shows also only little geometrical relaxation ($\Delta\mathrm{E_{relax,exc.state}}$=0.070 eV) and has possible emission at T'_e=2.67 eV (blue), close to the original absorption line ($\mathrm{T_e}$=2.73 eV). The bound excited electronic states have been found also for $\underline{\mathbf{4}}$ and $\underline{\mathbf{5}}$ with possible emission at T'_e=3.36 eV and T'_e=3.53 eV, respectively. Thus both should emit outside the visible regime.

Notice that although the excited states corresponding to the electronic transitions $\underline{\mathbf{1}}$ and $\underline{\mathbf{2}}$ exhibit close-lying minima, the absorption intensity is most likely not high enough for efficient emission (see Chapter 10). Therefore, only the very intense transitions **<u>4</u>** and **<u>5</u>** have a sufficiently high absorption intensity, and thus fluorescence should most likely occur from these states. However, it is necessary to determine the lifetimes of the corresponding states to fully answer this question.

In $Ag_6@F_{5c}$(**I**), many transitions with low intensity are found below $T_e\sim$ 3.5 eV. Therefore, after a population of the excited states non-radiative relaxation to lower lying excited states is most likely to occur. However, photoexcitation of the intense absorption band at $T_e\sim$3.5-3.9 eV leads to the population of corresponding excited electronic states **<u>5</u>**-**<u>9</u>** which exhibit close-lying minima. If coupling with other states is weak and thus the lifetime is long, in principle fluorescence can also occur from these states, which is outside the visible.

For the larger silver clusters $Ag_8@F_{5c}$ at the F_S center defect, a possible emission from the lowest-energy isomers has been examined and it has been found that the situation is similar to $Ag_6@F_{5c}$. A broad absorption with a high density of excited states is found for the third isomer $Ag_8@F_{5c}$(**III**) [C_{2h}]. The excited state corresponding to the intense absorption at T_e=2.66 eV (**<u>1</u>**, Figure 14.9) appears to be a good candidate for emission. However, this state is the 12th excited singlet state demonstrating the high density of low-lying excited states most likely preventing fluorescence from this state. Isomers **IV** and **V** of $Ag_8@F_{5c}$ show intense absorption well outside the visible spectrum, and furthermore they exhibit high density of excited electronic states at lower energies. Notice that in case of $Ag_8@F_{5c}$(**IV**) [D_{2d}] there are several low lying dark states (transition **<u>1</u>** is the 16th excited ^{1}A state) which is unfavorable for emissive properties. Therefore they do not represent good candidates for emission.

Table 14.1 summarizes findings on the absorption as well as the possible fluorescence lines for the small silver clusters at the F_S center support. For $Ag_2@F_{5c}$, strong fluorescence in the blue part of the visible spectrum ($T'_e\sim$2.8 eV) is suggested and most likely fluorescence can occur at considerably higher energy well outside the visible ($T'_e\sim$4.2 eV). For $Ag_4@F_{5c}$, fluorescence should most likely occur from the excited electronic states corresponding to the transitions with high intensity at higher energy ($T'_e\sim$3.4 eV). However, fluorescence from the excited electronic states at lower transition energies (blue and yellow part of the visible) is unlikely to occur but cannot be excluded.

The larger silver clusters ($Ag_{6,8}@F_{5c}$) exhibit a high density of excited electronic states which is unfavorable for emission since it reduces lifetime by non-radiative relaxation processes. Therefore, it is not likely that they will fluoresce.

Table 14.1: Absorption lines ($T_{e,abs}$ in eV) and possible fluorescence lines ($T'_{e,emiss}$ in eV) in the Ag_n clusters (n=2, 4, 6, 8) supported at the F_S center defect. In brackets, emission energies are given for excited electronic states which exhibit a close-lying minimum but most likely do not show fluorescence due to possible non-radiative relaxation processes or weak intensity.

Species	$T_{e,abs}$ [eV]	$T'_{e,emiss}$ [eV]
$Ag_2@F_{5c}$(**I**)	3.04 / 4.44	2.84 (∼4.2)
$Ag_4@F_{5c}$(**I**)	2.41 / 2.73	(2.17 / 2.67)
	3.51 / 3.62	3.36 / 3.53
$Ag_6@F_{5c}$(**I**)	3.5-3.9	(∼3.3-3.7)*
$Ag_8@F_{5c}$(**I-III**)	2.5-5.0	-
$Ag_8@F_{5c}$(**IV**,**V**)	∼3.7	-

* The fluorescence band has been estimated assuming that the fluorescence band is red-shifted by ≈0.2 eV [212] with respect to the absorption line.

Chapter 15

Discussion

15.1 Defect-Free MgO (100) Surface: The O_{5c} Adsorption Site

It has been shown, that the small silver clusters are only weakly bound to the defect-free MgO (100) surface by electrostatic interactions. Although this can change the ordering of the isomers (e.g. for $Ag_{4,8}$@O_{5c}) with respect to the gas phase, the overall geometries and electronic structures remain preserved at the MgO support. Consequently, also the absorption properties of the clusters are very similar to the corresponding gas-phase clusters. It has been found that some transitions are blue- or red-shifted depending on the polarization of the transition. For example, intense transitions with polarization perpendicular to the surface ($\overrightarrow{z}$) appear at the same energy or slightly higher energy than the corresponding transition in the gas phase. In contrast, if the polarization is perpendicular to the surface ($\overrightarrow{x}/\overrightarrow{y}$) the corresponding absorption line is red-shifted. The extent of the red-shift depends on the transition energy. It ranges from less than 0.2 eV for transitions at lower energy (T_e~3 eV) to 0.6 eV for transitions at higher energy (T_e>4 eV).

The analysis of the electronic transitions in terms of leading excitations revealed that the excitations within the cluster which are contributing to the electronic transitions in the gas phase can be differently mixed at the MgO surface. However, the overall character of the transitions (e.g. P→D) remains preserved. In contrast to the gas-phase clusters, the optical spectra for the supported species are not dominated by one or two intense transitions, since lowering of the symmetry causes splitting into several transitions with lower intensities. This is most pronounced for the larger clusters ($Ag_{6,8}$) which assume the highest symmetries in the gas phase.

The excited electronic states corresponding to the most intense transitions exhibit close-lying minima, and thus the fluorescence should occur near the absorption line (ΔE~0.2eV). For $Ag_2@O_{5c}$, emission is expected at T'_e~3.0 eV which is outside the visible. Also $Ag_6@O_{5c}$ and $Ag_8@O_{5c}$ might exhibit fluorescence at T'_e~3.2-3.6 eV and thus would emit in the ultra-violet. The only cluster at the MgO (100) surface in this study which exhibits possible fluorescence in the visible is $Ag_4@O_{5c}$. The two isomers can emit light in the yellow and blue part of the optical spectrum, respectively. Interestingly, the second isomer with a rhombic D_{2h} symmetric silver cluster has a bound excited electronic state from which fluorescence might occur at T'_e~2.6 eV. This is close to the measured fluorescence of Ag_4 in an argon matrix [61] which is known as a medium which only very weakly perturbs the electronic structure of the embedded cluster.

15.2 F_S Center Defect at the MgO (100) Surface: The F_{5c} Adsorption Site

The small silver clusters are bound much stronger to the F_S center defect site as compared to the defect-free surface. This is due to the charge transfer from the F_S center towards the cluster (Δq~0.8 e^-) and strong orbital interactions of cluster and F_S center orbitals of proper symmetry and energy. Both effects have a strong influence on the optical properties of the supported clusters as compared to those found for the gas-phase clusters.

Due to the charge transfer the supported silver clusters behave in a similar way as the anionic gas-phase clusters (Ag_n^-), e.g. they show a similar trend of ionization potentials as a function of the number of Ag atoms. Also the preference for a 3D structure in $Ag_6@F_{5c}$ in contrast to the most stable neutral isomer in the gas phase which is planar, can be understood from the properties of the anionic gas-phase Ag_6^-. In this case, the 2D and 3D isomer are almost energetically degenerated in contrast to the neutral Ag_6 in which the 3D isomers are considerably higher in energy.

As a result of the strong binding, the geometries of the supported clusters are more distorted than it has been the case for the clusters supported at the defect-free MgO support. This leads to the splitting of intense optical transitions of the gas-phase clusters upon adsorption. Similar to the defect-free MgO support, electronic transitions can have different leading excitations than in the corresponding transitions in the gas phase. However, a linear combination of cluster and F_S center orbitals leads to the formation of new molecular orbitals (P'_z, D', F') which are unique to the clusters at the F_S center defect. These orbitals have a contribution of electrons from the F_S center which leads to the overall increase in total intensity below T_e=5.0 eV. More importantly, these orbitals are involved in leading excitations in almost all intense transitions, thus coupling with the excitations within the cluster. This directly influences the optical spectra of the Ag clusters at the F_S center leading to effects similar to interference: The coupling with the excitations within the cluster leads to a set of electronic transitions with a decreased intensity at lower energies T_e<3.0 eV ("destructive interference") and a set of electronic transitions with an increased intensity at higher energies T_e∼3.7 eV ("constructive interference"). Interestingly, in larger silver clusters ($Ag_8@F_{5c}$), the enhancement of absorption intensity occurs in the middle between the high intense electronic transitions of the cluster (T_e∼4.0 eV) and the F_S center (T_e∼3.2 eV) alone. Moreover, for $Ag_6@F_{5c}$ and even more for $Ag_8@F_{5c}$, beginning nanoparticle behavior has been found which is expressed by many close-lying excited electronic states (highly split spectrum).

The differences in the optical spectra of supported and gas-phase clusters should lead also to different emissive properties. This is most pronounced for the larger supported silver clusters ($Ag_{6,8}@F_{5c}$) which exhibit high densities of excited electronic states. This is unfavorable for emission because non-radiative relaxation processes most likely prevent fluorescence. The smaller silver clusters ($Ag_{2,4}@F_{5c}$) show isolated intense transitions and thus are good candidates for emission. However, only $Ag_2@F_{5c}$ should exhibit strong fluorescence in the visible part of the spectrum (T'_e∼2.8 eV, blue). In the case of $Ag_4@F_{5c}$, the intensities of the transition at low energy are considerably decreased as compared to the most intense transition in gas-phase Ag_4. This is due to the coupling of the excitations within the cluster with excitations which have a contribution from the F_S center electrons. Therefore, although the corresponding excited electronic states exhibit close-lying minima, it is unlikely that fluorescence will occur from the corresponding excited electronic states. In contrast, the transitions at higher energy (T_e∼3.4 eV) have a sufficiently high intensity and the corresponding excited electronic states exhibit close-lying minima. Thus fluorescence from $Ag_4@F_{5c}$ is expected to occur most likely in the ultra-violet.

Chapter 16

Conclusions and Outlook

The structural as well as the optical properties of small neutral silver clusters supported at two typical adsorption sites of the MgO (100) surface have been studied. A state-of-the-art embedding scheme in combination with suitable DFT methods allowed us to obtain reliable structural, electronic as well as optical properties.

The structural and optical properties of the clusters, in particular the character of the electronic transitions and the corresponding excited electronic states, are mainly preserved at the defect-free MgO (100) surface. This is due to the weak electrostatic interaction which only shifts the transition energies and slightly influences the absorption intensities. However, both a blue-shift and a red-shift of electronic transitions have been found which is in line with the stronger interacting nature of MgO as compared to rare-gas matrices [63, 81, 82]. Notice that in the case of rare-gas matrices transition energies uniformly shift to the red due to the dielectric constant of the matrix.

In contrast, at the F_S center support, the optical properties of the gas-phase silver clusters are considerably modified due to the strong interaction between cluster and support. While the emissive properties of clusters at the defect-free MgO surface are mainly preserved and even large clusters such as Ag_8 might fluoresce, this is not the case at the F_S center support. At the F_S center defect, the splitting of intense transitions, in particular for larger clusters, leads to a high density of states which favors non-radiative relaxation processes in $Ag_6@F_{5c}$ and $Ag_8@F_{5c}$. These findings indicate that very small silver clusters are favorable candidates for photo-emission. However, in the case of Ag_4, the contribution of the F_S center electrons in the electronic transitions at low energy decreases their intensity and thus suppresses possible fluorescence in the visible from the corresponding excited states, but indicates that fluorescence is likely to occur in the ultra-violet regime.

In summary, it has been demonstrated that only the smallest supported silver clusters are potential emitters in the visible (Ag_4@O_{5c} and Ag_2@F_{5c}). Possible fluorescence lines outside the visible range have been found for $Ag_{2,6,8}$ clusters at the MgO surface and for Ag_4 at the F_S center defect. Possible fluorescence in Ag_4@F_{5c} in the visible is suppressed by interaction with the F_S center. Furthermore, due to the influence of the F_S center on the structural and optical properties of the larger silver clusters (Ag_6@F_{5c} and Ag_8@F_{5c}), the fluorescence, which is observed in the corresponding clusters embedded in rare-gas matrices, might not be present at the F_S center support.

However, in order to shift these transitions as well as the emission lines to the visible, a different environment might be more convenient. This can be either a different defect site of the MgO or a different support material. In this context, the influence of the metal substrate underlying the experimentally prepared MgO thin films (e.g. MgO/Mo or MgO/Ag) on the optical properties of supported clusters is not known. Moreover, the optical properties of small silver clusters supported at the strongly interacting Ag_2O surface could be revised on the basis of the conceptual findings of this study.

Most importantly, the lifetimes of the excited electronic states corresponding to intense transitions have to be calculated in order to establish which is more favorable, non-radiative relaxation processes or fluorescence. This requires non-adiabatic dynamical simulations for which an applicable methodology in the framework of the DFT method has been developed only very recently [218–220]. This will give us the excellent opportunity to follow time-dependent optical properties of small supported silver clusters also as a function of the temperature, and thus it might be the key for unraveling the dynamical multi-color blinking observed in experiments [43]. Also the determination of the optical stability of small emitting clusters at the support is mandatory for developing potential media for optical data storage.

Part IV

Summary

Chapter 17

Summary

In this thesis, the unique novel properties of noble metal clusters which arise in the sub-nanometer size regime due to quantum confinement have been theoretically explored. It has been demonstrated that by adding or removing a single atom the chemical and physical properties and functionality of noble-metal clusters can strongly change. The theoretical results have been derived in close cooperation with experimental findings of partner groups demonstrating that by joint theoretical and experimental efforts thorough understanding of fundamental processes and underlying mechanisms can be achieved. This thesis addresses the reactivity of charged gas-phase gold-oxide clusters in the context of the heterogeneous gold nano-catalysis, the ultrafast dynamical properties of noble-metal clusters and their complexes, and the optical properties of silver clusters at surfaces. The following results have been obtained:

Cluster Models for the Heterogeneous Catalysis The structure-reactivity relationship has been established for the anionic gold-oxide clusters $\mathrm{Au_mO_n^-}$ (m=1-6; n=1-5), and the reactive centers responsible for the CO oxidation have been identified [84, 100, 221]. It has been demonstrated on the example of $\mathrm{Au_2^-}$ reacting with O_2 and CO that the gold clusters alone cannot break the O-O bond. Therefore, anionic gold-oxide clusters with molecularly adsorbed oxygen cannot oxidize CO without further activation supported by cooperative effects [84, 86], i.e. at least two CO molecules are involved in the oxidation reaction. These theoretical findings contribute to understand the differences in observed reactivities under different experimental conditions [28, 84] since, as it has been shown, for the presence of cooperative effects higher pressures and longer reaction times are mandatory.

The role of atomic oxygen in the context of the gold nano-catalysis has also been addressed for the first time. $\mathrm{AuO^-}$ has been found to be the most reactive species in the oxidation of CO [100]. Indeed, it has been reported in the literature [37] that the AuO^- structural feature has been found at the catalytically active sites of supported gold clusters. The peripheral O atom is, in general, the most reactive center for the oxidation of CO, but its existence does not guarantee that the oxidation reaction proceeds [84, 100]. This demonstrates, that even if the molecular O-O bond is broken, the barriers for the subsequent oxidation reaction at the O atom can be sufficiently high, thus preventing the CO oxidation.

Since association of CO competes with the oxidation channel, the binding properties of CO to the anionic gold-oxide clusters $Au_mO_n^-$ ($m \leq 5$; $n \leq 4$) have been examined. The CO adsorption is strongly structure-dependent. A qualitative rule has been established which correlates the binding energy of CO with the geometrical and electronic structure of the anionic gold-oxide clusters. According to this rule, CO binds strongly only to anionic gold-oxide clusters which contain a peripheral Au atom [84]. This is because such a gold site carries a slightly positive charge which is favorable for CO adsorption due to its $2e^-$ donor nature. Moreover, the strong CO adsorption to such a $Au^{\delta+}$ site can even lead to fragmentation of the metal subunit [107] as has been demonstrated on the example of $Au_4O_{2,3}^-$ and Au_5O^-.

In order to address the role of the charge state on the reactivity of gold clusters, the structural and reactivity properties of small cationic gold-oxide clusters have been examined. It has been found that molecular binding of oxygen is preferred in contrast to the anionic charge state. The binding of CO has been found to be very strong in the case of cationic clusters due to the above-mentioned electron donating nature of the CO ligand. In fact, the high adsorption energy easily exceeds the low binding energy of the O_2 which, in contrast to the anionic clusters, is only bound by weak electrostatic interactions. Therefore, replacement of molecular oxygen and not the oxidation reaction is favored for cationic gold clusters.

Examining the reactivity of the prototype systems $Au_{1,2}O^+$ containing atomic oxygen revealed that at least two CO molecules need to be involved in the CO oxidation. The function of the first CO molecule is to strongly adsorb to a cationic Au site. This provides sufficient internal kinetic energy, so that the second CO can easily overcome subsequent barriers along the oxidation pathway. Thus, at high pressures of CO, the oxidation reaction is self-promoting in the presence of cationic gold species, i.e. the oxidation of one CO molecule is promoted by the binding of a second [108]. Therefore, the study of the cationic gas-phase model systems allows to propose that cationic centers which indeed have recently been found in gold nano-catalysts by Hutchings et al [36] might function as binding sites for CO in order to provide additional kinetic energy at the active site.

The theoretical results on the charged gas-phase gold-oxide clusters are fully supported by experimental findings obtained by Castleman and co-workers [84, 100, 107, 108].

In order to achieve a complete understanding of the Au-O and the valent isoelectronic Au-S bond, high-level ab initio study for the mono-gold oxide and sulfide clusters AuO_n^- and AuS_n^- (n=1, 2) has been performed. Both, strong spin-orbit coupling and electron correlation effects are found to play an important role [144]. The Au-X bond (X=O, S) has a strong covalent multiple bonding character due to strong activation of the d-electrons of the gold atom. The contribution of the d-electrons is also responsible for the directionality of the Au-X bonds and the preferred two-fold coordination.

Since Au^- does not bind molecular O_2, only the linear isomer $O\text{-}Au\text{-}O^-$ with dissociated oxygen is stable. In contrast, S_2 binds strongly to Au^- and thus the linear $S\text{-}Au\text{-}S^-$ as well as the $Au(S_2)^-$ complex are stable. The much stronger Au-S bond in $Au(S_2)^-$ arises due to the energetically favorable orbital interaction between Au^- and S_2, in contrast to O_2. The theoretical findings are in quantitative agreement with the corresponding experimental PES study of L.-S. Wang et al. Moreover, it has been demonstrated that by a joint theoretical and experimental study a fundamental insight into the nature of chemical bonding and the interpretation of photo-electron spectra can be achieved [144].

Ultrafast Dynamics of Noble-Metal Clusters The ultra-fast dynamics of noble metal clusters has been explored in order to unravel the role of dynamical effects such as internal vibrational energy distribution (IVR) on their reactivity. The efficiency of the IVR in collisions of Ag_6^- and Au_6^- with O_2 has been examined. Resonant IVR arises in gold clusters as a consequence of the strongly pronounced relativistic effects and serves as an additional activation of the strong O-O bond being suitable for reactions to proceed [163]. In contrast, dissipative IVR in silver clusters leads to a higher sticking probability of O_2, but the O-O bond is vibrationally deactivated and thus subsequent oxidation reactions with CO do not occur.

Therefore, the nature of IVR (resonant vs. dissipative) represents a new reactivity criterion. This demonstrates that in order to gain a full understanding of the reactivity in addition to the stationary energetic profiles also the intrinsic dynamical properties have to be accounted for [163]. Moreover, as has been demonstrated, the resonant IVR in gold clusters might govern the course of the CO oxidation reaction by noble-metal clusters. Thus the new findings on the importance of the IVR might contribute to better understand the unusually high low-temperature activity of supported gold clusters in the context of the gold nano-catalysis.

The optical response and photo-chemical properties of clusters are governed by their excited state dynamics. Therefore, the relaxation dynamics in the electronically excited small anionic gold clusters Au^-_{5-8} has been examined, which is found to be extremely size-dependent [164]. Au^-_5 exhibits a close-lying minimum near the initially populated S_1 excited electronic state, and thus oscillatory wave-packet motion in a bound electronic state with a long lifetime is found. In contrast, in Au^-_7 fast internal conversion into the electronic ground state initiates a melting-like transition after $\sim$1.9 ps. Both findings are in full agreement with corresponding experimental results obtained by Eberhardt et al [164].

Optical Properties of Supported Silver Clusters The non-scalable properties of clusters are perhaps most clearly reflected in their optical response. Therefore, for the development of novel nano-optical applications, which usually utilize surface-stabilized clusters, a thorough understanding of the properties of deposited clusters is mandatory. Here, the structural and optical properties of small neutral silver clusters $Ag_{2,4,6,8}$ supported at different sites of the MgO (100) surface have been explored [222].

Neutral small silver clusters are only weakly bound to the O_{5c} site of the defect-free MgO (100) surface. The structural and optical properties of the gas-phase silver clusters remain largely preserved at the stoichiometric support. The most intense transitions are slightly red- or blue-shifted depending on the polarization of the transition. In larger, highly symmetric clusters such as Ag_6 and Ag_8, the one or two characteristic intense transitions in the gas-phase clusters are replaced by a small number of moderately intense transitions caused by interaction with the MgO support. Possible emission has been found for $Ag_2@O_{5c}$ at 3.0 eV, $Ag_4@O_{5c}$ at 2.4 and 2.6 eV, $Ag_6@O_{5c}$ at 3.2 eV, and $Ag_8@O_{5c}$ at 3.0-3.6 eV. Only $Ag_4@O_{5c}$ has been found to exhibit possible fluorescence in the visible regime (green and blue).

The binding of the silver clusters to the F_S center defect (F_{5c} binding site) is considerably stronger due to favorable orbital interaction of cluster and F_S orbitals. Moreover, adsorption at the F_S center is accompanied by a pronounced charge transfer to the cluster, leading to cluster charging. Both effects strongly affect the structural properties of the supported clusters and influence their electronic structure. Therefore, the intense transitions of the gas-phase clusters remain only as optical fingerprints. New optical transitions arise due to the influence of the F_S center electrons and the excitation from newly created cluster / F_S center hybrid orbitals. Furthermore, resonance effects between excitations within the cluster and the new excitations involving F_S center electrons have been found. It has been demonstrated that these effects can suppress possible fluorescence in the visible regime and at the same time enhance emission at higher transition energies around 4 eV. The most promising candidates for emissive centers are $Ag_2@F_{5c}$ and $Ag_4@F_{5c}$. However, only $Ag_2@F_{5c}$ might exhibit fluorescence in the visible regime (blue part).

In conclusion, it was shown by examining model systems that the fascinating strongly size-dependent properties of noble-metal clusters can be functionalized in the context of catalysis and optical applications.

Chapter 18

Zusammenfassung

In dieser Dissertation wurden die ungewöhnlichen und einzigartigen Eigenschaften von Edelmetall-Clustern untersucht, die durch Quantum-Confinement im Sub-Nanometer-Bereich entstehen. Dabei zeigt sich, dass die chemischen und physikalischen Eigenschaften und damit die Funktionen nicht vom Festkörper abgeleitet werden können und stark von der Anzahl der Atome abhängen. Die erzielten theoretischen Ergebnisse wurden in enger Zusammenarbeit mit experimentell arbeitenden Partnergruppen erzielt. Dabei hat sich gezeigt, dass durch die enge Kooperation zwischen Theorie und Experiment ein tiefes Verständnis von fundamentalen Prozessen und den zugrunde liegenden Mechanismen erlangt werden kann. Im Rahmen dieser Dissertation wurden die Reaktivität von geladenen Goldoxid-Clustern in der Gasphase, die ultraschnelle Dynamik von Edelmetall-Clustern und deren Komplexen sowie die optischen Eigenschaften von kleinen, deponierten Silber-Clustern untersucht und damit Beiträge geliefert, die einzigartigen Eigenschaften von Edelmetall-Clustern im Zusammenhang mit der heterogenen Katalyse und Nano-Optik besser zu verstehen. Folgende neuen Erkenntnisse wurden gewonnen:

Cluster-Modelle für die heterogene Katalyse Die Struktur-Reaktivitätsbeziehung für kleine, anionische Goldoxid-Cluster $\mathrm{Au_mO_n^-}$ (m=1-6; n=1-5) wurde analysiert und die aktiven Zentren, die für die Oxidation von CO verantwortlich sind, ermittelt [84, 100, 221]. Gold-Cluster können die starke O-O-Bindung nicht alleine brechen, weshalb anionische Gold-Cluster, die ausschließlich molekular gebundenen Sauerstoff tragen, CO nicht ohne weitere Aktivierung oxidieren [84, 86]. An dem Beispiel der Reaktion von $\mathrm{Au_2^-}$ mit $\mathrm{O_2}$ und CO wurde explizit gezeigt, dass zusätzlich zur chemischen Aktivierung durch Ladungstransfer zum $\mathrm{O_2}$ kooperative Effekte notwendig sind. Diese zeichnen sich dadurch aus, dass mindestens zwei CO-Moleküle in den

Oxidationsmechanismus involviert sind. Durch diese theoretischen Ergebnisse konnten die unterschiedlichen Reaktivitäten bei verschiedenen experimentellen Bedingungen [28, 84] erklärt werden, da kooperative Effekte nur bei hohen Drücken und langen Reaktionszeiten wirken können.

Die Rolle von atomar gebundenem Sauerstoff in der goldbasierten Nano-Katalyse wurde ebenfalls zum ersten Mal untersucht. Die höchste Reaktivität konnte für AuO^- ermittelt werden [100], welches tatsächlich auch als Strukturelement in realen Gold-Katalysatoren durcg Fu et al [37] gefunden wurde. Das peripher gebundene Sauerstoffatom stellt im Fall der anionischen Goldoxid-Cluster das reaktivste Zentrum für die Oxidation von CO dar. Allerdings garantiert seine bloße Existenz nicht, dass die Oxidationsreaktion tatsächlich abläuft [84, 100]. Dadurch konnte gezeigt werden, dass selbst wenn die O-O-Bindung bereits gebrochen ist, die Barrieren für die nachfolgende Oxidation von CO durch atomar gebunden Sauerstoff ausreichend hoch sein können, um die Oxidation von CO zu verhindern.

Da die Adsorption von CO und die CO-Oxidationsreaktion miteinander konkurrieren, wurden die Bindungseigenschaften von CO an anionische Goldoxid-Cluster $Au_mO_n^-$ ($m \leq 5$; $n \leq 4$)untersucht. Die Adsorption von CO ist stark strukturabhängig. Eine allgemein gültige, qualitative Regel wurde abgeleitet, die die Bindungsenergie von CO mit der Struktur und den elektronischen Eigenschaften der anionischen Goldoxid-Cluster korreliert. Demzufolge bindet CO nur dann stark an anionische Goldoxid-Cluster, wenn diese ein endständig gebundenes Au-Atom enthalten [84]. Dieses Goldatom hat eine positive Partialladung, was die Adsorption des $2e^-$ Donors CO begünstigt. Ferner wurde am Beispiel von $Au_4O_{2,3}^-$ und Au_5O^-gezeigt, dass die starke Bindung von CO an solch eine $Au^{\delta+}$ Bindungsstelle sogar zur Fragmentierung der Metalleinheit führen kann [107].

Die Rolle des Ladungszustandes bei der Reaktivität von Gold-Clustern wurde anhand der Modellsysteme kleiner, kationischer Goldoxid-Cluster untersucht. Im Gegensatz zu den negativ geladenen Gold-Clustern ist Sauerstoff im Falle des kationischen Ladungszustandes bevorzugt molekular gebunden. Die Bindung von CO ist durch die bereits erwähnten Elektronen-Donor-Eigenschaften sehr stark, deutlich stärker als die von dem nur schwach durch elektrostatische Wechselwirkungen gebundenen O_2. Aus diesem Grund ist im Fall der kationischen Gold-Cluster der Austausch von molekularem Sauerstoff durch CO und nicht die Oxidationsreaktion bevorzugt.

Anhand der Reaktivität der Modell-Spezies $Au_{1,2}O^+$ mit atomar gebundenem Sauerstoff wurde gezeigt, dass mindestens zwei CO-Moleküle erforderlich sind, damit eine Oxidationsreaktion stattfinden kann. Die Rolle des ersten CO-Moleküls ist es, stark an ein positiv geladenes Au-Atom zu binden. Dadurch wird die nötige interne kinetische Energie bereitgestellt, um die weiteren Barrieren entlang des Reaktionspfades für das zweite CO-Molekül leicht überwinden zu können. Das bedeutet, dass sich die Oxidationsreaktion an kationischen Gold-Zentren bei hohen CO-Drücken selbst antreibt, d. h. die Oxidation von einem CO-Molekül wird durch die Bindung eines weiteren unterstützt [108]. Möglicherweise liegt darin auch eine Funktion von kationischen Zentren, die in goldbasierten Katalysatoren durch Hutchings et al [36]gefunden wurden. Diese könnten als Bindungsstellen für CO dienen, um zusätzliche kinetische Energie am aktiven Zentrum bereitzustellen.

Die theoretischen Ergebnisse über die Reaktivität von geladenen Goldoxid-Clustern als Modellsysteme für die heterogene Katalyse werden vollständig durch die experimentellen Beobachtungen durch Castleman et al unterstützt [84, 100, 107, 108].

Um ein vollständiges Bild der Au-O-Bindung und der isovalenzelektronischen Au-S-Bindung zu erhalten, wurden die Oxide und Sulfide des Gold-Atoms $\mathrm{AuO_n^-}$ und $\mathrm{AuS_n^-}$ (n=1, 2) auf der Basis von hoch-korrelierten ab initio-Methoden untersucht. Sowohl Spin-Bahn-Kopplung als auch Elektronen-Korrelationseffekte sind stark ausgeprägt und müssen für quantitative Beschreibungen explizit berücksichtigt werden [144]. Die Au-X-Bindung (X=O, S) hat durch die Aktivierung der d-Elektronen einen stark kovalenten Mehrfachbindungscharakter. Die Beteiligung der d-Elektronen ist darüber hinaus für den gerichteten Charakter der Au-X-Bindung und die bevorzugte Zweifach-Koordination von Gold verantwortlich.

Da das O_2-Molekül nicht an $\mathrm{Au^-}$ bindet, ist nur das lineare Isomer $\mathrm{O\text{-}Au\text{-}O^-}$ mit dissoziiertem Sauerstoff stabil. Im Gegensatz dazu bindet S_2 sehr stark an $\mathrm{Au^-}$, weshalb sowohl das lineare Isomer $\mathrm{S\text{-}Au\text{-}S^-}$ als auch der Komplex $\mathrm{Au(S_2)^-}$ mit molekular gebundenem Dischwefel stabile Isomere darstellen. Die viel stärkere Au-S-Bindung in $\mathrm{Au(S_2)^-}$ rührt von der im Gegensatz zu O_2 energetisch günstigen Orbitalwechselwirkung zwischen $\mathrm{Au^-}$ und S_2 her. Die theoretischen Ergebnisse stimmen quantitativ mit den entsprechenden experimentellen PES-Spektren von L.-S. Wang et al überein. Dabei ist es durch das Zusammenspiel von Theorie und Experiment möglich, den Charakter der chemischen Bindung im Detail zu verstehen und experimentelle, hoch-aufgelöste Photoelektronen-Spektren quantitativ zu interpretieren [144].

Ultraschnelle Dynamik in Edelmetall-Clustern Um ein grundlegendes Verständnis der Bedeutung von dynamischen Effekten, wie z. B. der Schwingungsenergie-Umverteilung (internal vibrational energy redistribution, IVR), für die Reaktivität zu erlangen, wurde die ultraschnelle Dynamik von Edelmetall-Clustern untersucht. Die Effizienz der IVR wurde am Beispiel der Kollisionsdynamik von Ag_6^- und Au_6^- mit O_2 untersucht. Aufgrund der stark ausgeprägten relativistischen Effekte ist eine resonante IVR für Gold-Cluster charakteristisch, was zu einer zusätzlichen Aktivierung der O-O-Bindung und damit einer Unterstützung nachfolgender Reaktionen führt [163]. Im Gegensatz dazu ist dissipative IVR in Silber-Clustern dafür verantwortlich, dass zwar die Haftungswahrscheinlichkeit für O_2 höher, dafür aber die O-O-Bindung schwingungsdeaktiviert ist. Eine nachfolgende Oxidationsreaktion mit CO findet daher nicht statt.

Zusammenfassend wurde gezeigt, dass die Natur der IVR, resonant bzw. dissipativ, ein neues Kriterium für die Reaktivität darstellt. Das zeigt, dass um ein vollständiges Verständnis von Reaktivität erlangen zu können, zusätzlich zu den stationären Energieprofilen auch die spezifischen dynamischen Eigenschaften der Cluster einbezogen werden müssen [163]. Am Beispiel der Edelmetall-Cluster wurde gezeigt, dass die resonante IVR maßgeblich die Reaktivität bezüglich der CO-Oxidation beeinflusst. Folglich könnte die hier dargestellte Untersuchung der Natur der IVR zu einem besseren Verständnis der ungewöhnlich hohen katalytischen Aktivität von deponierten Gold-Clustern im Zusammenhang mit der Gold-Nanokatalyse beitragen.

Da die optische Antwort und die photochemischen Eigenschaften von Clustern maßgeblich durch deren Dynamik im elektronisch angeregten Zustand bestimmt werden, wurde in dieser Arbeit die Relaxationsdynamik in kleinen, anionischen, elektronisch angeregten Gold-Clustern Au_{5-8}^- theoretisch untersucht. Es hat sich gezeigt, dass die Dynamik extrem von der Clustergröße abhängt [164]. Au_5^- weist ein Minimum in der Nähe des populierten elektronischen S_1-Zustandes auf. Folglich wurde eine oszillierende Wellenpaketbewegung in einem langlebigen, gebundenen elektronischen Zustand durch Simulation der Dynamik im angeregten Zustand gefunden. Im Gegensatz dazu führt eine schnelle interne Konversion vom elektronisch angeregten S_1 Zustand in den Grundzustand von Au_7^- zu einem großen Energieüberschuss, der zu einem schmelz-ähnlichen Zustand nach $\sim$1.9 ps führt. Beide Ergebnisse sind in voller Übereinstimmung mit entsprechenden experimentellen Ergebnissen von Eberhardt et al [164].

Optische Eigenschaften von deponierten Silber-Clustern Die Nicht-Skalierbarkeit der Eigenschaften von Clustern wird vielleicht am deutlichsten an deren optischen Eigenschaften sichtbar. Für die Anwendung von Clustern werden diese meist auf Oberflächen stabilisiert. Deshalb ist ein tiefes Verständnis der Eigenschaften von deponierten Clustern für die Entwicklung von Materialien mit neuartigen optischen Funktionen unerlässlich. In dieser Arbeit wurden die strukturellen und optischen Eigenschaften von kleinen, neutralen Silber-Clustern $Ag_{2,4,6,8}$ an verschiedenen Bindungsstellen der MgO (100)-Oberfläche untersucht [222].

Kleine, neutrale Silber-Cluster sind nur schwach an die O_{5c}-Bindungsstelle der perfekten, defekt-freien MgO (100)-Oberfläche gebunden. Die strukturellen und optischen Eigenschaften der Gasphasen-Cluster auf der stöchiometrischen Oberfläche bleiben dabei weitgehend erhalten. Die intensivsten Übergänge sind in Abhängigkeit von der Polarisation des Übergangs schwach rot- bzw. blauverschoben. In den größeren, höhersymmetrischen Clustern (Ag_6, Ag_8) sind die charakteristischen sehr intensiven Übergänge der Gasphasen-Cluster durch wenige Übergänge mittlerer Intensität ersetzt. Verantwortlich für diese Aufspaltung ist die Wechselwirkung mit der MgO-Oberfläche. Für die folgenden Spezies wurde eine wahrscheinliche Fluoreszenz ermittelt: Ag_2@O_{5c} bei 3.0 eV, Ag_4@O_{5c} bei 2.4 und 2.6 eV, Ag_6@O_{5c} bei 3.2 eV und Ag_8@O_{5c} bei 3.0-3.6 eV. Dabei würde einzig Ag_4@O_{5c} im sichtbaren Bereich fluoreszieren (grün und blau).

Die untersuchten Silber-Cluster binden wesentlich stärker an F_S-Zentrum-Defekte (F_{5c}-Bindungsstelle), da die F_S-Zentren und Cluster Orbitale besitzen, die eine für die Überlappung sehr günstige Orientierung und Energie aufweisen. Darüber hinaus ist die Adsorption an ein F_S-Zentrum mit einem starken Ladungstransfer von der Fehlstelle zum Cluster verbunden. Beide Effekte beeinflussen stark die strukturellen und elektronischen Eigenschaften der deponierten Silber-Cluster. Die intensiven optischen Übergänge der Gasphasen-Cluster sind nur noch als optischer Fingerabdruck zu erkennen. Dagegen entstehen durch die Beteiligung von Elektronen des F_S-Zentrums optische Übergänge, die völlig neu und charakteristisch für das Cluster-F_S-Zentrum-Interface sind, und Anregungen aus den durch Linearkombination neu gebildeten Orbitalen enthalten. Darüber hinaus wurden Resonanzeffekte zwischen Anregungen innerhalb des Clusters und den neuen Anregungen unter Beteiligung von Elektronen des F_S-Zentrums identifiziert, die die Fluoreszenz im sichtbaren Bereich unterdrücken, bei höheren Energien um 4 eV dagegen verstärken können. Die vielversprechendsten Kandidaten für eine Funktion als Emitter sind daher Ag_2@F_{5c} und Ag_4@F_{5c}. Allerdings dürfte nur Ag_2@F_{5c} im sichtbaren Bereich des Spektrums (blau) fluoreszieren.

Diese Dissertation hat anhand der Untersuchung von Modellsystemen gezeigt, dass die faszinierenden, stark größenabhängigen Eigenschaften der Edelmetall-Cluster im Bereich der Katalyse und bei Anwendungen in der Optik funktionalisiert werden können.

Part V

Appendix

Appendix A

Supplementary Material for Optical Properties of Small Supported Silver Clusters

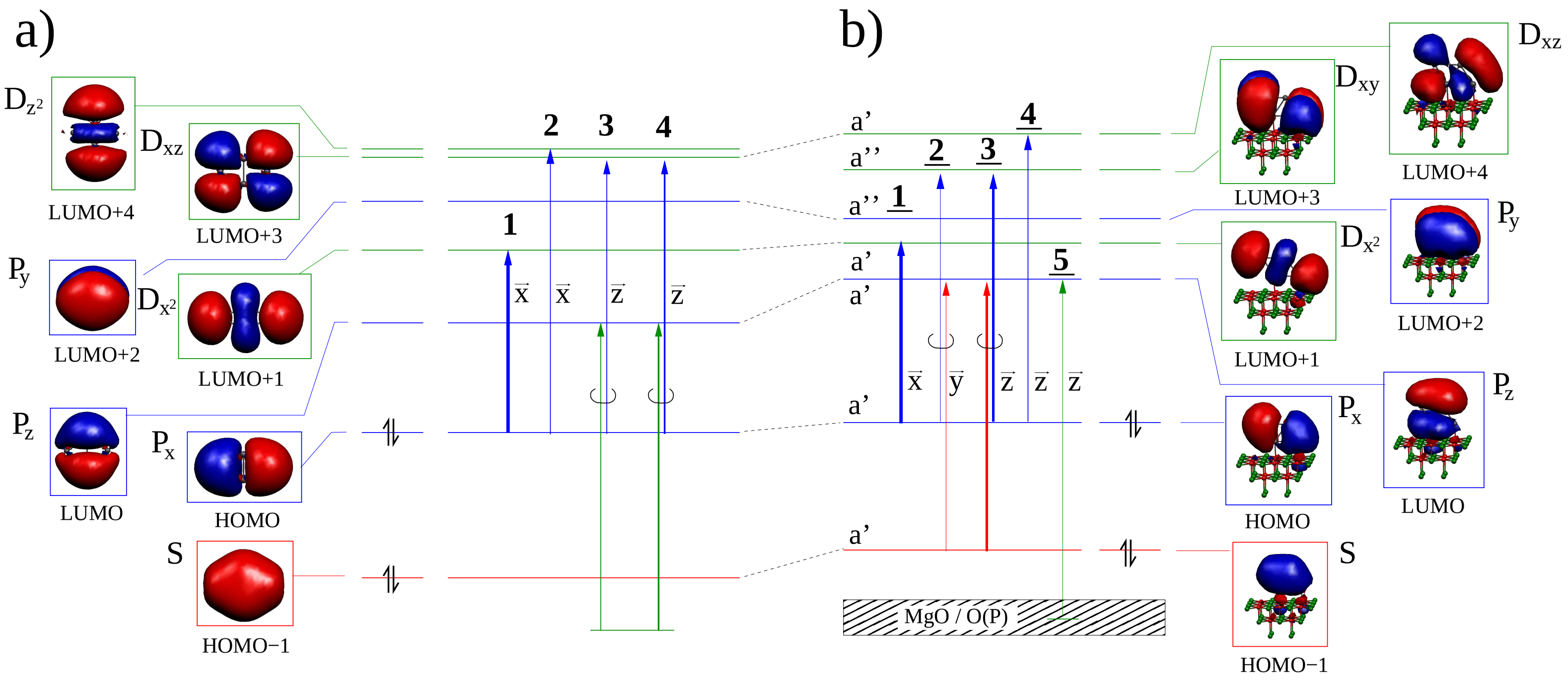

Figure A.1: MO diagram for a) gas phase Ag_4 (D_{2h}) and b) $Ag_4@O_{5c}$(**II**) [D_{2h}]. Corresponding orbitals are connected by dashed lines. The frames around the orbitals and the corresponding energy levels are colored in order to illustrate the character of the orbitals (red: S-type, blue: P-type, green: D-type). Leading excitations are indicated by vertical lines from initial to final orbitals (for weights see Table 11.1 and table in Figure 13.6) and $\overrightarrow{x}/\overrightarrow{y}/\overrightarrow{z}$ indicate the polarization of the corresponding transitions [**1-4** for a) and **1**-**5** for b)].

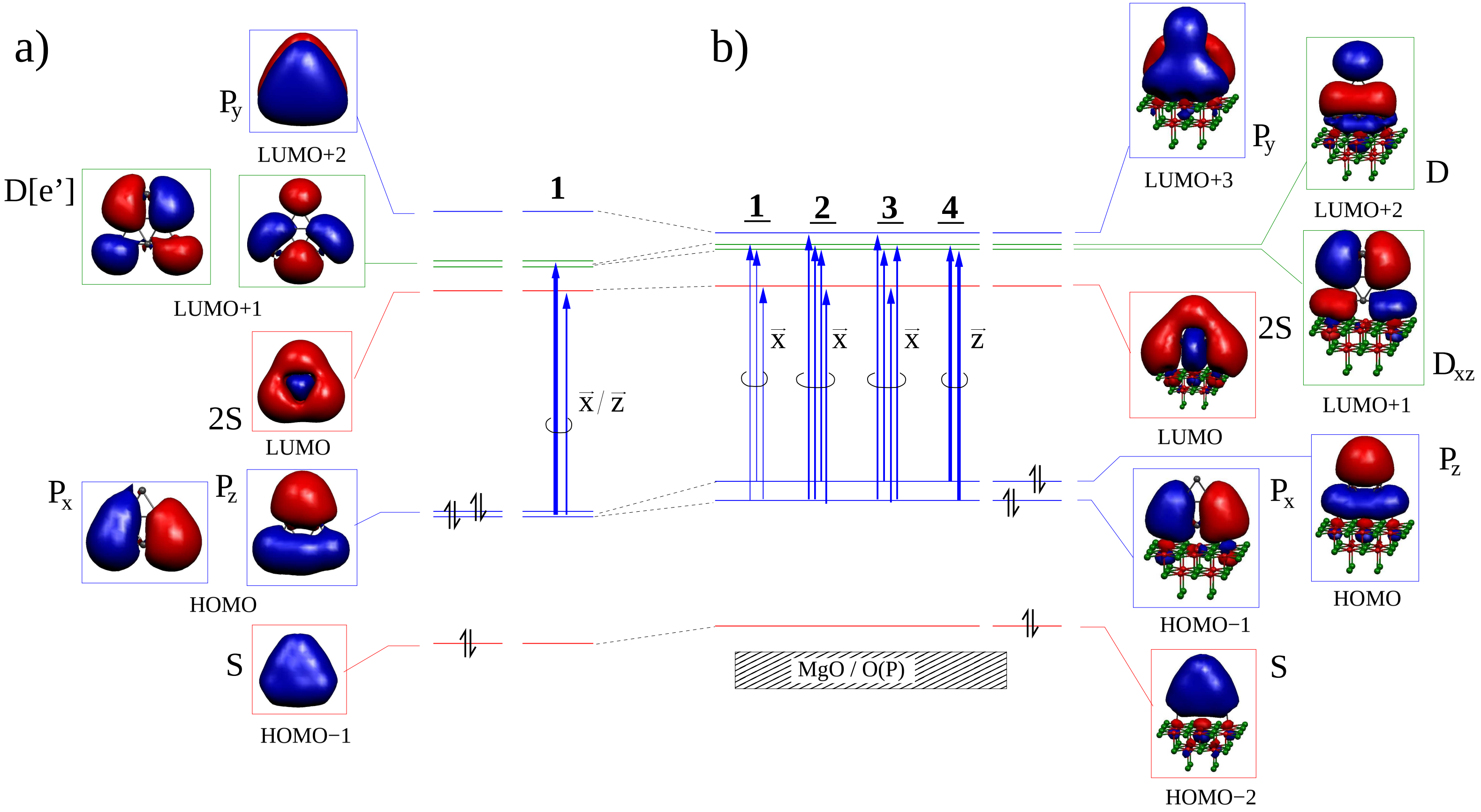

Figure A.2: MO diagram for a) gas phase Ag_6 (D_{3h}) and b) $Ag_6@O_{5c}(\mathbf{I})$ [D_{3h}]. Corresponding orbitals are connected by dashed lines. The frames around the orbitals and the corresponding energy levels are colored in order to illustrate the character of the orbitals (red: S-type, blue: P-type, green: D-type). Leading excitations are indicated by vertical lines from initial to final orbitals (for weights see table in Figure 11.4 and Table A.3 in Appendix A) and $\vec{x}/\vec{y}/\vec{z}$ indicate the polarization of the corresponding transitions [**1** for a) and **1**-**4** for b)].

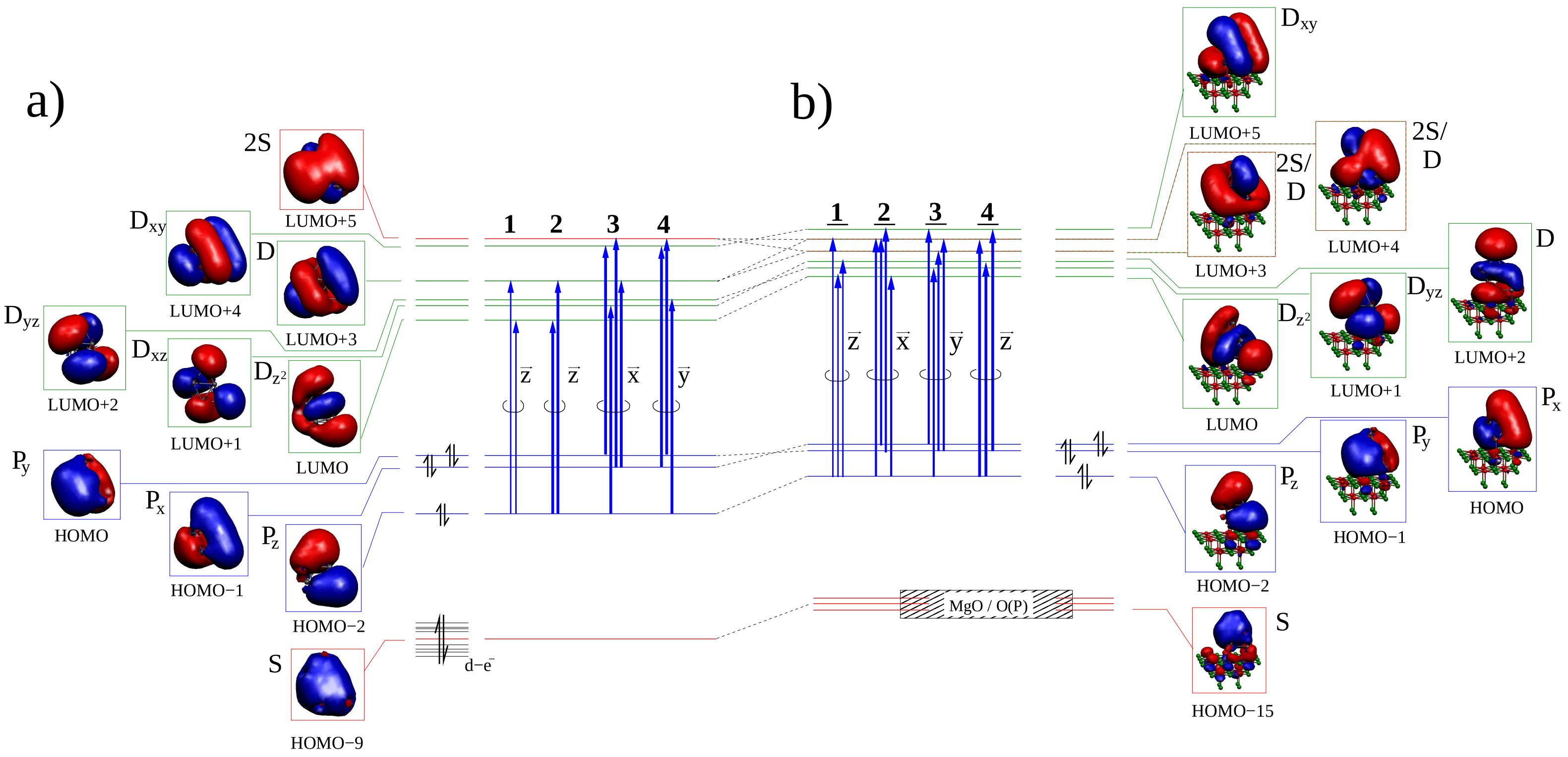

Figure A.3: MO diagram for a) gas phase Ag_8 (C_{2v}) and b) $Ag_8@O_{5c}(\mathbf{I})$ [C_{2v}]. Corresponding orbitals are connected by dashed lines. The frames around the orbitals and the corresponding energy levels are colored in order to illustrate the character of the orbitals (red: S-type, blue: P-type, green: D-type). Leading excitations are indicated by vertical lines from initial to final orbitals (for weights see Tables A.2 and A.4) and $\overrightarrow{x}/\overrightarrow{y}/\overrightarrow{z}$ indicate the polarization of the corresponding transitions [**1-4** for a) and $\underline{\mathbf{1}}$-$\underline{\mathbf{4}}$ for b)].

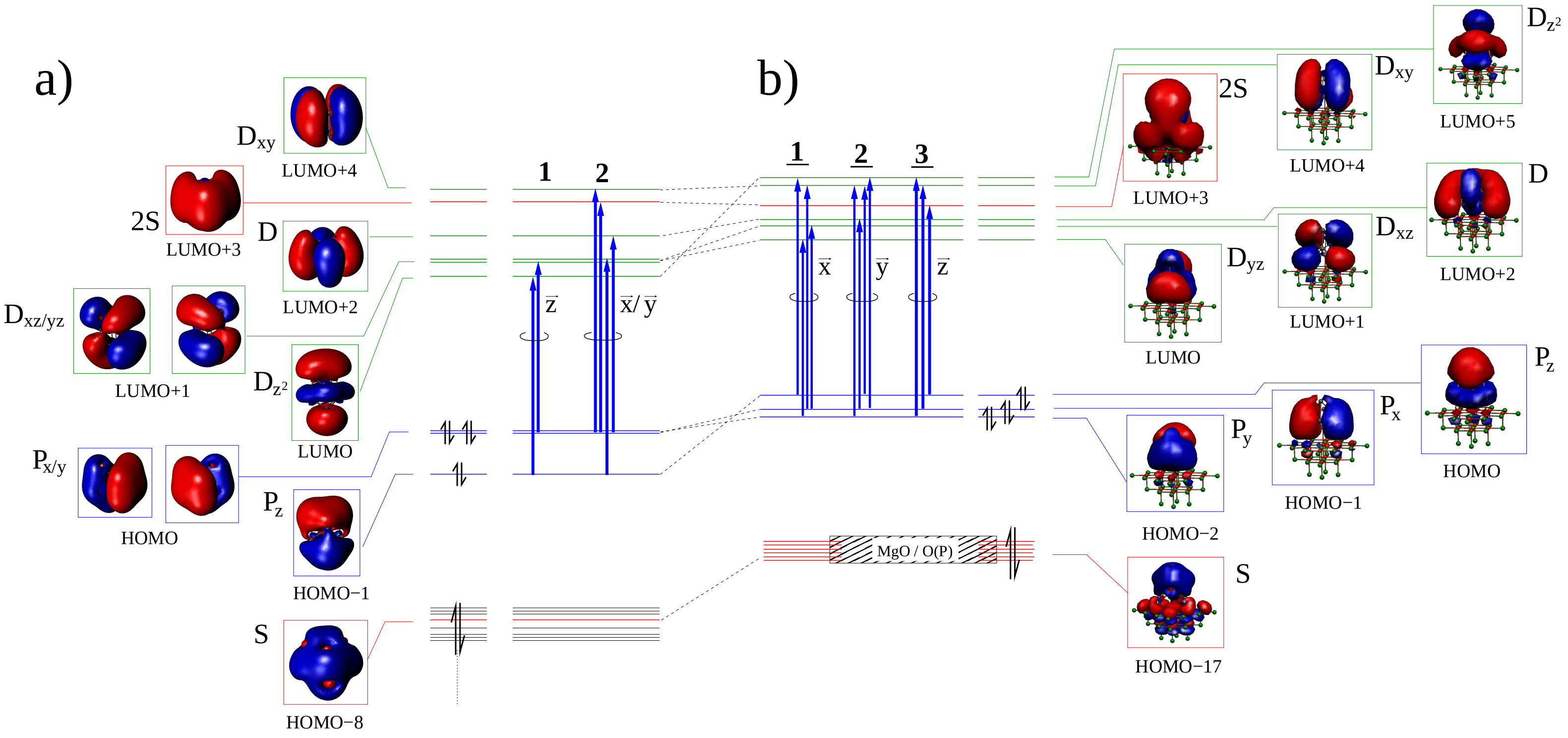

Figure A.4: MO diagram for a) gas phase Ag_8 (D_{2d}) and b) $Ag_8@O_{5c}$(**II**) [D_{2d}]. Corresponding orbitals are connected by dashed lines. The frames around the orbitals and the corresponding energy levels are colored in order to illustrate the character of the orbitals (red: S-type, blue: P-type, green: D-type). Leading excitations are indicated by vertical lines from initial to final orbitals (for weights see Tables 11.2 and A.5) and $\overrightarrow{x}/\overrightarrow{y}/\overrightarrow{z}$ indicate the polarization of the corresponding transitions [**1-2** for a) and **1**-**3** for b)].

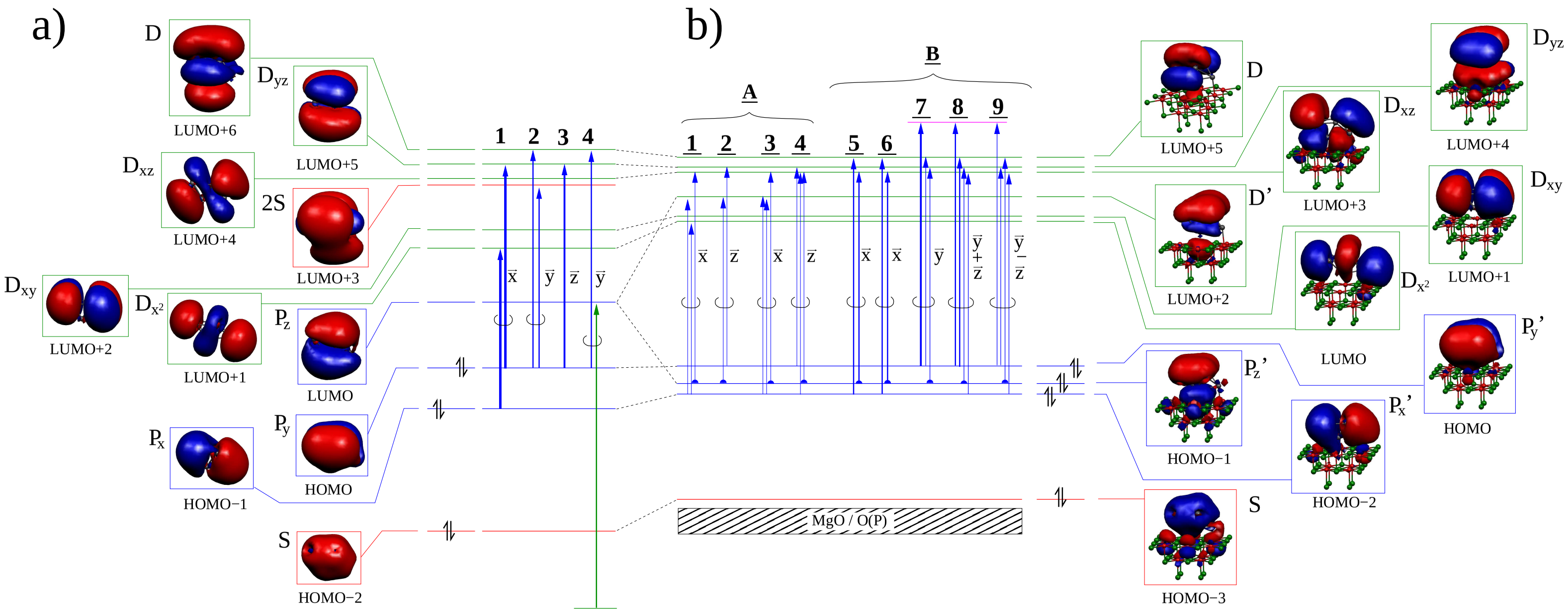

Figure A.5: MO diagram for a) gas phase Ag_6 (C_S) in geometry of most stable isomer of Ag_6 at F_S center ($Ag_6@F_{5c}(\mathbf{I})$ [C_S]) and b) $Ag_6@F_{5c}(\mathbf{I})$ [C_S]. Corresponding orbitals are connected by dashed lines. The frames around the orbitals and the corresponding energy levels are colored in order to illustrate the character of the orbitals (red: S-type, blue: P-type, green: D-type, purple: higher MO angular momentum quantum number). Leading excitations are indicated by vertical lines from initial to final orbitals (for weights see table in Figure 14.7 and Table A.6) and $\overrightarrow{x}/\overrightarrow{y}/\overrightarrow{z}$ indicate the polarization of the corresponding transitions [**1-4** for a) and **1**-**9** for b)].

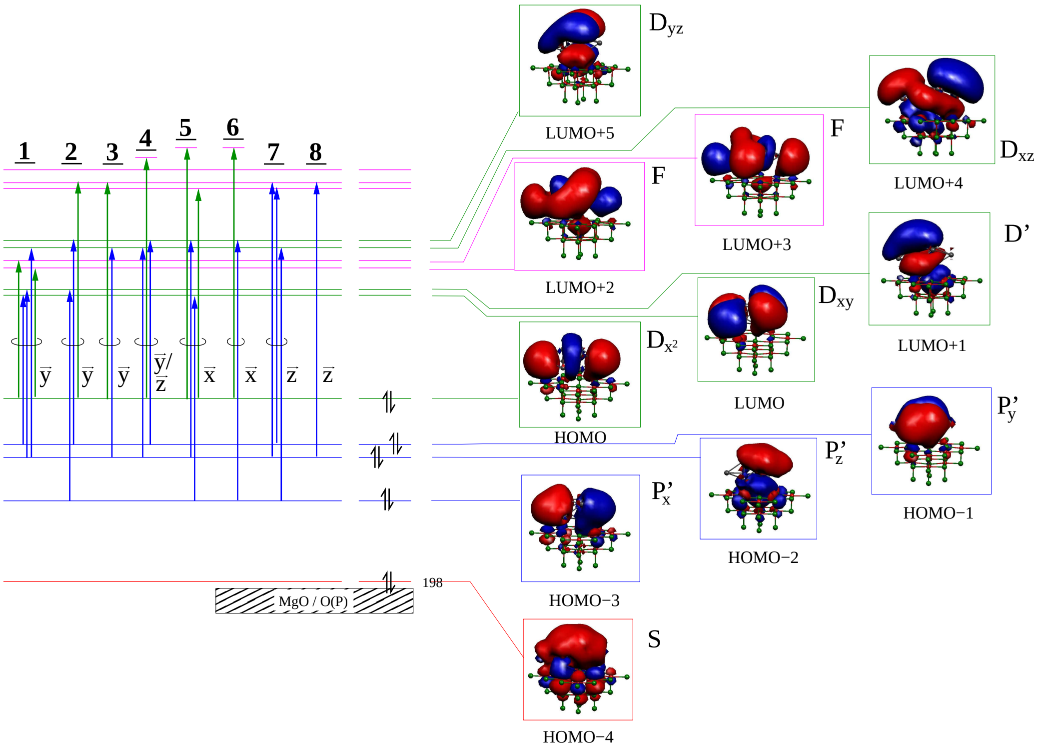

Figure A.6: MO scheme for Ag$_8$@F$_{5c}$(**III**) [C$_{2h}$]. The frames around the orbitals and the corresponding energy levels are colored in order to illustrate the character of the orbitals (red: S-type, blue: P-type, green: D-type, purple: higher MO angular momentum quantum number). Leading excitations are indicated by vertical lines from initial to final orbitals (for weights see Table A.7) and $\overrightarrow{x}/\overrightarrow{y}/\overrightarrow{z}$ indicate the polarization of the corresponding transitions (**1**-**8**).

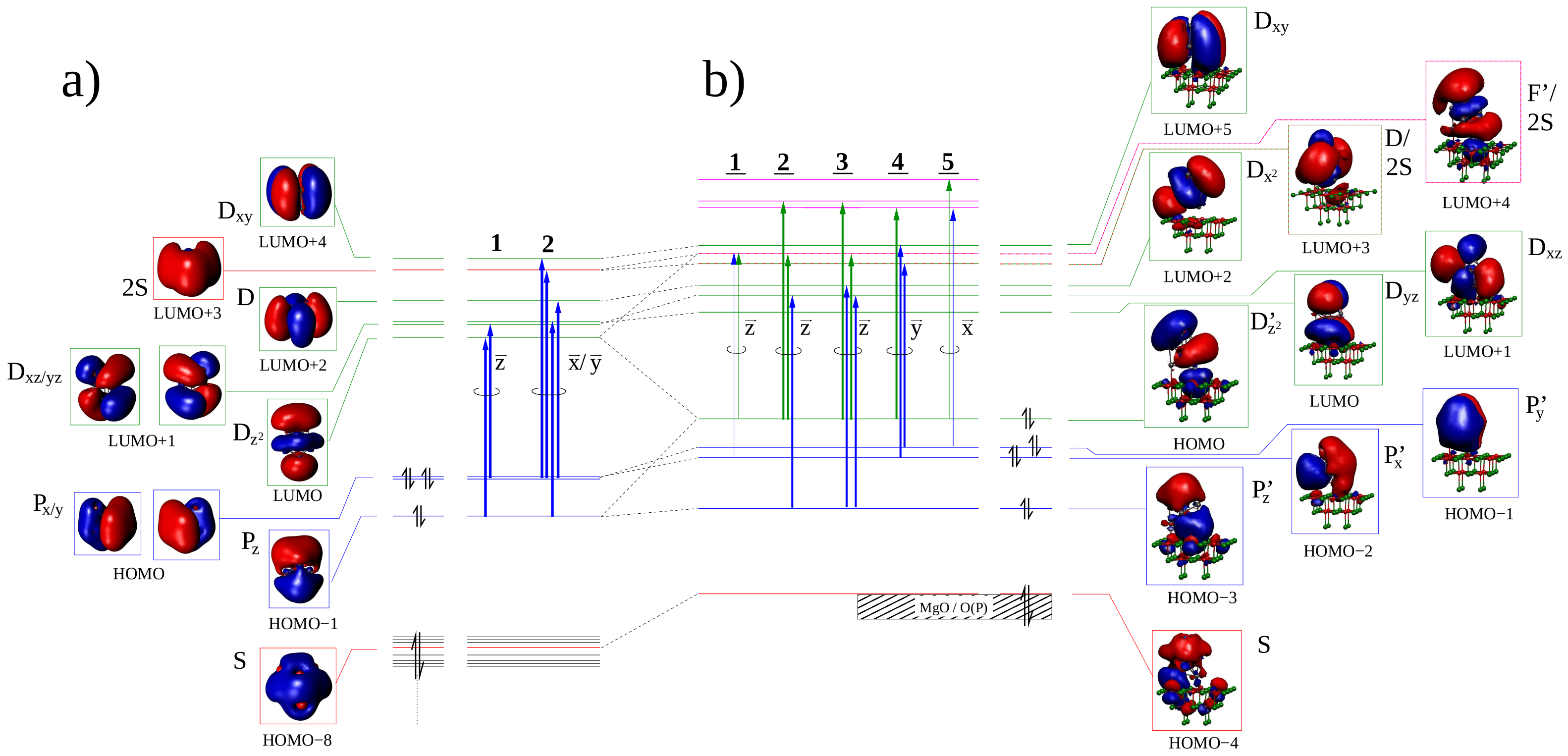

Figure A.7: MO diagram for a) gas phase Ag_8 (D_{2d}) and b) $Ag_8@F_{5c}$(**IV**) [D_{2d}]. Corresponding orbitals are connected by dashed lines. The frames around the orbitals and the corresponding energy levels are colored in order to illustrate the character of the orbitals (red: S-type, blue: P-type, green: D-type, purple: higher MO angular momentum quantum number). Leading excitations are indicated by vertical lines from initial to final orbitals (for weights see Tables 11.2 and A.8) and $\overrightarrow{x}/\overrightarrow{y}/\overrightarrow{z}$ indicate the polarization of the corresponding transitions [**1-2** for a) and **1**-**5** for b)].

Table A.1: Ionization potentials of gas phase $\mathrm{Ag_n}$ clusters and $\mathrm{Ag_n}$ clusters at the MgO (100) support ($\mathrm{O_{5c}}$) and the F_S center defect ($\mathrm{F_{5c}}$) (n=2, 4, 6, 8). For definitions of $\mathrm{IP_0}$ and $\mathrm{IP_I}$ see Chapter 10.

n	local symmetry	$\mathrm{Ag_n}$		$\mathrm{Ag_n@O_{5c}}$		$\mathrm{Ag_n@F_{5c}}$	
	of isomer	IP [eV]	$\mathrm{IP_{exp}}$ [eV][a]	$\mathrm{IP_0}$ [eV]	$\mathrm{IP_I}$ [eV]	$\mathrm{IP_0}$ [eV]	$\mathrm{IP_I}$ [eV]
0	-	-	-	7.409	6.716	4.115	3.458
2	$\mathrm{D}_{\infty h}$	7.888	7.60	6.320	5.981	4.315	3.913
4	D_{2h}	6.555	6.65	5.029	4.684	5.056	4.604
	C_{2v}	6.627		5.266	4.895	-	-
6	D_{3h}	7.129	7.15	5.327	5.027	-	-
	[C_S]	-		-	-	4.863	4.505
8	T_d	6.926	7.10	-	-	4.236	3.893
	D_{2d}	6.700		5.266	4.965	4.437	4.103
	C_{2v}	6.544		5.149	4.825	-	-
	[C_1][b]	-		-	-	4.559	4.186
	[C_{2v}][c]	-		-	-	4.532	4.165
	[C_{2h}][d]	-		-	-	4.286	3.917

[a] Experimental values obtained from Ref. [223].[b] $\mathrm{Ag_8@F_{5c}}$(**I**). [c] $\mathrm{Ag_8@F_{5c}}$(**II**). [d] $\mathrm{Ag_8@F_{5c}}$(**III**).

Table A.2: Weights of leading excitations for transitions in gas phase Ag_8 (**III**, C_{2v}). Transition energies T_e are in eV, oscillator strengths f_e are given in parenthesis. Transitions are labelled with **1-4** according to the notation in the spectrum (Figure 11.5). In cases where the same leading excitations with different weights are involved in two transitions, the contributing excitations are shown only once, and weights in corresponding transitions are separated by horizontal dashed lines.

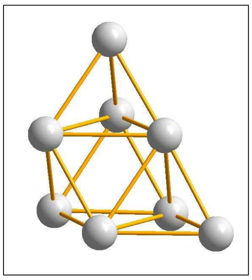

C_{2v}

Label	T_e[eV] (f_e)	Leading Excitations					
1	3.38 (0.26)	70% 41%	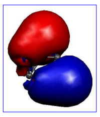	P_z	→	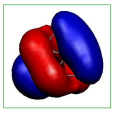	D
2	3.58 (0.97)	19% 28%	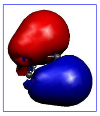	P_z	→	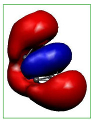	D_{z^2}
3	3.94 (1.07)	27%	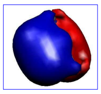	P_y	→	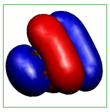	D_{xy}
		23%	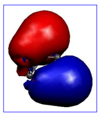	P_z	→	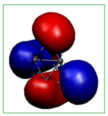	D_{xz}
		18%	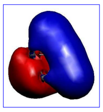	P_x	→	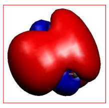	2S
		17%	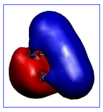	P_x	→	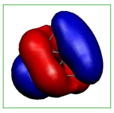	D
4	4.11 (1.07)	30%	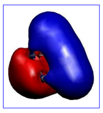	P_x	→	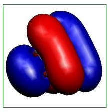	D_{xy}
		25%	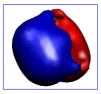	P_y	→	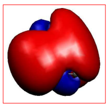	2S
		19%	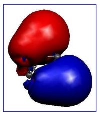	P_z	→	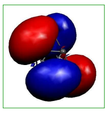	D_{yz}

Table A.3: Weights of leading excitations for transitions in $Ag_6@O_{5c}$(**I**) [D_{3h}]. Transition energies T_e are in eV, oscillator strengths f_e are given in parenthesis. Transitions are labelled with **1**-**5** according to the notation in the spectrum (Figure 13.8). In the cases where the same leading excitations with different weights are involved in three transitions (**1**-**3**), the contributing excitations are shown only once, and weights in corresponding transition are separated by horizontal dashed lines.

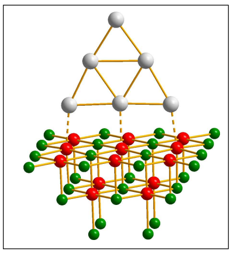

C_S

Label	T_e[eV] (f_e)	Leading Excitations					
1 **2** **3**	2.88 (0.18) 2.95 (0.13) 3.02 (0.30)	67% 17% 15%	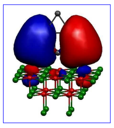	P_x	→	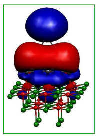	D
		17% 13% 24%	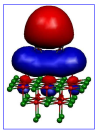	P_z	→	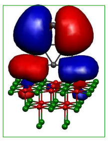	D_{xz}
		14% 9% 18%	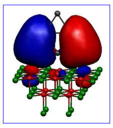	P_x	→	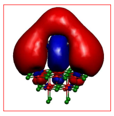	2S
		<1% 60% 39%	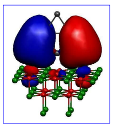	P_x	→	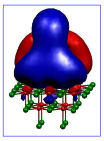	P_y
4	3.35 (1.26)	41%	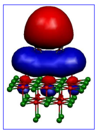	P_z		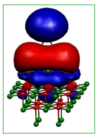	D
		37%	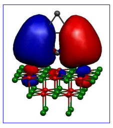	P_x		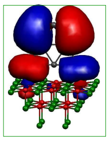	D_{xz}

Table A.4: Weights of leading excitations for transitions in $Ag_8@O_{5c}$(**I**) [C_{2v}]. Transition energies T_e are in eV, oscillator strengths f_e are given in parenthesis. Transitions are labelled with **1**-**4** according to the notation in the spectrum (Figure 13.9).

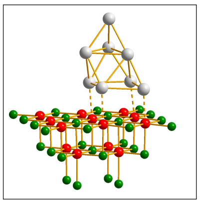

C_S [C_{2v}]

Label	T_e[eV] (f_e)	Leading Excitations					
1	3.19 (0.37)	50%	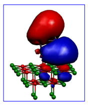	P_z	→	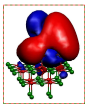	2S/ D
		15%	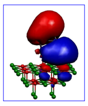	P_z	→	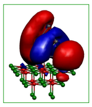	D_{z^2}
		13%	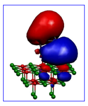	P_z	→	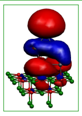	D
2	3.38 (0.56)	21%	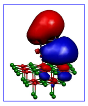	P_z	→	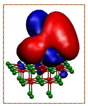	2S/ D
		18%	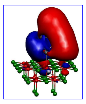	P_x	→	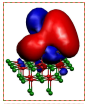	2S/ D
		16%	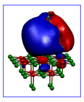	P_y	→	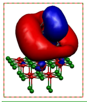	2S/ D
		15%	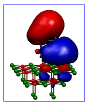	P_z	→	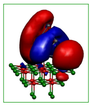	D_{z^2}
3	3.46 (0.72)	25%	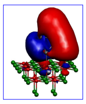	P_x		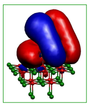	D_{xy}
		22%	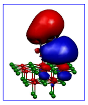	P_z		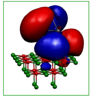	D_{yz}
		20%	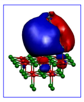	P_y		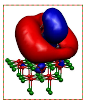	2S/ D
		12%	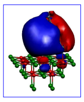	P_y		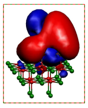	2S/ D
4	3.63 (1.32)	26%	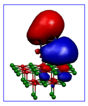	P_z		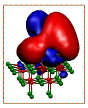	2S/ D
		23%	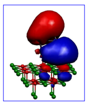	P_z		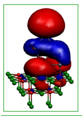	D
		15%	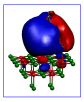	P_y		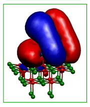	D_{xy}

Table A.5: Weights of leading excitations for transitions in $Ag_8@O_{5c}$(**II**) [D_{2d}]. Transition energies T_e are in eV, oscillator strengths f_e are given in parenthesis. Transitions are labelled with **1**-**3** according to the notation in the spectrum (Figure 13.9).

Label	T_e[eV] (f_e)	Leading Excitations					
1	3.53 (0.87)	32%	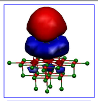	P_z	→	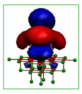	D_{z^2}
		23%	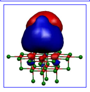	P_y	→	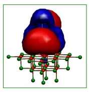	D_{yz}
		16%	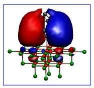	P_x	→	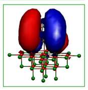	D_{xy}
		11%	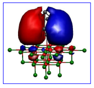	P_x	→	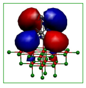	D_{xz}
2	3.54 (0.66)	30%	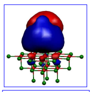	P_y	→	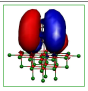	D_{xy}
		19%	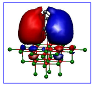	P_x	→	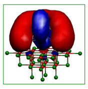	D
		15%	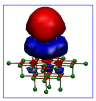	P_z	→	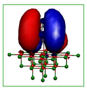	D_{xy}
		12%	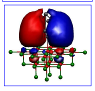	P_x	→	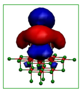	D_{z^2}

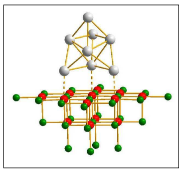

C_S [D_{2d}]

Label	T_e[eV] (f_e)	Leading Excitations					
3	3.82 (1.37)	41%	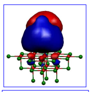	P_y	→	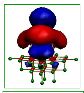	D_{z^2}
		22%	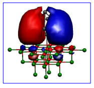	P_x	→	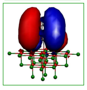	D_{xy}
		16%	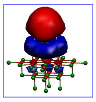	P_z	→	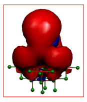	2S

Table A.6: Weights of leading excitations for transitions in $Ag_6@F_{5c}$(**I**) [C_S]. Transition energies T_e are in eV, oscillator strengths f_e are given in parenthesis. Transitions are labelled with **1**-**9** according to the notation in the spectrum (Figure 14.7a). In cases where the same leading excitations with different weights are involved in electronic transitions (e.g. **5** and **6**), the contributing excitations are shown only once, and weights in corresponding transition are separated by horizontal dashed lines.

Label	T_e[eV] (f_e)	Leading Excitations					
1	2.76 (0.04)	45% 46%	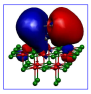	P_x'	→	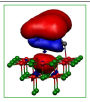	D’
		31% 17%	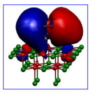	P_x'	→	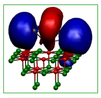	D_{x^2}
3	2.88 (0.16)	9% 16%	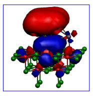	P_z'	→	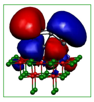	D_{xz}
2	2.79 (0.07)	56%	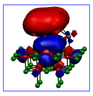	P_z'	→	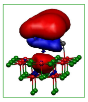	D’
		23%	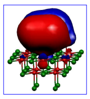	P_y'	→	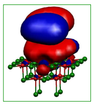	D_{yz}
4	3.10 (0.13)	41%	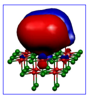	P_y'	→	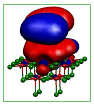	D_{yz}
		29%	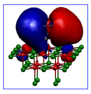	P_x'	→	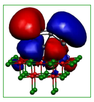	D_{xz}
		17%	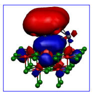	P_z'	→	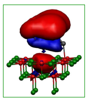	D’
5	3.55 (0.31)	56% 41%	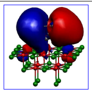	P_x'	→	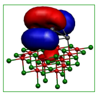	D
6	3.62 (0.39)	25% 30%	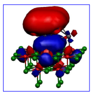	P_z'	→	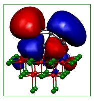	D_{xz}
7	3.72 (0.39)	56% 26% 16%	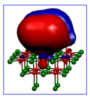	P_y'	→	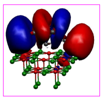	F
		16% 17% 5%	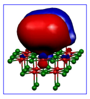	P_y'	→	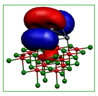	D
8	3.84 (0.65)	<1% 3% 12%	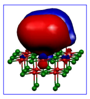	P_y'	→	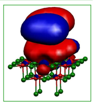	D_{yz}
9	3.85 (0.71)	<1% 2% 16%	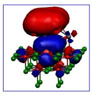	P_z'	→	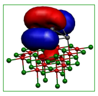	D
		14% 2% 5%	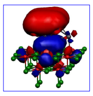	P_z'	→	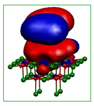	D_{yz}
		<1% 14% 19%	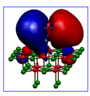	P_x'	→	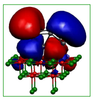	D_{xz}

Table A.7: Weights of leading excitations for transitions in Ag$_8$@F$_{5c}$ (**III**) [C$_{2h}$]. Transition energies T$_e$ are in eV, oscillator strengths f$_e$ are given in parenthesis. Transitions are labelled with **1**-**8** according to the notation in the spectrum (Figure 14.9).

Label	T$_e$[eV] (f$_e$)	Leading Excitations			
1	2.66 (0.57)	21%	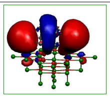 D$_{x^2}$	→	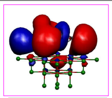 F
		19%	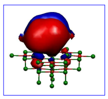 P$_y$’	→	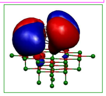 D$_{xy}$
		17%	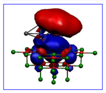 P$_z$’	→	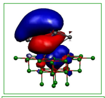 D’
		14%	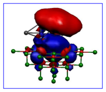 P$_z$’	→	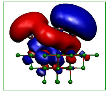 D$_{xz}$
		12%	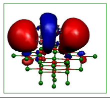 D$_{x^2}$	→	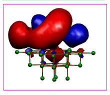 F
2	3.22 (0.29)	32%	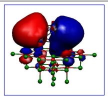 P$_x$’	→	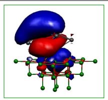 D’
		21%	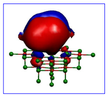 P$_y$’	→	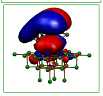 D$_{yz}$
		15%	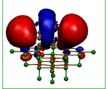 D$_{x^2}$	→	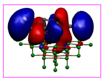 F
3	3.31 (0.29)	49%	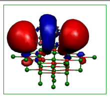 D$_{x^2}$	→	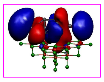 F
		25%	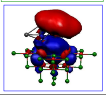 P$_z$’	→	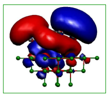 D$_{xz}$
4	3.46 (0.42)	32%	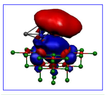 P$_z$’	→	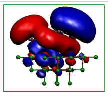 D$_{xz}$
		19%	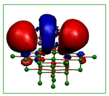 D$_{x^2}$	→	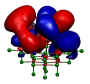 F
		11%	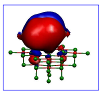 P$_y$’	→	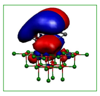 D$_{yz}$
5	3.66 (0.28)	35%	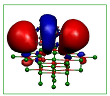 D$_{x^2}$	→	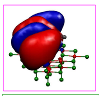 F
		20%	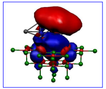 P$_z$’	→	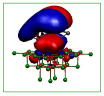 D$_{yz}$
		11%	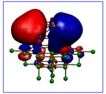 P$_x$’	→	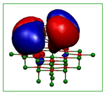 D$_{xy}$
		10%	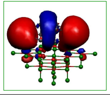 D$_{x^2}$	→	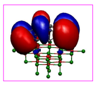 F
6	3.82 (0.25)	61%	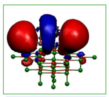 D$_{x^2}$	→	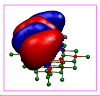 F
		15%	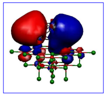 P$_x$’	→	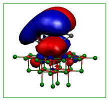 D$_{yz}$
7	4.15 (0.34)	28%	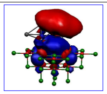 P$_z$’	→	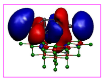 F
		16%	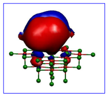 P$_y$’	→	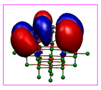 F
		16%	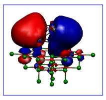 P$_x$’	→	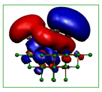 D$_{xz}$
8	4.31 (0.24)	68%	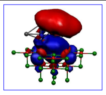 P$_z$’	→	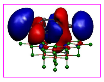

Table A.8: Weights of leading excitations for transitions in $Ag_8@F_{5c}$ (**IV**) [D_{2d}]. Transition energies T_e are in eV, oscillator strengths f_e are given in parenthesis. Transitions are labelled with **1**-**5** according to the notation in the spectrum (Figure 14.10a).

Label	T_e[eV] (f_e)	Leading Excitations			
1	3.04 (0.13)	72%	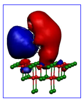 P'_x	→	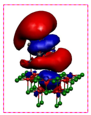 F'/ 2S
		7%	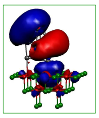 D'_{z^2}	→	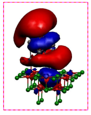 F'/ 2S
2	3.29 (0.80)	24% 34%	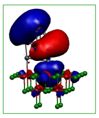 D'_{z^2}	→	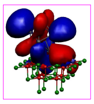 F
		21% 12%	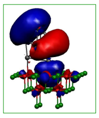 D'_{z^2}	→	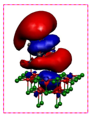 F'/ 2S
3	3.44 (0.84)	19% 9%	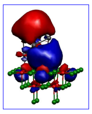 P'_z	→	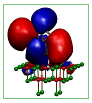 D_{xz}
		<1% 22%	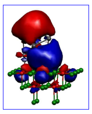 P'_z	→	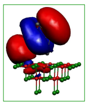 D_{x^2}
4	3.74 (0.62)	24%	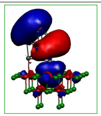 D'_{z^2}	→	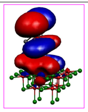 F
		22%	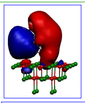 P'_x	→	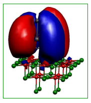 D_{xy}
		15%	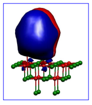 P'_y	→	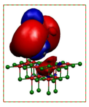 D/ 2S
5	3.93 (0.32)	29%	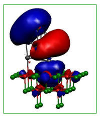 D'_{z^2}	→	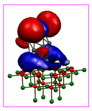 F
		21%	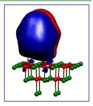 P'_y	→	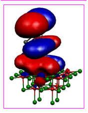 F

Table A.9: Weights of leading excitations for transitions in $Ag_8@F_{5c}$ (**V**) [T_d]. Transition energies T_e are in eV, oscillator strengths f_e are given in parenthesis. Transitions are labelled with **1**-**5** according to the notation in the spectrum (Figure 14.10b).

Label	T_e[eV] (f_e)	Leading Excitations			
1	2.66 (0.09)	49%	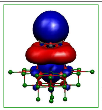 D'_{z^2}	→	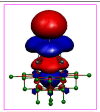 F'
		33%	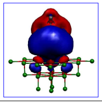 P'_y	→	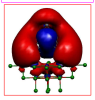 2S
2	3.21 (0.36)	30%	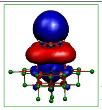 D'_{z^2}	→	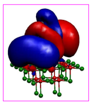 F
		15%	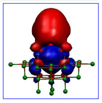 P'_z	→	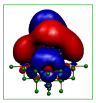 D
		13%	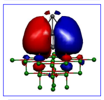 P'_x	→	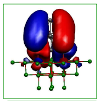 D
		11%	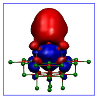 P'_z	→	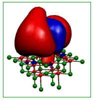 D_{y^2}
3	3.46 (0.18)	76%	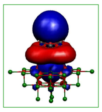 D'_{z^2}	→	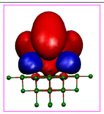 F
		11%	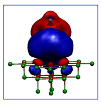 P'_y	→	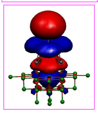 F'

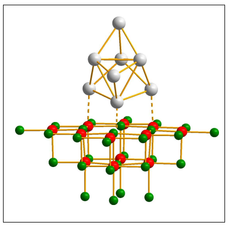

C_S

Label	T_e[eV] (f_e)	Leading Excitations			
4	3.66 (1.32)	37%	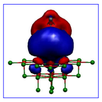 P'_y	→	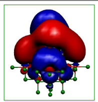 D
		14%	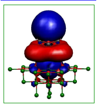 D'_{z^2}	→	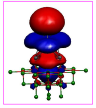 F'
		14%	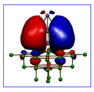 P'_x	→	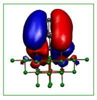 D
5	3.90 (0.55)	37%	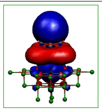 D'_{z^2}	→	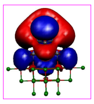 F
		21%	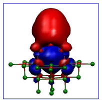 P'_z	→	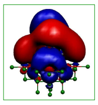 D

Bibliography

[1] M. Haruta, N. Yamada, T. Kobayashi, and S. Iijima. *J. Catal.*, 115(2): 301, 1989.

[2] M. Haruta, S. Tsubota, T. Kobayashi, H. Kageyama, M. J. Genet, and B. Delmon. *J. Catal.*, 144(1):175, 1993.

[3] M. Haruta. *Catal. Today*, 36(1):153, 1997.

[4] M. Daté and M. Haruta. *J. Catal.*, 201:221, 2001.

[5] P. Pyykkö. *Angew. Chem. Int. Ed.*, 43:4412, 2004.

[6] C. W. Corti, R. J. Holliday, and D. T. Thompson. *Appl. Catal. A: General*, 291:253, 2005.

[7] G. C. Bond, C. Louis, and D. T. Thompson. volume 6 of *Catalytic Science Series*. Imperial College Press, London, 2006.

[8] H. Huber, D. McIntosh, and G. A. Ozin. *Inorg. Chem.*, 16:975, 1977.

[9] D. M. Cox, R. Brickman, K. Creegan, and A. Kaldor. *Z. Phys. D*, 19: 353, 1991.

[10] K. J. Taylor, C. L. Pettiette-Hall, O. Cheshnovsky, and R. E. Smalley. *J. Chem. Phys.*, 96(4):3319, 1992.

[11] T. H. Lee and K. M. Ervin. *J. Phys. Chem.*, 98(40):10023, 1994.

[12] M. Valden, X. Lai, and D. W. Goodman. *Science*, 281:1647, 1998.

[13] G. C. Bond and D. T. Thompson. *Catal. Rev.-Sci. Eng.*, 41:319, 1999.

[14] A. Sanchez, S. Abbet, W.-D. Heiz, U. Schneider, H. Häkkinen, R. N. Barnett, and U. Landman. *J. Phys. Chem. A*, 103:9573, 1999.

[15] B. E. Salisbury, W. T. Wallace, and R. L. Whetten. *Chem. Phys.*, 262: 131, 2000.

[16] H. Häkkinen and U. Landman. *J. Am. Chem. Soc.*, 123:9704, 2001.

[17] H. S. Oh, C. K. Costello, C. Cheung, H. H. Kung, and M. C. Kung. *Stud. Surf. Sci. Catal.*, 139:375, 2001.

[18] J. Hagen, L. D. Socaciu, M. Elijazyfer, U. Heiz, T. M. Bernhardt, and L. Wöste. *Phys. Chem. Chem. Phys.*, 4(10):1707, 2002.

[19] J. Guzman and B. C. Gates. *J. Phys. Chem. B*, 106(31):7659, 2002.

[20] N. Lopez and J. K. Nørskov. *J. Am. Soc. Chem.*, 124(38):11262, 2002.

[21] W. T. Wallace and R. L. Whetten. *J. Am. Chem. Soc.*, 124:7499, 2002.

[22] W. T. Wallace, R. B. Wyrwas, R. L. Whetten, R. Mitrić, and V. Bonačić-Koutecký. *J. Am. Chem. Soc.*, 125:8408, 2003.

[23] Y. D. Kim, M. Fischer, and G. Ganteför. *Chem. Phys. Lett.*, 377:170, 2003.

[24] T. S. Kim, J. D. Stiehl, C. T. Reeves, R. J. Meyer, and C. B. Mullins. *J. Am. Chem. Soc.*, 125:2018, 2003.

[25] D. Stolčić, M. Fischer, G. Ganteför, Y. D. Kim, Q. Sun, and P. Jena. *J. Am. Chem. Soc.*, 125:2848, 2003.

[26] J. Guzman and B. C. Gates. *Angew. Chem. Int. Ed.*, 42:690, 2003.

[27] A. Cho. *Science*, 299(5613):1684, 2003.

[28] L. D. Socaciu, J. Hagen, T. M. Bernhardt, L. Wöste, U. Heiz, H. Häkkinen, and U. Landman. *J. Am. Chem. Soc.*, 125:10437, 2003.

[29] H. H. Kung, M. C. Kung, and C. K. Costello. *J. Catal.*, 216(1-2):425, 2003.

[30] C. K. Costello, M. C. Kung, H. S. Oh, Y. Wang, and H. H. Kung. *Appl. Catal. A: General*, 232:159, 2002.

[31] M. S. Chen and D. W. Goodman. *Science*, 306(5694):252, 2004.

[32] J. Guzman and B. C. Gates. *J. Am. Soc. Chem.*, 126(9):2672, 2004.

[33] T. M. Bernhardt. *Int. J. Mass. Spectrom.*, 243:1, 2005.

[34] G. A. Somorjai. John Wiley and Sons, New York, 1994. p. 402.

[35] E. F. Fialko, A. V. Kikhtenko, V. B. Goncharov, and K. I. Zamaraev. *J. Phys. Chem. B*, 101:5772, 1997.

[36] G. J. Hutchings, M. S. Hall, A. F. Carley, P. Landon, B. E. Solsona, C. J. Kiely, A. Herzing, M. Makkee, J. A. Moulijn, A. Overweg, J. C. Fierro-Gonzalez, J. Guzman, and B. C. Gates. *J. Catal.*, 242(1):71, 2006.

[37] L. Fu, N. Q. Wu, J. H. Yang, F. Qu, D. L. Johnson, M. C. Kung, H. H. Kung, and V. P. Dravid. *J. Phys. Chem. B*, 109:3704, 2005.

[38] J. C. Love, L. A. Estroff, J. K. Kriebel, R. G. Nuzzo, and G. M. Whitesides. *Chem. Rev.*, 105(4):1103, 2005.

[39] L. D. Socaciu, J. Hagen, J. Le Roux, D. Popolan, T. M. Bernhardt, L. Wöste, and S. Vajda. *J. Chem. Phys.*, 120:2078, 2004.

[40] S. Lochbrunner, J. J. Larsen, J. P. Shaffer, M. Schmitt, T. Schultz, J. G. Underwood, and A. Stolow. *J. Electron Spectrosc. Relat. Phenom.*, 112 (1-3):183, 2000.

[41] A. Stolow. *Annu. Rev. Phys. Chem.*, 54:89, 2003.

[42] V. Bonačić-Koutecký and R. Mitrić. *Chem. Rev.*, 105:11, 2005.

[43] L. A. Peyser, A. E. Vinson, A. P. Bartko, and R. M. Dickson. *Science*, 291:103, 2001.

[44] L. A. Peyser, T. H. Lee, and R. M. Dickson. *J. Phys. Chem. B*, 106 (32):7725, 2002.

[45] T. H. Lee and R. M. Dickson. *Proc. Natl. Acad. Sci.*, 100:3043, 2003.

[46] M. A. Duncan. *Advances in Metal and Semiconductor Clusters*, volume 1, pages 123–157. JAI Press, New York, 1993.

[47] T. Gleitsmann, B. Stegemann, and T. M. Bernhardt. *Appl. Phys. Lett.*, 84:4050, 2004.

[48] P. Fayet, F. Granzer, G. Hegenbart, E. Moisar, B. Pischel, and L. Wöste. *Phys. Rev. Lett.*, 55(27):3002, 1985.

[49] R. S. Eachus, A. P. Marchetti, and A. A. Münter. *Annu. Rev. Phys. Chem.*, 50:117, 1999.

[50] J. Zheng and R. M. Dickson. *J. Am. Chem. Soc.*, 124:13982, 2002.

[51] J. Zheng, J. T. Petty, and R. M. Dickson. *J. Am. Chem. Soc.*, 125: 7780, 2003.

[52] T.-H. Lee and R. M. Dickson. *J. Phys. Chem. B*, 107:7387, 2003.

[53] T.-H. Lee, J. I. González, J. Zheng, and R. M. Dickson. *Acc. Chem. Res.*, 38:534, 2005.

[54] T. Gleitsmann, T. M. Bernhardt, and L. Wöste. *Appl. Phys. A*, 82: 125, 2006.

[55] L. Peyser-Capadona, J. Zheng, J. I. González, T.-H. Lee, S. A. Patel, and R. M. Dickson. *Phys. Rev. Lett.*, 94:058301, 2005.

[56] J. Yu, S. A. Patel, and R. M. Dickson. *Angew. Chem. Int. Ed.*, 46: 2028, 2007.

[57] J. Yu, S. Choi, and R. M. Dickson. *Angew. Chem. Int. Ed.*, 48:318, 2009.

[58] T. Baumert, R. Thalweiser, V. Weiss, and G. Gerber. *Z. Phys. D*, 26 (1-4):131, 1993.

[59] S. Fedrigo, W. Harbich, and J. Buttet. *Phys. Rev. B*, 47(16):10706, 1993.

[60] S. Fedrigo, W. Harbich, and J. Buttet. *Phys. Rev. B*, 58(11):7428, 1998.

[61] C. Félix, W. Harbich, J. Buttet, I. Rabin, W. Schulze, and G. Ertl. *Chem. Phys. Lett.*, 313:105, 1999.

[62] C. Félix, C. Sieber, W. Harbich, J. Buttet, I. Rabin, W. Schulze, and G. Ertl. *Phys. Rev. Lett.*, 86:2992, 2001.

[63] C. Sieber, J. Buttet, W. Harbich, C. Félix, R. Mitrić, and V. Bonačić-Koutecký. *Phys. Rev. A*, 70:041201, 2004.

[64] U. Kreibig. *Handbook of optical properties*, volume 2. CRC Press, Boca Raton, 1997.

[65] C. Bürgel, R Mitrić, and V. Bonačić-Koutecký. *Appl. Phys. A*, 82(1): 117, 2006.

[66] A. M. Ferrari and G. Pacchioni. *J. Phys. Chem.*, 100:9032, 1996.

[67] I. Yudanov, G. Pacchioni, K. M. Neyman, and N. Rösch. *J. Phys. Chem. B*, 101:2786, 1997.

[68] A. M. Ferrari, C. Xiao, K. M. Neyman, G. Pacchioni, and N. Rösch. *Phys. Chem. Chem. Phys.*, 1:4655, 1999.

[69] A. V. Matveev, K. M. Neyman, I. V. Chudanov, and N. Rösch. *Surf. Sci.*, 426:123, 1999.

[70] A. V. Matveev, K. M. Neyman, G. Pacchioni, and N. Rösch. *Chem. Phys. Lett.*, 299:603, 1999.

[71] A. Bogicevic and D. R. Jennison. *Surf. Sci.*, 515:L481, 2002.

[72] K. M. Neyman, C. Inntam, V. A. Nasluzov, R. Kosarev, and N. Rösch. *Appl. Phys. A*, 78:823, 2004.

[73] G. Barcaro and A. Fortunelli. *J. Chem. Theory Comput.*, 1:972, 2005.

[74] K. M. Neyman, C. Inntam, A. V. Matveev, V. A. Nasluzov, , and N. Rösch. *J. Am. Chem. Soc.*, 127:11652, 2005.

[75] B. Yoon, H. Häkkinen, U. Landman, A. S. Wörz, J. M. Antonietti, S. Abbet, K. Judai, and U. Heiz. *Science*, 307:403, 2005.

[76] L. Giordano, M. Baistrocchi, and G. Pacchioni. *Phys. Rev. B*, 72: 115403, 2005.

[77] C. Inntam, L. V. Moskaleva, I. V. Yudanov, K. M. Neyman, and N. Rösch. *Chem. Phys. Lett.*, 417:515, 2006.

[78] C. Inntam, L. V. Moskaleva, K. M. Neyman, V. A. Nasluzov, and N. Rösch. *Appl. Phys. A*, 82:181, 2006.

[79] A. del Vitto, C. Sousa, F. Illas, and G. Pacchioni. *J. Chem. Phys.*, 121: 7457, 2004.

[80] M. Walter and H. Häkkinen. *Phys. Rev. B*, 72:205440, 2005.

[81] V. Bonačić-Koutecký, J. Pittner, M. Boiron, and P. Fantucci. *J. Chem. Phys.*, 110:3876, 1999.

[82] V. Bonačić-Koutecký, V. Veyret, and R. Mitrić. *J. Chem. Phys.*, 115: 10450, 2001.

[83] J. H. Schulman and W. D. Compton. Pergamon Press, New York, 1962.

[84] M. L. Kimble, N. A. Moore, G. E. Johnson, A. W. Castleman, Jr., C. Bürgel, R. Mitrić, and V. Bonačić-Koutecký. *J. Chem. Phys.*, 125 (20):204311, 2006.

[85] C. Bürgel, 2004. Humboldt Universität zu Berlin, Diplomarbeit.

[86] V. Bonačić-Koutecký, R. Mitrić, C. Bürgel, and B. Schäfer-Bung. *Comput. Mater. Sci.*, 35(3):151, 2006.

[87] L. M. Molina and B. Hammer. *Appl. Catal. A: General*, 291(1-2):21, 2005.

[88] A. Bongiorno and U. Landman. *Phys. Rev. Lett.*, 95(10):106102, 2005.

[89] C. Zhang, B. Yoon, and U. Landman. *J. Am. Soc. Chem.*, 129(8):2228, 2007.

[90] K. Honkala and H. Häkkinen. *J. Phys. Chem. C*, 111(11):4319, 2007.

[91] G. C. Bond and D. T. Thompson. *Gold Bull.*, 33(2):41, 2000.

[92] X. Q. Gong, P. Hu, and R. Raval. *J. Chem. Phys.*, 119(12):6324, 2003.

[93] M. Sterrer, T. Risse, U. M. Pozzoni, L. Giordano, M. Heyde, H.-P. Rust, G. Pacchioni, and H.-J. Freund. *Phys. Rev. Lett.*, 98(9):096107, 2007.

[94] A. D. Becke. *J. Chem. Phys.*, 98:5648, 1993.

[95] C. Lee, W. Yang, and R. G. Parr. *Phys. Rev. B*, 37:785, 1988.

[96] S. J. Vosko, L. Wilk, and M. Nusair. *Can. J. Phys.*, 58:1200, 1980.

[97] P. J. Stephens, F. J. Devlin, C. F. Chabalowski, and M. J. Frisch. *J. Phys. Chem.*, 98:11623, 1994.

[98] D. Andrae, U. Haeussermann, M. Dolg, H. Stoll, and H. Preuss. *Theor. Chim. Acta*, 77:123, 1990.

[99] S. Gilb, P. Weis, F. Furche, R. Ahlrichs, and M. M. Kappes. *J. Chem. Phys.*, 116(10):4094, 2002.

[100] M. L. Kimble, A. W. Castleman, Jr., R Mitrić, C. Bürgel, and V Bonačić-Koutecký. *J. Am. Soc. Chem.*, 126(8):2526, 2004.

[101] A. E. Reed, R. B. Weinstock, and F. Weinhold. *J. Chem. Phys.*, 83(2): 735, 1985.

[102] B. I. Dunlap, J. W. D. Connolly, and J. R. Sabin. *J. Chem. Phys.*, 71: 3396, 1979.

[103] K. Eichkorn, O. Treutler, H. Öhm, M. Häser, and R. Ahlrichs. *Chem. Phys. Lett.*, 240:283, 1995.

[104] J. P. Perdew, K. Burke, and M. Ernzerhof. *Phys. Rev. Lett.*, 77:3865, 1996.

[105] R. C. Bell, K. A. Zemski, D. R. Justes, and A. W. Castleman, Jr. *J. Chem. Phys.*, 114:798, 2001.

[106] L. M. Molina and B. Hammer. *Phys. Rev. B*, 69(15):155424, 2004.

[107] M. L. Kimble, A. W. Castleman, Jr., C. Bürgel, and V. Bonačić-Koutecký. *Int. J. Mass. Spectrom.*, 254(3):163, 2006.

[108] C. Bürgel, N. M. Reilly, G. E. Johnson, R. Mitrić, M. L. Kimble, A. W. Castleman, Jr., and V. Bonačić-Koutecký. *J. Am. Chem. Soc.*, 130: 1694, 2008.

[109] O. K. Rice and H. C. Ramsperger. *J. Am. Chem. Soc.*, 49:1617, 1927.

[110] L. S. Kassel. *J. Phys. Chem.*, 32:1065, 1928.

[111] D. C. Lim, I. Lopez-Salido, R. Dietsche, M. Bubek, and Y. D. Kim. *Angew. Chem. Int. Ed.*, 45:2413, 2006.

[112] M. L. Kimble and A. W. Castleman, Jr. *Int. J. Mass. Spectrom.*, 233: 99, 2004.

[113] G. E. Johnson, Nelly M. Reilly, E. C. Tyo, and A. W. Castleman, Jr. *J. Phys. Chem. C*, 112:9730, 2008.

[114] R. Meyer, C. Lemire, S. K. Shaikhutdinov, and H.-J. Freund. *Gold Bull.*, 37(1-2):72, 2004.

[115] S. S. Lee, C. Y. Fan, T. P. Wu, and S. L. Anderson. *J. Am. Soc. Chem.*, 126(18):5682, 2004.

[116] M. Date, M. Okumura, S. Tsubota, and M. Haruta. *Angew. Chem. Int. Ed.*, 43(16):2129–2132, 2004.

[117] C. Lemire, R. Meyer, S. Shaikhutdinov, and H.-J. Freund. *Angew. Chem. Int. Ed.*, 43(1):118, 2004.

[118] X. Y. Deng, B. K. Min, A. Guloy, and C. M. Friend. *J. Am. Soc. Chem.*, 127(25):9267, 2005.

[119] J. D. Stiehl, T. S. Kim, S. M. McClure, and C. B. Mullins. *J. Phys. Chem. B*, 109(13):6316, 2005.

[120] M. Sterrer, M. Yulikov, T. Risse, H.-J. Freund, J. Carrasco, F. Illas, C. Di Valentin, L. Giordano, and G. Pacchioni. *Angew. Chem. Int. Ed.*, 45(16):2633, 2006.

[121] M. Sterrer, M. Yulikov, E. Fischbach, M. Heyde, H. P. Rust, G. Pacchioni, T. Risse, and H.-J. Freund. *Angew. Chem. Int. Ed.*, 45(16): 2630, 2006.

[122] D. Matthey, J. G. Wang, S. Wendt, J. Matthiesen, R. Schaub, E. Laegsgaard, B. Hammer, and F. Besenbacher. *Sience*, 315(5819):1692, 2007.

[123] Y. D. Kim, M. Niemietz, P. Gerhardt, F. von Gynz-Rekowski, and G. Ganteför. *Phys. Rev. B*, 70(3):035421, 2004.

[124] T. Ichino, A. J. Gianola, D. H. Andrews, and W. C. Lineberger. *J. Phys. Chem. A*, 108(51):11307, 2004.

[125] L. C. O'Brien, S. C. Hardimon, and J. J. O'Brien. *J. Phys. Chem. A*, 108(51):11302, 2004.

[126] T. Okabayashi, F. Koto, K. Tsukamoto, E. Yamazaki, and M. Tanimoto. *Chem. Phys. Lett.*, 403(1-3):223, 2005.

[127] L. C. O'Brien, A. E. Oberlink, and B. O. Roos. *J. Phys. Chem. A*, 110 (43):11954, 2006.

[128] W. Zheng, X. Li, S. Eustis, A. Grubisic, O. Thomas, H. de Clercq, and K. Bowen. *Chem. Phys. Lett.*, 444(4-6):232, 2007.

[129] D. McIntosh and G. A. Ozin. *J. Organomet. Chem.*, 121(1):127, 1976.

[130] M. J. Griffiths and R. F. Barrow. *J. Chem. Soc - Farad. Trans. II*, 73: 943, 1977.

[131] J. A. Howard, R. Sutcliffe, and B. Mile. *J. Phys. Chem.*, 88(19):4351, 1984.

[132] P. H. Kasai and P. M. Jones. *J. Phys. Chem.*, 90(18):4239, 1986.

[133] A. Citra and L. Andrews. *Theochem-J. Mol. Struct.*, 489(2-3):95, 1999.

[134] X. F. Wang and L. Andrews. *J. Phys. Chem. A*, 105(24):5812, 2001.

[135] Q. Sun, P. Jena, Y. D. Kim, M. Fischer, and Ganteför. *J. Chem. Phys.*, 120:6510, 2004.

[136] P. Schwerdtfeger, M. Dolg, W. H. E. Schwarz, G. A. Bowmaker, and P. D. W. Boyd. *J. Chem. Phys.*, 91(3):1762, 1989.

[137] M. Okumura, Y. Kitagawa, M. Haruta, and K. Yamaguchi. *Chem. Phys. Lett.*, 346:163, 2001.

[138] P. D. Jadzinsky, G. Calero, C. J. Ackerson, D. A. Bushnell, and R. D. Kornberg. *Science*, 318:430, 2007.

[139] D. Figgen, G. Rauhut, M. Dolg, and H. Stoll. *Chem. Phys.*, 311(1-2):227, 2005.

[140] K. A. Peterson and C. Puzzarini. *Theor. Chem. Acc.*, 114(4-5):283–296, 2005.

[141] H.-J. Werner and P. J. Knowles. *J. Chem. Phys.*, 89:5803, 1988.

[142] P. J. Knowles and H.-J. Werner. *Chem. Phys. Letters*, 145:514, 1988.

[143] H.-J. Werner, P. J. Knowles, R. Lindh, F. R. Manby, M. Schütz, P. Celani, T. Korona, A. Mitrushenkov, G. Rauhut, T. B. Adler, R. D. Amos, A. Bernhardsson, A. Berning, D. L. Cooper, M. J. O. Deegan, A. J. Dobbyn, F. Eckert, E. Goll, C. Hampel, G. Hetzer, T. Hrenar, G. Knizia, C. Köppl, Y. Liu, A. W. Lloyd, R. A. Mata, A. J. May, S. J. McNicholas, W. Meyer, M. E. Mura, A. Nicklass, P. Palmieri, K. Pflüger, R. Pitzer, M. Reiher, U. Schumann, H. Stoll, A. J. Stone, R. Tarroni, T. Thorsteinsson, M. Wang, and A. Wolf, 2008. see http://www.molpro.net.

[144] H.-J. Zhai, C. Bürgel, V. Bonačić-Koutecký, and L.-S. Wang. *J. Am. Soc. Chem.*, 130(28):9156–9167, 2008.

[145] P. Pyykkö, S. Riedel, and M. Patzschke. *Chem. Eur. J*, 11(12):3511, 2005.

[146] H. B. Wu, S. R. Desai, and L. S. Wang. *J. Chem. Phys.*, 103(10):4363, 1995.

[147] H. B. Wu, S. R. Desai, and L. S. Wang. *J. Phys. Chem. A*, 101(11): 2103, 1997.

[148] V. Bonačić-Koutecký, R. Mitrić, C. Bürgel, H. Noack, M. Hartmann, and J. Pittner. *Eur. Phys. J. D*, 34:113, 2005.

[149] J. Ho, K. M. Ervin, and W. C. Lineberger. *J. Chem. Phys.*, 93:6987, 1990.

[150] M. Arenz, U. Landman, and U. Heiz. *ChemPhysChem*, 7(9):1871, 2006.

[151] G. Mills, M. S. Gordon, and H. Metiu. *Chem. Phys. Lett.*, 359:493, 2002.

[152] Y. D. Kim, G. Ganteför, Q. Sun, and P. Jena. *Chem. Phys. Lett.*, 396: 69, 2004.

[153] V. Bonačić-Koutecký, J. Burda, R. Mitrić, M. Ge, G. Zampella, and R. Fantucci. *J. Chem. Phys.*, 117:3120, 2002.

[154] H. Häkkinen, M. Moseler, and U. Landman. *Phys. Rev. Lett.*, 89(3): 033401, 2002.

[155] F. Furche, R. Ahlrichs, P. Weis, C. Jacob, S. Gilb, and M. M. Bierweiler, T. Kappes. *J. Chem. Phys.*, 117:6982, 2002.

[156] V. Bonačić-Koutecký, L. Češpiva, P. Fantucci, and J. Koutecký. *J. Chem. Phys.*, 98:7981, 1993.

[157] V. Bonačić-Koutecký, L. Češpiva, P. Fantucci, J. Pittner, and J. Koutecký. *J. Chem. Phys.*, 100:490, 1994.

[158] L. Verlet. *Phys. Rev.*, 159:98, 1967.

[159] M. Bixon and J. Jortner. *J. Chem. Phys.*, 48:715, 1968.

[160] L. R. Khundkar and A. H. Zewail. *Ann. Rev. Phys. Chem.*, 41:15, 1990.

[161] I. Schek and J. Jortner. *J. Chem. Phys.*, 104(11):4337–4342, 1996.

[162] D. R. Lide, editor. Handbook of Chemistry and Physics. CRC Press, Cleveland, 71st edition, 1990-1991.

[163] R. Mitrić, C. Bürgel, and V. Bonačić-Koutecký. *Proc. Natl. Acad. Sci.*, 104(25):10314, 2007.

[164] J. Stanzel, F. Burmeister, M. Neeb, W. Eberhardt, R. Mitrić, C. Bürgel, and V. Bonačić-Koutecký. *J. Chem. Phys.*, 127(16):164312, 2007.

[165] A. Assion, M. Geisler, J. Helbing, V. Seyfried, and T. Baumert. *Phys. Rev. A*, 54(6):R4605, 1996.

[166] V. Blanchet, M. Z. Zgierski, T. Seideman, and A. Stolow. *Nature*, 401 (6748):52, 1999.

[167] G. Luttgens, N. Pontius, P. S. Bechthold, M. Neeb, and W. Eberhardt. *Phys. Rev. Lett.*, 88(7):076102, 2002.

[168] N. Pontius, P. S. Bechthold, M. Neeb, and W. Eberhardt. *Phys. Rev. Lett.*, 84(6):1132, 2000.

[169] J. R. R. Verlet, A. E. Bragg, A. Kammrath, O. Cheshnovsky, and D. M. Neumark. *J. Chem. Phys.*, 121(20):10015, 2004.

[170] A. E. Bragg, J. R. R. Verlet, A. Kammrath, O. Cheshnovsky, and D. M. Neumark. *J. Chem. Phys.*, 122(5):054314, 2005.

[171] M. Niemietz, P. Gerhardt, G. Ganteför, and Y. D. Kim. *Chem. Phys. Lett.*, 380(1-2):99, 2003.

[172] H. Häkkinen, B. Yoon, U. Landman, X. Li, H. J. Zhai, and L. S. Wang. *J. Phys. Chem. A*, 107(32):6168, 2003.

[173] S. Gilb, K. Jacobsen, D. Schooss, F. Furche, R. Ahlrichs, and M. M. Kappes. *J. Chem. Phys.*, 121(10):4619, 2004.

[174] M. Hartmann, J. Pittner, V. Bonačić-Koutecký, A. Heidenreich, and J. Jortner. *J. Chem. Phys.*, 108:3096, 1998.

[175] N. Pontius, P. S. Bechthold, M. Neeb, and W. Eberhardt. *Appl. Phys. B*, 71(3):351, 2000.

[176] V. A. Spasov, Y. Shi, and K. M. Ervin. *Chem. Phys.*, 262(1):75, 2000.

[177] G. Luttgens, N. Pontius, C. Friedrich, R. Klingeler, P. S. Bechthold, M. Neeb, and W. Eberhardt. *J. Chem. Phys.*, 114(19):8414, 2001.

[178] B. S. de Bas, M. J. Ford, and M. B. Cortie. *J. Phys. Condens. Matter*, 18(1):55, 2005.

[179] M. Walter, H. Häkkinen, J. Stanzel, M. Neeb, and W. Eberhardt. *Phys. Rev. B*, 76(15):155422, 2007.

[180] M. Schmidt, R. Kusche, W. Kronmüller, B. von Issendorff, and H. Haberland. *Phys. Rev. Lett.*, 79(1):99, 1997.

[181] P. S. Bechthold, U. Kettler, H. R. Schober, and W. Krasser. *Z. Phys. D*, 3:263, 1986.

[182] W. Harbich, S. Fredrigo, F. Meyer, D. M. Lindsay, J. Lignieres, J. C. Rivoal, and D. Kreisle. *J. Chem. Phys.*, 93:8535, 1990.

[183] A. M. Ellis, E. S. J. Robles, and T. A. Miller. *Chem. Phys. Lett.*, 201 (1-4):132, 1993.

[184] L. König, I. Rabin, W. Schulze, and G. Ertl. *Science*, 274:1353, 1996.

[185] I. Rabin, W. Schulze, and G. Ertl. *J. Chem. Phys.*, 108:5137, 1998.

[186] T. Diederich, J. Tiggesbäumker, and K. H. Meiwes-Broer. *J. Chem. Phys.*, 116:3263, 2002.

[187] E. Scorza, U. Birkenheuer, and C. Pisani. *J. Chem. Phys.*, 107:9645, 1997.

[188] M. C. Paganini, M. Chiesa, E. Giamello, S. Coluccia, G. Martra, D. M. Murphy, and G. Pacchioni. *Surf. Sci.*, 421(3):246, 1999.

[189] C. Sousa, G. Pacchioni, and F. Illas. *Surf. Sci.*, 429(1-3):217, 1999.

[190] M. Sterrer, O. Diwald, E. Knözinger, P. V. Sushko, and A. L. Shluger. *J. Phys. Chem. B*, 106:12478, 2002.

[191] P. V. Suhsko, J. L. Gavartin, and A. L. Shluger. *J. Phys. Chem. B*, 106:2269, 2002.

[192] D. Ricci, G. Pacchioni, P. V. Sushko, and A. L. Shluger. *J. Chem. Phys.*, 117(6):2844, 2002.

[193] J. Kramer, C. Tegenkamp, and H. Pfnür. *Phys. Rev. B*, 67:235401, 2003.

[194] M. Sterrer, T. Berger, O. Diwald, and E. Knözinger. *J. Am. Chem. Soc.*, 125:195, 2003.

[195] D. Ricci, C. Di Valentin, G. Pacchioni, P. V. Sushko, A. L. Shluger, and E. Giamello. *J. Am. Chem. Soc.*, 125(3):738, 2003.

[196] M. Chiesa, M. C. Paganini, E. Giamello, C. Di Valentin, and G. Pacchioni. *Angew. Chem. Int. Ed.*, 42(15):1759, 2003.

[197] M. Sterrer, T. Berger, S. Stankić, and E. Knözinger. *ChemPhysChem*, 5:1695, 2004.

[198] M. Chiesa, M. C. Paganini, G. Spoto, E. Giamello, C. Di Valentin, A. Del Vitto, and G. Pacchioni. *J. Phys. Chem. B*, 109(15):7314, 2005.

[199] M. Chiesa, M.C. Paganini, E. Giamello, D.M. Murphy, C. DiValentin, and G. Pacchioni. *Acc. Chem. Res.*, 39(11):861–867, 2006.

[200] M. Sterrer, M. Heyde, M. Novicki, N. Nilius, T. Risse, H.-P. Rust, G. Pacchioni, and H.-J. Freund. *J. Phys. Chem. B*, 110(1):46–49, 2006.

[201] A. Del Vitto, G. Pacchioni, F. O. Delbecq, and P. Sautet. *J. Phys. Chem. B*, 109(16):8040, 2005.

[202] K. M. Neyman, C. Inntam, L. V. Moskaleva, and N. Rösch. *Chem. Eur. J.*, 13:277, 2007.

[203] P. V. Sushko, A. L. Shluger, and C. R. Catlow. *Surface Science*, 450: 153, 2000.

[204] P. J. Hay and W. R. Wadt. *J. Chem. Phys.*, 82:284, 1985.

[205] B. G. Dick and A. W. Overhauser. *Phys. Rev.*, 112:90, 1958.

[206] A. L. Shluger, A. L. Rohl, D. H. Gay, and R. T. Williams. *J. Phys.: Condens. Matter*, 6:1825, 1994.

[207] R. Ahlrichs, M. Bär, M. Häser, H. Horn, and C. Kölmel. *Chem. Phys. Lett.*, 162:165, 1989.

[208] D. Rappoport and F. Furche. *J. Chem. Phys.*, 122:064105, 2005.

[209] F. Furche and D. Rappoport. *Density functional theory for excited states: equilibrium structure and electronic spectra*, volume 16 of *Computational and Theoretical Chemistry*, chapter III. Elsevier, Amsterdam, 2005.

[210] R. H. Byrd, P. Lu, J. Nocedal, and C. Zhu. *SIAM J. Scientific Computing*, 16:1190, 1995.

[211] V. Beutel, H.-G. Krämer, G. L. Bhale, M. Kuhn, K. Weyers, and W. Demtröder. *J. Chem. Phys.*, 98:2699, 1993.

[212] V. Bonačić-Koutecký, C. Bürgel, L. Kronik, A. E. Kuznetsov, and R. Mitrić. *Eur. Phys. J. D*, 45(3):471, 2007.

[213] L. N. Kantorovich, A. L. Shluger, P. V. Sushko, J. Günster, P. Stracke, D. W. Goodman, and V. Kempter. *Faraday Discuss*, 114:173, 1999.

[214] V. E. Henrich, G. Dresselhaus, and H. J. Zeiger. *Phys. Rev. B*, 22: 4764, 1980.

[215] P. A. Cox and A. A. Williams. *Surf. Sci.*, 175:L782, 1986.

[216] C. A. Kraus. *J. Am. Chem. Soc.*, 30:1323, 1908.

[217] D. Ochs, W. Maus-Friedrichs, M. Brause, J. Günster, V. Kempter, V. Puchin, A. L. Shluger, and L. Kantorovich. *Surf. Sci.*, 365:557, 1996.

[218] E. Tapavicza, I. Tavernelli, and U. Rothlisberger. *Phys. Rev. Lett.*, 98: 023001, 2007.

[219] R. Mitrić, U. Werner, and V. Bonačić-Koutecký. *J. Chem. Phys.*, 129: 164118, 2008.

[220] U. Werner, R. Mitrić, T. Suzuki, and V. Bonačić-Koutecký. *Chem. Phys.*, 349:319, 2008.

[221] M. L. Kimble, N. A. Moore, A. W. Castleman, Jr., C. Bürgel, R. Mitrić, and V. Bonačić-Koutecký. *Eur. Phys. J. D*, 43(1-3):205, 2007.

[222] to be published.

[223] C. Jackschath, I. Rabin, and W. Schulze. *Z. Phys. D*, 22:517, 1992.

Liste der Veröffentlichungen - Christian Bürgel

1. C. Bürgel, “Theoretische Untersuchung der Struktur-Reaktivitäts-Beziehung von anionischen Gold-Clustern bei der Oxidation von CO”, Diplomarbeit, Humboldt Universität zu Berlin, (2004).

2. R. Mitrić, C. Bürgel, J. Burda, V. Bonačić-Koutecký, P. Fantucci, “Structural properties and reactivity of bimetallic silver-gold clusters”, *Eur. Phys. J. D* **24**, 41 (2003).

3. M. L. Kimble, A. W. Castleman, Jr., R. Mitrić, C. Bürgel, V. Bonačić-Koutecký, “Reactivity of atomic gold anions toward oxygen and the oxidation of CO: Experiment and theory”, *J. Am. Soc. Chem.* **126**, 2526 (2004).

4. V. Bonačić-Koutecký, R. Mitrić, C. Bürgel, H. Noack, M. Hartmann, J. Pittner, “Tailoring the chemical reactivity and optical properties of clusters by size, structures and lasers”, *Eur. Phys. J. D* **34**, 113 (2005).

5. A. Springer, C. Bürgel, V. Böhrsch, R. Mitrić, V. Bonačić-Koutecký, M. W. Linscheid, “The gas-phase chemistry of cis-diammineplatinum(II) complexes: A joint experimental and theoretical study”, *ChemPhysChem* **7**, 1779 (2006).

6. M. L. Kimble, N. A. Moore, G. E. Johnson, A. W. Castleman, Jr., C. Bürgel, R. Mitrić, V. Bonačić-Koutecký, “Joint experimental and theoretical investigations of the reactivity of $\mathrm{Au_2O_n^-}$ and $\mathrm{Au_3O_n^-}$ (n=1-5) with carbon monoxide”, *J. Chem. Phys.* **125**, 204311 (2006).

7. M. L. Kimble, A. W. Castleman, Jr., C. Bürgel, V. Bonačić-Koutecký, “Interactions of CO with $\mathrm{Au_nO_m^-}$ (n$\geq$4)“, *Int. J. Mass. Spectrom.* **254**, 163 (2006).

8. C. Bürgel, R. Mitrić, V. Bonačić-Koutecký, “Emissive properties of silver particles at silver oxide surface defects“, *Appl. Phys. A* **82**, 117 (2006).

9. V. Bonačić-Koutecký, R. Mitrić, C. Bürgel, B. Schäfer-Bung, “Cluster properties in the regime in which each atom counts”, *Comput. Mater. Sci.* **35**, 151 (2006).

10. V. Bonačić-Koutecký, C. Bürgel, L. Kronik, A. E. Kuznetsov, R. Mitrić, “Optical properties of small silver clusters supported at MgO”, *Eur. Phys. J. D* **45**, 471 (2007).

11. T. Gleitsmann, M. E. Vaida, T. M. Bernhardt, V. Bonačić-Koutecký, C. Bürgel, A. E. Kuznetsov, R. Mitrić, “Mass-selected Ag_3 clusters soft-landed onto MgO/Mo(100): femtosecond photoemission and first-principles simulations”, *Eur. Phys. J. D* **45**, 477 (2007).

12. J. Stanzel, F. Burmeister, M. Neeb, W. Eberhardt, R. Mitrić, C. Bürgel, V. Bonačić-Koutecký, “Size-dependent dynamics in excited states of gold clusters: From oscillatory motion to photoinduced melting”, *J. Chem. Phys.* **127**, 164312 (2007).

13. R. Mitrić, C. Bürgel, V. Bonačić-Koutecký, “Reactivity-promoting criterion based on internal vibrational energy redistribution”, *Proc. Natl. Acad. Sci.* **104**, 10314 (2007).

14. R. Mitrić, U. Werner, C. Bürgel, V. Bonačić-Koutecký, “Dynamical aspects and the role of IVR for the reactivity of noble metal clusters towards molecular oxygen”, *Eur. Phys. J. D* **43**, 201 (2007).

15. M. L. Kimble, N. A. Moore, A. W. Castleman, Jr., C. Bürgel, R. Mitrić, V. Bonačić-Koutecký, “Reactivity of anionic gold oxide clusters towards CO: experiment and theory”, *Eur. Phys. J. D* **43**, 205 (2007).

16. V. Bonačić-Koutecký, R. Mitrić, C. Bürgel, M. Nössler, “Ultrafast dynamics in noble metal clusters: The role of internal vibrational redistribution”, *Chem. Phys.* **350**, 111 (2008).

17. H.-J. Zhai, C. Bürgel, V. Bonačić-Koutecký, L.-S. Wang, “Probing the electronic structure and chemical bonding of gold oxides and sulfides in AuO_n^- and AuS_n^- (n=1,2)”, *J. Am. Soc. Chem.* **130**, 9156 (2008).

18. C. Bürgel, N. M. Reilly, G. E. Johnson, R. Mitrić, M. L. Kimble, A. W. Castleman, Jr., V. Bonačić-Koutecký, “Influence of charge state on the mechanism of CO oxidation on gold clusters”, *J. Am. Chem. Soc.* **130**, 1694 (2008).

Selbständigkeitserklärung

Hiermit erkläre ich, Christian Bürgel, die Dissertation selbständig und nur unter Verwendung der angegebenen Hilfen und Hilfsmittel angefertigt zu haben. Ich habe mich anderweitig nicht um einen Doktograd beworben und besitze einen entsprechenden Doktograd nicht. Ich erkläre die Kenntnisnahme der dem Verfahren zugrunde liegenden Promotionsordnung der Mathematisch-Naturwissenschaftlichen Fakultät I der Humboldt-Universität zu Berlin vom 01. Oktober 2002.

Berlin, 19.01.2009